

# Nanogap Capacitive Biosensor for Label-Free Aptamer-Based Protein Detection

A thesis submitted to the School of Mathematics and Physical Sciences in  
the University of Hull in partial fulfilment of the requirements  
for the degree of Doctor of Philosophy

Zahra Ghobaei Namhil, BSc. MSc.

January 2018

*“Everyone is genius. But if you judge a fish on its ability to climb a tree, it will live its whole life believing that it is stupid.”*

Albert Einstein

## ABSTRACT

Recent advances in nanotechnology offer a new platform for the label free detection of biomolecules at ultra-low concentrations. Nano biosensors are emerging as a powerful method of improving device performance whilst minimizing device size, cost and fabrication times. Nanogap capacitive biosensors are an excellent approach for detecting biomolecular interactions due to the ease of measurement, low cost equipment needed and compatibility with multiplex formats.

This thesis describes research into the fabrication of a nanogap capacitive biosensor and its detection results in label-free aptamer-based protein detection for proof of concept. Over the last four decades many research groups have worked on fabrication and applications of these type of biosensors, with different approaches, but there is much scope for the improvement of sensitivity and reliability. Additionally, the potential of these sensors for use in commercial markets and in everyday life has yet to be realized.

Initial work in the field was limited to high frequency ( $>100$  kHz) measurements only, since at low frequency there is significant electronic thermal noise ( $\langle V^2 \rangle = 4k_B TR$ ) from the electrical double layer (EDL). This was a significant drawback since this noise masked most of the important information from biomolecular interactions of interest. A novel approach to remove this parasitic noise is to minimize the EDL impedance by reducing the capacitor electrode separation to less than the EDL thickness. In the case of aptamer functionalized electrodes, this is particularly advantageous since device sensitivity is increased as the dielectric volume is better matched to the size of the biomolecules and their binding to the electrode surface. This work has demonstrated experimentally the concepts postulated theoretically.

In this work we have fabricated a large area ( $100 \times 5 \mu\text{m} \times 5 \mu\text{m}$ ) vertically oriented capacitive nanogap biosensor with a 40 nm electrode separation between two gold electrodes. A silicon dioxide support layer separates the two electrodes and this is

partially etched (approximately 800 nm from both sides of each 5  $\mu\text{m}$  x 5  $\mu\text{m}$  capacitor), leaving an area of the gold electrodes available for thiol-aptamer functionalization.

AC impedance spectroscopy measurements were performed with the biosensor in the presence of air, D.I. water, various ionic strength buffer solutions and aptamer/protein pairs inside the nanogap. Applied frequencies were from 1 Hz to 500 kHz at 20 mV AC voltage with 0 DC. We obtained relative permittivity results as a function of frequency for air ( $\epsilon=1$ ) and DI water ( $\epsilon\sim 80$ ) which compares very favorably with previous works done by different research groups.

The sensitivity and response of the sensors to buffer solution (SSC buffer) with various ionic strengths (0.1x SSC, 0.2x SSC, 0.5x SSC and 1x SSC) was studied in detail. It was found that in the low frequency region (<1 kHz) the relative permittivity (capacitance) was broadly constant, that means it is independent from the applied frequency in this range. With increasing buffer concentration, the relative permittivity starts to increase (from  $\epsilon=170$  for 0.1x SSC to  $\epsilon=260$  for 1x SSC).

The sensor performance was further investigated for aptamer-based protein detection, human alpha thrombin aptamers and human alpha thrombin protein pairs were selected for proof of concept. Aptamers were functionalized into the gold electrode surface with the Self-Assembly-Monolayer (SAM) method and measurements were performed in the presence of 0.5x SSC buffer solution ( $\epsilon=180$ ). Then the hybridization step was carried out with 1  $\mu\text{M}$  of human alpha thrombin protein followed by measurements in the presence of the same buffer ( $\epsilon=130$ ). The response of the sensors with different solutions inside the nanogap was studied at room temperature (5 working devices were tested for each step). The replacement of the buffer solution ( $\epsilon=250$ ) with lower relative permittivity biomolecules (aptamer  $\epsilon=180$ ) and further binding proteins to immobilized aptamer ( $\epsilon=130$ ) was studied. To validate these results, a control experiment was carried out using different aptamers, in this case which are not able to bind to human alpha thrombin protein. It was found that the relative permittivity did not change after the hybridization

step compared to the aptamer functionalization step, which indicates that the sensors performance is highly sensitive and reliable.

This work serves as a proof of concept for a novel nanogap based biosensor with the potential to be used for many applications in environmental, food industry and medical industry. The fabrication method has been shown to be reliable and consistent with the possibility of being easily commercialized for mass production for use in laboratories for the analysis of a wide range of samples.

## **ACKNOWLEDGEMENT**

I am full of gratitude to many people in this project that helped and supported me through these 5 years of research. My special thanks to those who have helped contribute to this thesis at the University of Hull. Although I may not list you all by name in the following lines, please forgive me and note that I give you the first place in my acknowledgements.

I would like to express my special appreciation and thanks to my first supervisor Dr. Neil Kemp, you have been a tremendous mentor for me. I would like to thank you for encouraging my research and for allowing me to grow as a research scientist. Your advice on research, writing of this thesis as well as on my career have been priceless. You were involved in every aspect of my research, helped enormously by sharing your invaluable experience and enlightened my path with your guidance and support. I could not have imagined having a better advisor and mentor for my Ph.D. study.

Besides my first supervisor, I would like to specially thank to my second supervisors Dr. Ali Adawi and Prof. Nicole Pamme, for the continuous support and great guidance of my Ph.D. study and related research. They were always available and happy to help me to solve any difficult moment of my research project.

My sincere thanks also goes to Dr. Cordula Kemp for her contribution on biological aspect of this thesis, Dr. Chris Walton and all other technical staff whom provided me access to the laboratory and research facilities. Without their precious support it would not be possible to conduct this research.

I thank my fellow lab-mates in for the stimulating discussions, for the days we were working together before deadlines, and for all the fun we have had in the past five years.

A special thanks to my family. Words cannot express how grateful I am to my parents, to my husband for his endless love and support and to my little son to be joy of my life for the past 2.5 years.

# TABLE OF CONTENTS

<b>Abstract .....</b>	<b>3</b>
<b>Acknowledgement .....</b>	<b>6</b>
<b>Table of contents .....</b>	<b>7</b>
<b>Chapter 1. Introduction .....</b>	<b>11</b>
1.1. Introduction .....	12
1.2. Biosensors .....	16
1.2.1 .Biosensor categories - biological recognition elements.....	17
Immobilization techniques .....	17
Enzyme-based biosensor.....	20
Antibody-based biosensor.....	22
Aptamer-based Biosensor.....	24
1.2.2. Biosensor categories - type of transducer .....	26
Mechanical.....	28
Optical.....	29
Electrochemical.....	31
Amperometric.....	31
Potentiometric .....	33
Impedimetric .....	35
1.3. Motivations .....	36
Objectives.....	39

Research scope.....	39
<b>Chapter 2. Electrochemical impedance spectroscopy and Nano-gap capacitive sensor principle and background theory .....</b>	<b>41</b>
2.1. Introduction .....	42
2.2. Basic principle of electrochemical impedance spectroscopy.....	43
2.2.1. Alternating Current (AC) circuit theory.....	44
2.2.2. Electrical double layer.....	48
2.2.3. Equivalent Circuit models and elements for Faradaic and non-Faradaic scheme.....	52
2.2.4. Data presentation .....	59
2.2.5. Electrode size and material.....	63
2.3. Nanogap capacitive sensor .....	66
2.3.1. Benefits of a Nanogap Structure for Impedance Spectroscopy .....	71
2.3.2. Current state of the art use of Nano-gap capacitors for label-free detection.....	80
<b>Chapter 3. Nanogap capacitive sensor design and fabrication .....</b>	<b>87</b>
3.1. Sputtering and etching optimizations .....	88
3.1.1. SiO <sub>2</sub> Dielectric layer sputtering .....	88
3.1.2. Metal-Oxide-Semiconductor (MOS) fabrication for SiO <sub>2</sub> characterization ...	90
3.1.3. Substrate temperature experimental study.....	92
3.1.4. HF etching experimental study.....	93
3.2. Nanogap capacitor fabrication process.....	96



3.2.1. Sensor structure and photomask design .....	96
Photomask design.....	98
3.3.2 Sensor fabrication.....	101
Substrate and surface preparation .....	102
Photolithography and bottom electrode formation .....	102
SiO <sub>2</sub> sputtering .....	109
Fabrication of the top electrode .....	111
Nano gap formation via HF etching of SiO <sub>2</sub> layer .....	116
Top window lithography for introducing solution to Nano-gap.....	120
3.5. Summary of trial prototypes and fabrication methods .....	130
<b>Chapter 4. Results and Discussion .....</b>	<b>136</b>
4.1. Introduction .....	137
4.2. Optimization and characterization results .....	138
4.2.1. Substrate temperature .....	138
4.2.2. Metal-Oxide-Semiconductor (MOS) devices .....	141
4.2.3. hydrofluoric acid (HF) etching .....	146
4.2.4. Permittivity calculations.....	151
4.3. Sensitivity and buffer solutions tests.....	155
4.4. Aptamer and protein measurements.....	157
4.5. Discussion.....	160
<b>Chapter 5. Conclusion and future work .....</b>	<b>165</b>

5.1. Conclusion .....	166
5.2. Future work .....	168
<b>References.....</b>	<b>170</b>

# Chapter 1. INTRODUCTION

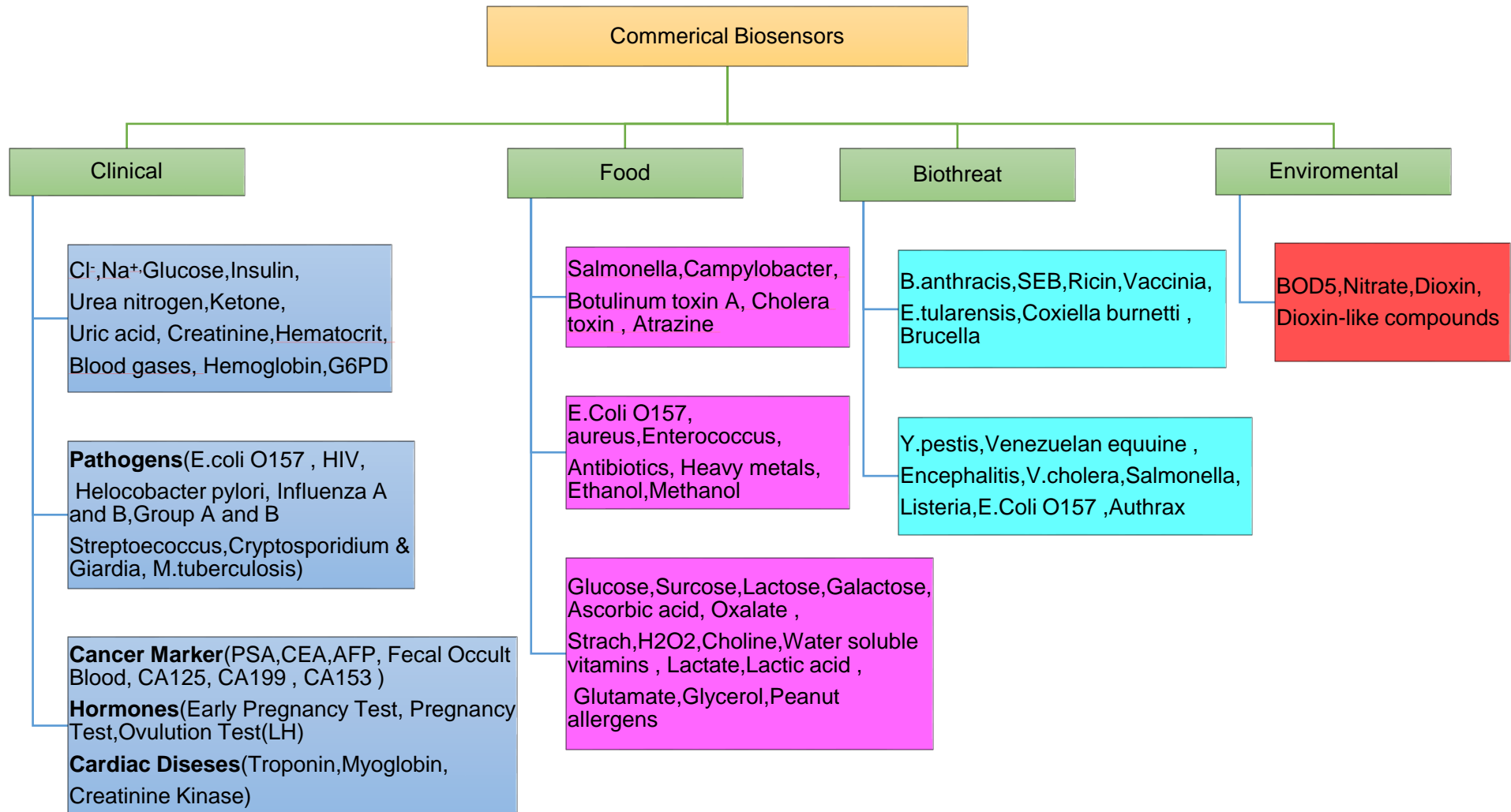
## 1.1. INTRODUCTION

The very general definition of a sensor is a device that can be used to identify the presence or absence of an object <sup>1</sup>. This could be on the macro scale, such as an automatic door sensor detecting a person walking into a building or on the microscopic scale, where a sensor can detect the presence of a very small object such as a biomolecule. Sensors are commonly used in a wide variety of technological applications and have become an essential detecting tool in most areas of daily life. Examples of this include: clinical applications (such as diagnostic and drug delivery), biological threat detection, use in the food industry and environmental monitoring <sup>2</sup>. Table 1.1 illustrates commercial available biosensors for such application.

The main challenge faced by practitioners in the diagnosis and monitoring of cancer and various diseases is the time intensive nature and cost of routine blood and urine tests and other related diagnostic processes. Even routine tests require analytical laboratory facilities, professional staff, high sample volumes and time. Analytical sensors have many potential advantages which address these challenges such as low cost, fast response times, high sensitivity and straightforward operation. These factors could allow operation without the requirement of expensive laboratory equipment <sup>3,4</sup>.

Diagnostic and drug delivery based on lab-on-chip (LOC) technology is a highly promising area of research that brings a huge variety of opportunities to healthcare professionals in terms of saving time and cost <sup>5</sup>. These LOC platforms are commonly based on a technology called microfluidics, which is, simply put, the science and engineering of fluid flow on the microscale <sup>6,7,8</sup>.

Table 1-1. Commerically available biosensors on the world market.modified from ref <sup>2</sup>.



The use of sensors in society covers a broad spectrum of applications. The detection of pathogens is one key area of use. Some pathogenic bacteria have high mortality and transmission rates. Examples include influenza, HIV (Human Immunodeficiency Virus), tuberculosis, malaria and *Yersinia pestis*, which significantly threaten public health <sup>8</sup>. These pathogens can also be classified as a biothreat and necessitate a fast response and reliable detection to avoid transmission. Early detection of biothreat agents allows rapid decision making leading to efficient mobilization of suitable and effective responses during a biological emergency <sup>9</sup>. Existing identification and detection process can be slow, expensive and require specialist laboratory facilities, whereas advanced biosensing techniques allow highly sensitive detection with the added advantage of being rapid, low cost and precise <sup>2, 10</sup>.

Food is one of the essential daily needs for humans. It is also one of the primary environments for pathogens like *Escherichia coli*, *Salmonella* spp., *Campylobacter jejuni* and *Listeria monocytogenes* to develop, causing most of the foodborne diseases <sup>11,12, 13</sup>. The dairy industry requires high testing rates because, despite quality control, refrigeration and pasteurization, it is still one of the main causes of foodborne illnesses due to contaminants <sup>14,15</sup>.

With an exponentially increasing population in recent decades, the use of chemicals in industrial areas have also been massively increased. The release of many toxic compounds into water, air and soil can cause many serious environmental problems globally <sup>16,17</sup>. The exposure of live biological cells to these toxic chemical compounds can cause illness in humans, animals and plants. Hence, the monitoring, identification and detection of these chemicals is very important for the safety and security of all living things<sup>18</sup>. Using biosensors, scientists have been able to perform instant monitoring and detection of a large number of chemicals in various ecosystems which could have otherwise caused a hazard and risk to our planet<sup>19</sup>.

Lab-On-Chip technology has huge potential as a tool for portable, real time and label-free medical diagnostics and it can also be used for detecting foodborne pathogens in an extremely short period of time and with very high sensitivity. Additionally, environmental contaminants can be quickly detected and identified to reduce risk to the environment and the living things within an ecosystem <sup>14, 20</sup>.

This thesis will continue by explaining biosensors; the general definition and categorization of the different types of biosensor based on the recognition element and transducer being utilized. The final part of this chapter will cover the motivations, research objective and scope of this work. In Chapter 2, the basic principles of electrochemical impedance spectroscopy will be introduced in the first part of the chapter. The second part of Chapter 2 will focus on nanogap capacitive sensors in the literature (state-of-the-art) and the final part will cover identifying the demand for this type of sensor and how this project will take steps towards nanogap capacitive biosensor for label-free detection. Chapter 3 will focus on sensor design and fabrication and the visual characterization of the sensor with optical microscopy, scanning electron microscopy (SEM) and atomic force microscopy (AFM). This chapter also covers the details of measurement setup, surface functionalization. Chapter 4 will present sensor performance results in terms of sensitivity and reliability, as well as critical analysis on these results. Finally, in Chapter 5, a brief summary of the project will be presented with its key achievements and conclusion. The final part of this chapter will explain the future work for this project.

## 1.2. BIOSENSORS

Biosensors are powerful analytical tools with the potential to be used in the applications mentioned in the previous section. As discussed, there are several properties which make biosensors more favorable when compared to other lab-based detection techniques: reliability, accuracy, cost effectiveness and, perhaps most importantly, they are time saving and easy to use<sup>21, 22, 23</sup>.

A biosensor consists of three main components: the biological recognition element (with samples from blood, urine, food, water or soil, for example), the transducer element (electrochemical, optical, colorimetric, mass or magnetic) and detector (signal amplification and processing)<sup>24</sup>.

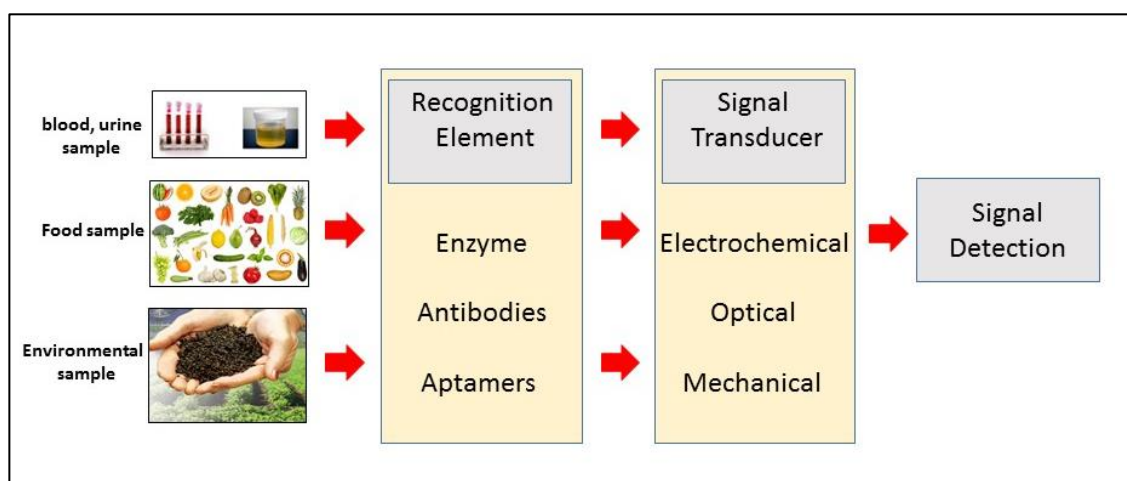


Figure 1.1. Main parts of a system to be called " biosensor". Here the start point is the sample, from which recognition elements (DNA, enzyme, antibody or aptamer) are extracted. The signal transducer follows, which converts the biological event (target molecule binding to recognition element) to a measurable signal at the end.

Biosensors in general can be categorized according to the type of biological recognition element and immobilization technique or the type of transducers used.



## 1.2.1 .BIOSENSOR CATEGORIES - BIOLOGICAL RECOGNITION ELEMENTS

The biological recognition element controls the selectivity and specificity which allows the biosensor to respond to a specific target with minimum interference from undesired substances. The recognition elements include: enzymes, antibodies and aptamers. The four main immobilization techniques for these elements include adsorption, covalent binding, affinity bonding and entrapment.

### IMMOBILIZATION TECHNIQUES

Immobilization in biosensors can be explained as the attachment of molecules (enzymes, antibodies and aptamer for this case) to a surface such that there is restricted or complete loss of molecule mobility. Depending on the approach, it may change the molecules activity due to random orientation and structural deformation. It is crucial to maintain the biological activity with no impact on conformation and function during immobilization <sup>25</sup>. Figure 1.2 shows the immobilization techniques <sup>26</sup>.

The method for immobilization is strongly dependent on the immobilization surface, molecule (analyte) properties and the purpose of the biological interaction. The four common immobilization techniques will be explained in more detail below.

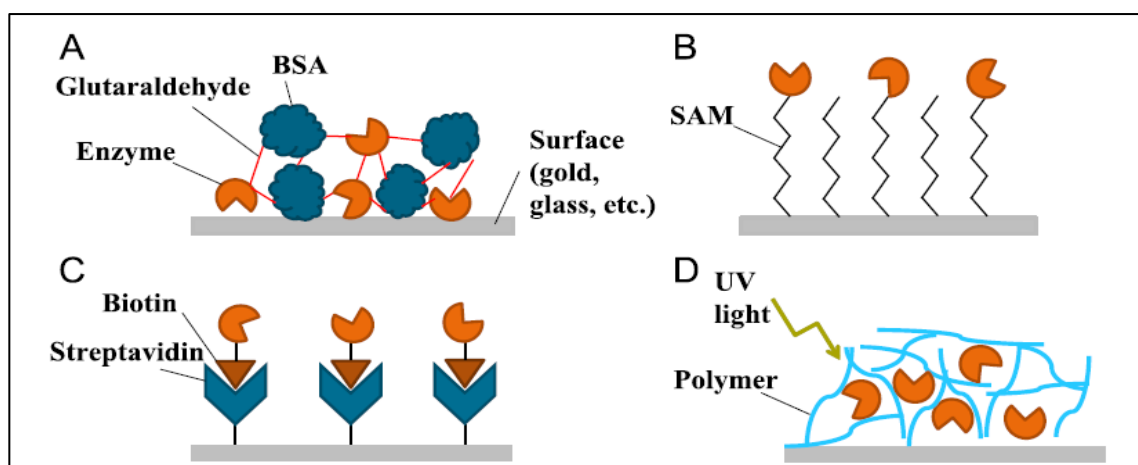


Figure 1.2 . Immobilization techniques A) adsorption, B) covalent bonding, C) affinity bonding and D) entrapment <sup>26</sup>.

Absorption is the simplest and easiest approach. It is also known as Physisorption (i.e. physical adsorption). Biomolecules, such as proteins and enzymes, are adsorbed on the surface via intermolecular interactions (for example electrostatic, van der Waals, hydrogen bonding, hydrophobic) <sup>27</sup>.

The formation of a bond layer comes about by introducing the prepared solution to the immobilization surface, either by direct contact or the continuous flow of the solution. This layer is most likely heterogeneous and randomly orientated, because each molecule can create more than one contact in a variety of orientations. Potential disadvantages of the adsorption technique are this random orientation and weak attachment. Moreover, the intermolecular interaction in the adsorption mechanism is extremely dependent on environmental conditions in the solution such as pH, ionic strength, temperature and surface condition <sup>25</sup>.

Covalent bonding is a more complicated technique and involves the formation of a covalent bond between the protein and support surface. In this method, the immobilization surface is activated by a reactive reagent. This surface will then react with an amino acid on the outer area of a protein due to the formation of an irreversible linkage with high and stable protein coverage <sup>27</sup>.

The covalent bonding method contains two groups of linker molecules: the first group corresponds to the immobilization surface and forms a so-called self-assembled monolayer (SAM) and the second group forms a covalent bond with enzymes. There are many advantages of utilizing this technique, such as high uniformity of the layer, precise control of sample quantity and low possibility of denaturation. In comparison with adsorption, this method requires complex and sophisticated preparation and extended fabrication time. Additionally, the chemicals need to be as pure as possible.

Affinity bonding method is related to the naturally strong affinity of certain pairs of biomolecules to one another. In contrast to adsorption and covalent bonding, the interaction in affinity bonding produces stronger, highly specific and oriented

immobilization. Moreover, this method of immobilization is reversible using chemical or heat treatment and pH change. This will allow re-use of the same surface. Affinity bonding can also be used in conjunction with other techniques such as adsorption and covalent binding. A bio-affinity reagent can be used as an intermediate binding species between the surface of interest and the target protein <sup>27, 28</sup>.

There are several known protein interactions such as Avidin-biotin, biotin-streptavidin and a protein to immunoglobulins (G) (known as A/G proteins) which are based on affinity bonding. Also, affinity captured ligand, DNA hybridization, antibody and aptamer are the common biomolecules which show high affinity to target proteins <sup>27</sup>. For example, both biotin-Avidin and biotin-streptavidin proteins can be attached to a wide range of substrates. Avidin and Streptavidin can be directly immobilized to the surface via adsorption or covalent bonding. Biotin will then covalently bond to the enzyme and, when the bonded enzyme comes into contact with the surface, a strong affinity based bond will form <sup>26, 25</sup>.

Nevertheless, the interactions in all the immobilization techniques described above will occur through direct contact with solution. In the entrapment method, however, the biomolecules are embedded into a three dimensional polymer matrix which is absorbent to aqueous solution and thus able to retain a high amount of water <sup>26</sup>.

An example of this technique is the use of hydrogels for enzyme immobilization. Hydrogels are crosslinked polymers with a three-dimensional structure and high water absorbency and provide an excellent environment for enzymes to carry out their biological functions with less denaturation. They also create a protective environment for entrapped enzymes preventing degeneration and non-specific adsorption <sup>29</sup>.

The enzyme is mixed with a monomer solution (hydrogel), followed by introducing the mixture to the electrodes. When a constant current or cyclic voltage sweep is applied between the working and counter electrode for a set period of time, the monomer polymerizes on the electrode and entraps the enzyme.

## ENZYME-BASED BIOSENSOR

Enzymes are proteins (except some RNA molecules which can act as enzymes) which catalyze or accelerate chemical reactions. The activity of an enzyme mainly depends on a cofactor (i.e. a small molecule), which attaches to enzyme and forms the enzyme catalytic action.

Enzyme names can be categorized using the: “-ase” (for example Oxidase, dehydrogenase, carboxylase, Glucose oxidase) or “-in” (for example trypsin, chymotrypsin, papain )<sup>30, 31</sup>.

Enzymes are important tools in biosensing because of their specificity, a theory first proposed by the German chemist Emil Fischer in 1894. Fischer described the enzyme and substrate interaction in his “key-lock” hypotheses whereby only the correct key shape (substrate) will fit the appropriate lock (enzyme). A simplified representation of this is shown in Figure 1.3. In 1958, Daniel Koshland extended Fischer’s hypothesis and proposed the “induced-fit model” for enzyme and substrate binding.

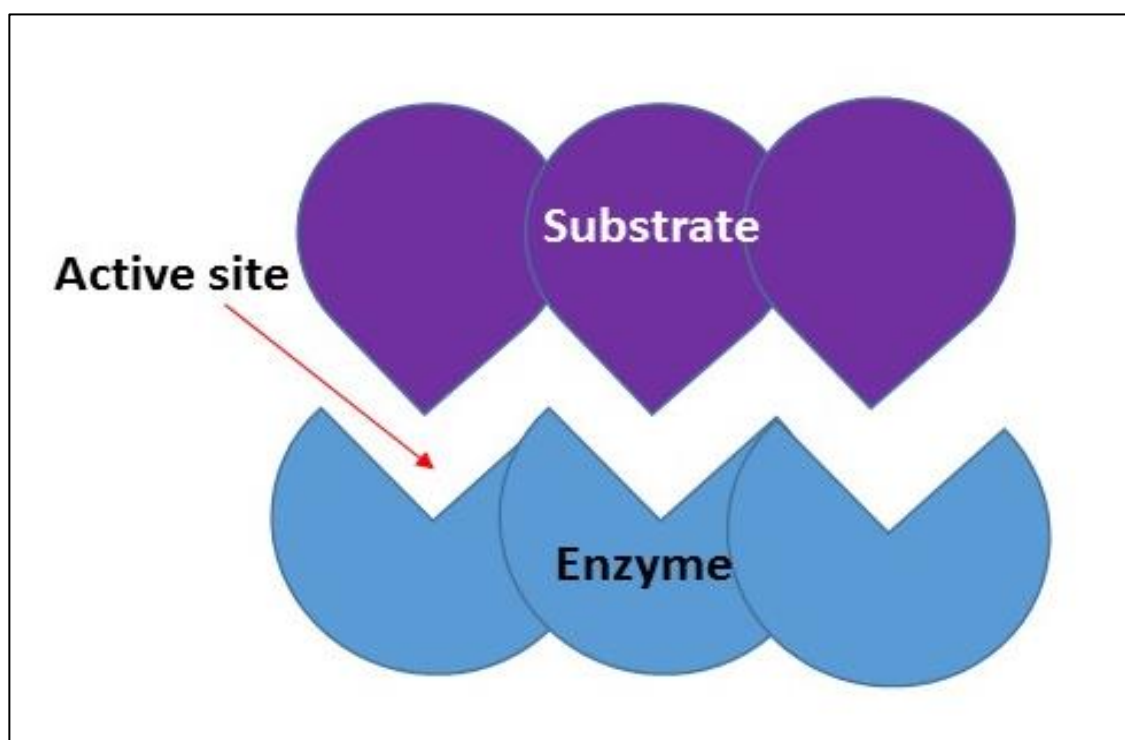


Figure 1.3. Illustration of enzyme and substrate binding at active site showing the lock and key theory.

The substrate binds to the enzyme in an area called the active site. The shape and charge properties of active site allows enzyme to bind to a specific type of substrate molecule, hence the specificity.

Enzymatic biosensors are analytical tools consisting of enzymes (as the biological recognition element) and transducers (electrodes). In this type of device, the interaction between the enzyme and the electrode results in a signal that is proportional to the concentration of the target analyte. There are a variety of signals to detect, for example temperature change, Redox (reduction-oxidation) reaction rate, proton concentration, light generation and mass difference. This signal is then transformed into a measurable response, such as a current, voltage, temperature difference or electrochemical absorption of light. Finally, the signal can be amplified, where necessary, to fit the detection purposes <sup>32</sup>.

The first enzyme biosensor was reported by Clark et al., in 1962 <sup>33</sup>. This glucose biosensor was used for the detection and measurement of diabetes mellitus and was based on glucose oxidase (GOx enzyme) catalyzing the oxidation of glucose to hydrogen peroxide and D-glucono-lactone. From this well studied chemical reaction, it is possible to calculate the glucose concentration by screening the consumption of oxygen or creation of hydrogen peroxide <sup>34</sup>. In 1975, Clark's proposed research was commercialized under the brand name 23A Glucose Analyzer by Yellow Springs Instruments Company. This early enzyme biosensor was able to directly measure glucose levels in human blood <sup>31, 34</sup>.

## ANTIBODY-BASED BIOSENSOR

The immune system of a human body plays a vital defense role against all infective diseases. Part of this defense mechanism is the production of antibodies (Ab) via an immunological response in the presence of a foreign substance: an antigen (Ag).

The antibody is generally represented as a Y-shape molecule consisting of two heavy and two light chains. The shorter light chain (light blue in the figure) interacts with the N-terminus of heavy chains (Fc, dark blue in the figure) to form the two “arms” or antigen binding ('Fab') domains, which are composed of both constant and variable regions <sup>35</sup>.

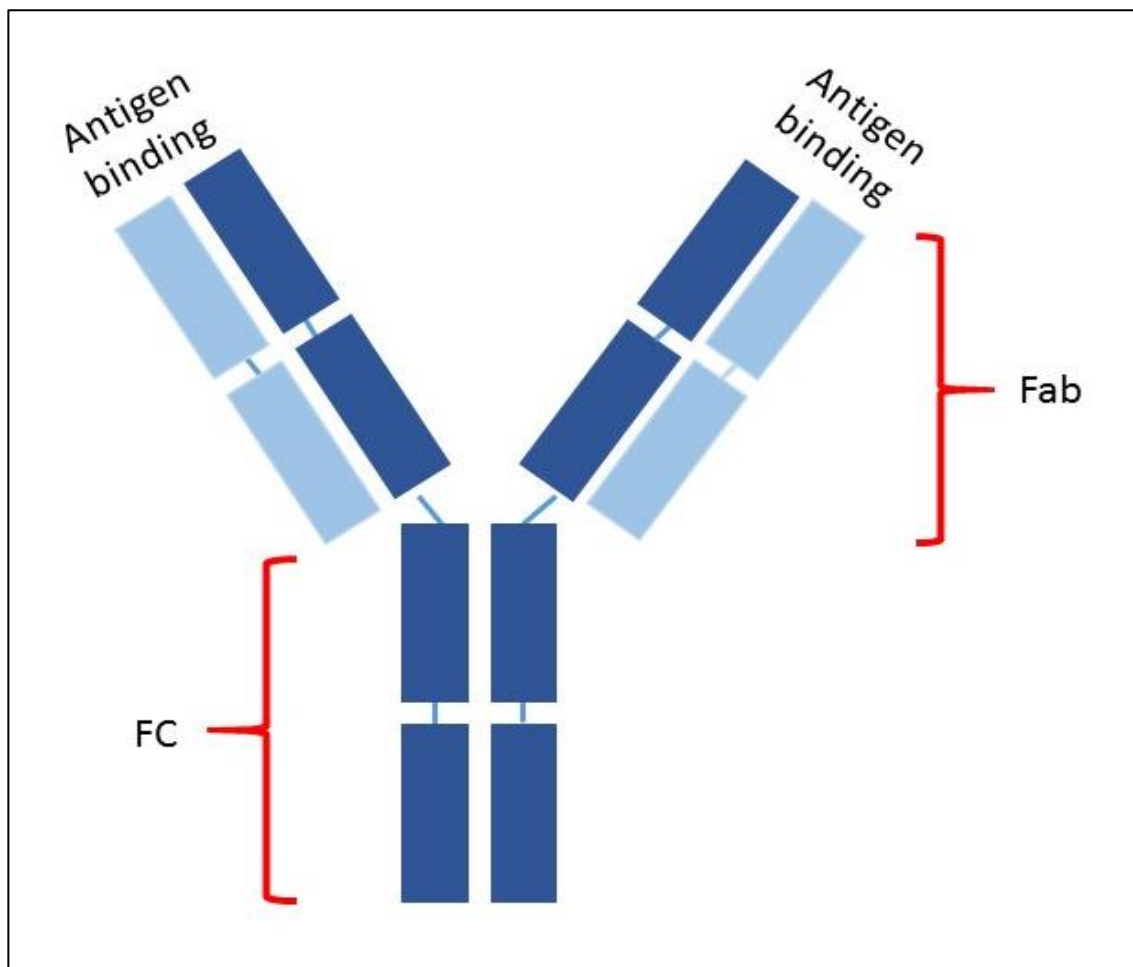


Figure 1.4. General structure of an IgG antibody (~ 150kDa), showing the heavy and light chains, the Fab, Fc domains and antigen binding sites.

The two arms in the Fab domain contain six variable amino acid loops, which are known as the complementarity determining regions (CDRs) and are responsible for binding to the antigen. The constant region is located at the bottom of Y-shape and is known as the

Fc domain. This mediates the antibody's interaction with macrophages and other cells expressing Fc receptors<sup>35, 36</sup>.

The amino acids within the variable region vary from one antigen-specific antibody to another (the region name comes from this), whereas the amino acids within the constant region are very similar between one class of antibody and another. There are five classes of antibody based on their heavy chains: IgA, IgG, IgM, IgD and IgE<sup>37</sup>.

Antibody-based biosensors are known as immunosensors that are specifically able to detect the binding of an antibody and an antigen at the transducer surface. In this type of sensor, a measurable signal can be produced with the binding of an antibody and antigen<sup>38</sup>. Immunosensors can be divided into two main classes according to the type of transducer: optical and electrochemical. Optical transducers have some disadvantages when compared to electrochemical due to being less sensitive due to labeling, large detection setup, associated health hazards and disposal problems<sup>39, 40</sup>. On the other hand, electrochemical detection shares none of these disadvantages and enables label-free, fast, simple and cost effective measurement<sup>41, 42, 39</sup>.

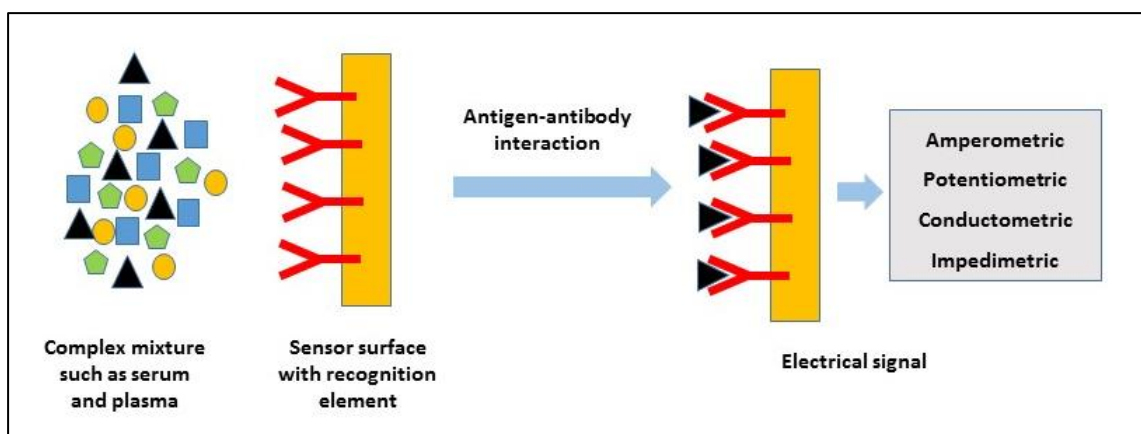


Figure 1.5. Schematic presentation of an electrochemical immunosensors.

In the electrochemical technique, the antibodies act as bio-receptors and the antigen acts as a target analyte. With antibody-antigen binding, the transducer generates a signal which can be detected based on an amperometric, potentiometric, impedimetric or

conductometric principal<sup>43,44</sup>. Figure 1.5. illustrates the process of the binding interaction in electrochemical immunosensors.

## APTAMER-BASED BIOSENSOR

The word aptamer is derived from the Latin word '*aptus*' (meaning 'fit') and Greek word '*-meros*' (meaning 'part'). Aptamers are single-stranded DNA or RNA molecules with high affinity to proteins, organic or inorganic substrates and other macromolecular compounds.

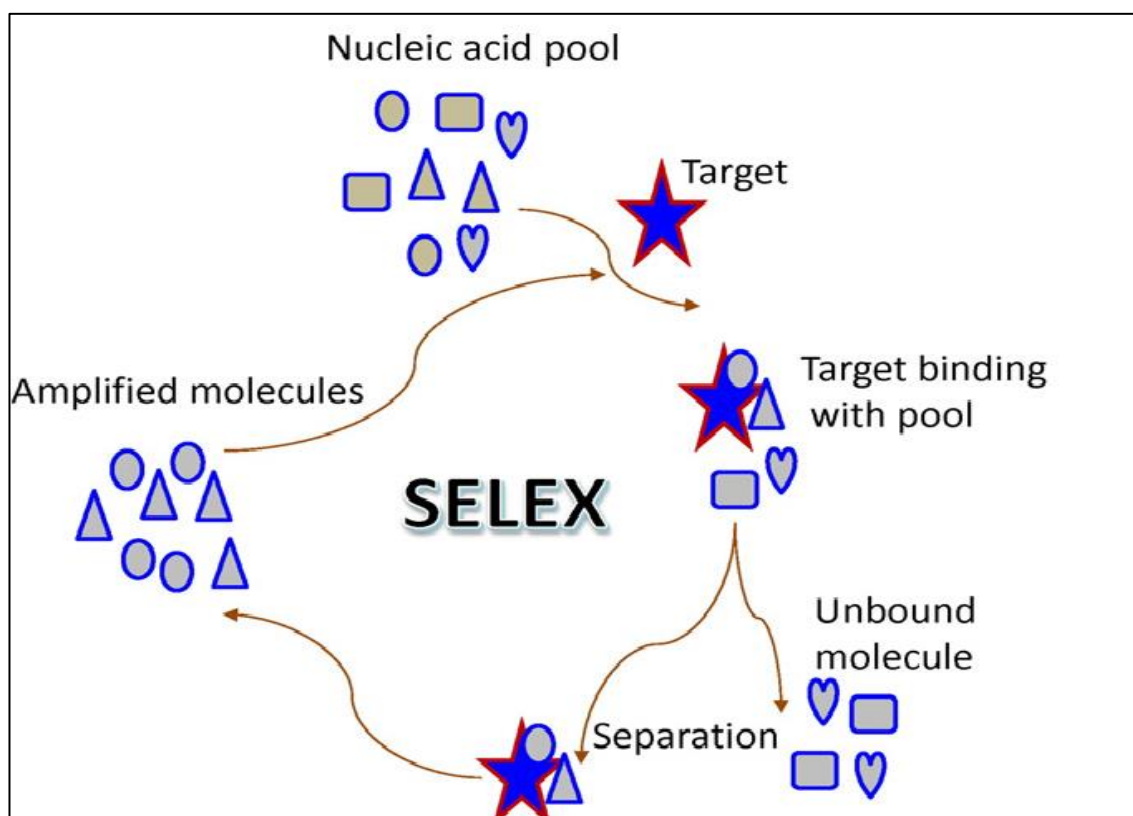


Figure 1.6. Schematic process of systematic evolution of ligands by the exponential enrichment (SELEX). A large nucleic acid library is created and introduced to a target molecule. Unbound molecules are removed and the bound ones are separated followed by the amplification of remaining molecules via polymerase chain reaction (PCR)<sup>45</sup>.

Aptamers are generated for the specific-target fabricated from a randomized library of molecules by a synthetic process known as systematic evolution of ligands by exponential enrichment (SELEX)<sup>45</sup>. This approach was first described in 1990 by three



independent research groups; Ellington and Szostak <sup>46</sup>, Tuerk and Gold <sup>47</sup> and Robertson and Joyce <sup>48</sup>.

The SELEX schematic process shown in Figure 1.6 is an iterative process based on in-vitro selection and enzymatic amplification techniques that mimic a Darwinian-type selection of relatively few, but optimized, structural motifs. The process of the selection of target-specific aptamers is based on the repetition of three critical steps: (1) the incubation of the nucleic acid pool and the target molecules, (2) separation of the bound and unbound molecules and (3) the amplification of the bound molecules via polymerase chain reaction (PCR) <sup>45</sup>.

In the first part of the SELEX procedure, the binding step takes place where the analyte of interest is exposed to a chemically synthesized random DNA oligonucleotide library containing  $10^{13}$  to  $10^{15}$  different sequence motifs. The un-wanted and unbound molecules are removed by separation and the bound ones are amplified for the next round of selection. This process is repeated at least 12 times. After the 12<sup>th</sup> round, the selected aptamers are cloned and sequenced for appropriate applications <sup>49</sup>.

Aptamers have many advantages, such as the ability to fold upon binding, affinity, selectivity and specificity of target binding interactions. These desirable factors make aptamers more popular than natural biological recognition elements, such as antibodies and enzymes, due to high stability in harsh experimental environments such as high temperatures and high salinity. Most importantly, the interaction between aptamer and target molecules can be reversed via intermolecular hybridization. Additionally, they can be easily synthesized and developed to detect a variety of in-vitro targets, such as proteins, peptides, drugs, small molecules, metal ions or even whole cells <sup>50, 51</sup>.

Aptamer-based biosensors (also known as aptasensors) are based on capturing a specific aptamer and target molecule binding event and converting it into a measurable signal. There are varied detection methods for this type of sensor such as mechanical,

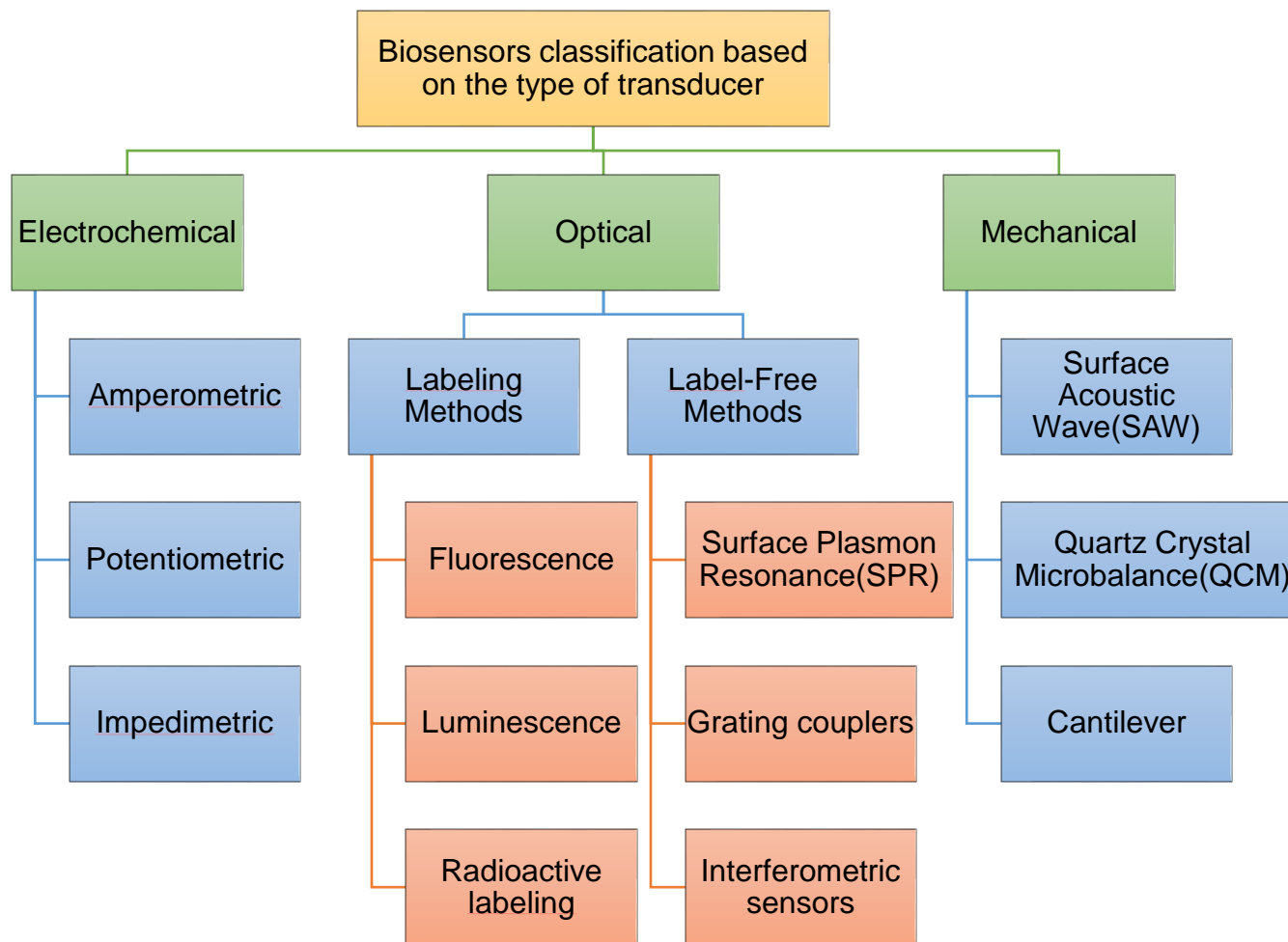
optical and electrochemical. Among these, electrochemical techniques are the most popular <sup>52, 53, 54</sup>.

### **1.2.2. BIOSENSOR CATEGORIES - TYPE OF TRANSDUCER**

The transducer of a biosensor converts the biological binding interaction into a measurable signal. This signal can be optical or electrical, depending on the physics and chemistry of the change that occurs during the sensing event <sup>24</sup>.

There are three main detection methods: 1) mechanical, 2) optical and 3) electrochemical. Furthermore, these approaches can be divided into two main categories: non-labeled and labeled. The non-labeled type (or label-free) method is where direct measurement of the interaction between the target biomolecule, bio recognition element and transducer surface is performed. However, in a labeled approach, a specific label has to be assigned and attached to the target biomolecule and the label itself will be detected <sup>55</sup>. Table 1-2 shows the biosensors classification according to the type of transducer.

Table 1-2. Biosensor categories according to the type of transducer. Modified from 24, 55, 56.



## **MECHANICAL**

Mechanical detection is based on monitoring the high-speed mass transformation arising from the interaction between target molecule and the immobilized recognition element species. This interaction followed by mechanical forces defines motility and adhesion, leading to control mobility and affinity on micro and nanoscale. Mechanical transducers are able to detect forces, motions and mass changes for a range of biomolecular interactions<sup>55, 57</sup>.

Mechanical transducers can be divided into three main techniques: surface acoustic waves (SAW), quartz crystal microbalance (QCM) and cantilever (see Table 1-2).

As implied by the name, a surface acoustic wave is a type of acoustic wave that propagates along the surface of a material. These waves are generated by Interdigital Transducers (IDTs), which are periodic comb-like metal structures deposited on a piezoelectric material (electrodes). When a sinusoidal wave with a period identical to the IDT period is present, vibration occurs underneath the IDT, which then generates an acoustic wave perpendicular to the direction of the IDT. This wave propagates on the surface of the piezoelectric material in both directions<sup>58</sup>.

According to the acoustic wave guiding process, acoustic wave devices can be sub-categorized into three groups: bulk acoustic wave (BAW), surface acoustic wave (SAW) and acoustic plate mode (APM) devices. In BAW devices, the acoustic wave propagates unguided through the volume of the substrate. For SAW devices the acoustic wave propagates, either guided or unguided, along a single surface of the substrate and in APM devices, the waves are guided by reflection from multiple surfaces<sup>59</sup>.

Quartz Crystal Microbalance (QCM) based biosensors is a good example of BAW devices<sup>60, 61, 62</sup>. In this type of biosensor, an AT-cut thin quartz disk (a disk cut from a quartz mineral at an orientation of  $35.25^\circ$  to the optical axis) is sandwiched between two metal electrodes (typically made from gold). Due to the piezoelectric nature of quartz material, when an electric field is applied, a measurable deformation is produced

whereby both surfaces move in parallel but opposite directions, thus generating acoustic waves which propagate through the bulk material through the crystal. The direction of this acoustic wave is perpendicular to the surface and the wavelength is double the thickness of the substrate <sup>63, 64</sup>.

Cantilever sensors are the last in this category, these can be operated in different modes which return different information. Additionally, when used in combination with other methods, this method can be used to record a specific set of coupled data <sup>65, 66</sup>.

## **OPTICAL**

The properties of electromagnetic radiation can be characterized as amplitude, frequency (and consequently wavelength), phase, polarization state and time dependency. In the field of optical spectroscopy, absorbance, transmittance and reflectance of the material are the main measurable properties <sup>67</sup>. Optical sensing is non-destructive, long distance applicable and, most importantly, independent of environmental conditions (for example in the presence of high voltages, chemicals or biohazards) <sup>68</sup>.

In general, there are two detection methods used in optical biosensors: label-free and labelled methods<sup>69</sup>. In labelled methods, either the target molecules or bio recognition molecules are labeled with a tag. In this case changes in the optical transmission/absorption/emission of light at the specific wavelength indicates the presence of the target molecule and the interaction strength between the target and bio recognition molecule <sup>70</sup>. This method is extremely sensitive, with potential detection limits down to a single molecule, but the main disadvantage is the complex labeling process which has the potential to interfere with the functionality of the target or bio recognition molecules.

In the label-free method, the target molecules (or recognition element) do not require any

alteration in any way and are detectable in their natural form. This approach is relatively simple and low cost to operate.

As mentioned, for the sensing application using labeling methods, the process itself demands additional time and cost and can alter the molecular interaction by blocking a binding site leading to potentially undesirable results <sup>71</sup>. Also, many sensor compounds are hydrophobic and are very sensitive to background binding (i.e. unwanted binding). In comparison, label-free methods allow real time binding reaction detection that are simply not possible with labelling methods.

The most desirable features of label-free <sup>72,73</sup> and real time detection are:

- 1) Improvement of the measurement accuracy and sensitivity at the binding event by real time binding monitoring.
- 2) Enabling monitoring of key biophysical parameters such as binding rate and affinity constant.
- 3) Less reagent consumption, especially for applications related to low affinity interactions, which demand high protein concentration for saturation.

Surface plasmon resonance (SPR) is one of a most popular label-free optical detection methods <sup>74</sup>. It is based on light energy (photon) transfer to free electrons on a metal surface (commonly gold). Light can be coupled into the thin metallic surface using either a prism or grating. The excited photons generate a charge density wave, a so-called surface plasmon (SP), which propagates along the interface between metal surface and a dielectric medium. The propagation of the plasmon in the metal surface produces an electromagnetic field in the form of evanescent waves which exponentially decay within 100-200 nm of the surface. These waves are extremely sensitive to changes in the dielectric constant of the relevant medium and due to this, SP waves are more sensitive to local refractive index changes than traditional measurements techniques <sup>67, 71, 73, 75</sup>.

## **ELECTROCHEMICAL**

Electrochemical detection is based on the interaction between biological elements and electrodes and generates a measurable electrical signal. As shown in Table 1-2, the electrically measured signals can be Amperometric (current based), potentiometric (potential difference based) or Impedimetric (impedance based) <sup>76, 77</sup>.

### **AMPEROMETRIC**

The Amperometric detection method is based on applying a potential to a working electrode against a reference electrode and measuring the resulting change in current. In this technique, the current is generated via an electrochemical reduction or oxidation at the working electrode and the change in the current can be directly monitored with a constant potential applied between the working and reference electrodes. The current is proportional to the concentration of the electroactive species in the solution <sup>76</sup>.

There are either two or three electrode configurations in the electrochemical cell. The three electrode system consists of: one working electrode made of chemically stable solid and conductive material (such as platinum, gold or carbon), one reference electrode (typically silver metal coated with a layer of silver chloride; Ag/AgCl) and one counter electrode (platinum wire). In the process of current measurement, the reference electrode is removed from the site of redox reaction in order to maintain a known and stable reference potential. The benefit of this setup is that the charge generated from electrolysis passes through the counter electrode instead of the reference electrode, which protects the reference electrode from changing its half-cell potential.

In a two electrode system, there are only the working and counter electrodes and, if the current density is low enough (micrometre scale), the counter electrode can carry the charge with no adverse effects. Two electrodes are usually preferred for disposable sensors because the long-term stability of the reference electrode is not required and also the cost of this system is favourable compared to those using three electrodes.

Screen-printed electrodes (SPEs) have become very popular in the production of electrochemical biosensors using three electrode systems due to the low cost, simplicity and speed of mass production to apply the thick film technology required <sup>78, 79, 80</sup>.

Interdigitated array (IDA) electrodes are another example of amperometric electrochemical transducers used in biosensors <sup>76</sup>. IDAs consist of two pairs of working electrodes with parallel strips of metal fingers which are separated by an insulating material. One electrode array works as an anode for oxidation and the other acts as a cathode for reduction. The redox cycling of the electroactive species which occurs when different potentials are applied to the two electrodes causing oxidation-reduction cycling is presented in Figure 1.7.

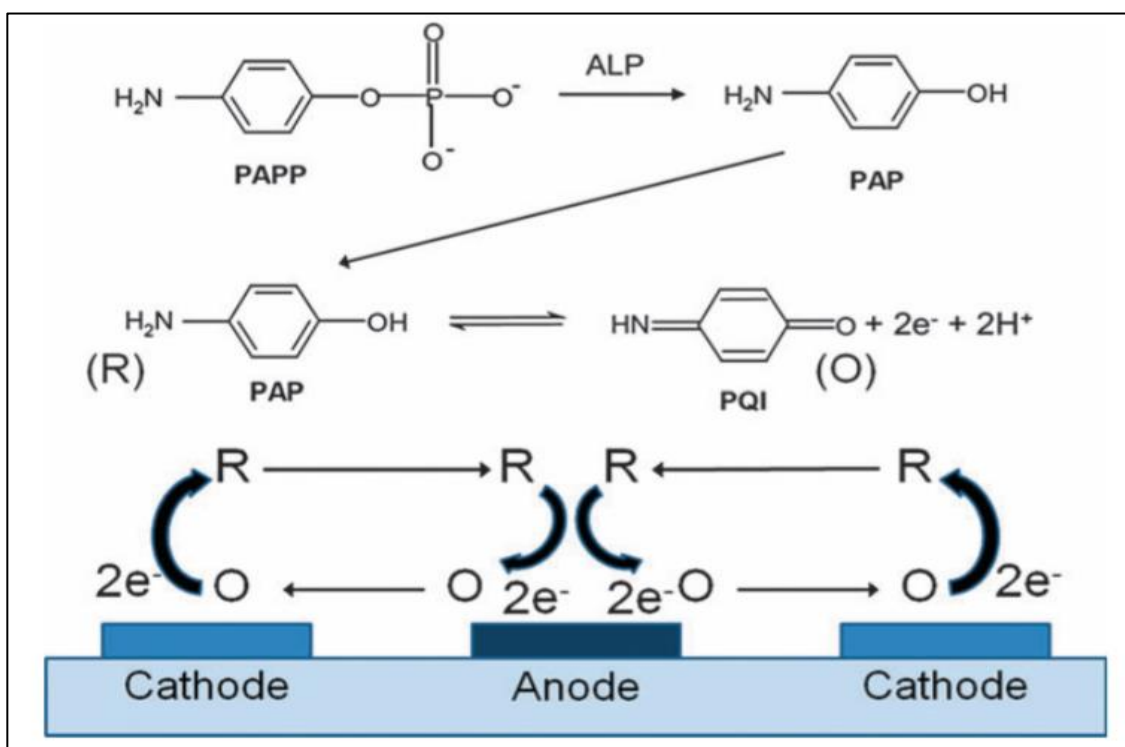


Figure 1.7. Interdigitated array (ADI) electrode for cycling of a redox active species. Alkaline phosphatase (ALP) hydrolyzes O-phosphate from a P-Aminophenyl phosphate (PAP) under alkaline conditions <sup>76</sup>.

There are many advantages of IDA based biosensors with redox cycling. The electrode reaction is reversible and the detection limits are low because the current used



contributes multiple times to the detection current, hence the signal-to-noise ratio is improved.

## **POTENTIOMETRIC**

Potentiometric sensors are based on monitoring of the potential difference of an electrochemical cell in the absence of a current between the electrodes. The measured potentiometric signals are usually produced by changes in pH, redox or ionic states resulting from the interaction between biomolecules and the sensor surface. Potentiometric biosensors can be categorised as three different types: ion-selective electrodes (ISE), field effective transistor (FET) and light addressable potentiometric (LAPS) <sup>81</sup>.

ISE immunoassay is based on a standard multilayer structure with a secondary enzyme labelled antibody. The signal generation arises from the adsorption of target molecules onto sensor surface and this interaction leads to a measurable change in the potential of the system.

FET sensors are an alteration of the ISE format in which the electrode is replaced with the FET transducer. These type of biosensors can be fabricated by coating the sensing surface with a bio recognition biomolecule specific to the application of interest <sup>81, 76</sup>. A FET biosensor is shown in Figure 1.8 consisting of a gold electrode and a FET transducer.

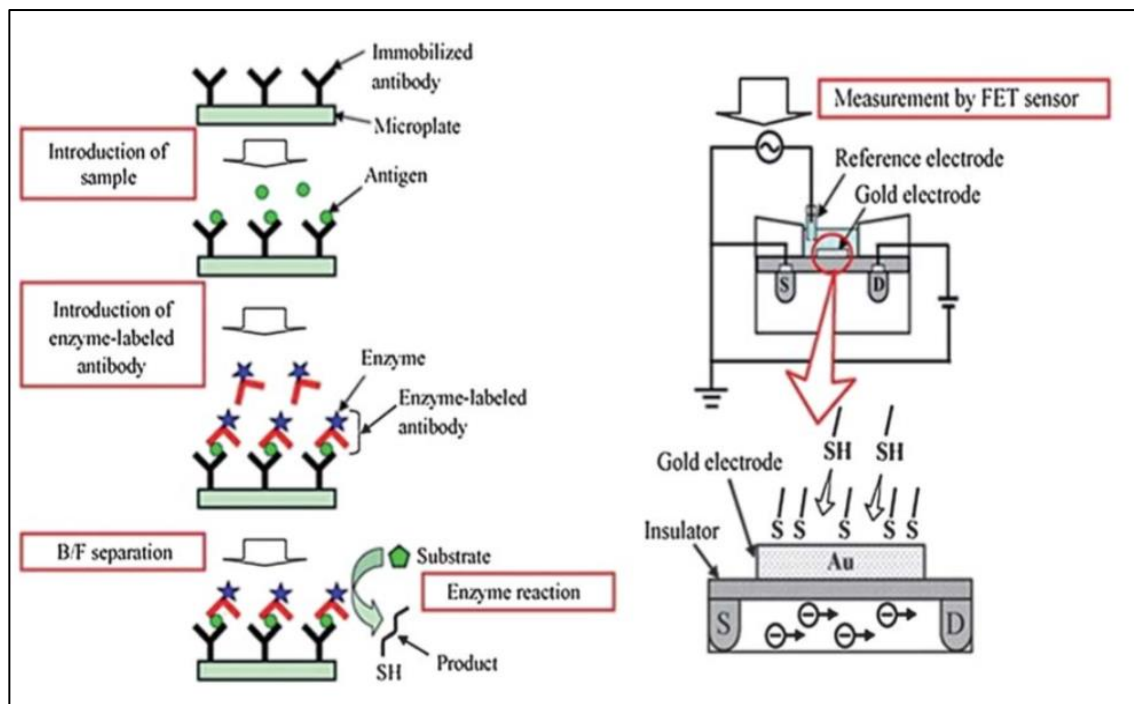


Figure 1.8. The principle of an enzyme immunoassay by using a FET biosensor <sup>81</sup>.

In this case, the biosensor was fabricated to operate inside a microplate including immobilised specific antibody (Interleukin 1 $\beta$ ) and the standard antibody/antigen structure for capture of the target antigen. The secondary antibody is labelled with a specific enzyme (AChE) and enzymatic catalysis of this enzyme occurs and generates a thiol compound on the surface of gold electrode. The FET unit transduces this chemical reaction into a potentiometric signal therefore allowing the detection of Interleukin 1 $\beta$ .

Finally, LAP sensors are based on the measurement of surface potential optically, via the photovoltaic effect. In this type of biosensor, a silicon sensor substrate is activated by a modulated LED light source, generating a photocurrent with a characteristic current and voltage profile. The LAP sensor works as an electrode which measures voltage per time differentials resulting from a change in the pH of reaction medium, effectively performing as a pH electrode.

## **IMPEDIMETRIC**

Impedimetric biosensors measure a change in impedance resulting from changes in resistance or capacitance at the sensor surface due to a biomolecule interaction. Impedance is defined as the ratio of an incremental change in voltage to the resulting change in current. An AC test voltage or AC test current is applied while the other parameters are measured <sup>81, 82</sup>.

Electrochemical impedance spectroscopy (EIS) is a technique used in impedimetric sensors. The main advantage of EIS compared with amperometry or potentiometry is that this method can be label-free which, as mentioned previously, simplifies the preparation process <sup>83</sup>. The basic principle and theory behind EIS is presented in Chapter 2.

### 1.3. MOTIVATIONS

Thrombin is a  $\text{Na}^+$ -activated, allosteric serine protease, it is not present in blood under normal conditions, after vascular injury, thrombin is rapidly generated from Inactive prothrombin by a series of enzyme cleavages<sup>84, 85</sup>. During coagulation, the concentration of thrombin may vary from  $\mu\text{M}$  to  $\text{mM}$  levels, the activated thrombin cleaves fibrinogen into fibrin and clots are formed at the site of vascular injury to prevent bleeding. The important roles of thrombin and inactivated prothrombin in physiological and pathological coagulation, also involved in various diseases, such as Deep vein thrombosis (DVT), Alzheimer and Parkinson<sup>86,87, 88</sup>.

The main role of alpha thrombin is in coagulation but it also causes contractions and relaxations of vascular smooth muscle depending on the loci of blood vessels and species<sup>85</sup>. Inactive prothrombin is proteolytically converted to active alpha thrombin which may be further hydrolyzed to beta and gamma thrombin<sup>89</sup>. Since the ability of beta and gamma thrombin in blood clotting are much less than alpha thrombin, many researches has been focused on alpha thrombin because of it is physiological significance.

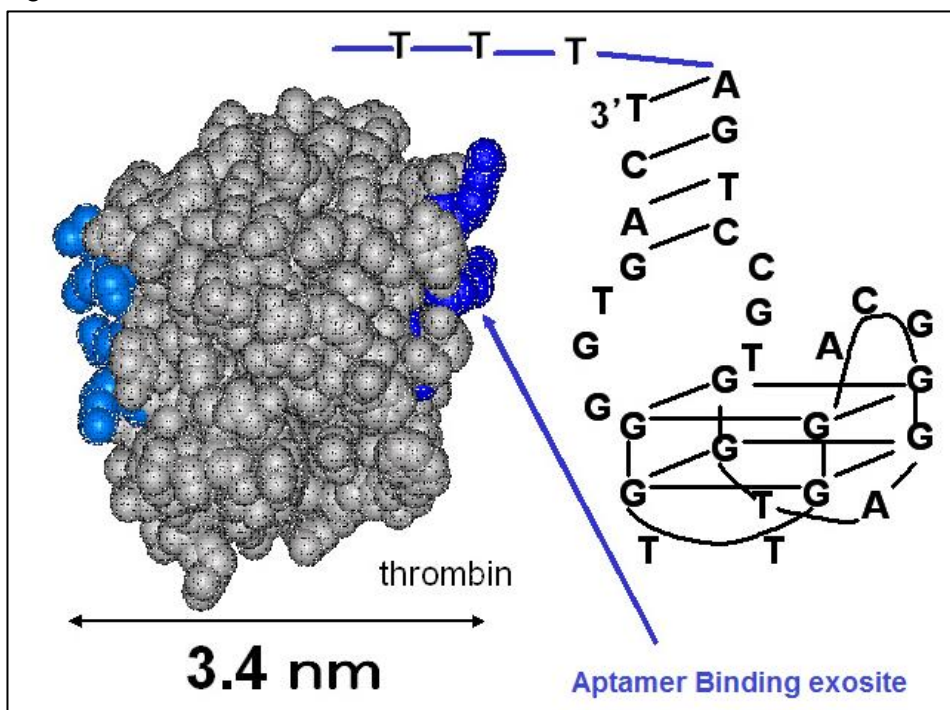


Figure 1.9. Alpha thrombin protein size and the binding site for aptamer. Modified from<sup>90</sup>.

Since detection and optimization of alpha thrombin is crucial for many applications mentioned earlier, and aptamers are a very strong candidate to serve in this purposes (see section 1.2.1) we will focus on aptamer binding to alpha thrombin in biosensing techniques.

Figure 1.9 illustrates the physical size of alpha thrombin and the binding site for aptamer. With using this concept, the detection of this biomolecules can be done by different biosensing methods. This is because alpha thrombin aptamer and protein are known to have highest binding affinity and specificity. In the literature, these pair is commonly used as a proof-of concept procedure for sensor technology <sup>84</sup>.

Table 1.3. Biosensors based on label-free and labelled (low detection limit) for aptamer-based human alpha thrombin protein detection in the literature.

Structure based on	Transducer	Method	Detection limit	Year	Ref
A Reagentless Signal-On Architecture	Electrochemical	Label-Free	260nM	2005	91
Nucleic Acid-Functionalized Pt Nanoparticles	Optical	Labelled	0.1pM	2006	92
Aptamer-Capped Nanocrystal Quantum Dots	Optical	Label-Free	182nM	2006	93
Bio bar code assay	Electrochemical	Label-Free	0.1ng/mL	2007	94
Impedimetric Aptasensor	Electrochemical	Label-Free	100fM-100nM	2009	95
Nanogap Dielectric Spectroscopy	Electrochemical	Label-Free	1µM	2010	96
G-quadruplex-based DNAzyme as sensing platform	Optical	Label-Free	0.01-0.12nM	2011	97
Electrochemical Proximity Assay	Electrochemical	Label-Free	2.5nM	2012	98
Turn-On Assay Using Aptamer-Functionalized Silver Nanocluster DNA Probes	Optical	Label-Free	5nM-2µM	2012	99

Structure based on	Transducer	Method	Detection limit	Year	Ref
Aptamer Modified Organic-Inorganic Hybrid Silica	Optical	Label-Free	3.4nM	2012	100
On-Chip Synthesis of RNA Aptamer	Optical	Label-Free	10fM	2012	101
Glucose oxidase-functionalized bioconjugate	Electrochemical	Label-Free	0.2pM	2012	102
Aptamer Hairpin Switch and Nicking Enzyme Assisted	Optical	Label-Free	100pM	2012	103
Neutralizer displacement	Electrochemical	Label-Free	100pM	2012	104
Structure-Switching Aptamers	Optical	Label-Free	1 $\mu$ M	2012	105
Solid phase binding-induced DNA	Electrochemical	Label-Free	2aM	2013	106
Disposable Graphite Electrodes	Electrochemical	Label-Free	19.02nM	2015	107
Carbon nanofibers enriched screen printed electrodes	Electrochemical	Label-Free	18.83nM	2015	108
Microplate assay	Optical	Labelled	10fM	2016	109
Silver nanoparticles Aptasensor	Optical	Labelled	20pM	2016	110
Target-induced catalytic hairpin	Electrochemical	Label-Free	6pM	2017	111
Self-powered triboelectric	Electrochemical	Label-Free	0.41nM	2017	112

Table 1.3. showing the available sensing techniques for aptamer-based alpha thrombin detection, but to the best of our knowledge in the time of writing this thesis, there are none commercially available biosensor for alpha thrombin detection.

In this project we used alpha thrombin aptamer modified with thiol linkers and human alpha thrombin protein in the label-free detection platform based in electrochemical

approach. The theoretical detection limit achieved was in femtoMol which is the lowest limit according to table 2.2, this can be further improved to be used in clinical application with low cost disposable nanogap biosensor. This was the initial idea to purpose this project: the need for this type of label-free capacitive biosensing principle.

## **OBJECTIVES**

The research objective of this project is to develop a highly sensitive and selective nanogap sensor for the label-free detection of human alpha-thrombin protein, using high speed quantitative impedance based measurements. Our approach is the design and fabrication of a novel vertically structured nano-gap capacitor consisting of two gold electrodes separated by a 40nm gap of SiO<sub>2</sub> as an insulator.

The aim of the thesis is to detail the design, fabrication, electronic characterization and optimization of sensor sensitivity, with the aim being to investigate its use in DNA and biomolecule detection.

## **RESEARCH SCOPE**

The scope of this project is as follows:

- ❖ Theoretical review of electrochemical impedance spectroscopy (EIS), Nanogap fabrication methods, existing Nanogap bio-sensor devices and their advantages and disadvantages
- ❖ Detail of fabrication steps and material and methods.
- ❖ Optical and electronic characterization of the nano-gap capacitor using scanning electron microscopy (SEM), atomic force microscopy (AFM) and impedance measurements.
- ❖ Analysis of the results for the response of the device with: air, DI water and buffer solution with various ionic concentrations.

- ❖ Surface functionalization of 20-base pair Aptamer (ss-DNA), and hybridization of sensor with human alpha thrombin protein. Conduction of control experiment for testing sensor selectivity and sensitivity to nonspecific binding.
- ❖ Discussion of results and future work.



## **Chapter 2. ELECTROCHEMICAL IMPEDANCE**

### **SPECTROSCOPY AND NANO-GAP CAPACITIVE SENSOR**

#### **PRINCIPLE AND BACKGROUND THEORY**

## 2.1. INTRODUCTION

Electrochemical impedance spectroscopy (EIS) is a technique used for analyzing electrochemical systems. Applications can be both biological and non-biological (for example material deposition, batteries and fuel cells). EIS is a non-destructive, steady-state method enabling the monitoring of relaxation phenomena over a wide frequency spectrum, typically in the range  $10^{-4}$  to  $10^6$  Hz<sup>113, 114</sup>, with the advantage of obtaining real-time and *in situ* measurements.

The technique was first postulated by Heaviside in the late 19<sup>th</sup> century and is based on mathematical transforms in a two-dimensional complex number plane. He also introduced the terminologies of impedance, admittance and conductance which were then used to describe the term “operational impedance” as the complex ratio of the voltage and current in an AC. This can be shown mathematically by the following formula:

$$Z(j\omega) = \frac{V(j\omega)}{I(j\omega)} \quad (2.1)$$

where  $Z$  is the impedance,  $V$  is the voltage,  $I$  is the current,  $j$  is the imaginary component and  $\omega$  is the frequency<sup>115, 116, 117</sup>.

The first use of EIS in biological applications was reported in 1925 for the estimation of the overall impedance of biological cell<sup>114</sup>. Nowadays, it has become one of the essential techniques for bioanalysis and has, for example, been utilized to investigate the activity of enzymes and target molecules<sup>117</sup>.

The use of EIS for non-biological applications is also very important and has been the center of attention for commercial applications over the last few decades. EIS for non-biological applications was introduced by Menges and Schneider in 1973 where it was used for the detection of corrosion on metallic surfaces.

## 2.2. BASIC PRINCIPLE OF ELECTROCHEMICAL IMPEDANCE SPECTROSCOPY

The very basic definition of electrical Resistance ( $R$ ), unit ohm ( $\Omega$ ), is the opposition force to current flow.  $R$  is used to describe Direct Current (DC) circuits, where the current and voltage are in same phase with each other. This opposition to current flow ( $R$ ) is frequency dependent with alternating current (AC) and in this case the term impedance ( $Z$ ) is used, along with the angle between current and voltage vectors to describe the phase difference. For a pure resistance,  $Z=R$  and  $\theta=0^\circ$ , whilst for a pure capacitance  $\theta=90^\circ$  and  $Z=-j/\omega C$ <sup>116, 117</sup>. Using a phasor diagram, (see Figure 2.1 ) an ideal resistance has no phase difference between the applied voltage and current through the element, whilst in a capacitor the voltage lags the current by  $90^\circ$  and in an inductor the voltage leads the current by  $90^\circ$ .

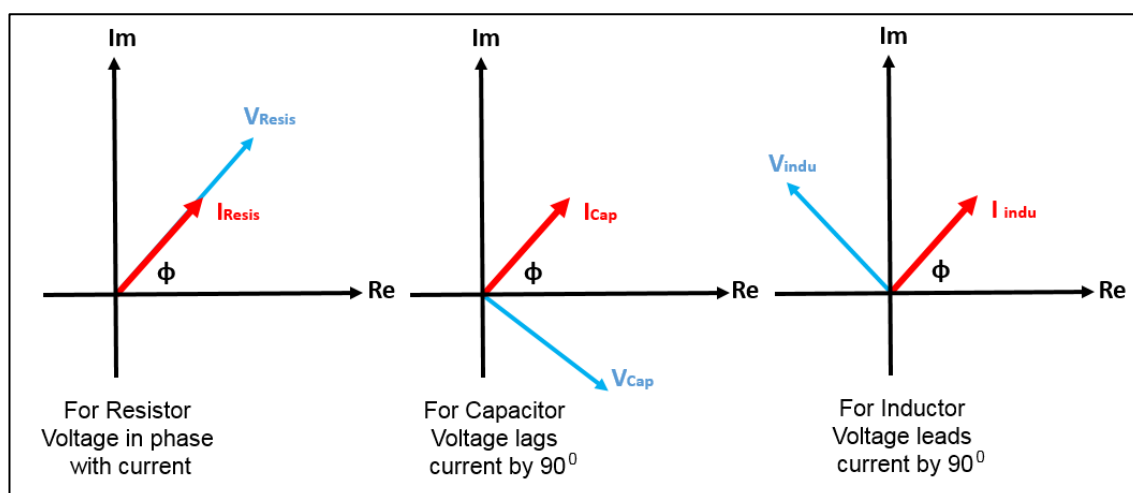


Figure 2.1. Phasor diagram for resistor, capacitor and inductor in AC circuit.

In EIS spectroscopy a very low amplitude of sinusoidal AC voltage (typically 2-20 mV) is applied to the system and the current response is measured. The frequency can be either single frequency or over a particular range (for example, in the range 500 Hz-10 kHz).

In impedance based biosensors, the applied AC voltage must be equal or less than 20 mV. The first reason for this is that the voltage and current relationship is often linear only for small perturbations. In this condition the system is known as pseudo-linear and the impedance can therefore be defined clearly <sup>116, 82</sup>.

The second reason for using low AC voltage is to maintain the boundary layer created between the electrode surface and the biomolecule. Since the covalent bond energies are less than 3eV, <sup>82</sup>, for these structures, and the energy between the biomolecules and the target species is even less, an applied voltage means applying an extra force to the charged biomolecules.

### **2.2.1. ALTERNATING CURRENT (AC) CIRCUIT THEORY**

The theoretical definition and calculation for EIS has been developed by many researchers in the field. In this section, only the very fundamental definitions and equations of AC circuit theory related to impedance spectroscopy are presented. The reader is referred to other sources for more detailed information <sup>116, 118</sup>.

The working principle of EIS is based on the response of a circuit to an AC current or voltage as a function of frequency. For the case when the frequency is zero (DC voltage), the resistance is defined as:

$$R = \frac{V}{I} \quad (2.2)$$

Where,  $R$  is resistance,  $V$  is the DC voltage and  $I$  is the current. However, at non-zero frequency and when either an inductance and/or capacitance is present, the impedance ( $Z$ ) is used to describe the response of the system. For electrochemical cells or electrodes, the current response to a sinusoidal AC voltage will be a sinusoid with the same frequency but shifted in phase <sup>119</sup>.

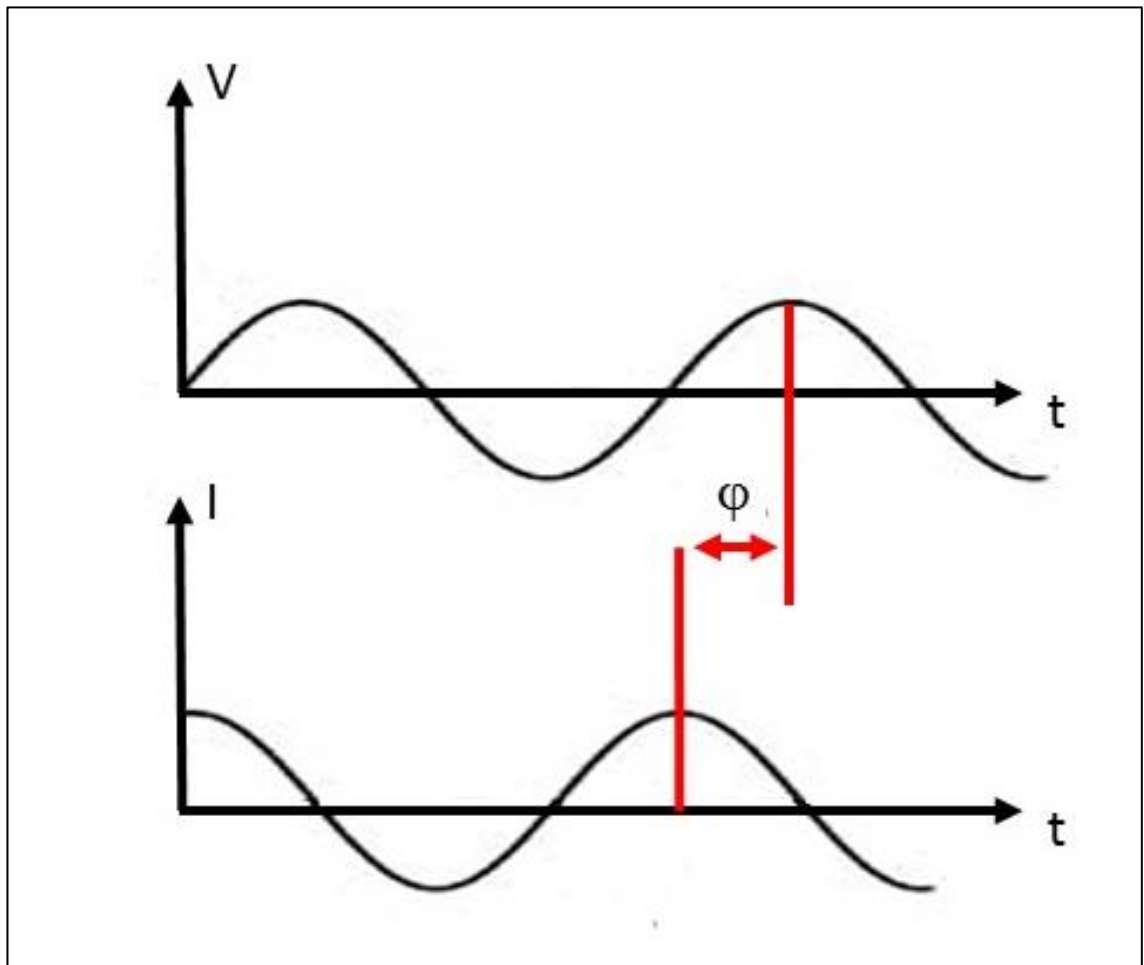


Figure 2.2. Sinusoidal AC voltage and current response with phase shift,  $\phi$ .

Sinusoidal AC voltage (see Figure 2.2.) can be defined as:

$$V(t) = V_0 \sin(\omega t) \quad (2.3)$$

Where  $V(t)$  is the voltage at the time  $t$ ,  $V_0$  is the amplitude of applied AC voltage and  $\omega$  is the radial frequency. The relationship between radial frequency (radian/sec) and frequency  $f$  (in Hz) is:

$$\omega = 2\pi f \quad (2.4)$$

The response current with phase shift ( $\phi$ ) with a different amplitude than  $I_0$  can be written as:

$$I(t) = I_0 \sin(\omega t + \varphi) \quad (2.5)$$

Where  $I$  is the current amplitude at time  $t$ ,  $I_0$  is the current amplitude at the start and  $\varphi$  is the phase shift. The impedance  $Z$  for the relevant circuit is therefore:

$$Z = \frac{V(t)}{I(t)} = \frac{V_0 \sin(\omega t)}{I_0 \sin(\omega t + \varphi)} = \frac{1}{Y} \quad (2.6)$$

Where  $Y$  is the complex conductance or admittance in Siemens (S). The impedance is a complex value due to the fact that the current amplitude changes (see Figure 2.5.) and shows a phase shift ( $\varphi$ ) compared to the voltage-time function. Therefore, the  $Z$  value can be described either as modulus  $|Z|$  and the phase shift  $\varphi$ , or by the real part  $Z_R$  and the imaginary part  $Z_I$  of impedance.

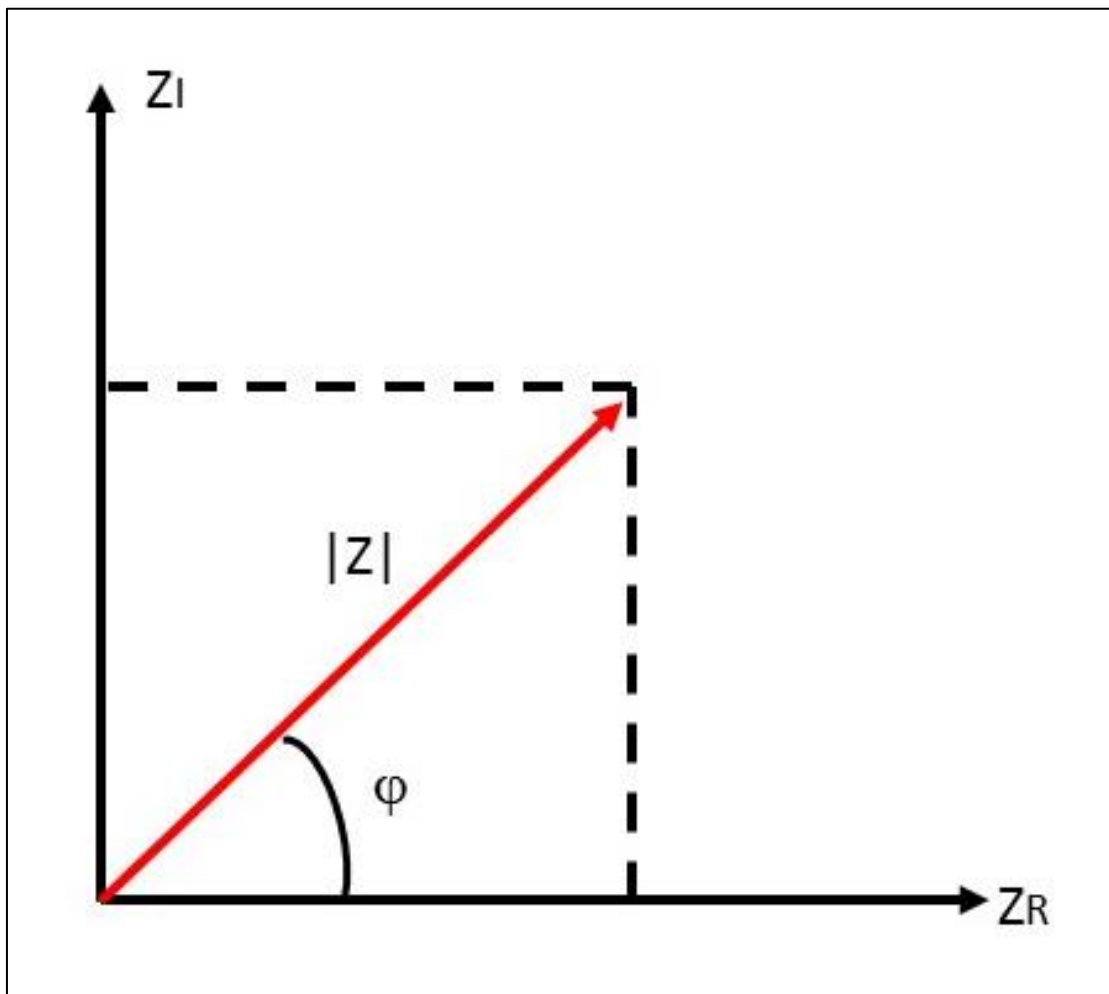


Figure 2.3. Graphical presentation of impedance, where  $Z_R$  is the real part of impedance and  $Z_I$  is the imaginary part.

The mathematical form for the diagram shown in in Figure 2.3. can be shown to be:

$$|Z| = \sqrt{Z_R^2 + Z_I^2} \quad (2.7)$$

Or

$$Z = Z_R + jZ_I \quad (2.8)$$

Where  $j = \sqrt{-1}$ ,  $|Z|$  is the absolute impedance,  $Z_R$  is the real part of impedance and  $Z_I$  is the imaginary part. Once the impedance of an electrical circuit is obtained, it can be used to determine the other parameters of a sensing system.

## 2.2.2. ELECTRICAL DOUBLE LAYER

When a charged surface (i.e. electrode) is in contact with an electrolyte (i.e. sample solution), the electrostatic charges on the solid surface will influence the distribution of nearby ions in the electrolyte solution. Ions of opposite charges to that of the surface are attracted towards the surface, while ions of like charges are repelled from the surface; thus, an electric field is established. The charges on the solid surface and the balancing charges in the liquid is called the "electric double layer" (EDL). The sign and magnitude of the EDL field depend on the nature of the surface and the liquid<sup>120</sup>.

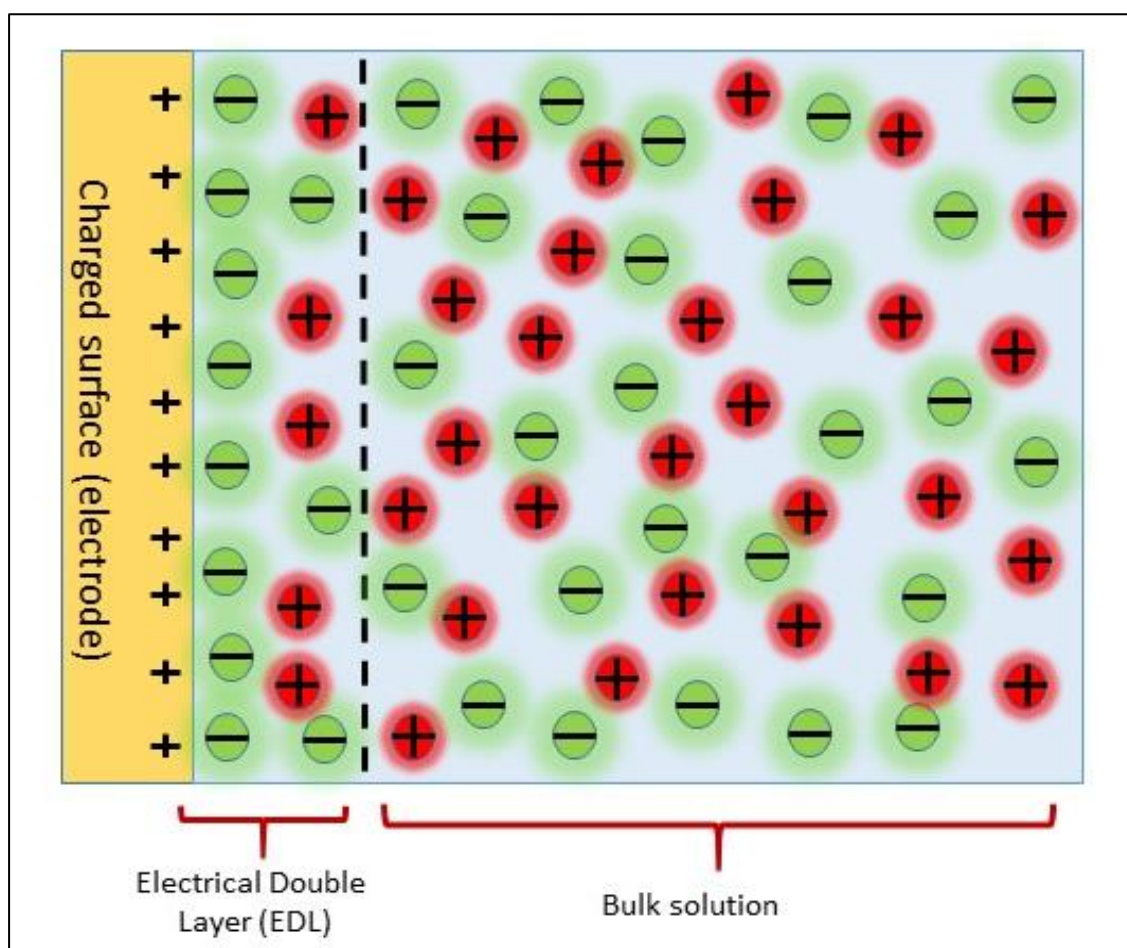


Figure 2.4. Schematic presentation of Electrical Double Layer (EDL) structure, in presence of charged surface the ions of opposite charge in sample solution accumulate near the electrode/electrolyte interface area.

Historically the first concept of electrical double layer in electrode/electrolyte interface was introduced by Von Helmholtz in the 19<sup>th</sup> century<sup>118,121,122,123</sup>. This was called Helmholtz model in which under the influence of an external field the free ions in solution can migrate to the electrode/electrolyte interface area and create a layer of adsorbed



ions and he called this layer Helmholtz layer(see Figure 2.5.a). He described the charge separation at interfaces which indicated that the counter-charge in solution exists at the surface. Therefore, a simple parallel-plate capacitor exists at the interface consisting of charges with opposite polarities separated by a distance in the molecular order of magnitude. This arrangement is often called electrical double layer(EDL), the term ‘double layer’ came from his early writings on this subject <sup>118</sup>.

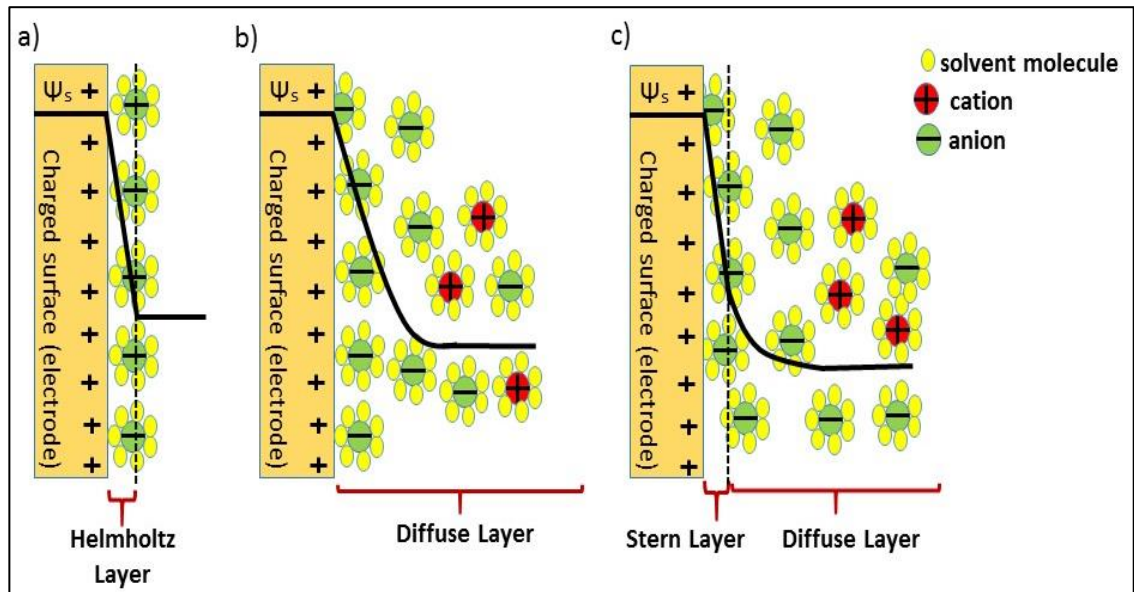


Figure 2.5. Three models of EDL with the positively charged electrode surface. a) The Helmholtz model, b) the Gouy-Chapman model and c) the Stern model,  $\psi_s$  is the potential at the electrode surface.

The simple parallel-plate capacitor which is able to store the charge density can be defined as:

$$\sigma = \frac{\epsilon \epsilon_0}{d} \psi \quad (2.2)$$

Where  $\sigma$  is the charge density,  $\epsilon$  is the dielectric constant of the medium,  $\epsilon_0$  is the permittivity of free space,  $d$  is the interplate distance and  $\psi$  is the potential drop between the plates <sup>118</sup>.

The differential capacitance can therefore be written as:

$$\frac{\partial \sigma}{\partial \psi} = C_d = \frac{\epsilon \epsilon_0}{d} \quad (2.10)$$

The main problem with this model is the assumption that  $C_d$  is a constant, but it is known that in real systems,  $C_d$  varies with potential and ion concentration which suggests that either  $\epsilon$  or  $d$  depend on these parameters<sup>118</sup>. Gouy and Chapman modified the Helmholtz model to include consideration of the thermal motion of ions and introduced a diffuse double layer (see Figure 2.5 b)<sup>121,122, 123</sup>. According to this model the potential drop across the diffuse layer can be modelled as an exponentially decreasing as a function of distance. The physical length of this exponential decay is given by Debye-Hückel length ( $\lambda_D$ ).

$$\lambda_D = \sqrt{\frac{\epsilon_r \epsilon_0 k_B T}{2e^2 \sum n_j}} \quad (2.11)$$

Where  $\epsilon_r$  is the relative permittivity of the medium,  $\epsilon_0$  is the absolute permittivity of free space,  $k_B$  is Boltzmann's constant  $1.381 \times 10^{-23} JK^{-1}$ ,  $T$  (kelvin) is the temperature,  $e$  is the elementary electronic charge  $1.6021 \times 10^{-19} C$  and  $\sum n_j$  is the concentration of free ions. The results obtained by considering the ions near the electrode (charged surface) as in an ideal solution and solving the truncated Poisson-Boltzmann equation. The theoretical thickness of EDL can be calculated from equation 2.11.

Stern introduced an improved model which is the combination of Helmholtz model and Gouy-Chapman model (see Figure 2.5.c) also known as Gouy-Chapman-Stern (GCS) model. According to this model the EDL consists of two regions, the first region close to electrode/electrolyte interface called Stern layer and the second region called the diffuse layer<sup>124</sup>. In the diffuse layer, the ions are mobile under the coupled influence of diffusion and electrostatic forces, and the Gouy-Chapman model applies in this layer.

In 1947, Grahame improved this model by eliminating a number of deficiencies. He further divided the Stern layer into inner and outer Helmholtz planes and this was due to the fact that in the Stern layer, specific (covalent) and non-specific adsorption of ions at the same electrode surface lead to different closest distances from the charged surface. Figure 2.6. presents a schematic structure of Helmholtz layers ,the inner Helmholtz plane (IHP) consists of ions adsorbed by specific (covalent) forces and the outer Helmholtz plane (OHP), or Stern layer, of ion adsorbed by non-specific (electrostatic) forces. IHP and OHP are in series with the increase in concentration of ions the OHP increases relative to this.

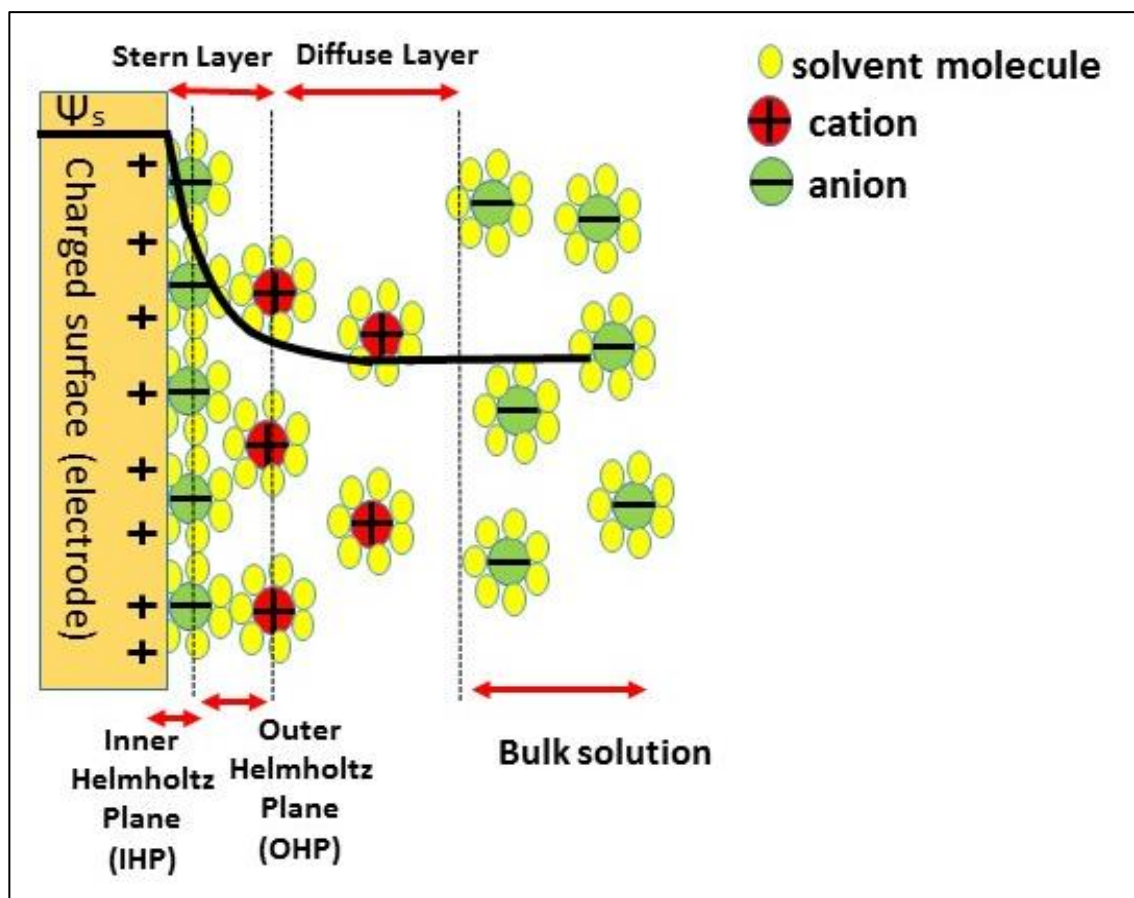


Figure 2.6.A schematic of Helmholtz layers according to Grahame' definition.in his definition the Stern Layer is divided in to inner and outer Helmholtz layers.

The potential  $\psi$  starts to decrease at the interface (electrode/electrolyte) and, with the formation of the IHP and OHP, the whole system very quickly (few tens of a microsecond) acts as a EDL capacitor <sup>122</sup>.

Later in 1953 Parsons introduced the further definition for ions with finite size and in 1981 Kornyshev proposed a mean field theory, who obtained new results for the diffuse double-layer capacitance <sup>123</sup>. In his approach the limiting case is based on Gouy-Chapman model for low ionic concentration, but this model was not satisfied for high currents.

The concept of a bare electrode surrounded by ionic solution is similar to a double-plate capacitor with the thickness equal to the Debye-Hückel length ( $\lambda_D$ )<sup>82</sup>. This represents the characteristic thickness of the EDL, which can vary from < 1 nm at high ionic concentration to a few micrometers at low ionic concentration <sup>125</sup>. This is represented by  $1/\kappa$  (the Debye-Huckel parameter) <sup>96</sup> and can be defined as:

$$\kappa = \sqrt{\frac{2e^2 n^0}{\epsilon k_B T}} \quad (2.12)$$

Where,  $e$  is the elementary electronic charge  $1.6021 \times 10^{-19} C$ ,  $n^0$  is the bulk ion concentration,  $\epsilon$  is the bulk dielectric constant,  $k_B$  is Boltzmann's constant  $1.381 \times 10^{-23} JK^{-1}$  and  $T$  (kelvin) is the temperature. As can be seen from Equation 2.12 by increasing the ionic concentration of bulk solution the double layer therefore EDL will decrease. in part 2.3. of this chapter we will focus on this phenomena in more details.

### **2.2.3. EQUIVALENT CIRCUIT MODELS AND ELEMENTS FOR FARADAIC AND NON-FARADAIC SCHEME**

EIS is an excellent technique for investigating the mechanisms of electrochemical systems. Specifically, with the help of this method, the impedance can be derived as a function of kinetic parameters such as resistance, capacitance or inductance for any related sensing system. In terms of the data analysis, the common approach is to fit the

collected data to an equivalent circuit which then can be used to derive the physical meaning of elements such as capacitors or resistors <sup>126</sup>.

Fitting the data into an equivalent circuit is necessary for understanding the system, but more importantly it is because most commercially available software packages for impedance data fitting purposes (e.g. CASIDIE , PIRoDE and NOVA) are based on equivalent circuit theory <sup>127, 128</sup>.

In general, there are two types of equivalent circuit model for Faradaic and non-Faradaic schemes which include circuit elements such as resistors, capacitors and other relative components. Equivalent circuit model for both of these scheme illustrated in Figure 2.7. Faradaic processes involve the repeated transfer of charge across an interface, typically involving a redox reaction with the transfer of an electron either from or to a metal electrode. This is achieved by coupling an AC signal with a DC bias. The general principle for this method is to form an electrochemical cell <sup>129, 82, 130, 131</sup>. The interaction between the charged redox and the electrode surface generates a charge transfer resistance ( $R_{ct}$ ), which increases when a binding event occurs at the electrode surface. When the target molecule (for example, an antigen) binds to the surface of the electrode (with immobilized antibodies) the redox couple is delayed causing an increase in  $R_{ct}$ , which leads to a decrease in capacitance <sup>131</sup>.  $R_{sol}$  represents the resistance generated in the solution and  $Z_w$  refers to the difficulty of mass transport of the redox species <sup>129</sup>.

In contrast, non-Faradaic methods do not involve a redox reaction and have no  $R_{ct}$ . Electron transfer occurs across the solution interface and this is associated with a  $R_{et}$  for electrons. In non-Faradaic methods, the detection can be achieved by measuring changes in  $C_{EDL}$  or the phase. The term 'capacitive biosensor' indicates a sensor based on a non-Faradaic technique where the measurements can be done at a single frequency <sup>82</sup>.

In general, based on the structure of the electrodes and the components, the Faradaic scheme refers to a system where the surface of the electrodes are partially or wholly covered by a non-insulating layer (in some systems the electrodes are partially covered with insulator so the redox probe is able to catalyze). In this method, the main measured parameter is the charge transfer resistance ( $R_{ct}$ ). Whereas in the non-Faradaic scheme, the surface of electrode is completely covered by a dielectric layer and the device behaves as an insulator. Also, there is no redox probe and the capacitive current is measured under a small amplitude sinusoidal voltage signal at low frequencies (in the range 10-1000 Hz) <sup>132</sup>. Since the subject of this thesis is capacitive sensors in the nano scale (i.e. in the non-Faradaic scheme), Section 2.3 of this chapter will focus on this method of sensing.

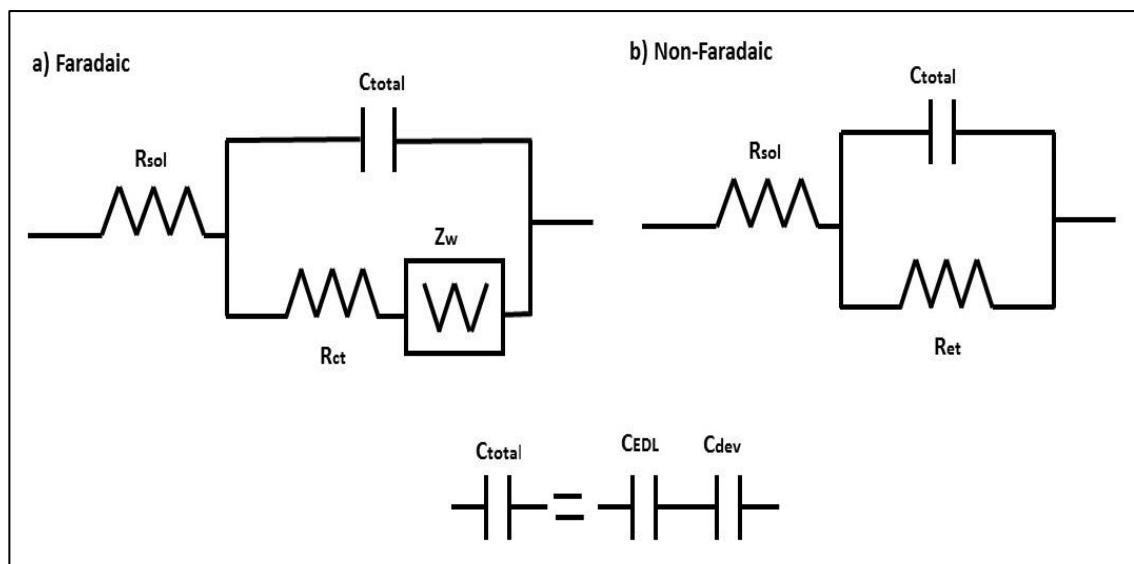


Figure 2.7. Common equivalent circuit models for a) Faradaic based sensors and b) Non-Faradaic based sensors. Where  $R_{sol}$  is the solution resistance,  $R_{ct}$  is the charge transfer resistance,  $C_{total}$  is the total capacitance of the system which is the total of  $C_{EDL}$  (double layer capacitance) and  $C_{dev}$  is the physical capacitor used in sensor,  $Z_w$  is Warburg impedance and  $R_{et}$  is the electron transfer resistance.

In the Figure 2.7  $R_{sol}$  is the solution resistance coming from the finite conductance of the ions in bulk solution. This resistance is independent of the frequency <sup>117</sup>, and the equivalent impedance element can be defined as:

$$Z_{Rel} = R_{sol} \quad (2.13)$$

The total capacitance of the system  $C_{total}$  is a series combination of the double layer capacitance ( $C_{EDL}$ ) and the surface modification capacitance ( $C_{device}$ )<sup>82</sup>. The capacitance due to surface modification (which is the physical capacitor used as a transducer in the sensor), depends on the thickness and dielectric constant<sup>113, 132, 133</sup>. This capacitance is as follows:

$$C_{dev} = \frac{\epsilon_r \epsilon_0 A}{d} \quad (2.14)$$

Where  $\epsilon_0$  the permittivity of the dielectric layer is,  $\epsilon_0$  is the permittivity of free space  $8.85419 \text{ pFm}^{-1}$ ,  $A$  is the electrodes area, and  $d$  is the insulator thickness. The total capacitance ( $C_{total}$ ) for the both models is:

$$C_{total} = C_{dev} + C_{EDL} \quad (2.15)$$

The impedance of the capacitance ( $Z_C$ ) in electrochemical systems can then be defined as:

$$Z_C = \frac{-j}{\omega C} \quad (2.16)$$

Theoretical modelling of EIS assumes that the capacitor under investigation is an ideal capacitor with a homogenous surface, whereas in real systems this is not the case. The term Constant Phase Element (CPE) can be used to address this lack of homogeneity<sup>128</sup>, so the capacitance  $C_{total}$  is usually modelled by a CPE instead of pure capacitance<sup>82</sup>. The impedance of this element can therefore be defined as:

$$Z_{CPE} = \frac{1}{Y_0 (j\omega)^n} \quad (2.17)$$

Where  $j = \sqrt{-1}$ ,  $Y_0$  is the admittance of an ideal capacitance,  $\omega = 2\pi f$  and  $n$  is experimental constant which can be 0, 0.5 or 1. When  $n=1$ , the CPE shows a behavior as a pure capacitor and for  $n=0$  the CPE behaves as a pure resistance. For  $n=0.5$  the

CPE is equivalent to another element known as the Warburg element <sup>128</sup>. According to modelling,  $n$  for the  $C_{surf}$  is typically between 0.85 and 0.98 which brings about a sub- $90^\circ$  phase shift to the system which can be equivalent to the frequency dependent resistor in addition to a pure capacitor <sup>82</sup>.

The Warburg element relates to the diffusion of ions in the solution, specifically in an electrochemical reaction with a redox active site. The Warburg impedance  $Z_w$ , which only exists in Faradaic EIS, defines the delay arising from the diffusion of the electroactive species (redox) to the electrode surface <sup>82</sup>. The Warburg impedance can be determined from:

$$Z_w = \frac{1}{Y_0 \sqrt{j\omega}} \quad (2.18)$$

Where  $Y_0$  is the diffusion admittance. The Warburg impedance has the identical real and imaginary contributions with a phase angle equal to  $45^\circ$  and is only applicable in low frequencies <sup>82, 128</sup>.

Finally, the last parameter for the Faradaic EIS circuit model is the charge transfer resistance ( $R_{ct}$ ). According to Equation 2.6, the resistance of the solution is independent of the frequency. However, at higher frequencies  $R_{ct}$  is the opposition force to electron movement in the solution, which is a real quantity <sup>117</sup> and can be calculated using the following equation:

$$R_{ct} = \frac{RT}{i_0 F} \quad (2.19)$$

Where  $R$  is the molar gas constant,  $T$  is the temperature,  $F$  is the Faraday constant,  $i_0$  is the exchange current density ( $i_0 = FK^0C$ ),  $K^0$  is the electron transfer rate constant and  $C$  is the concentration of the electroactive species (redox). For non-Faradaic impedance sensors there are no-surface reactions (so  $i_0 = 0$ ) and therefore,  $R_{ct} \rightarrow \infty$



and can be neglected <sup>134</sup>. This resistance is indicative of two main effects: the energy potential related to the oxidation and reduction events at electrode surface and the energy barrier of the electroactive species reaching the electrode due to electrostatic repulsion.  $R_{ct}$  is the main indicator of affinity binding for Faradic EIS <sup>82</sup>.

The equivalent circuit model for analyzing the impedance data for a Faradaic sensor is shown in 2.8. In the presence of electroactive species this can be modified by the CPE circuit element to replicate the real EIS system mechanism <sup>135</sup>.

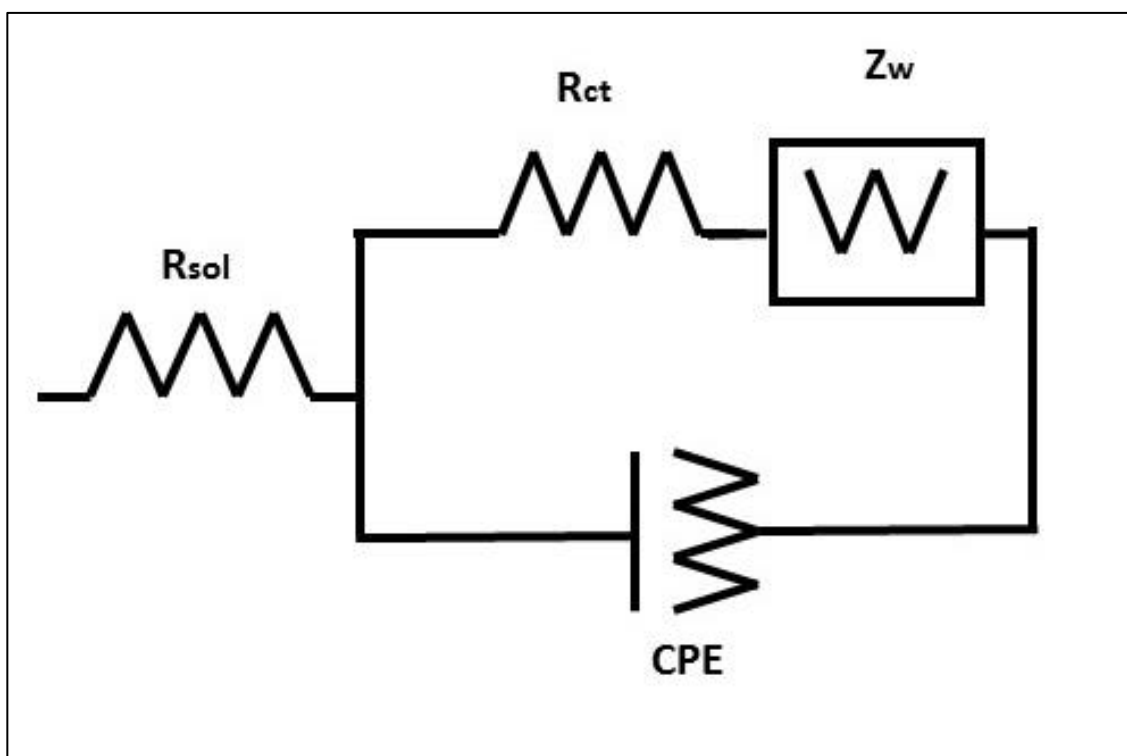



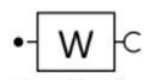


Figure 2.8. Schematic presentation of equivalent circuit model in presence of redox species. Where  $R_{sol}$  is the solution resistance,  $R_{ct}$  is charge transfer resistance  $Z_w$  is Warburg impedance and CPE is Constant Phase Element.

In the equivalent circuit model for the non-Faradaic case (see Figure 2.8.a), the  $R_{et}$  is the parasitic resistance of the substrate in which the electrodes are placed. Theoretically, for an ideal capacitor with a good insulator, this resistance is infinite. In this model, the main indication of affinity binding is  $C_{total}$ .

Combining the basic theory given in the previous section of this thesis and having introduced the equivalent circuit models in this section, the impedance expressions for both Faradaic and non-Faradaic sensors can be determined as a function of frequency Table 2.1. Showing the frequency dependence of each circuit element as well as phase angle and impedance definition.

Table 2.2. Circuit symbols, impedance definition, frequency dependence and phase shifts for most circuit elements for describing the equivalent circuit models.

Circuit element	Impedance definition	Phase angle	Frequency dependence
Resistance 	$Z = R$	$0^{\circ}$	No
Capacitance 	$Z_C = \frac{1}{j\omega C}$	$90^{\circ}$	Yes
CPE 	$Z_{CPE} = \frac{1}{Y_0(j\omega)^n}$	$0-90^{\circ}$	Yes
Warburg impedance 	$Z_W = \frac{1}{Y_0\sqrt{j\omega}}$	$45^{\circ}$	Yes

Finally, an Ohm's law-like relationship can be utilized to calculate the total impedance of a Faradaic or non-Faradaic circuit model <sup>117</sup>. As stated, all impedance components are in series and therefore the sum of the impedance for each element gives the total impedance of the electrochemical impedance based sensor and can be defined as:

$$Z_{total} = Z_1 + Z_2 + Z_3 + \dots + Z_x \quad (2.20)$$

For analyzing the impedance spectra, the equivalent circuit models with the definition of relevant elements is essential to validate the measurements for each system under investigation. The number and type of circuit elements can also be used to distinguish between the mechanisms of each impedance based sensor.

#### **2.2.4. DATA PRESENTATION**

In EIS, the collection, analysis and interpretation of data from binding events is a crucial step in the detection process. In many EIS based sensors, instead of studying the equivalent circuit model and extracting the mathematical equations, it is more efficient to run an experiment on the proposed circuit and analyze the resulting plot. This gives the investigator a good overview of the real and imaginary impedance, as well as the phase shift as a function of frequency<sup>82, 136</sup>.

With applying the desired frequency and voltage (or indeed, current), the electrical signal analyzer unit of the measurement setup is used to show or record the responsive parameters such as current (real and imaginary) or voltage (real and imaginary). Additionally, the phase shift for each applied frequency can be determined. The total impedance of the system (real and imaginary part) can therefore be computed as a function of frequency. The data can be presented in different types of plot depending on the characteristic of the electrochemical system. There are two important types of plot used to present the data from real system; the Nyquist plot and the Bode plot<sup>137</sup>.

The Nyquist plot (also known as complex-impedance-plane), shows the imaginary impedance which refers to the capacitive and inductive behavior of the sensor, as a function of the real impedance of the sensor<sup>138</sup>. An example of this is shown in Figure 2..

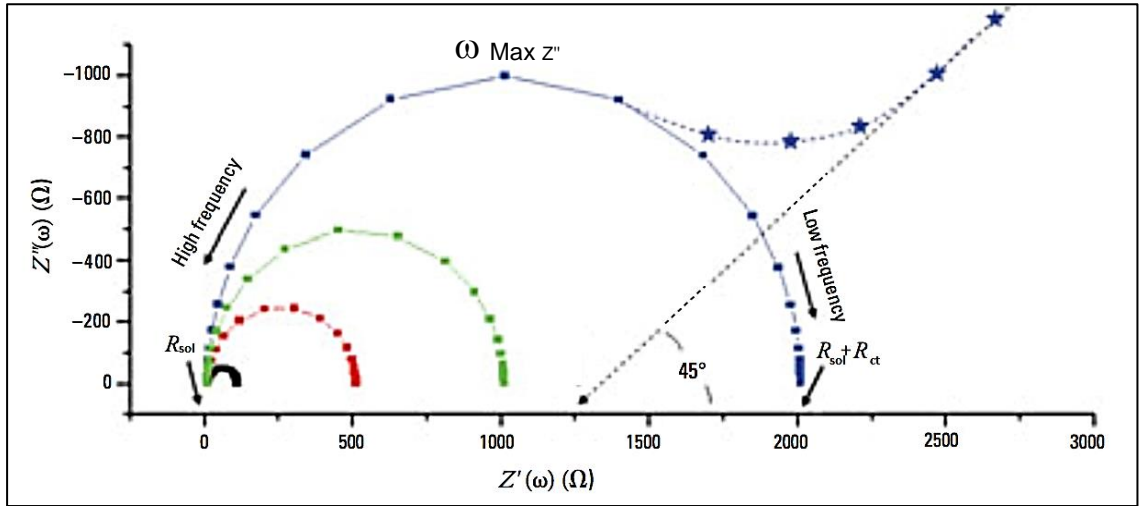


Figure 2.9. Example of a Nyquist plot with computer-generated data for different charge transfer resistance values (blue  $2\text{k}\Omega$ , green  $1\text{ k}\Omega$ , red  $500\Omega$ , black  $100\Omega$ ). Here,  $Z''$  is the imaginary and  $Z'$  is the real part of the impedance. Blue stars show the contribution of Warburg impedance (with a phase shift of  $45^\circ$ ). Modified from <sup>136, 138</sup>.

In order to extract the system characteristics, the Nyquist plot is interpreted at both high and low frequency. The x-axis of the plot shows the resistance of the system which is the sum of  $R_{sol}$  (solution resistance) and  $R_{ct}$  (charge transfer resistance). For high frequency, the impedance of the system is completely due to the solution resistance ( $R_{sol}$ ). For the low frequency case (from the  $\omega_{max} Z''$  to rightmost end of the semicircle), the impedance value is calculated as  $R_{sol} + R_{ct}$ .

In the middle of the semicircle ( $\omega_{max} Z''$ ), when the frequency reaches the highest limit, the relationship between the double layer capacitance, charge transfer resistance and frequency can be used to define the time constant of the electrochemical reaction ( $\tau_{rxn}$ ) using the following equation:

$$R_{ct} \times C_{EDL} = \frac{1}{\omega_{max}} = \frac{1}{2\pi f_{max}} = \tau_{rxn} \quad (2.20)$$

$\tau_{rxn}$  indicates how fast the electrochemical reaction take place. It is important to remember that if the total  $R_{ct} \times C_{EDL}$  is known then the double layer capacitance ( $C_{EDL}$ ) can be calculated because the  $R_{ct}$  for low frequency is also known.

Using the Nyquist plot has many advantages in as much as it can give all the important information about the electrode-electrolyte interface and the reaction. On the other hand, this plot has some disadvantages. The frequency does not appear clearly in the plot itself and to calculate the important parameters such as the double layer capacitance, the frequency needs to be determined. The other issue regarding this plot is that since the Nyquist plot presents the impedance of elements in series, the low impedance circuit will not be clearly determinable because the larger impedance overrides the plot scaling.

The Bode plot shows the absolute impedance  $|Z|$  and the phase shift  $\varphi$  as a function of frequency on a logarithmic scale. The Bode plot can provide more detailed information about the frequency-dependent behavior of the electrochemical system. The phase shift versus frequency plot is highly sensitive to system parameters and therefore can be used to compare the experimental results with the theoretical equivalent circuit model of the sensor. The absolute impedance versus frequency is significantly less sensitive to system parameters, but the asymptotic values at low frequency define the DC value and at high frequency equals the electrolyte resistance <sup>136, 137, 138</sup>.

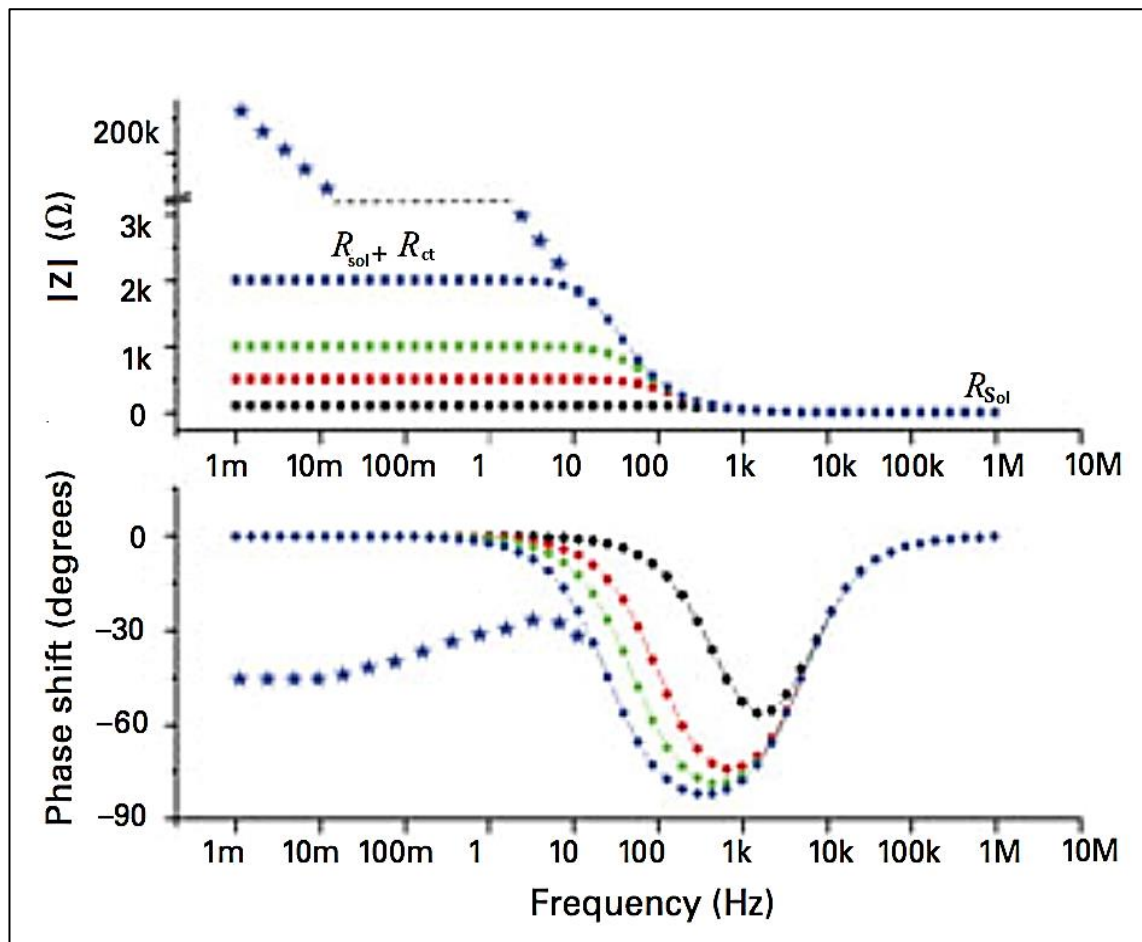


Figure 2.10. Example of Bode plot with computer-generated data for different charge transfer resistance values (blue 2k $\Omega$ , green 1 k $\Omega$ , red 500 $\Omega$  and black 100 $\Omega$ ). The blue stars show the contribution of Warburg impedance (with a phase shift of 45°). Modified from <sup>136, 138</sup>.

It can be clearly shown in Figure 2. that at high and low frequency, the impedance of the system is resistive as no phase shift recorded, however at intermediate frequencies, it can be capacitive with the phase shift of -90°.

The main disadvantage of using this plot is that, due to the solution resistance effects on the impedance of the system, the use of phase shift plot can prove to be very confusing when being used to estimate the characteristic frequencies.

The comparison of system element behavior in both the Faradaic and non-Faradaic impedance sensors can be useful to understand the mechanism and characteristic of each element. Figure 2.1 shows both Nyquist and Bode plots of such data.

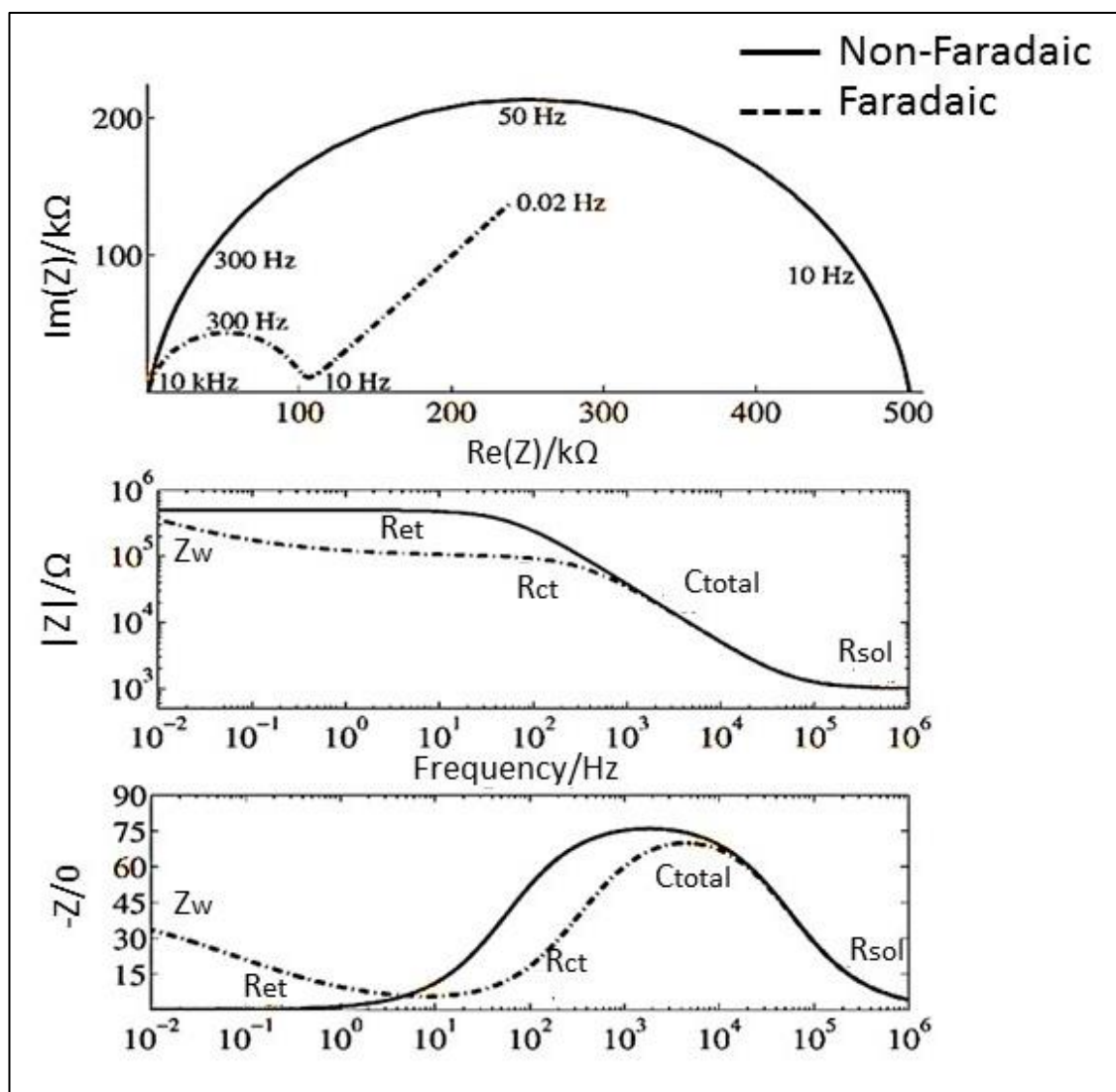


Figure 2.11. Example of Faradaic and non-Faradaic impedance data in a) Nyquist and b) Bode plot presentation.

Data presentation tools are a crucial part of the analysis for EIS based sensors and are provided in most of software packages (such as LEVM, ZView and ZSimpWin) in order to check the validity of experimental results.

### 2.2.5. ELECTRODE SIZE AND MATERIAL

There are many factors which depend on the electrode size in EIS based sensors such as the sensitivity of the method, the cost of mass production and the ability to adapt to different immobilization techniques. Therefore, it is vital to optimize the electrode size for

impedance based sensors, due to the fact that the electrode size also has a great impact on the measured impedance <sup>82, 139</sup>.

The electrode material for this type of sensor is commonly platinum, gold, forms of carbon nanotubes (CNT's <sup>140</sup>), epoxy graphite, graphene or Teflon coated rods <sup>139</sup>. These materials are very attractive from an experimental point of view, but are relatively expensive for large scale applications. However, traditional photolithography and screen-printing techniques offer more opportunities in terms of low-cost fabrication, mass production and customizability.

In recent EIS based sensors, most of the fabrication techniques are centered on interdigitated microelectrodes (ID $\mu$ E), which consist of a series of parallel micro-band electrodes separated by an insulation layer and connected together. This technique introduces many advantages such as faster reaction kinetics (due to the high mass transfer in ultra-small electrodes over a shorter time-scale), higher sensitivity, large electrode aspect ratio (w/l) and increased signal-to-noise ratio. ID $\mu$ E structures are two-electrode systems which do not require a third reference electrode for impedance measurements (more detail of three electrode system can be found in Chapter 1). Additionally, the space between the two electrodes is very small, which improves the speed of oxidation and reduction cycles which, in turn, results in a higher efficiency of data collection <sup>141, 142, 143</sup>.



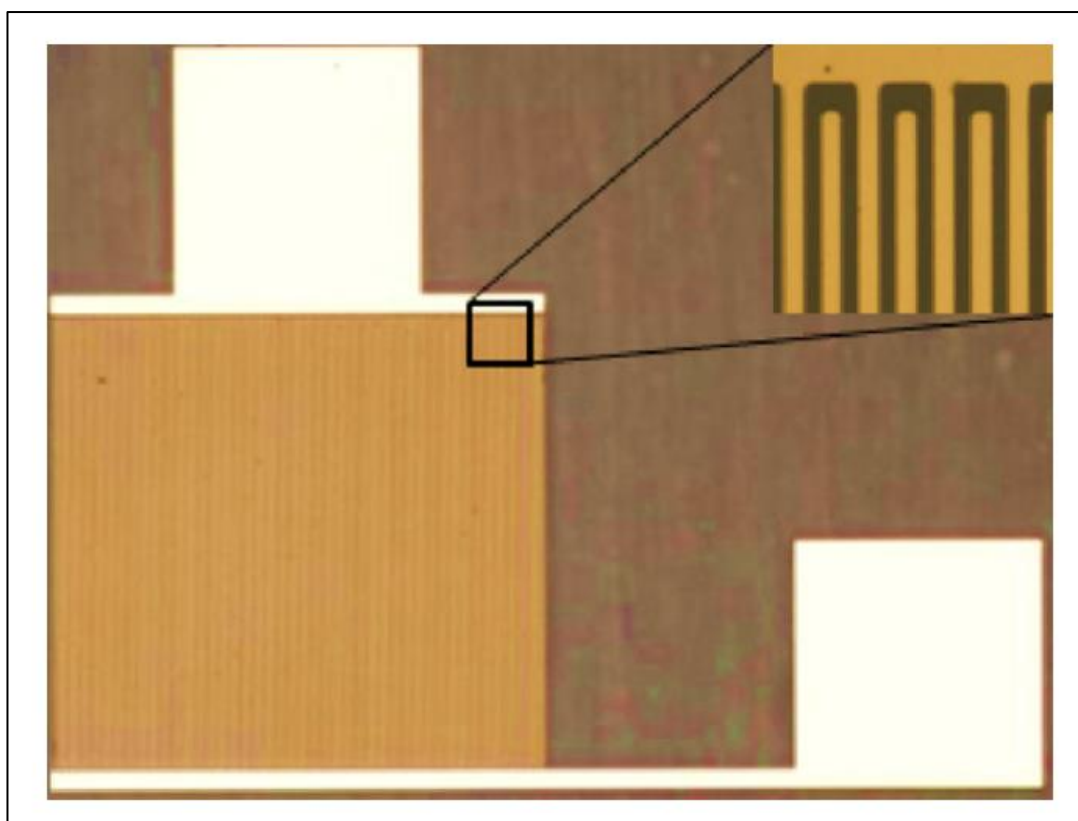


Figure 2.12. An example of interdigitated microelectrodes (ID $\mu$ E) <sup>142</sup>.

The ID $\mu$ E approach improves the kinetic efficiency with higher sensitivity and selectivity and can also reduce the experimental time scale <sup>144</sup>. These advantages, along with simple fabrication methods because all electrodes are patterned by photolithography or screen printing with the same material, makes it favourable for the mass production of disposable sensors. In the last 10 years, many EIS biosensors based on ID $\mu$ E have been reported for immunosensors, DNA sensors, affinity sensors using aptamer probes and biosensors for bacterial cells and viruses <sup>143</sup>.

## 2.3. NANOGAP CAPACITIVE SENSOR

The aim of this thesis is to fabricate a novel EIS based nanogap capacitive sensor in the non-Faradaic scheme. In this section, the theoretical structure of the nanogap capacitive sensor will be introduced, followed by an overview and discussion of the literature and current state of the art sensors of this type.

Electrical nanogap sensors have become powerful devices for detecting biomolecules in small quantities. One of the most important advantages of this type of sensor is the capability to directly transform (or transduce) binding events into measurable electrical signals (label-free) such as resistance/impedance, capacitance/dielectric or field-effects. This topic in EIS sensing has become an active area for many researchers and is continually growing <sup>145, 146</sup>.

The geometry of the detection region can be categorized as: 1D nanogap (which refers to point like gap junctions), 2D devices (which consist of coplanar electrodes) - where the ratio between height and thickness of electrode is around the gap size - and 3D nanogap (known as nano cavities) where the ratio between height and thickness of electrode is greater than gap size. In the case of the 3D nanogap, the cavities result in a significant area relative to the gap length <sup>147</sup>. A simplified representation of the geometries is shown in Figure 2.13.

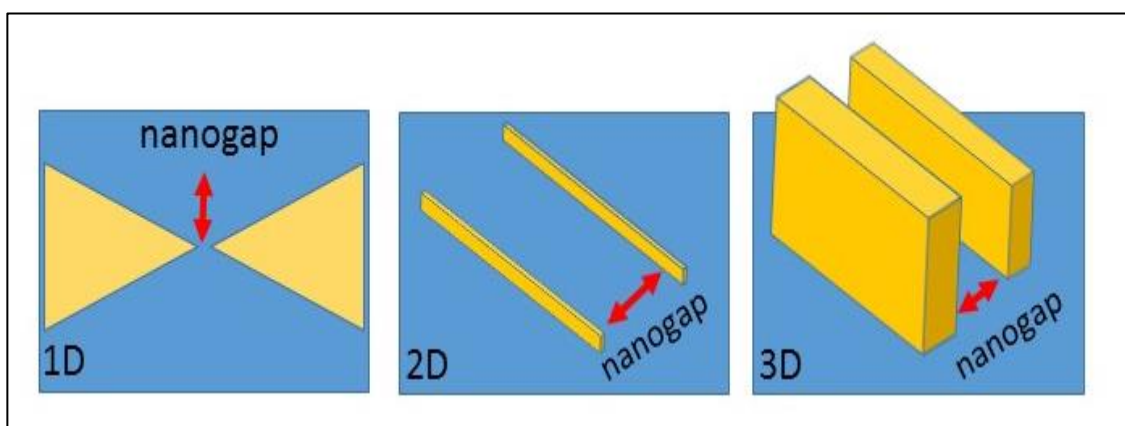


Figure 2.13. Three main types of Nanogap fabrication with respect to the dimensions. Where in 1D nanogap the gap area is only a single point like, in 2D nanogap the height and width of the electrode facilities the gap and in 3D the height, width and volume can be used.

Generally the measurement techniques and application can be related to the geometry of the device. Typically 1D and 2D nanogaps can be assessed with DC voltages for resistivity measurements, whereas in the 3D nanogap, mostly AC measurement methods can be done for analyzing complex impedance responses.

The key advantage of 1D and 2D nanogap is the opportunity for surface-bound molecules to occupy a significant portion of the interelectrode spacing, therefore enabling even a single molecule to be detected. 3D Nanogap sensors are considerably different from 1D and 2D Nanogap devices. These devices contain a high volume relative to the Nanogap width, which allows both surface-bound and free biomolecules to be screened.

3-D Nanogap devices based on EIS, can be divided into two main categories: planar and vertical <sup>145</sup>. Figure 2.14.illustrates both structure, in planar Nanogap sensors, the two electrodes face each other horizontally and in some cases a nanoparticle can be used for labelling or enhancement of the biomolecules which is positioned in the Nanogap area. The vertical Nanogap devices have a sandwich structure in which the electrodes are on top of each other with an insulator layer in between. The structure of these devices can contain two or three terminals.

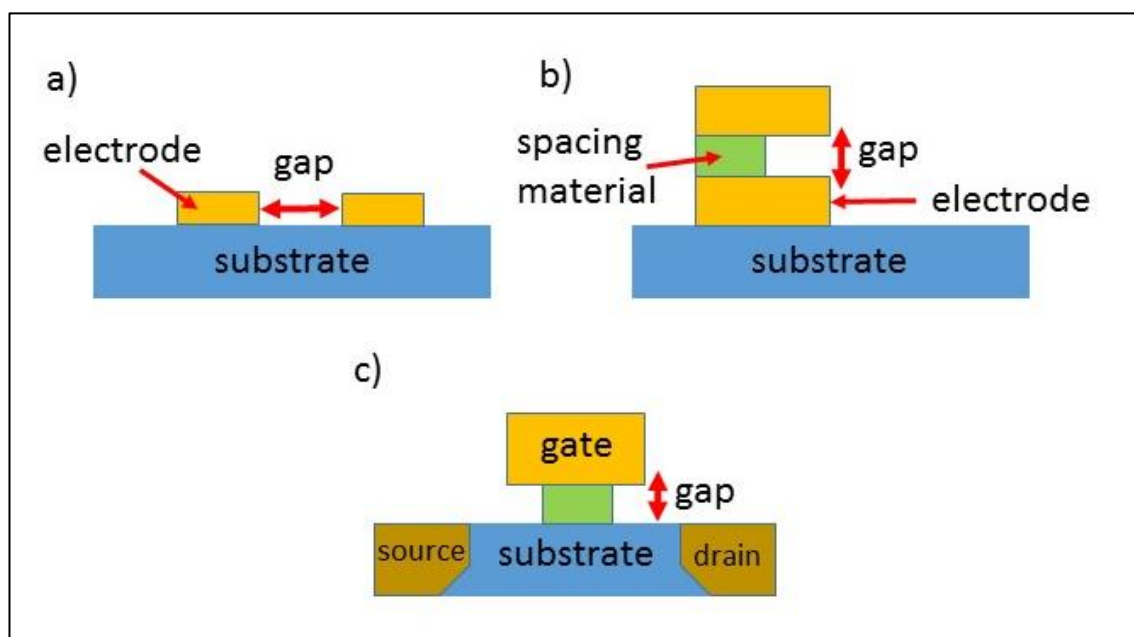


Figure 2.14. Schematic representation of 3D nanogap. Where a) is planar structure , b) two terminal vertical and c) three terminal vertical structure .in the vertical structure, there is spacing layer which separates the top and bottom electrodes and will be etched partially to obtain the gap.

As can be seen in 2.14.b, the two electrodes are separated by an insulator spacer in the middle layer. With the use of selective etching, the desired area of insulator can be removed to immobilize the biomolecules.

In the three terminal structure (Figure 2.13.c), a common field effect transistor (FET) structure can be seen, where current flows between the source and drain electrodes when the applied voltage to the gate electrode exceeds a threshold voltage ( $V_T$ ). The capacitance between the gate electrode and the Nanochannel determines the  $V_T$  and consequently this can be controlled through a change in dielectric material of the gate. When biomolecules sit in the Nanogap, the capacitance between the gate and Nanogap (compared to the air in gap) increases followed by a negative shift in  $V_T$ . Therefore, by determining the changes in  $V_T$ , specific binding can be detected.

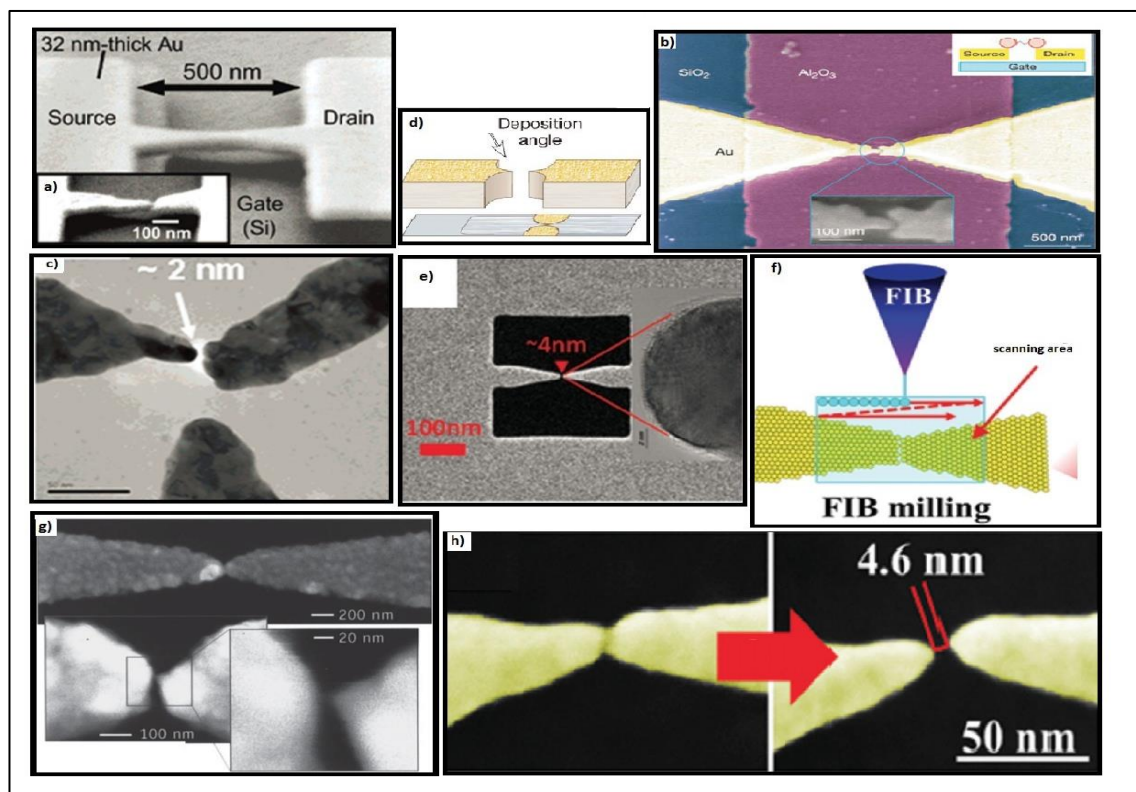


Figure 2.15. Examples of 1D Nano-gap devices with different fabrication techniques. a) SEM image of a gated mechanical break junction, b) SEM image of Nano-gap fabricated by electromigration (electrodes are fabricated with Electron Beam Lithography(EBL), c) device for molecular detection fabricated by Focused Ion Beam (FIB), d) fabrication method for oblique angle deposition technique in order to make Nano-gap electrodes with photoresist as a mask, e) gold antenna with 4nm separation done by FIB lithography, f) fabrication method involving FIB milling, g) SEM image of Nano-gap electrode fabricated by chemical deposition and h) SEM image of a single grain boundary junction obtained via a thermal process. Modified from <sup>148</sup>.

Several available 1D nanogap structures in the literature are shown in figure 2.15. Since the gap size is very small and the application of these devices is mainly based on monitoring and detection of a single molecule or DNA a precise gap size needed.

With improvements in nanofabrication techniques, new strategies have been developed in the detection and discrimination of single-molecules. At the time of writing, available techniques for fabrication of electrical Nanogap devices are as follows: mechanical break junctions, electromigration, focused ion beam (FIB) related techniques (electron beam lithography, electron beam induced deposition, electron beam induced sputtering and migration), FIB milling and deposition, nanostructured mask and oblique angle deposition, chemical deposition techniques, scanning probe lithography, synthesis and assembly of metal nanorods, carbon material-based (carbon nanotubes, CNTs), nanogap electrodes and the combination of sacrificial layers and selective etching<sup>146,</sup>

<sup>148, 149</sup>.

Figure 2.16. Presents different nanogap biosensor structure in planar and vertical format with different fabrication techniques and electrode materials. Nevertheless, there are a number of disadvantages for 1D and 2D structures. For example, there can be difficulty in ensuring specificity in the measurements, hence they need proper pre-treatment steps before introducing the target biomolecules in order to determine presence or absence of specific biomolecules. The fabrication of these nanogap is an expensive and slow throughput process, with the added demand of advanced high-resolution Nanolithography techniques such as electron- or ion-beam lithography (EBL, IBL), focused ion beam (FIB) milling, scanning tunneling or atomic force microscopy or nanoimprint lithography.

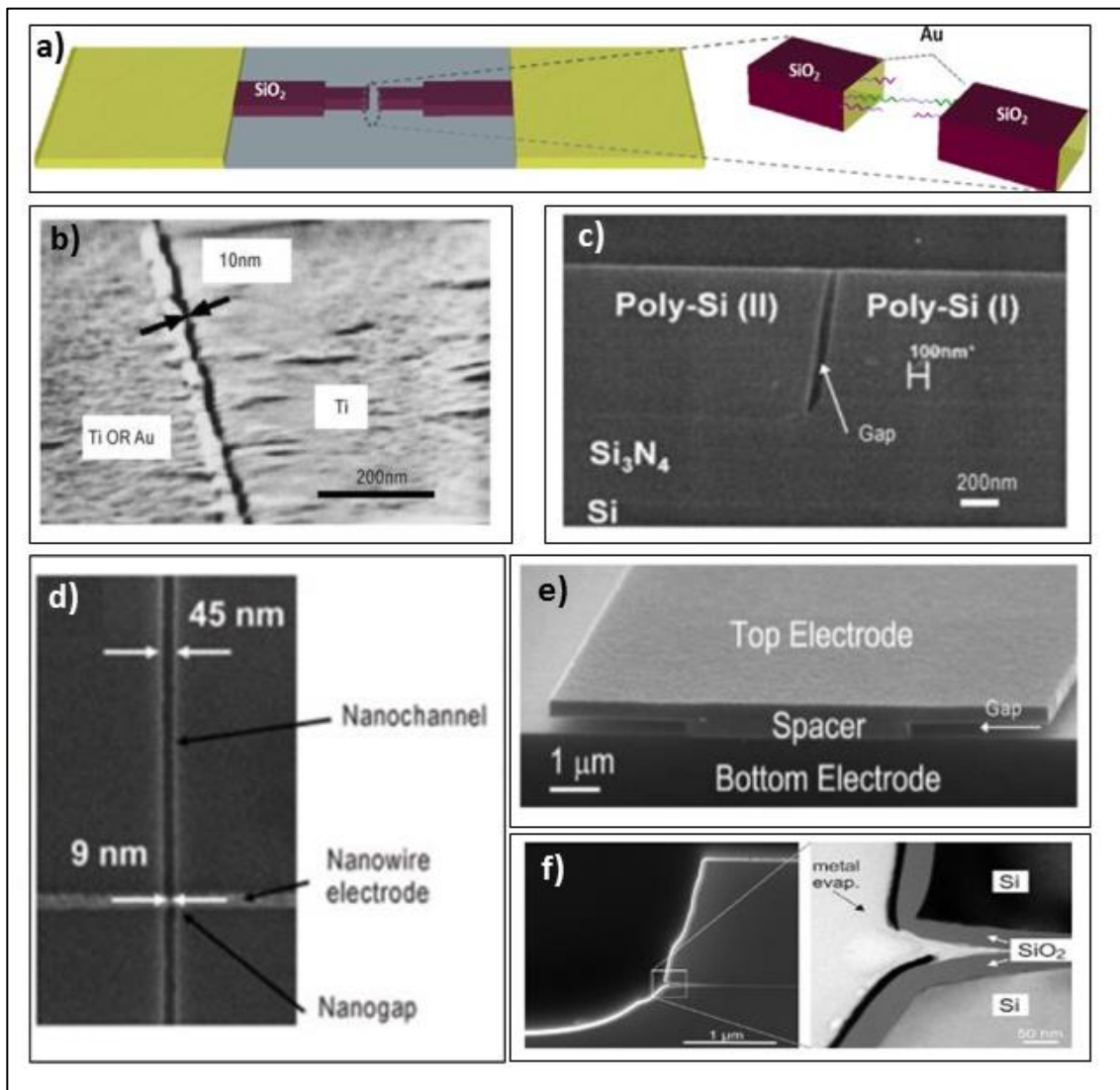


Figure 2.16. Examples of 2D planar and 3D vertical nano-gap devices with different electrode material. a) Scheme of nanogap biosensor with the gold pads for connecting the source meter unit separated by a bridge covered with 45 nm of  $\text{SiO}_2$ <sup>150</sup>. b) Nanaogap using two Ti electrodes or Ti/Au electrodes<sup>148</sup>. c) Nanogap using polysilicon as electrodes. d) A DNA detector with a nanogap inside a nanofluidic channel with top-view SEM image of a nanogap detector including a fluidic channel. e) A nanogap biosensor consists of a heavily doped single crystal silicon electrode and a polysilicon electrode vertically separated by a fixed distance of 20-300 nm, defined by a small silicon dioxide spacer. f) SEM image of the cross section of a completed nanogap device mesa edge, as prepared by focused ion beam (FIB) milling<sup>151</sup>.

In terms of fabrication methods and applications, 3D nanogap devices are mainly different from 1D and 2D nanogaps. Since nanocavity in this structures can facilitate both surface bound molecules and free molecules, the whole system can be used for deep understanding the molecules behavior in narrow gap where the size of nanogap is compatible with the molecule size itself. AC measurements techniques such as dielectric or impedance spectroscopy, which provides important information about binding

efficiency of biomolecules or hydrodynamic radius of proteins, can be applied to these structures in a very simple approach <sup>147</sup>. In the next part of this chapter benefits of nanogap for impedance spectroscopy will be discussed in more detail.

The main disadvantage of 3D nanogap structures are complex fabrication, difficulty in coupling to external equipment without introducing parasitic component and the need for reference electrodes on the devices itself <sup>147, 148</sup>.

### **2.3.1. BENEFITS OF A NANOGAP STRUCTURE FOR IMPEDANCE SPECTROSCOPY**

One type of impedance spectroscopy (IS) is a dielectric spectroscopy (DS), in which the dielectric properties of a medium can be measured as a function of frequency<sup>152</sup>. DS is based on interaction of an external field with the electric dipole moment of the sample. One major advantage of this method is to provide excellent platform for label-free detection of biomolecular structure and binding events.

The dielectric properties of a biomolecule depend on three factors: electron transfer, atomic bonding and large-scale molecular structure (molecular motion). The characteristic time scale varies from  $10^{-12}$  seconds for electron transfer,  $10^{-9}$  seconds for atomic bonds to  $10^{-3}$  seconds for molecular structure. When a sinusoidal AC voltage excites these biomolecules, they respond differently depending on the frequency of the excitation. Most of the molecular motions, such as the target binding to the immobilized probe, occur in the low frequency response regime due to the fact that, at low frequency, the perturbations occur in the biomolecules themselves and the ionic environment surrounding them are more stressed.

The dielectric response of different biomolecules, especially DNA, has been studied in great detail since 1963 by many research groups.<sup>153, 154, 155, 156, 157, 158, 159</sup> According to these works, the dielectric relaxation of nucleic acid solutions can occur in three different



frequency regions:  $\alpha$  (a few kHz or less),  $\beta$  (from approximately 1MHz to 1GHz), and  $\gamma$  (above 1GHz). Within these frequency regions,  $\alpha$  relaxation has a large dielectric contribution. This is due to the migration of counter ions over the charged nucleic acid sequences results in electrode polarization (EP) which leads to the formation of electrical double layer (EDL see part 2.2.2) at this close distance to electrodes<sup>160</sup>. Nevertheless, the associated capacitance and complex impedance arising from this polarization is so large that shadows the measured capacitance at low frequency (<1 kHz) which may also hide the dielectric property changes coming from target binding to the immobilized probe<sup>123, 161</sup>. The main two problems in this case are: 1) strong polarization in the vicinity of the electrodes can cause a large impedance which can be dominant over the impedance change related to biomolecule interaction and 2) the parasitic effect from the buffer solution due to high ionic electrical conductivity can also mask the dielectric relaxations of biomolecules of interest.

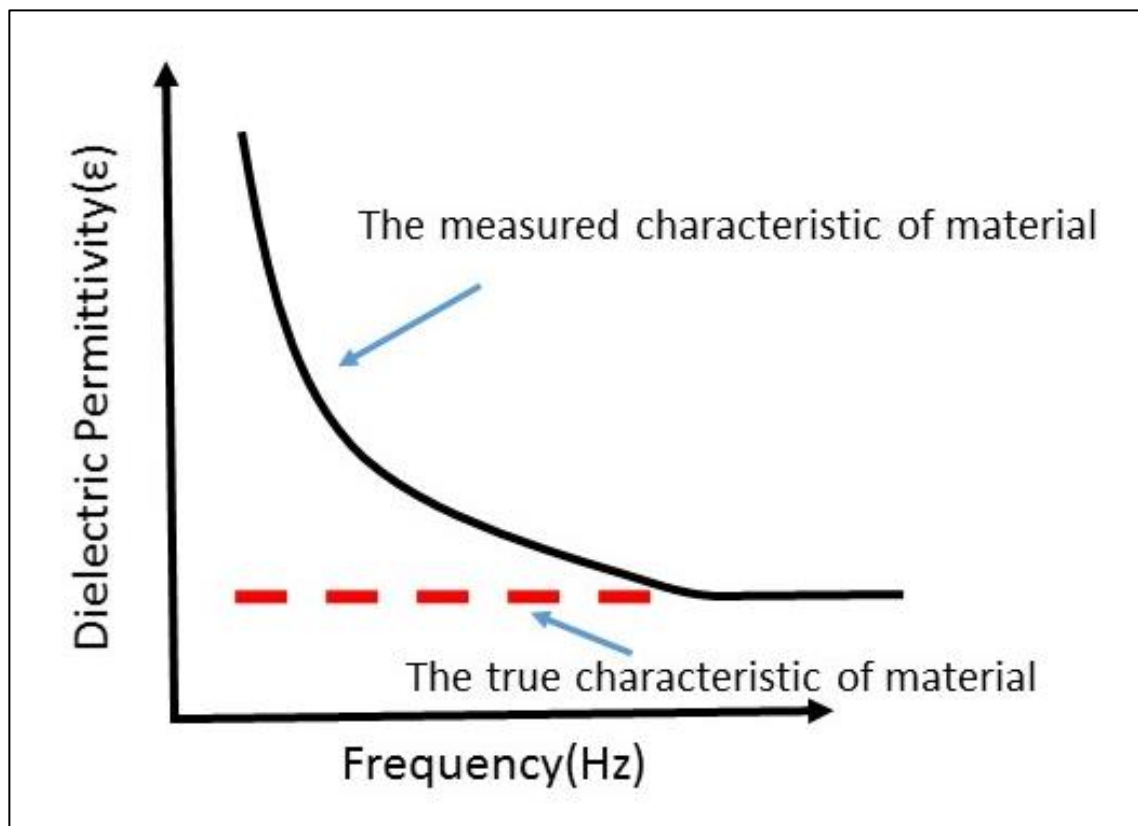


Figure 2.17. A schematic representation of electrode polarization (EP) effect in a measured signal. It is clear that at low frequency the dielectric properties of material is shadowed by EP effect.



To stress electrode polarization effect of the measured dielectric permittivity experimentally, Mannoor et al.<sup>96</sup> used an interdigitated capacitive sensor (the electrode separation is 100  $\mu\text{m}$ ). The obtained results for various samples were much higher than expected values in literature.

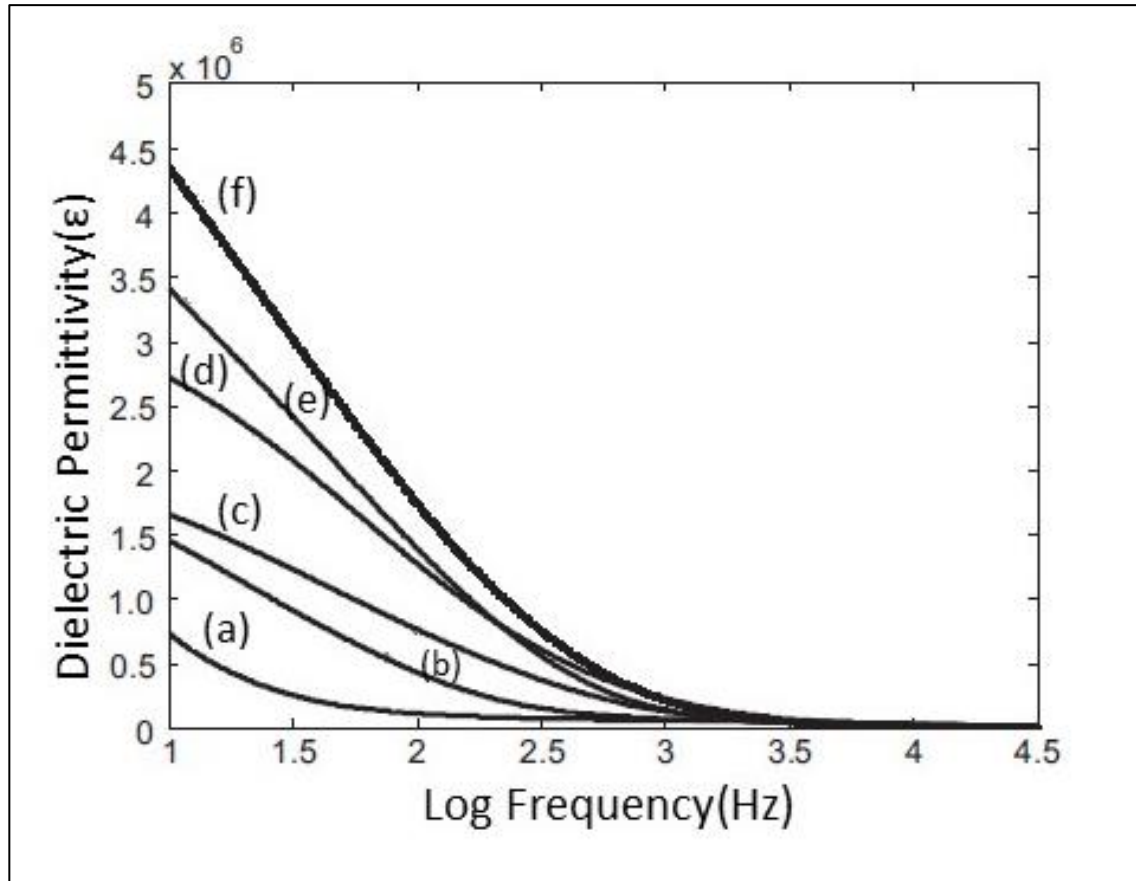


Figure 2.18. Relative permittivity as a function of frequency for air (a), distilled (DI) water (b), 0.05x SSC(c), 0.1x SSC(d), 0.25x SSC (e) and 0.5xSS(f), the SSC(Salt Sodium Citrate) buffer used were the dilutions of 0.15M NaCl, 0.15M sodium citrate to pH 6.8<sup>96</sup>.

In this experiment the dielectric spectra of air, DI water and various concentration of buffer solutions studied over a frequency range of 10 Hz to 100 kHz with 0  $V_{DC}$  bias and 20  $mV_{AC}$  signals and the results shown in Figure 2.18. the dielectric permittivity values are in order of  $\times 10^6$  which is much higher than expected values available in literature ( $\epsilon_{air} = 1$  and  $\epsilon_{DI\ water} = 80$ )<sup>162,163</sup>. This is clearly due to the electrode polarization effect and it becomes more dominant in low frequency ( $<1$  kHz) measurements<sup>96,123, 161</sup>.

There were several different methods proposed to minimize electrode polarization effect (EP). Fricke and Curtis<sup>164</sup>, introduced an approach with different electrode spacing. In this method, the induced parasitic capacitance is assumed to be same for two different spacing, which is not true when the polarization effect is large. Many other important studies were carried out by Schwan for EP correction techniques<sup>123,165</sup>. He was also the first to proposed coating the electrode with platinum black. Four electrode measurement was another suggestion to avoid EP, however it requires a complex measurements setup<sup>166</sup>.

One of the important approach to reduce this electrode polarization effect and allowing low frequency measurements is to use of capacitive element with nanoscale electrode separation. This approach can result in a significant overlap of the double layers of two electrodes and provide the important advantage of having the volume of electrical double layers occupy a major fraction of the dielectric sample volume and reducing the contribution of the bulk solution impedance<sup>96,145, 147, 161,167, 168</sup>.

Since electrode polarization effect is a major source of error for measuring the impedance of a biological samples in solution, Schwan<sup>169</sup> analyzed the system and represented it with an equivalent circuit model to isolate this polarization impedance effect. The definition of polarization impedance commonly known as a series arrangement of a resistor (polarization resistance,  $R_p$ ) with a capacitor (polarization capacitance,  $C_p$ ). this choice of equivalent circuit is not suggested by any polarization theory therefore is arbitrary. Polarization resistance and capacitance are functions of frequency and can be used for electrodes with different separation distance. The other element of equivalent circuit for the system is the actual biological sample impedance which is a resistor (sample resistance,  $R_s$ ) in parallel to a capacitor (sample capacitance,  $C_s$ ). Based on these circuit elements the equivalent circuit model for the system with two charged electrodes in presence of sample solution for both micro and nanoscale separation distance can be presented (see Figure 2.19.).

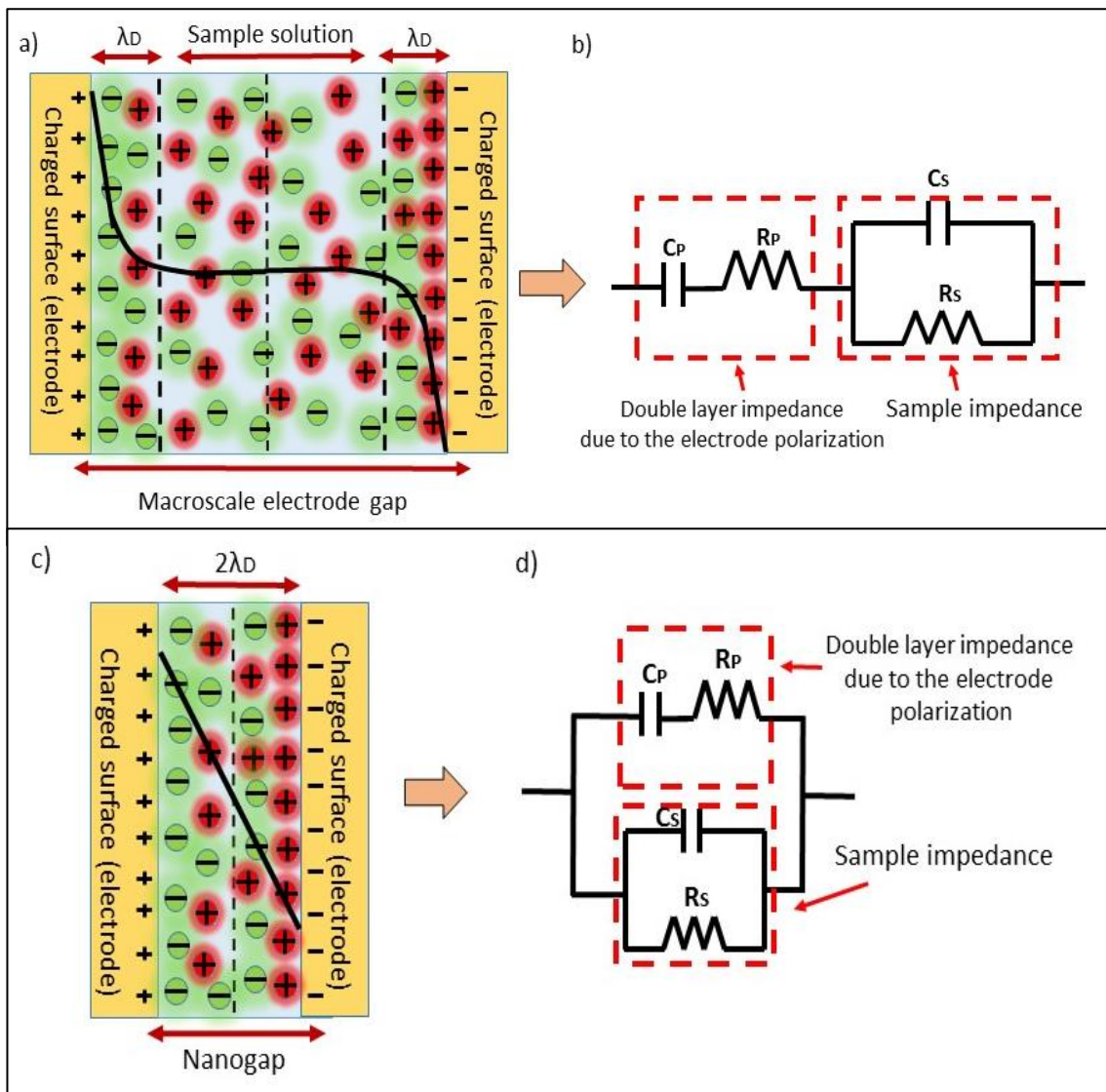


Figure 2.19. Schematic diagram and equivalent circuits of macro scale electrode polarization (a) and (b) and nano scale electrodes (where subscripts s and p represent the sample and electrode polarization).

As can be seen from Figure 2.19.a and 2.19.b, electrode polarization impedance in macroscale is in series with the sample impedance, whereas in nanogap structure (2.19.c and 2.19.d) due to the overlapping of double layers the polarization impedance is in parallel with sample impedance<sup>125, 145, 147, 161, 152, 170, 162</sup>.

For the micro-size electrode separation with the polarization and sample impedance in series the total measured impedance (measured capacitance,  $C_m$  and measured resistance,  $R_m$ ) is given by:

$$C_m = C_s + \frac{1}{\omega^2 R_m^2 C_p} \quad (2.21)$$

$$R_m = R_s + R_p + \omega^2 R_m^2 C_m^2 R_s \quad (2.22)$$

Where subscripts S and P represent the sample and electrode polarization and  $\omega$  is applied frequency. In the case of low frequency measurements, which are of particular importance in molecular conformational changes and DNA hybridization, equation 2.21 shows that the electrode polarization term dominates the measured capacitance value ( $C_m$ ) due to the second term on the right side of the equation. The measured total resistance values ( $R_m$ ) will also be distorted by the EP since  $R_p$  (EDL resistance) will increase as the frequency decreases. Therefore, EP effect will make it extremely difficult to measure the actual impedance of biological sample in macro scale setup.

In contrast, nanogap electrodes can minimize the EP effect regardless of applied frequency. Figure 2.19. (c) and (d) presents the schematic diagram of the nanogap electrode and equivalent circuit in nanogap measurements. In the nanoscale region, where the characteristic sizes of electrode separations can be of order of the double layer or smaller, the EDL from the electrode/solution interface overlaps inside the Nanogap structure and this fills the entire Nano-gap space. The measured capacitance ( $C_m$ ) and resistance ( $R_m$ ) can be calculated from:

$$C_m = \frac{C_p}{1 + \omega^2 C_p^2 R_p^2} + C_s \quad (2.23)$$

$$\frac{1}{R_m} = \frac{\omega^2 C_p^2 R_p}{1 + \omega^2 C_p^2 R_p^2} + \frac{1}{R_s} \quad (2.24)$$

In a simplified manner we can clearly see the difference between the parallel and series connection. When the frequency goes to zero,  $C_m \sim C_p + C_s$  and  $R_m \sim R_s$ . Therefore, in the low frequency region, the measured resistance values are almost equal to the sample

(solution) resistance values for the measured capacitance and it has the parasitic term which is equal to the double layer capacitance. In large gap size (macro scale) with series equivalent circuit model, the parasitic double layer effects are amplified in low frequency (see Figure 2.19) even when the double layer capacitance values are small. In comparison, the parasitic double layer effects in nanogap electrode will not be amplified in low frequency region.

Also when the double layers overlaps, the potential drop across the electrodes approaches a linear regime. Whereas in macro-size gap (see Figure 2.19. a), the actual potential drop is only within electrical double layer (region close to electrode surface) and the bulk solution has a zero potential.

The first theoretical model to evaluate the electrical potential distribution in an overlapped electrical double layer region (See Figure 2.19.c) was introduced by Verwey<sup>171</sup> based on Gouy-Chapman electrical double layer theory in 1935. For the simplicity of analysis the Verwey-Overbeek model was developed later in 1948<sup>172</sup>, for an overlapped double layer field between two infinitely large flat electrodes which have the same surface potential.

For infinitely large electrodes, the electrical double layer field between them is one dimensional and under the additional assumption of a 1:1 electrolyte, the Poisson-Boltzmann equation can be written by:

$$\frac{d^2\psi}{dx^2} = \frac{2en^0}{\epsilon} \sinh\left(\frac{e\psi}{k_b T}\right) \quad (2.25)$$

Where  $x$  is the distance from the electrode surface,  $\psi$  is the electrical potential,  $\epsilon$  is the relative permittivity of the bulk,  $k_b$  is Boltzmann's constant  $1.381 \times 10^{-23} JK^{-1}$ ,  $T$  (kelvin) is the temperature,  $e$  is the elementary electronic charge  $1.6021 \times 10^{-19} C$  and  $n^0$  is the bulk ion concentration.

According to Verwey-Overbeek model the applied boundary condition for Poisson-Boltzmann equation can be written by:

$$\psi|_{x=0} = \psi_0 \quad (2.26)$$

and

$$\left. \frac{d\psi}{dx} \right|_{x=b} = 0 \quad (2.27)$$

Where  $\psi_0$ , is the electrical potential at the surface, and  $2b$  is the separation distance between the electrodes. Assuming the  $\psi$  is small and  $\frac{e\psi}{k_b T} \ll 1$ , the right hand side of Equation 2.25 can be simplified by using the approximation,  $\sinh x \approx x$ . This simplification is referred to the Debye-Hückel approximation (see Equation 2.12). Therefore Equation 2.25 can be written as:

$$\frac{d^2\psi}{dx^2} = \kappa^2\psi \quad (2.28)$$

Where  $\kappa$  is defined in Equation 2.12 previously. Equation 2.28, together with the boundary conditions, Equation 2.26. and 2.27 can be solved and the solution predicts the potential distribution in the overlapped double layer region by:

$$\psi(x) = \psi_0 \frac{\cosh(\kappa(b-x))}{\cosh(\kappa b)} \quad (2.29)$$

This electrical potential distribution between the capacitive electrodes were simulated<sup>96</sup> and are illustrated in Figure 2.20. Here the DL is the Debye length which can be calculated from Equation 2.11 .

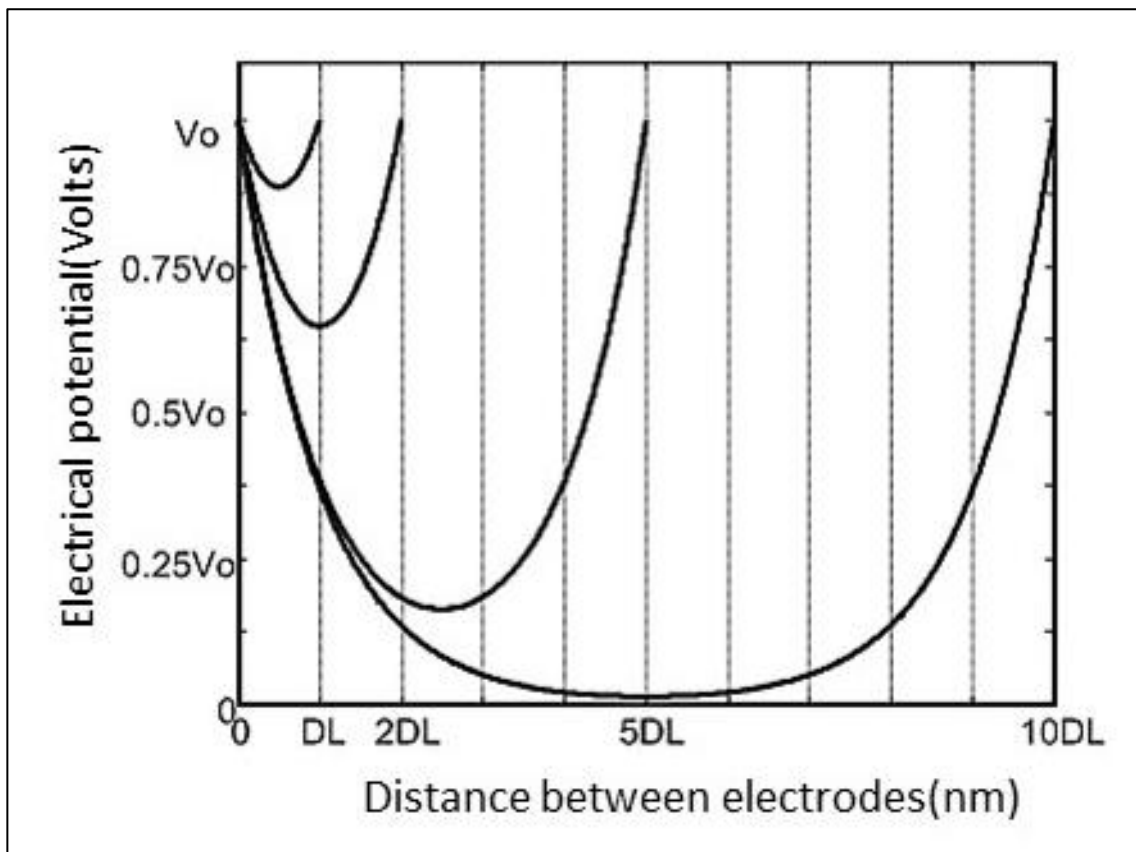


Figure 2.20. Calculated potential distribution of overlapping double layers between capacitive electrodes when the position of the second electrode is varied along the x axis with respect to the first electrode. Here the first electrode is fixed at the position  $x=0$  and the second electrode is moving away from the first electrode along the x axis <sup>96</sup>.

According to the potential distribution shown in Figure 2.20, the position of second electrode is at  $x=DL$ ,  $x=2 DL$ ,  $x=5 DL$  and  $x=10 DL$ , where  $DL=1/\kappa$  (see Equation 2.11). hence the potential drop across the double layers is minimized when the separation distance between the electrode approaches the width of EDL, this effect minimize the contribution of the double layer impedance to the measured impedance. Therefore eliminates the EP effect in low frequency dielectric spectrum.

This theoretical explanation is a very important point in biosensors, due to the fact that the entire solution inside the biosensor should be subjected to the same conditions. Clearly for the macroscale systems, biomolecules in the middle of the gap will behave more differently from the biomolecules accumulating in the electrode surface or nearby region. Having a uniform electric field inside a nanogap is a significant advantage for

these type of biosensors, because all the biomolecules inside gap will face the same electrical conditions.

### **2.3.2. CURRENT STATE OF THE ART USE OF NANO-GAP CAPACITORS FOR LABEL-FREE DETECTION**

In order to solve the issues relating to low frequency impedance measurements, a concept nanogap capacitive sensor with an electrode separation of less than 100nm has been developed. With this approach, the sensitivity of detection of the intermolecular interaction can be enhanced. Reducing the gap size between the electrodes results in the overlapping of the two EDL (one on each electrode) and decreases the potential drop across the electrodes spacing. This facilitates low frequency measurements.

The first nanogap based capacitors were reported by Lee *et al.* in 2002<sup>173</sup>. They fabricated a vertical poly-Si/insulator/poly-Si capacitor with a gap size of 50nm between two 70mm wide electrodes. The capacitance values were measured at frequencies ranging from 75 kHz to 5MHz using 0 V<sub>DC</sub> bias and 25mV<sub>AC</sub> signals.

The recorded capacitance change after DNA hybridization was around 9%. The results have also been verified using contact angle measurements and Fourier Transform Infrared Spectroscopy (FTIS). This approach has a number of issues, one being that with increasing DNA concentration after target binding to immobilized DNA, the capacitance change with hybridization is also increased. Therefore, to achieve a significant capacitance change, as well as higher sensitivity, the concentration of DNA should be reduced. Additionally, the electrode area must be increased with the reduction in gap size and operating at lower frequencies.

The other issue is that the electrode material (polysilicon) suffers from a parasitic resistance, low conductivity and the limitation of the type of self-assembled monolayers



(SAM) which are compatible with various biomolecules. To solve this issue, highly conductive electrode materials should be used which are compatible with different SAMs.

The same group also developed nanogap biosensors for detecting changes in the structure of water and ice <sup>162</sup> and conformational changes of proteins <sup>170</sup>. This sensor had another element consisting of a small polydimethylsiloxane (PDMS) reservoir adhered to the device to place the sample onto the nanogap for measurements. Further improvements to this sensor were achieved in 2005 and resulted in the fabrication of a more enhanced nanogap capacitor with 60nm gap size, in which the doped silicon substrate acted as the bottom electrode (electrode II), the polysilicon layer as the top electrode (electrode I) and an oxide layer was thermally grown between the electrodes. With selective etching of the oxide layer, the nanogap is created and for impedance measurements the top and bottom electrode were connected to two gold pads (see Figure 2.21) <sup>167</sup>.

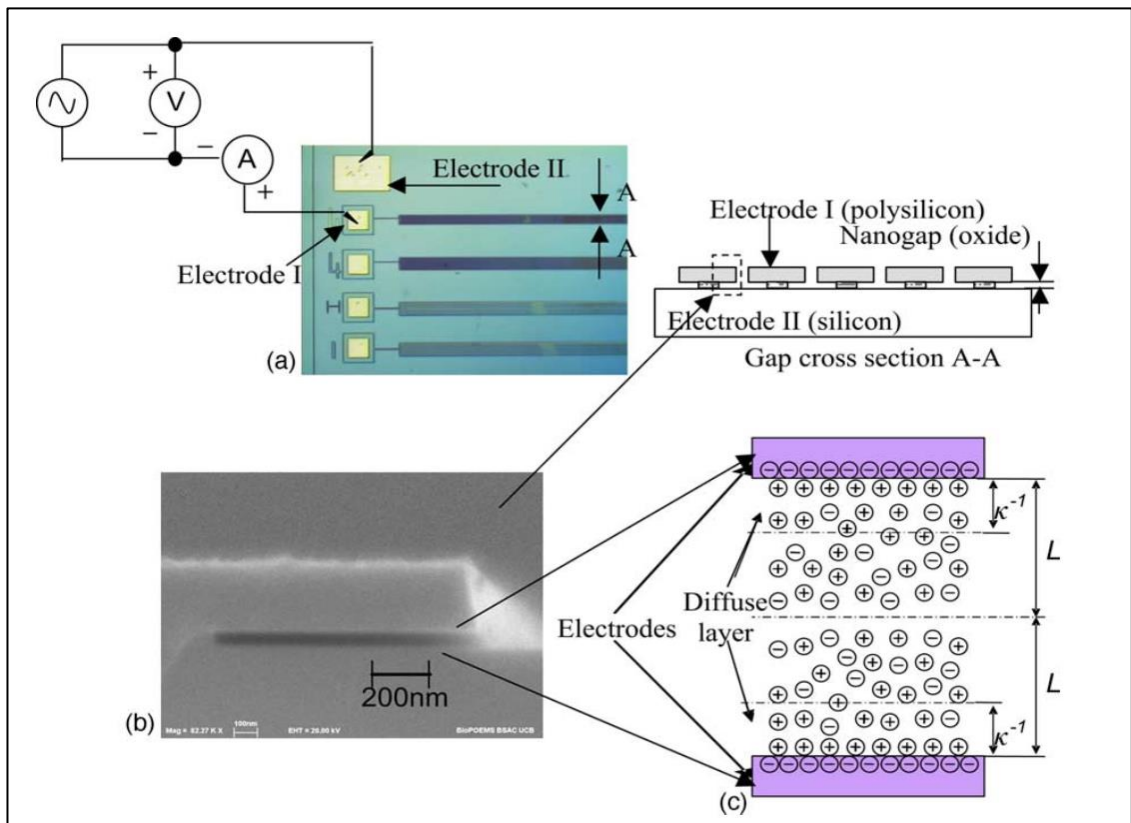


Figure 2.21. Experimental setup for nanogap capacitive biosensor. (a) sketch of wires connected to the gold pads connected to top and bottom electrodes, (b) SEM image of a nanogap fabricated with the same masks for tested nanogap, (c) nanogap filled with electrolytes where  $\kappa^{-1}$  (Debye length) is the EDL thickness and  $L$  is gap size<sup>167</sup>.

For the experiment, the  $V_{AC}$  was set to 30mV with zero  $V_{DC}$  and the measurements were performed at frequencies from 1 MHz down to 1Hz, with a frequency spacing factor of 1.5. The measured permittivity as a function of frequency decreased with the ionic strength increasing from  $10^{-7}$  ( $\kappa^{-1}=960$  nm) to  $10^{-4}$  M ( $\kappa^{-1}=30$  nm). With increasing ionic strength further to  $10^{-3}$ - $10^{-2}$  the permittivity started to increase. This observation confirmed the limit of capacitance change with ionic strength variation from  $10^{-7}$  M ( $\kappa^{-1}=960$  nm) to  $10^{-2}$  M ( $\kappa^{-1}=3$  nm) which was estimated to be  $10^{-4}$ M ( $\kappa^{-1}=30$  nm). The capacitance change between the nanogaps filled with DI water was 3.5 nF compared with the results for nanogap filled with 100 nM DNA solution which was 4.1 nF, indicated a 30% capacitance change.

The improvement of nanocapacitor based biosensors by the same research group resulted in fabrication of a slightly different device with four different geometries for top electrodes (see Figure 2.2 c) <sup>152</sup>. Three 'comb' like geometries with a separation of 10  $\mu\text{m}$  (device A), 5 $\mu\text{m}$  (device B) and 4 $\mu\text{m}$  (device C) wide 'fingers' and 'serpentine' geometry with a single 10  $\mu\text{m}$  wide finger (device D). In this work, the interdigitated nanocapacitors connected to the measurement setup via gold contact pads.

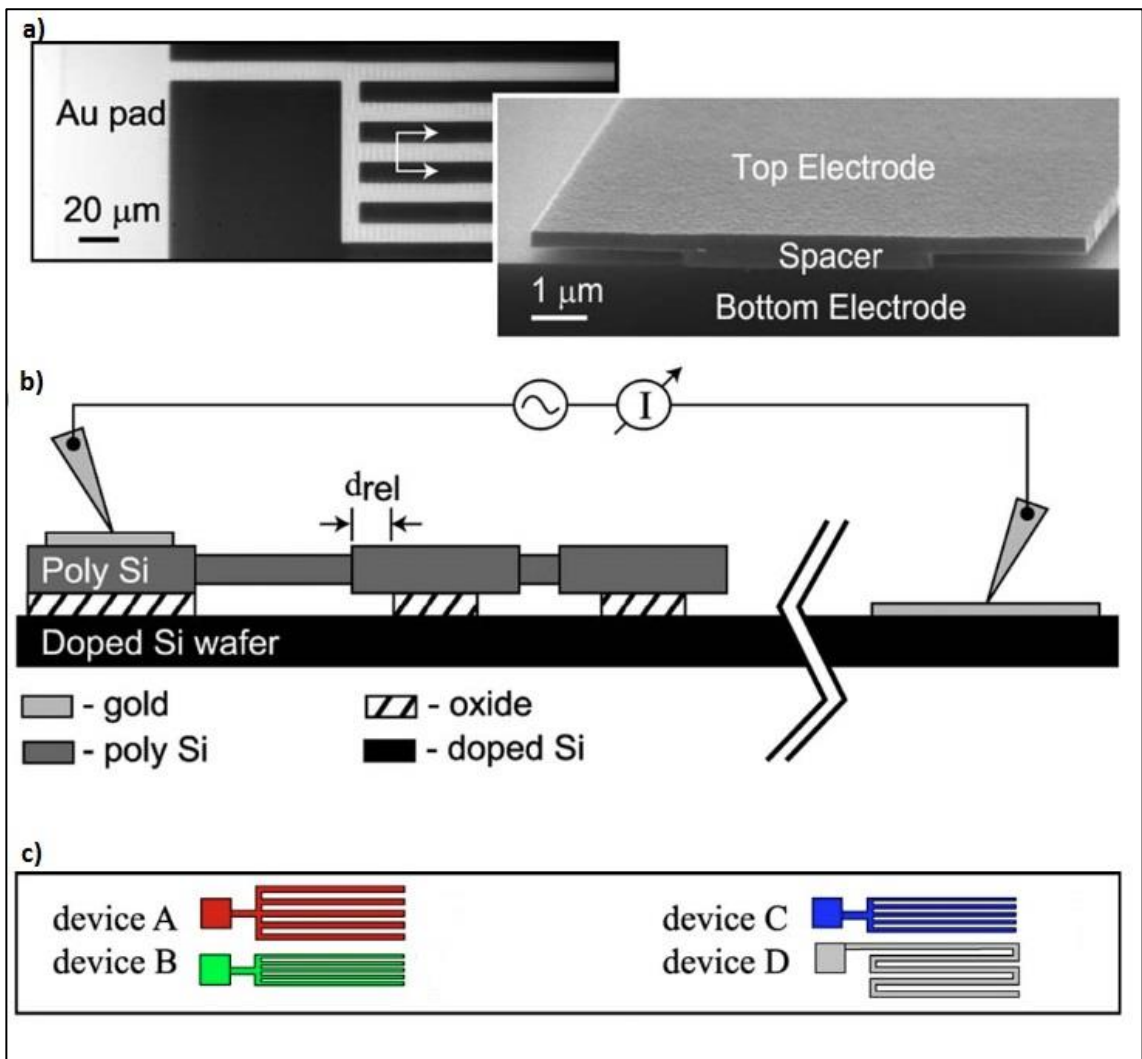


Figure 2.22. Device geometry a) top-view optical image of the polysilicon top electrode containing a gold contact pad (left) and cross sectional SEM image of 10 μm-wide finger b) Schematic representation of material used in Nanogap capacitor fabrication process and the measurements setup contact point to device c) illustration of four different device geometries, Three "comb" like geometry with the separation of 10 μm (device A), 5 μm (device B) and 4 μm (device C) wide 'fingers' and 'serpentine' geometry with a single 10 μm wide finger<sup>152</sup>.

The principal aim of this work was to determine the sensitivity of a nanogap capacitor with a change in the permittivity constant of the capacitor material. It was reported that the permittivity changes were in the range of 2- 4.25  $\epsilon_0$  which is similar to the permittivity of low hydration protein powders which range from 1 to 5  $\epsilon_0$ . This approach could be utilized for measuring the permittivity changes between different dehydrated organic molecule samples.

Another main parameter, the detection limit, was characterized in this work. This defines the smallest change in sample permittivity which results in a detectable change in the measured quantities of modular of impedance and phase change. Here the lowest detection limit for impedance was below 2% of  $\epsilon$  in the frequency region from  $10^2$  to  $10^5$  Hz.

In 2010 Mannoor et al. worked on metal electrode nanogap capacitors in a planar structure for aptamer-based protein detection<sup>96</sup>. An Au/SiO<sub>2</sub>/Au structure was fabricated (see Figure 2.21) with a separation less than 50 nm via a SiO<sub>2</sub> sacrificial layer (the oxide layer is removed completely at the final stage). Two gold electrodes were patterned onto the substrate using a conventional lithographic technique.

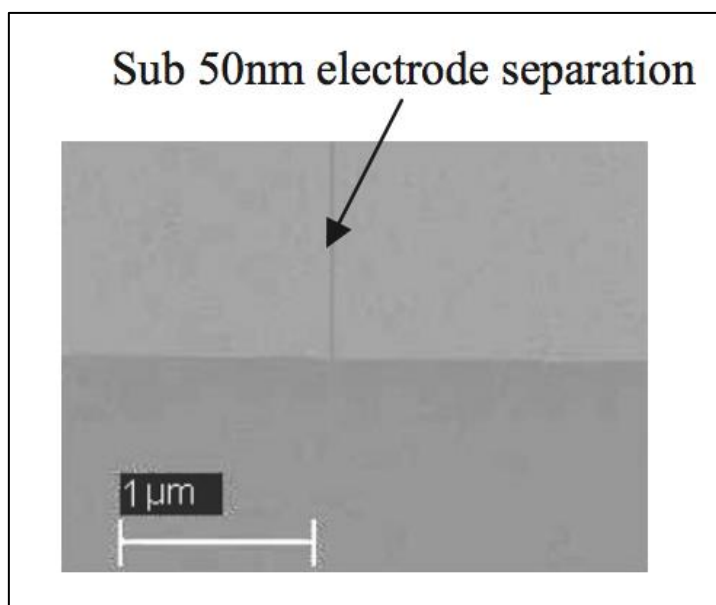


Figure 2.21. SEM image of the nanogap capacitor with <50nm gap separation<sup>96</sup>.

The dielectric spectra of the nanogap were studied over a frequency range of 10 Hz to 100 kHz with 0 V<sub>DC</sub> bias and 20 mV<sub>AC</sub> signals. The relative permittivity as a function of the log frequency results in the presence of buffer solution was high (~250). By coating the nanogap surface with SAM of specific aptamer this value decreased (~190) and finally with SAM formation following by  $\alpha$ -thrombin binding, the permittivity value decreased further (~120). This indicated that replacement of water molecules ( $\epsilon=80$ ) by

monolayer with lower dielectric permittivity had occurred. The binding of  $\alpha$ -thrombin protein to SAM further enhanced this effect. For testing the sensitivity of the sensor, the nanogap was prepared with the same SAM but different target molecules which were nonspecific and the permittivity change was negligible. Also, in this work, it was shown that the permittivity of DI water ( $\epsilon=80$ ) measured by this nanogap at low frequency was equal to the theoretical value.

Since then, several academic papers detailing nanogap devices with different electrode materials (polysilicon and gold) have been published based on resistivity and conductivity measurements in the frequency range from 10 Hz to 100 kHz<sup>174, 175, 176,177</sup>.

In most of these works, the fabrication technique was based on conventional lithography combined with chemical and oxidation etching process, with two different masks, one for the nanogap pattern and the second one for the pad electrode. The gap size was optimized with increasing the oxidation time range from 5 min to 90 min. These fabricated devices were tested for air, DI water and different buffer solution (PBS) but no measurements were performed in the presence of immobilized biomolecules.

So far, in this thesis we have identified the need for a nanogap sensor based on capacitance measurements at low frequency which can be used for real time and label-free detection of different species. We have designed and fabricated a novel 3D vertical nanogap capacitor with two gold electrodes separated by 40nm SiO<sub>2</sub> and finally, by selective etching of oxidation layer, the nanocavity has been obtained.

The nanogap capacitive sensor has been fabricated at low cost using a simple and straightforward fabrication method which can lead to mass production of label-free biosensors for clinical applications in the near future. In the next chapter the fabrication and experimental setup of the proposed nanogap sensors is introduced. This is followed by the capacitance measurements for air, D.I.water, various ionic strength buffer solutions and an aptamer-based human alpha thrombin protein in the results chapter.

One of the most common and convincing methods for nanogap electrode fabrication is to use selective etching of a sacrificial oxide layer deposited between two stacked planar electrodes. The technique we have developed uses only traditional photolithography techniques and is cost effective and straight forward to implement.

# **Chapter 3. NANOGAP CAPACITIVE SENSOR DESIGN AND FABRICATION**

## **3.1. SPUTTERING AND ETCHING OPTIMIZATIONS**

In the previous chapter the advantages of Nanogap capacitive sensors was described in detail. This chapter will detail the realization of the Nanogap capacitor developed in this work. Initial optimization experiments carried out for the SiO<sub>2</sub> and Hydrofluoric Acid (HF) etching which will be introduced in the first part of this chapter. The second part of this chapter will focus on the novel design of the Nanogap capacitor, followed by a detailed step-by-step account of the different fabrication processes used to construct the device.

### **3.1.1. SiO<sub>2</sub> Dielectric layer sputtering**

The dielectric layer for separation of the two electrodes has a crucial role for the fabrication of good devices in this project. This layer must have a very low current leakage in order to electrically separate both electrodes and to reduce the effects of parasitic resistance on the device. In this work, we deposited high quality SiO<sub>2</sub> using an RF magnetron Sputtering technique.

Sputtering is a technique where an energetic Radio Frequency wave (~13.56MHz) runs through an inert gas (Argon mixed with Oxygen) in a vacuum chamber which becomes ionized. The target material (in this case a solid disk of SiO<sub>2</sub>) is bombarded by these high energy ions, resulting in the sputtering off of atoms to give a fine spray which covers the substrate.



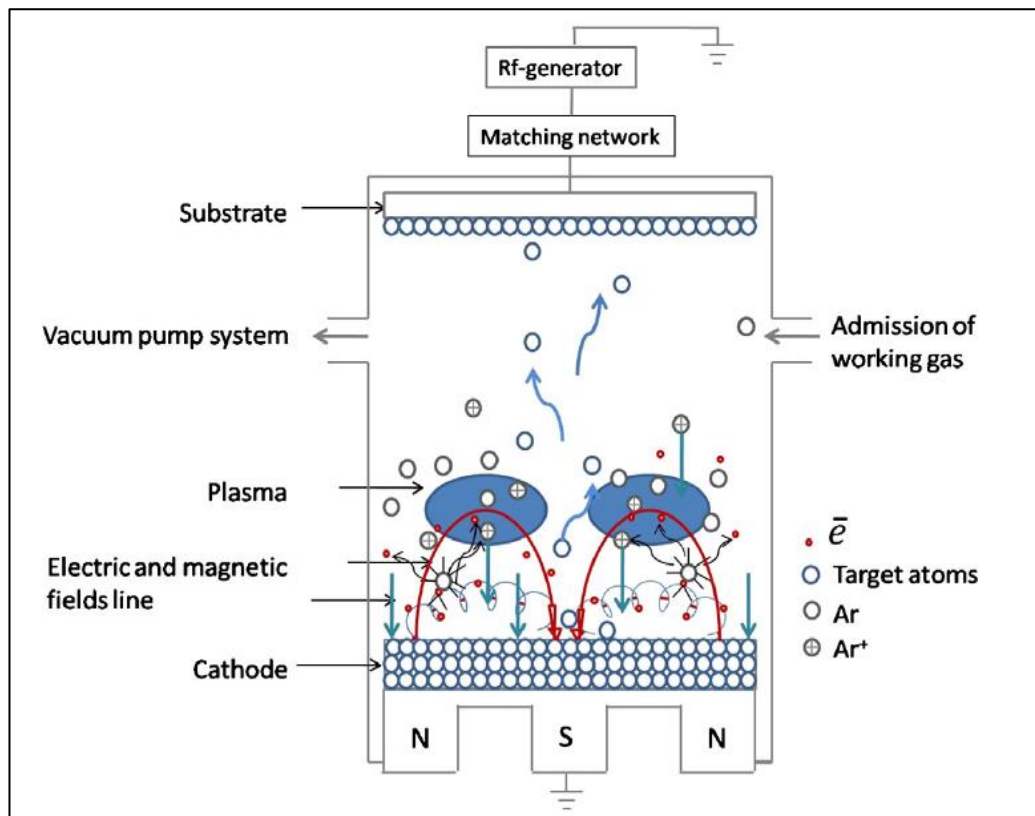


Figure 3.1. Schematic diagram for RF magnetron sputtering system <sup>178</sup>.

Figure 3.1. Illustrates the schematic diagram of sputtering system based on RF deposition. In this system Argon is used to bombard the source and in the presence of electric and magnetic field the target atoms accelerate towards the substrate to cover the desired area. The most important advantages of this technique can be listed as: 1) It produces better film quality and step coverage compared to evaporation. 2) It helps in the deposition of a wide variety of insulators, metals, alloys, composites, etc. 3) This technique works well for insulating targets. 4) Charge-up effects are avoided and arcing is reduced due to the use of an AC RF source of frequency 13.56 MHz. This is due to the fact that the electric field sign at every surface inside the plasma chamber changes with RF. 5) RF sputtering can operate at low pressures (1 to 15 mTorr) while sustaining plasma. Hence RF sputtering offers higher efficiency. 6) This sputtering technique is used to sputter any type of film

178,179,180.

### 3.1.2. METAL-OXIDE-SEMICONDUCTOR (MOS) FABRICATION FOR $\text{SiO}_2$

#### CHARACTERIZATION

In order to study the quality of sputtered  $\text{SiO}_2$ , a series of Metal-Oxide-Semiconductor (MOS) devices was fabricated. These devices were made in three different oxide thicknesses: 20 nm, 40 nm and 60 nm and in two different temperatures: 100 °C and 300 °C. The metal contact pad sizes were three different hole size diameters: small (100  $\mu\text{m}$ ), medium (200  $\mu\text{m}$ ) and big (400  $\mu\text{m}$ ).

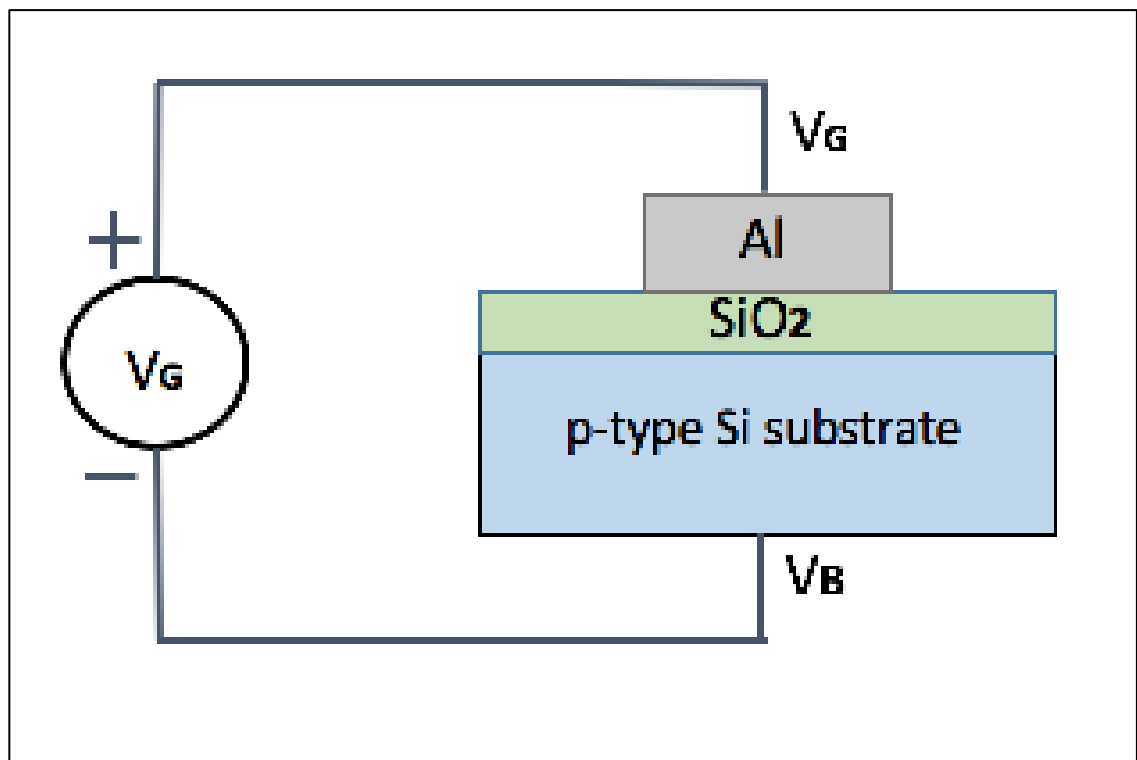


Figure 3.2. Schematic structure of MOS device. Where the gate material is aluminum and the  $V_G$  is the applied voltage to the gate and  $V_B$  is the bias voltage which applies to the back of substrate.

The fabrication of these devices started with cleaning of a p-type silicon substrate. Prior to the oxide layer deposition procedure, the substrates were ultrasonically cleaned in acetone ( $(\text{CH}_3)_2\text{CO}$ ) for 10 minutes, followed by 10 minutes in isopropanol  $(\text{CH}_3)_2\text{CHOH}$  and rinsed thoroughly with DI water.

The clean substrate was placed in RF magnetron sputtering system and for the first set of devices, the temperature of the substrate holder was adjusted to 100°C with a ratio of

Argon/Oxygen of 1:3 inside the chamber. The oxide layer were of three different thicknesses; 20 nm, 40 nm and 60 nm. For the second set of devices, all the parameters were same except the temperature which was 300 °C.

A specific metal mask (mesh) with circular shape holes in three different diameters was used to fabricate the metal contact pads (see Figure3.3). The mesh was placed in physical contact with the SiO<sub>2</sub> layer and inserted into the thermal evaporator. A layer of aluminum (Al) of around 240nm thickness was then deposited on the devices. In order to have better bulk contact, the back of p-type Si substrate was physically scratched and a thick layer of Al was deposited on the back of the devices.

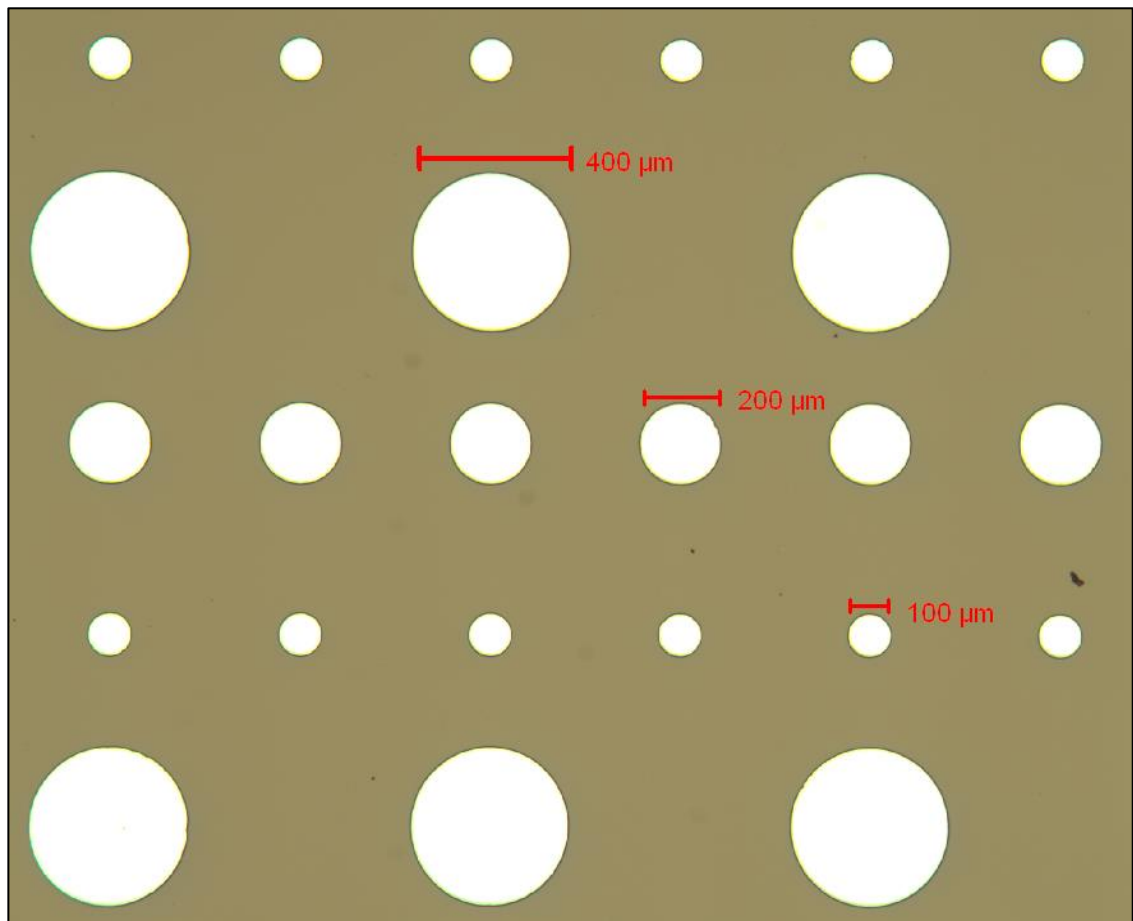


Figure 3.3. Optical image of fabricated MOS devices with three different hole sizes; 400µm, 200µm and 100µm.

As can be seen from Figure 3.3 the three different diameter size aluminum contact pads are evaporated on top of SiO<sub>2</sub> layer. For each measurements different contact can be selected.

### 3.1.3. SUBSTRATE TEMPERATURE EXPERIMENTAL STUDY

In this part of experimental work, for studying the temperature effect on sputtering/deposition time, the substrate holder of RF magnetron sputterer (home made in hull university physics department , chamber from ION TECH Ltd.) were replaced with a vacuum suitable heater unit (made in our lab).

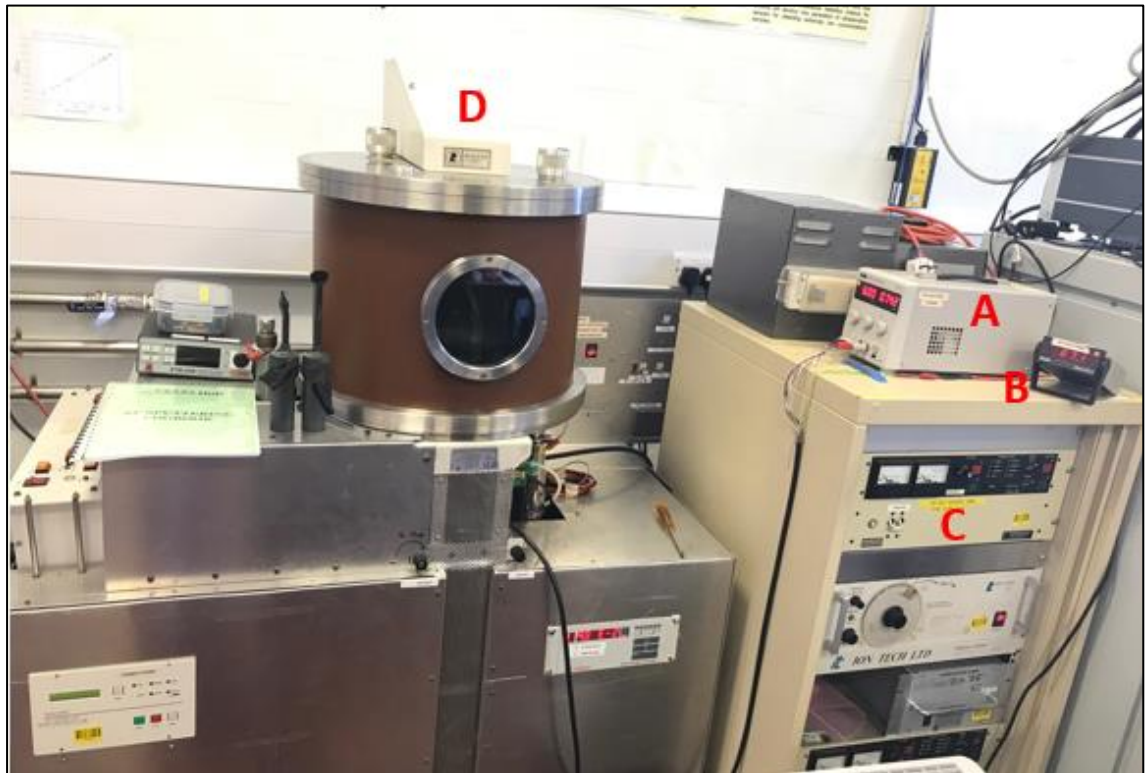


Figure 3.4 .Picture of RF magnetron sputtering system used in this project. A: power supply for applying voltage to substrate holder in deposition time, B: thermometer for reading a temperature at deposition time .C: RF power supply unit and impedance matcher, D RF supporting system with an argon oxygen inlet, thickness monitor unit and vacuum chamber.

Figure 3.4. shows the RF sputtering system used in this project, this was include a RF power unit , power supply for the heater inside chamber .The heater unit contains lines of vacuum suitable resistor and with applying DC voltage from the power supply this resister heats up to a desired temperature(see Figure 3.5).

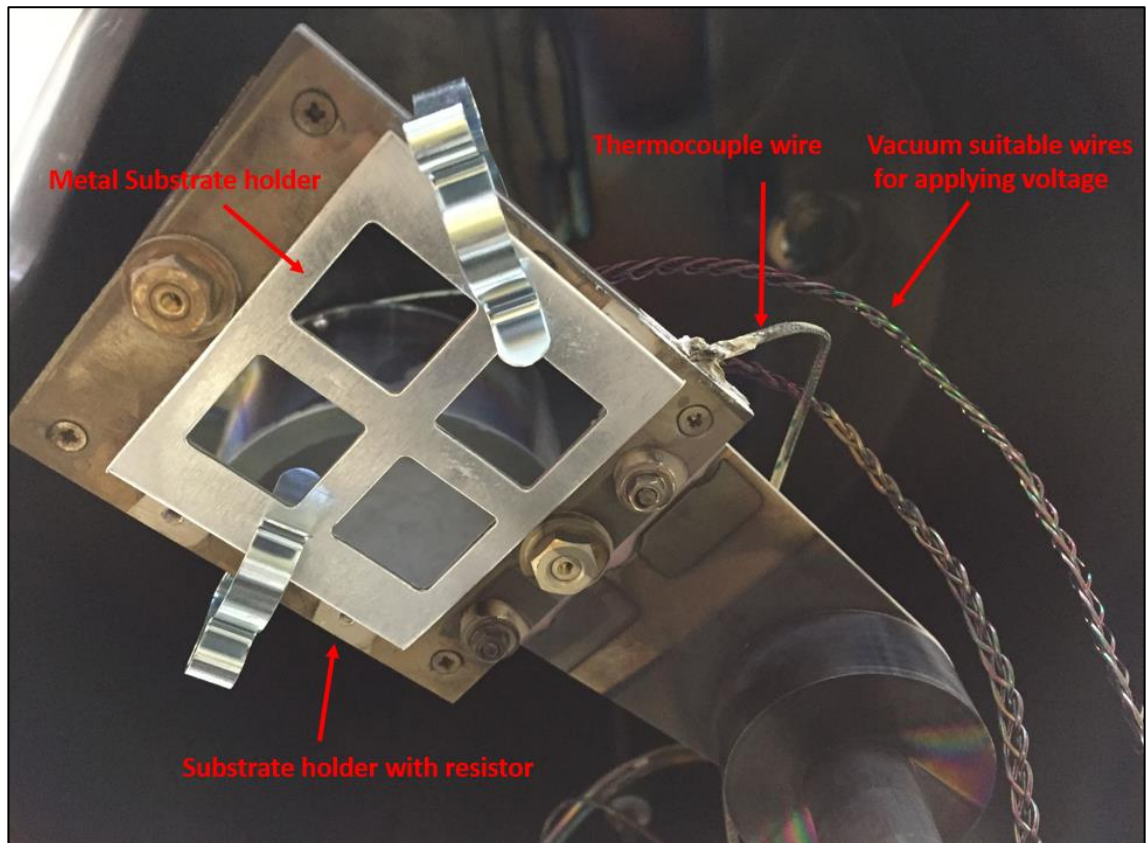


Figure 3.5. Substrate holder with a heater inside the chamber. Where the unit attached to the substrate holder and thermocouple wires and vacuum wires attached to this unit with glue.

Systematic experiments were carried out to find the best voltage to temperature ratio, with two set of experiments in atmospheric pressure and vacuum pressure ( $\sim 2 \times 10^{-5}$  mbar). DC voltage were set to three different values: 18.22 V, 21.89 V and 25.5 V and the temperature were recorder every 2 minutes.

### 3.1.4. HF ETCHING EXPERIMENTAL STUDY

In this thesis for HF etching experimental study, we have started with 5 sample (one for thickness characterization) the substrate were p-type Si. First a thick layer of  $\text{SiO}_2$  ( $\sim 250$  nm) were sputtered into substrate at  $300^\circ\text{C}$ , then in order to obtain the step that can be used for before and after HF, a photoresist layer spin coated in top of  $\text{SiO}_2$  layer, and

standard photolithography carried out with chrome mask used for nanogap biosensor. HF etching characterization were done in 4 different time: 30sec, 1min, 2min and 3 min.

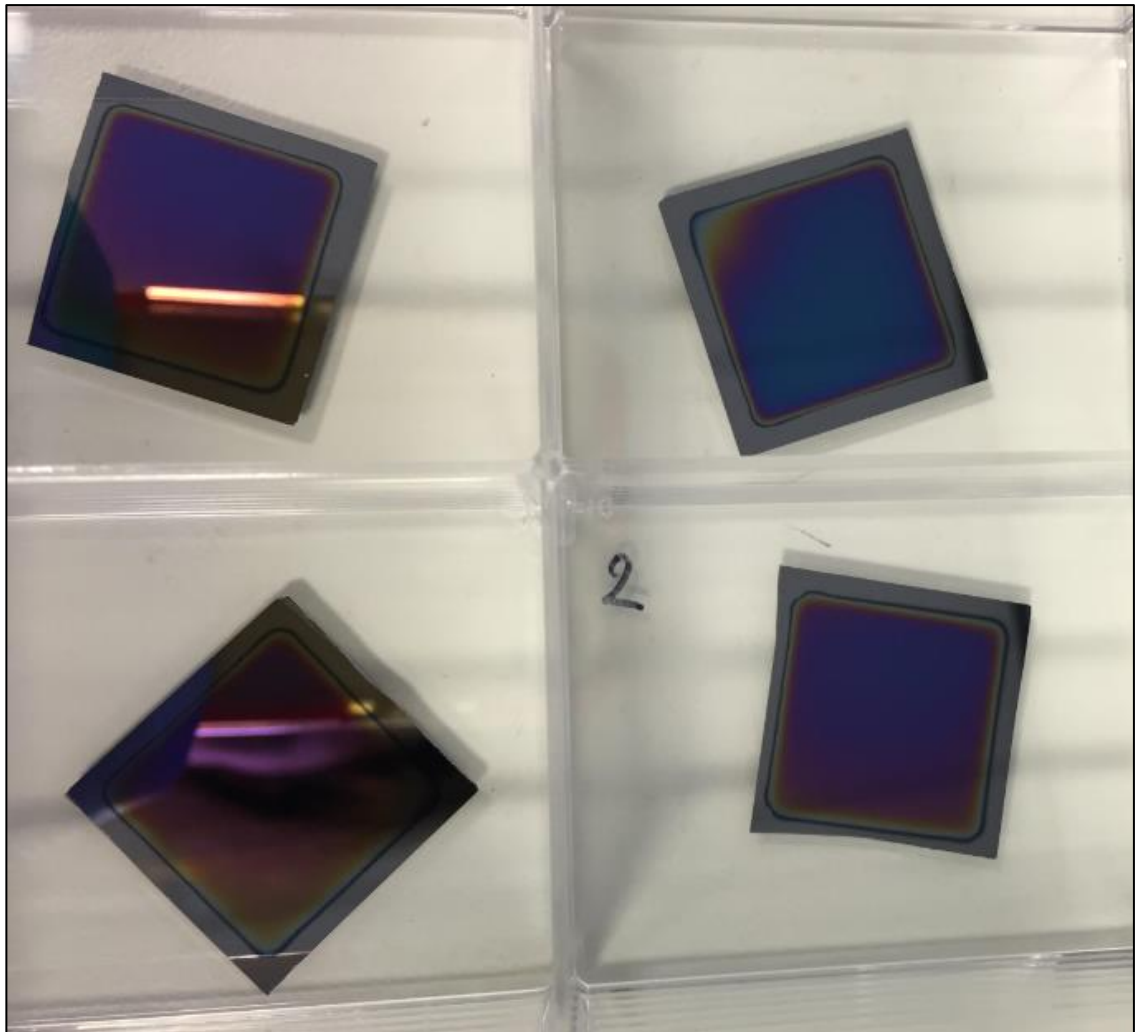


Figure 3.6. Picture of 4 sample with a thick layer of SiO<sub>2</sub> on top of Si substrate before lithography. Where the dark color indicated the thick layer of oxide in substrate and the edges were used for surface profiling aid.

After this step the samples were patterned with photoresist, and taken into HF etching lab, for health and safety reason staff members in microfabrication lab assisted us to carry the etching activity.

The samples after the HF were ready to lift-off to remove the photoresist from the sides of a window opened in SiO<sub>2</sub>, dektak surface profiler were used to characterize the thickness.

Since we were interested in high etch rate, in order to obtain 1 $\mu$ m etch profile from each side of nanogap capacitor, the 3 min HF time selected for more investigations. For the second experimental study we start with two samples , the substrates were same as previous experiment (p-type Si ) , this time first the lithography pattern were fabricated in Si substrate and then , the SiO<sub>2</sub> were sputtered on top of resist.at the final step both samples were lift-off to remove the resist from substrate and obtain the sputtered SiO<sub>2</sub>. One sample were taken to the HF etching with same parameters with 3 min etch time .Both samples were investigated with white light microscopy.



## 3.2. NANOGAP CAPACITOR FABRICATION PROCESS

### 3.2.1. SENSOR STRUCTURE AND PHOTOMASK DESIGN

The principal of operation of the Nanogap capacitor developed in this thesis is to detect changes in capacitance between two metal electrodes separated by a Nanogap when a bio molecule enters and binds to the aptamer functionalized metal electrode surface. For this purpose, a vertical 3D tri-layered stack with a central Nanogap layer was developed (Figure 3.7). The two main deciding factors that determined the choice of this structure were firstly, that a high degree of control of the Nanogap thickness can be achieved using standard thin-film deposition and etching technology, and secondly that devices of this type can be easily integrated with microfluidics technology, enabling the development of a lab-on-chip capacitive sensor that would have wide applications.

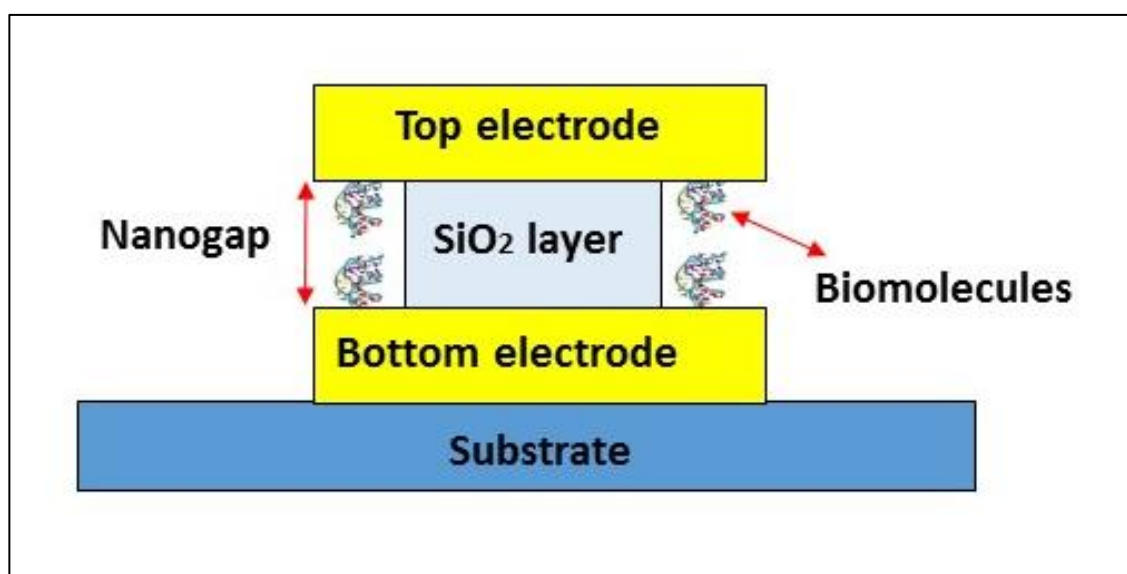


Figure 3.7. Schematic presentation of Nanogap capacitor. Where the  $\text{SiO}_2$  layer separates the top and bottom electrode and will be etched to optimize the nanogap. The biomolecules of interest can be immobilized inside the gap and the capacitive measurements can be achieved. The schematic structure of the biosensors illustrated in this chapter for the layer thickness ratio and the edge of electrode are based on ideal condition and purely are for the presentation purpose. For the real images of the biosensor at each step please see section 3.3.2 of this chapter.

In order to maximize the sensitivity of the device and to achieve a capacitance that is large enough to be easily measured, the Nano-capacitor devices were designed to have a structure in which a single device consisted of 100 Nano-capacitors in a parallel array.



Figure 3.7. shows a schematic of a single Nanogap capacitor. The gold electrodes are  $5\ \mu\text{m} \times 5\ \mu\text{m}$  and have a gap separation of  $40\ \text{nm}$  between the bottom and top electrode. The  $\text{SiO}_2$  is partially etched, approximately  $1\ \mu\text{m}$  from each side, to permit solutions to enter and modify the active dielectric sensing region. The un-etched  $\text{SiO}_2$  region (width  $3\ \mu\text{m}$ ) acts to provide structural stability to the top electrode layer. To maximize the sensitivity of the device the aim is to minimize this area much as possible. Minimizing this area is one of the key aims of future work in the project.

The equivalent circuit model of a device containing a solution (see Figure 3.8) can be treated, in a simplistic manner, as three capacitors in parallel. Two of the capacitors contain the active dielectric sensing region (i.e. the solution in this case) and the third capacitor, containing the  $\text{SiO}_2$  as the dielectric material, is for structural rigidity of the top electrode. The  $\text{SiO}_2$  region is mostly inactive (except for the surface regions) and its contribution to the overall capacitance of the device remains unchanged. In our Nanogap structure the electrodes are separated by a distance of the Debye length (for example Debye length for DI water is around  $960\ \text{nm}$ <sup>167</sup>) and the effect of electrical double layer disappears by overlapping. Therefore, electrical double layer can be neglected and the overall structure can be treated with capacitance in parallel.

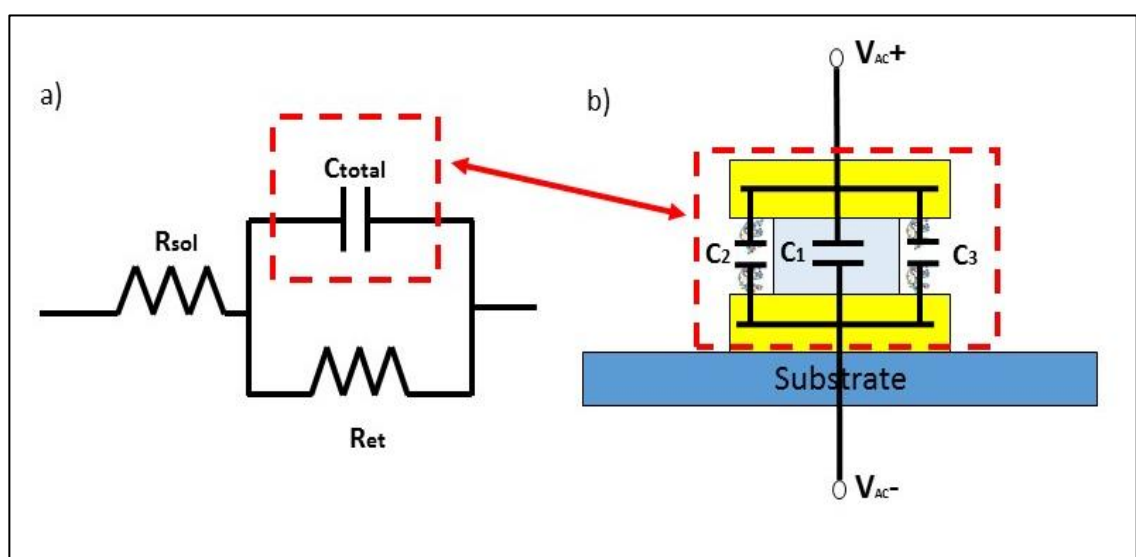


Figure 3.8. a) Equivalent circuit model for whole device, b) Equivalent circuit model for the Nanogap sensor, the  $\text{SiO}_2$  dielectric layer is modelled with capacitor  $C_1$  and the Nanogap is modelled with capacitors  $C_2$  and  $C_3$ .

The capacitors in Figure 3.8.b are in parallel and can be written as:

$$C_{total} = C_1 + C_2 + C_3 \quad (3.1)$$

Since  $C_2$  and  $C_3$  will be filled with the same medium, the total capacitance will be:

$$C_{gap} = C_2 + C_3 \quad (3.2)$$

$$C_{gap} = 2 \times \left( \frac{\epsilon_0 \epsilon_r A}{d} \right) \quad (3.3)$$

Where  $\epsilon_r$  is the relative permittivity of the solution which will be filling the gap,  $\epsilon_0 = 8.854 \times 10^{-12} \text{ Fm}^{-1}$  is the absolute permittivity of free space, A is the area of the electrode (here A is the area that is etched away and the target is to etch around  $1 \mu\text{m}$  on each side so the effective area on both sides will be  $\sim 1 \mu\text{m} \times 5 \mu\text{m}$ ) and d is the distance between plates.  $C_1$  is the capacitance of the oxide layer. Here we have used  $\text{SiO}_2$  to cover the space between top and bottom plate (electrodes) and the relative capacitance can be written as:

$$C_1 = C_{\text{SiO}_2} = \frac{\epsilon_0 \epsilon_{\text{SiO}_2} A}{d} \quad (3.4)$$

where A is the area of  $\text{SiO}_2$  which remains un-etched ( $\sim 3 \mu\text{m} \times 5 \mu\text{m}$ ) and  $\epsilon_{\text{SiO}_2}$  is the permittivity constant of  $\text{SiO}_2$  which is 3.9 for the high quality and pinhole free oxide<sup>179, 181</sup>. Each sensor contains 100 capacitors in parallel so the total capacitance of the device can be calculated as 100 multiplied by the capacitance of a single capacitor.

## PHOTOMASK DESIGN

The fabrication of the devices was carried out in the University of Hull Physics and Engineering microelectronics cleanroom facilities. The fabrication method involved standard photolithography methods to pattern and deposit the metal electrode. The chrome photomask used for the photolithography was designed using AutoCAD

software. The photoresist used was AZ5214E (Microchem), which is a negative image reversal photoresist material, hence the designed mask contains the chrome area (dark area) for the geometry of electrode and the transparent area.

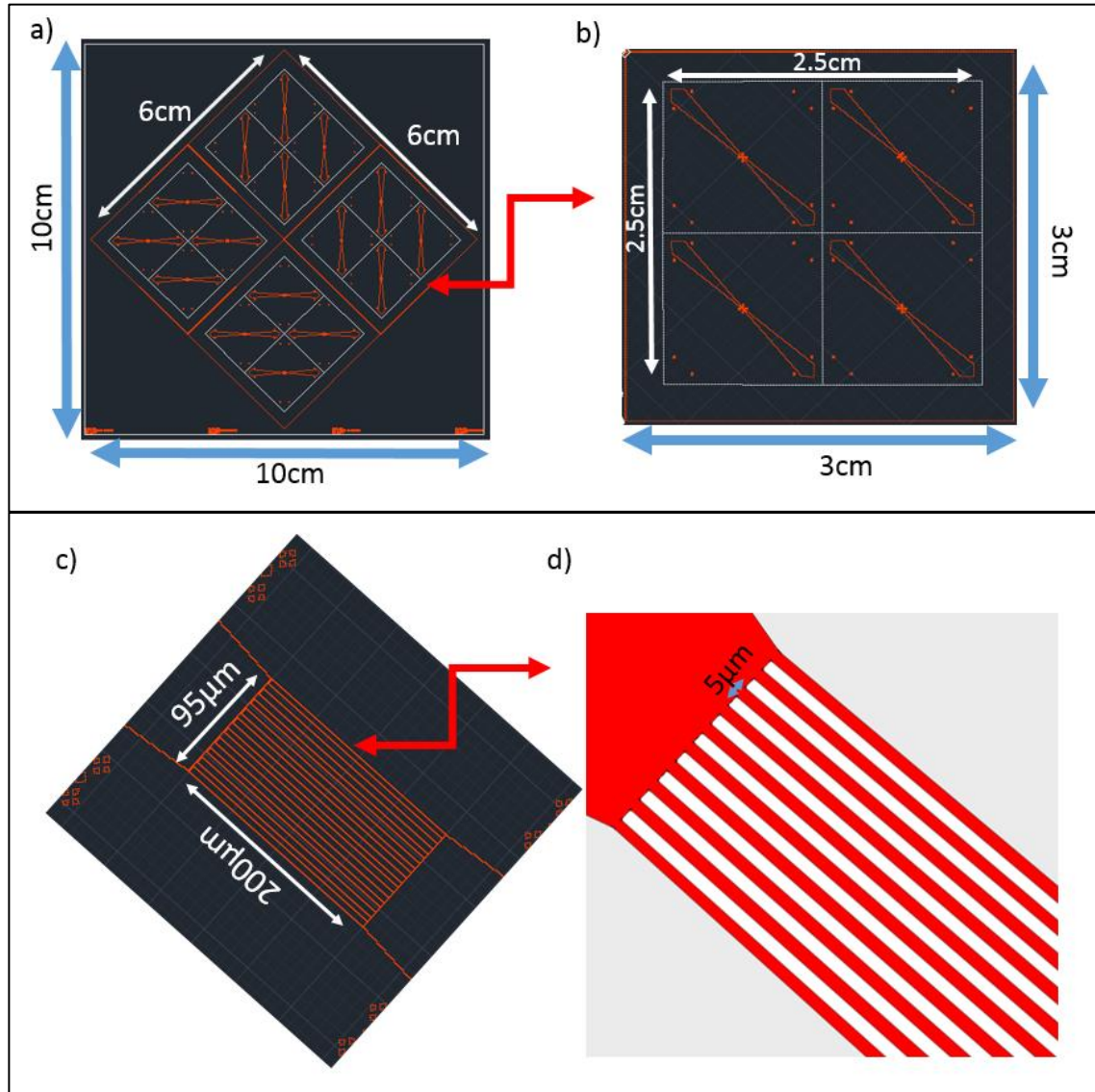


Figure 3.9. Auto Cad design of the chrome photomask; a) top view of whole photomask 10cm x 10cm containing multiple copies of the bottom and top electrode patterns, b) top view of one device with the effective size same as the UV fused quartz substrate (25mm height x 25mm width x 1mm thickness) used for the sensor fabrication. c) The center area for one Nanogap capacitive sensor with 200µm height x 95µm width, including alignment marks around it in order to align the top electrode in the center with 90° rotations. d) Top view of central area contains 10 lines of 5µm electrodes (red area represents the electrode geometry and white area is the separation between each line)

The optical image of a final devices after bottom electrode lithography, lift-off, oxide layer sputtering and top electrode fabrication presented in Figure 3.10.

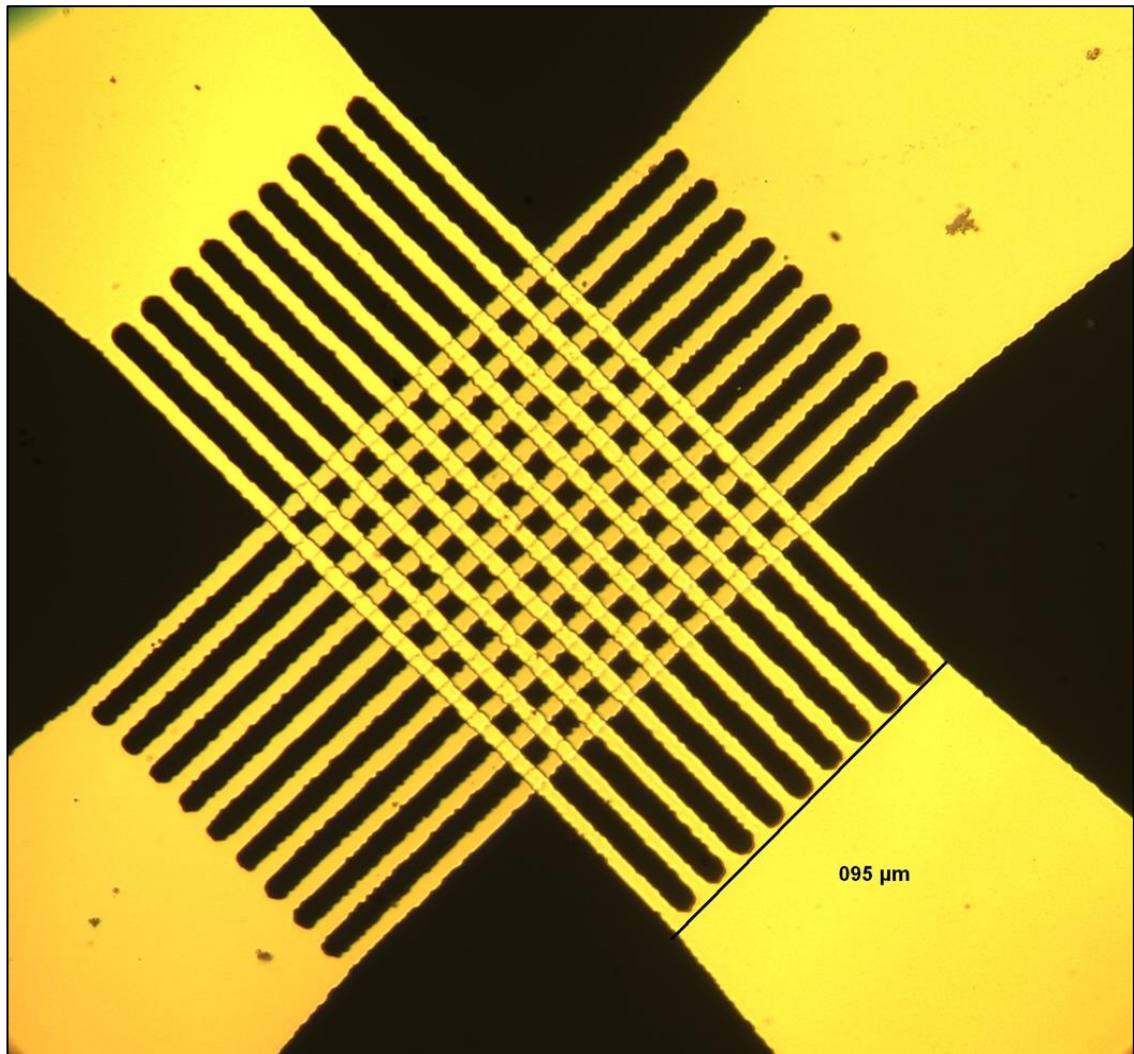


Figure 3.10. Optical image of top and bottom electrode, here after the formation of bottom electrode, following by  $\text{SiO}_2$  sputtering, for the top electrode the photomask has been rotated  $90^\circ$  clockwise or anticlockwise.

The initial observation from the optical image shows the color difference between bottom and top electrode and this is due to the fact that the bottom electrode were covered with 40 nm of  $\text{SiO}_2$ .this layer will be partially etched in final step for the optimization of nanogap.

### 3.3.2 SENSOR FABRICATION

In general, the fabrication process from start to end involves four main steps. In the first step, a layer of photoresist (1.3  $\mu\text{m}$ ) was patterned with standard photolithography for the formation of first set of Au electrodes acting as the bottom electrode (Figure 3.11.A). In the next step a very thin and uniform layer of  $\text{SiO}_2$  (40 nm) was deposited using RF sputtering technique, to form the nanometer spacer between the bottom and top electrode (Figure 3.11B). A second layer of 100nm gold metallization was applied using previous method for the top electrode (Figure 3.11.C). A sputtered thin oxide layer was then partially etched with HF to define the separation between bottom and top electrode (Figure 3.11.D). This technique allows the fabrication of capacitive structure with electrode separation lower than the resolution limit of optical or e-beam lithography.

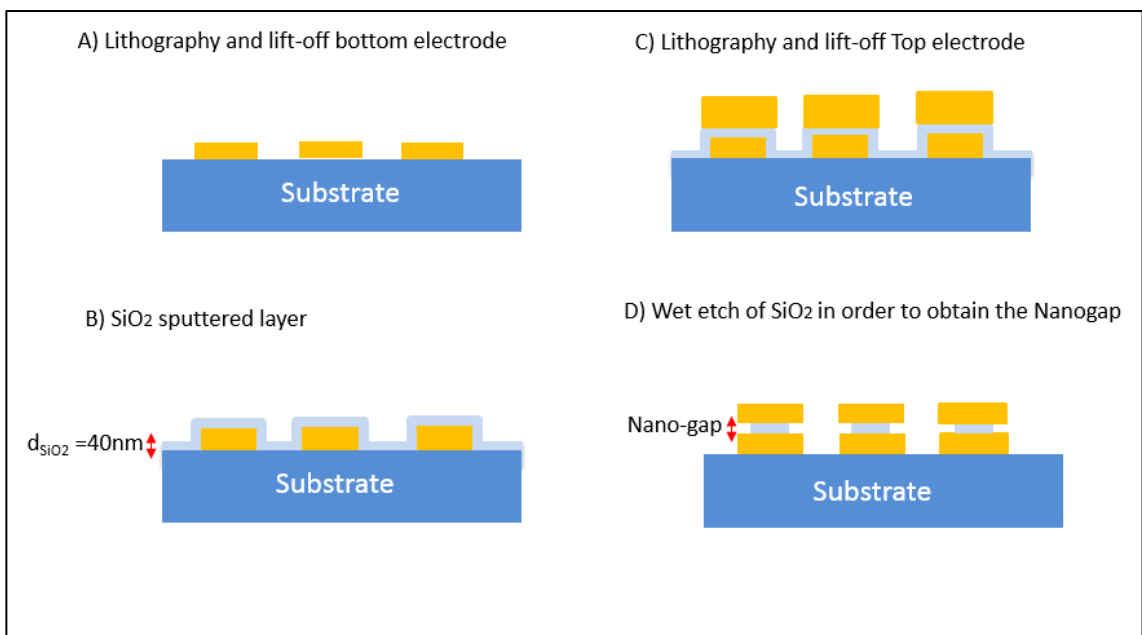


Figure 3.11. fabrication process, A) start with bottom electrode lithography, metal evaporation for the formation of bottom electrode, B)  $\text{SiO}_2$  sputtering C) top electrode lithography, metal evaporation for the formation of top electrode and finally D) HF etching of sputtered  $\text{SiO}_2$ , the schematic structures

In the following parts of this section materials and methods for each step will be explained in details with relevant images.

## **SUBSTRATE AND SURFACE PREPARATION**

In this project, UV Grade polished Fused Silica Quartz substrate with dimensions of 25 mm x 25 mm x 1 mm thick, purchased from APEX Optical services was used as the substrate material. Electrical resistivity for this type of substrate is more than  $10^{21}$   $\Omega$ .cm and the dielectric constant is 3.78 (very close to the dielectric constant of  $\text{SiO}_2$  with 3.8). Fused silica quartz was used because of its high electrical resistivity. Initially, devices were made on oxidized silicon wafers but they proved to have too high parasitic capacitance, since the large gold electrode coupled with the underlying silicon.

Prior to the photolithography procedure the substrates were ultrasonically cleaned in acetone ( $(\text{CH}_3)_2\text{CO}$ ) for 10 minutes, followed by 10 minutes in isopropanol  $(\text{CH}_3)_2\text{CHOH}$  and rinsed thoroughly with DI water. The cleaning step also includes final UV plasma cleaning for another 5-10 minutes just prior to starting the fabrication.

## **PHOTOLITHOGRAPHY AND BOTTOM ELECTRODE FORMATION**

For the formation of bottom electrode, the photolithography step was carried out beforehand in order to transfer the electrode geometry to the substrate. The specific electrode design on the photomask is shown in Figure 3.9 and was used for the image reversal technique.

The photolithography process was carried out inside the 5000sqft class 100 cleanroom facility at Hull University. The photoresist (AZ5214E) and TI PRIME (adhesion promoter) was purchased from Microchemicals GmbH. Image reversal (negative photolithography) technique was used for the formation of both electrodes. TI prime was used to improve the adhesion of the photoresist to the quartz substrate and was spin coated at 3000 rpm for 30 second on to substrate following by a 2 minute bake on a hotplate at  $120$   $^{\circ}\text{C}$ . Following this step, the photoresist was spin coated at 3000 rpm for 30 sec following by 3 minute bake on a hotplate at  $90$   $^{\circ}\text{C}$  and then allowed to cool down for 5 minutes.



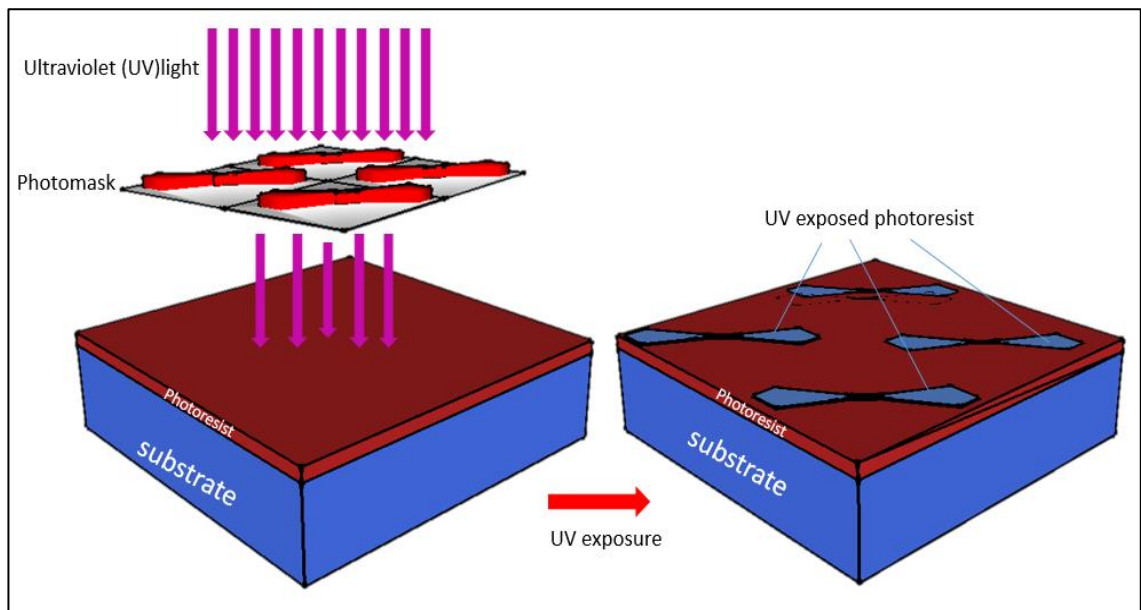


Figure 3.12. Photolithography process for transferring the electrode geometry on to substrate. Prior to the spin coating the photoresist the TI prime were used to promote the adhesion of photoresist to the glass substrate.

The UV light irradiation of the photoresists was achieved with a mask aligner (KarlSuss MJB 3). The exposure time used was 4sec, followed by a post bake for 2 minutes on a hotplate with temperature of 120 °C. The post bake step in this method is necessary for improving the resolution and breaking the polymer links of photoresist. The sample was then left to cool down for another 5 minutes and finally flood exposure without photomask was performed for an extra 15 sec. After the UV exposure process, AZ726 MIF (purchased from Microchemicals GmbH) was used to remove the un-exposed photoresist leading to the formation of desired electrode pattern on the quartz substrate. At every final step a post-bake was performed for 50 sec at 120 °C to harden the photoresist before removing from the clean room.

At this stage the fabricated sample with photolithography patterns was investigated with atomic force microscopy (AFM) to study surface topography in more detail. AFM is a form of scanning probe microscopy, in which a sharp tip is systematically scanned across a sample surface, producing a nanometer-resolution topographic map. The tip is attached to a soft cantilever which deflects and quantifies the force. The cantilever

deflection can be detected by a laser beam reflected from the free end of the cantilever into a position sensitive photodiode <sup>182, 183</sup>.

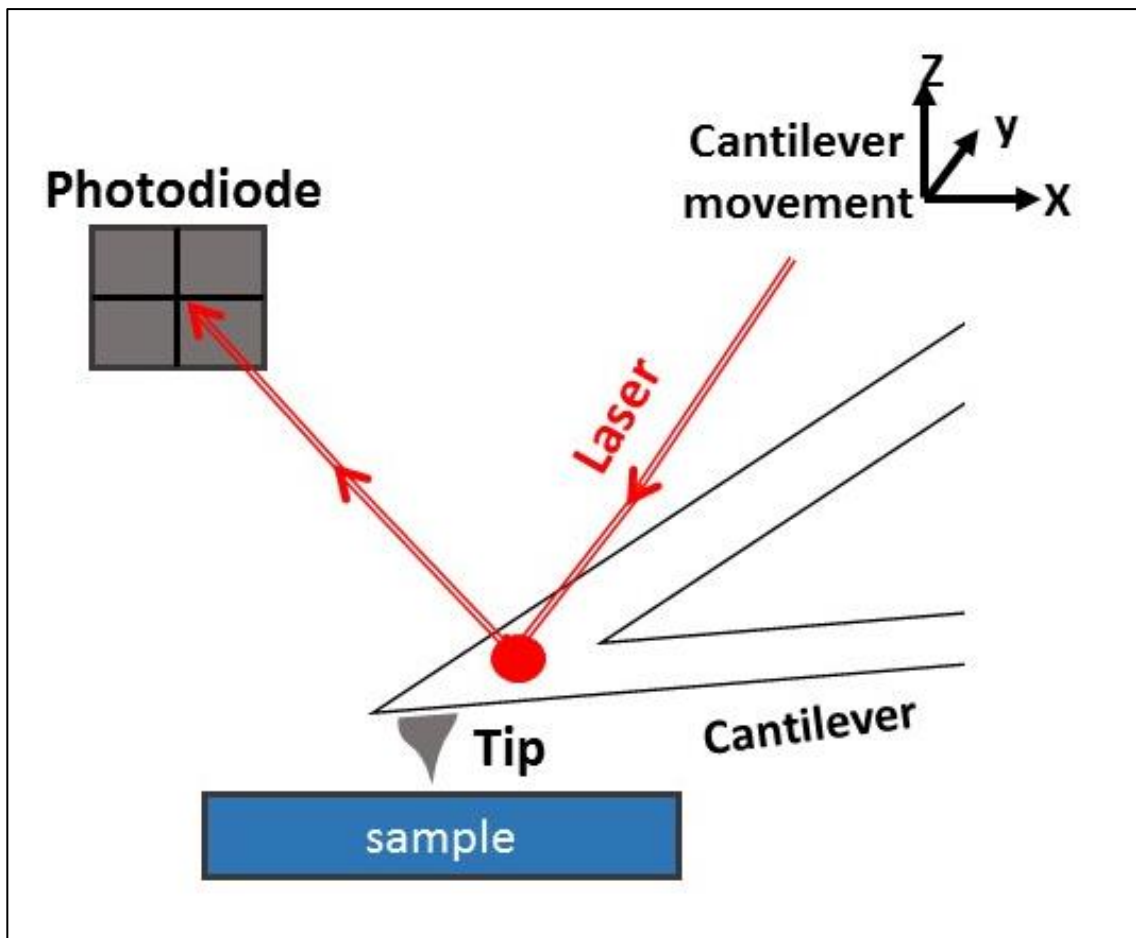


Figure 3.13. Schematic presentation for Different parts of Atomic Force Microscopy. Where the laser beam focused on to the edge of the cantilever with the tip attached to it and the reflected laser from tip will be focused on to photodiode which will be converted to the image ,modified from <sup>183</sup>.

For each point on the sample surface, the tip locally senses forces which are used for cantilever deflection feedback for creating a high resolution image of sample surface. AFM (Bruker Dimension Edge) was used to create image of obtained structure for each step and, in order to achieve a high resolution image, the scanning area were chosen to be a small.



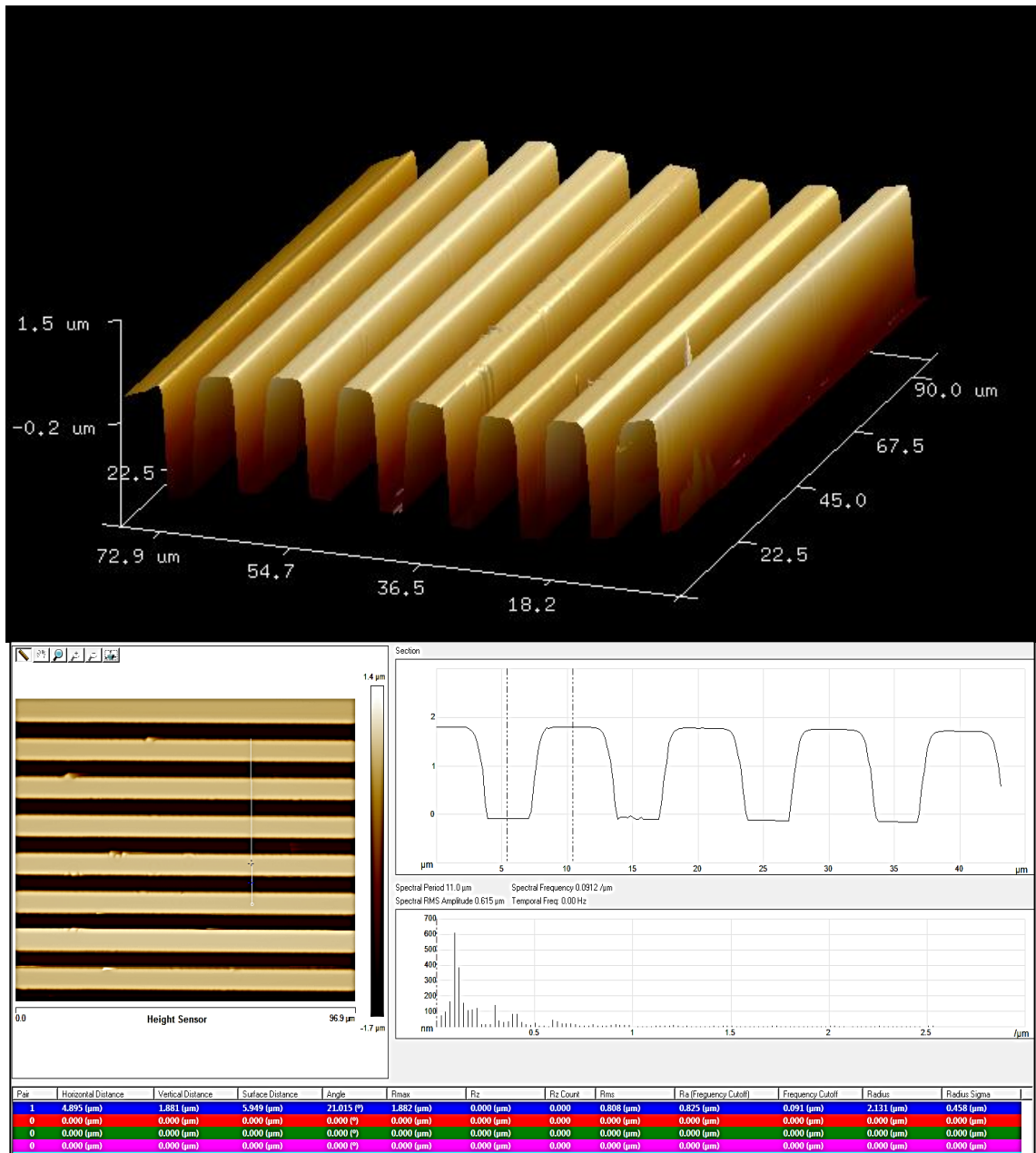


Figure 3.14. AFM analysis of the photoresist layer after the photolithography process. Top image presents the 3D image of the pattern and the bottom image shows thickness profile of the photoresist layer, the resist thickness is ~ 1.3μm.

Figure 3.14 shows the 3D image of the photolithography pattern in one part of substrate with 72.9 μm x 90 μm area (top image). The thickness and depth results in 2D version will presented in bottom image. The confirmed thickness of the photoresist for different samples are between 1.3μ and 1.8μm.

Metal evaporation was achieved using either a multi-current Electron Beam Evaporator (HHV Auto 500) or thermal evaporator (Edwards vacuum systems). The metal layer

deposited was typically 10nm Chromium followed by 50 nm of gold. The thin layer of Chromium is used for adhesion of gold to the glass substrate. This pair (Cr/Au) is been used in other experimental work also and the results are highly satisfying <sup>141,142,184</sup> .

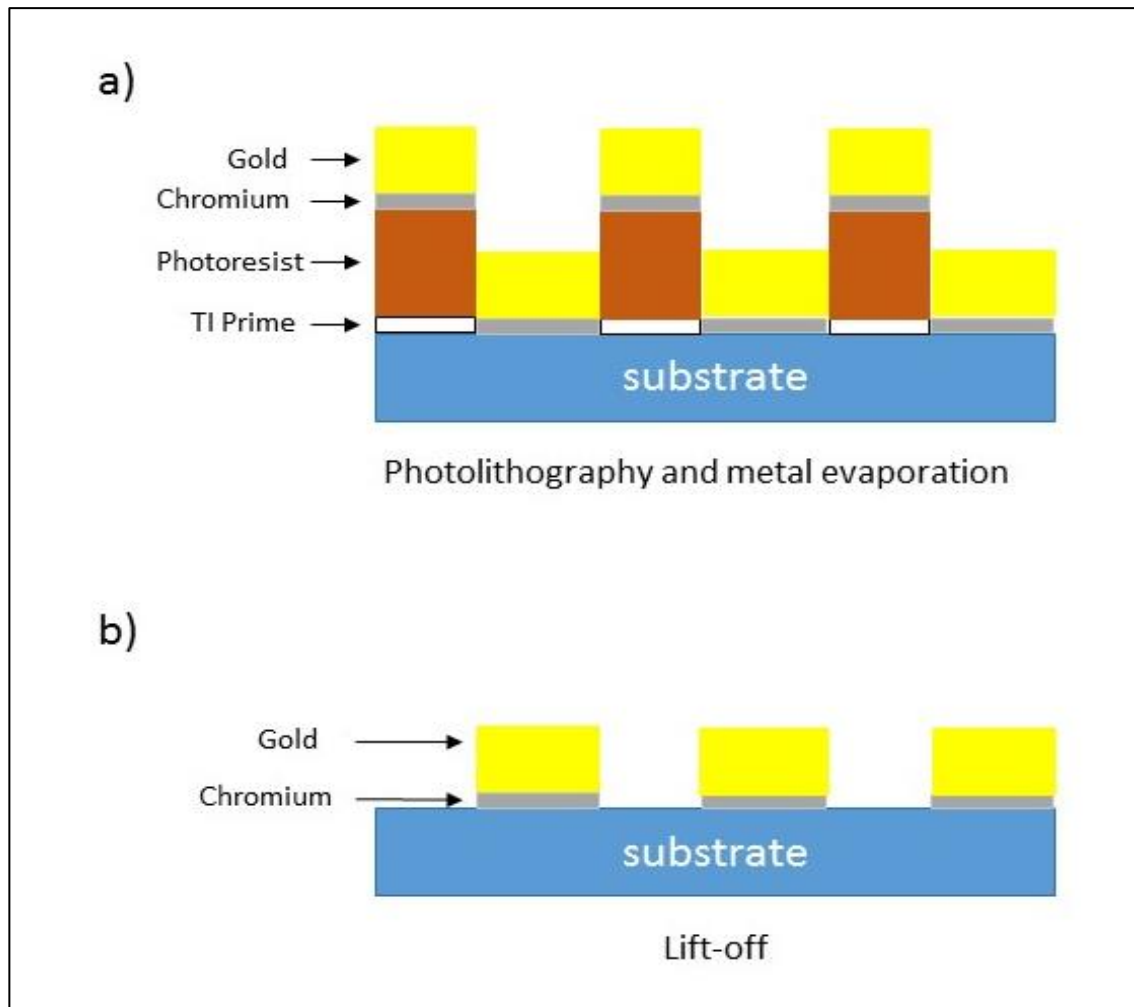


Figure 3.15. Cross sectional view for lithography, metal evaporation and lift-off steps. a) for high adhesion of photoresist to substrate a thin layer of TI Prime spin coated before photoresist coating, following by evaporation of thin layer of Cr (10nm), Au (50nm).b) the formation of bottom electrode after lift-off.

After photolithography and metal evaporation, the un-wanted photoresist and metal layer was removed using a “Lift-Off “procedure using TechniStrip P1316 (purchased from Technic, France). The procedure involved leaving the device in the TechniStrip solution for 2 hours followed by thorough rinsing in DI water and drying on a hotplate at 120 °C for 10 minutes.

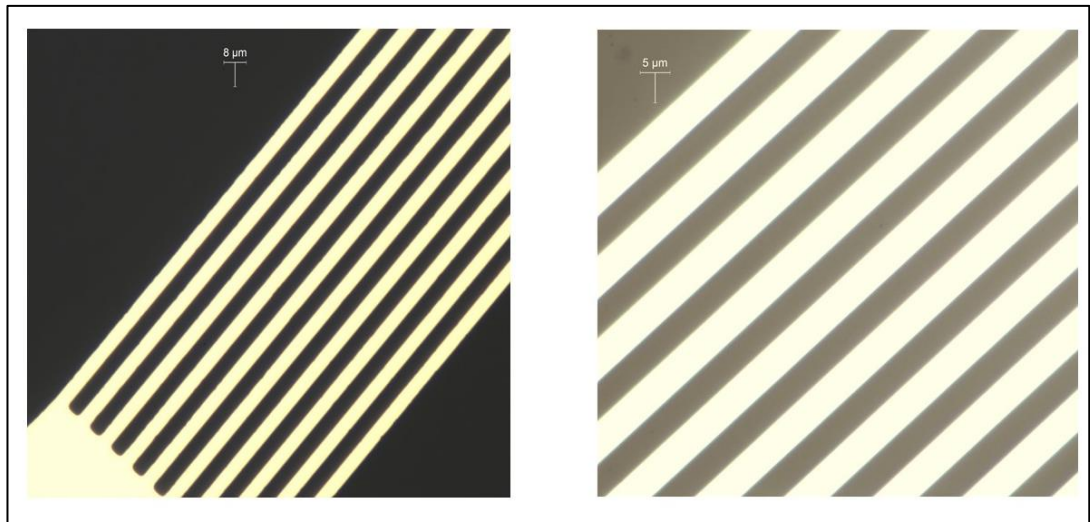


Figure 3.16. Optical image of bottom electrode after lift-off. The scale bar for this two image are both 5 $\mu\text{m}$ , where the left image is contains all 10 lines of bottom electrode and the right image zoomed on few of these lines.

After the fabrication, the devices were examined under an optical microscope, AFM (Figure 3.16 and Figure 3.17) and electrically tested for continuity across the electrodes and for the existence of an open-circuit between the two electrodes.

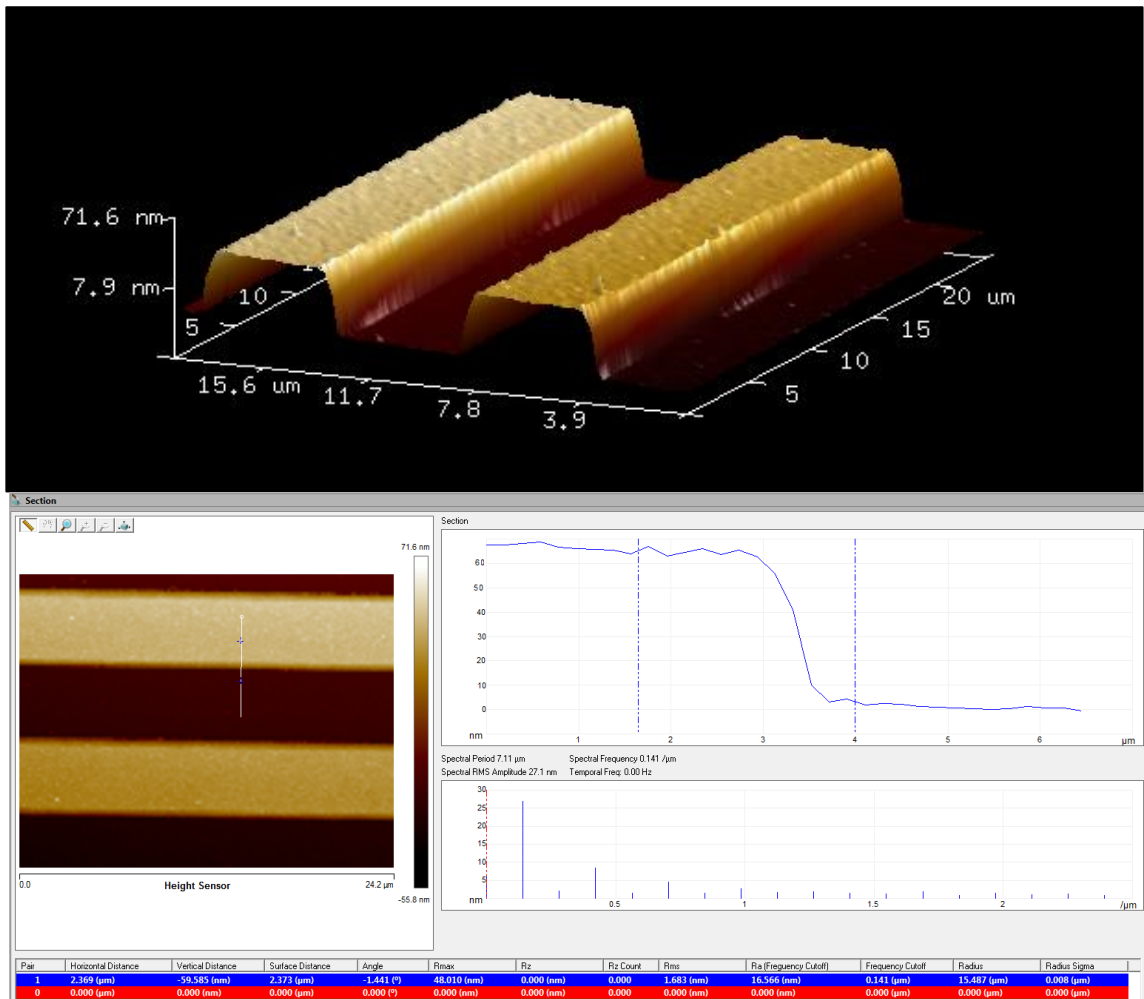


Figure 3.17. AFM images bottom electrode after lift-off for two line of electrodes (top). Where the small part of the 10 lines electrode were chosen (15.6μm x 20μm). Bottom image shows thickness profile of the first electrode in 2D, the electrode edges are very sharp and this indicates the negative lithography step is well worked for these electrode.

Figure 3.17 shows the 3D AFM image of the bottom electrode where, we zoom on a small area to investigate the efficiency of gold coverage on glass substrate. After the visual inspection the samples were tested for continuity of the electrode lines before approaching the next stage. The 2D image (bottom) shows the thickness profile for this layer which is confirmed to be between 60nm and 70nm. For this purpose an electronic test setup (see Figure 3.18) were built and includes a power supply (Thurlby 30V-1A), a multimeter (Thurlby Thandar) and 100 KΩ resistor.

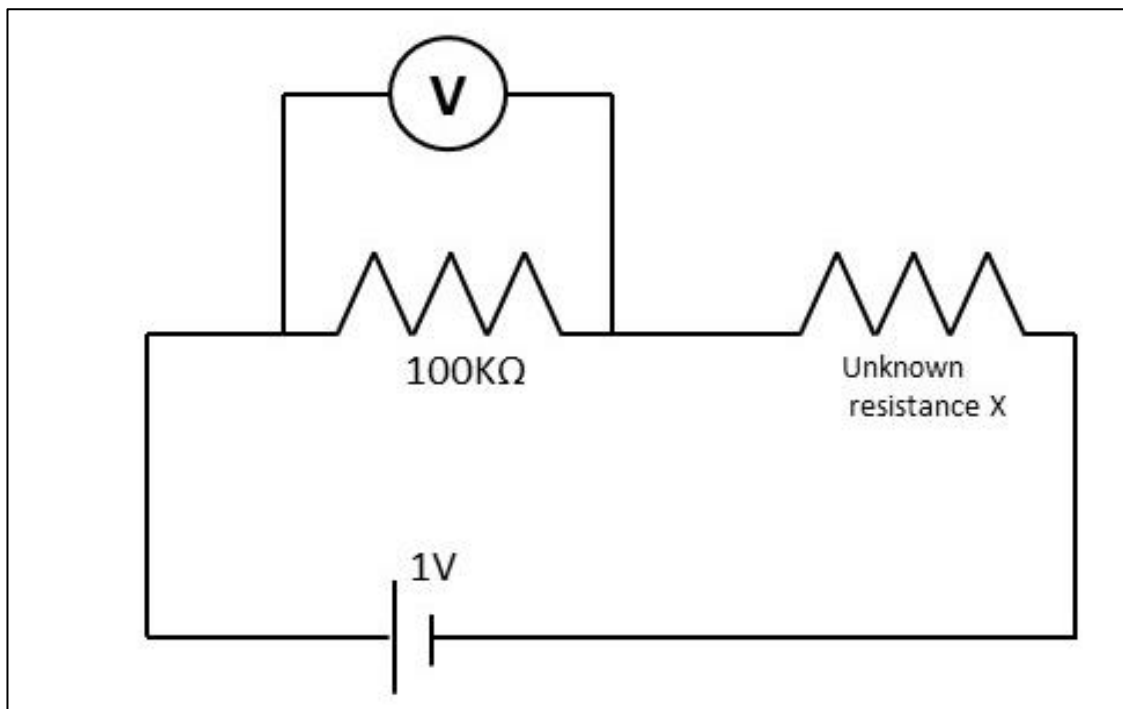


Figure 3.18. Setup for testing continuity and short-circuits between electrodes. Where a resistor with 100KΩ is in parallel connection with the voltmeter. The whole setup has 1V DC voltage and the unknown resistor is where we will place the fabricated samples.

By placing the electrode in circuit (where unknown resistance is located) and recording  $V_{\text{read}}$  for the bottom electrode, the continuity check can be performed. For faulty electrodes (e.g. with broken lines)  $V_{\text{read}}=0$  and this indicates that the circuit is not close. Whereas for a working electrode all these 10 lines are carrying the voltage across and the  $V_{\text{read}}=1$  as expected.

## **SiO<sub>2</sub> SPUTTERING**

Insulating the bottom electrode carried out using RF sputtering rig (custom made at Hull University Physics department). In order to reduce pin holes and grow a high quality oxide, the substrate holder is connected to a thermal heater that heats the samples up to 300°C before sputtering takes place. For the optimization experiments please see part 3.1 of this chapter. When the chamber achieves a good vacuum pressure ( $\sim 2.5 \times 10^{-5}$  mbar), the sputtering process starts by adding Argon and Oxygen to the chamber (3:1 ratio Argon added till pressure at stabilizes at  $9 \times 10^{-3}$  mbar and the Oxygen is then added

until the pressure stabilizes at  $1.2 \times 10^{-2}$  mbar. Finally, power (maximum 100W) is slowly introduced to chamber and from this moment the plasma start to glow.

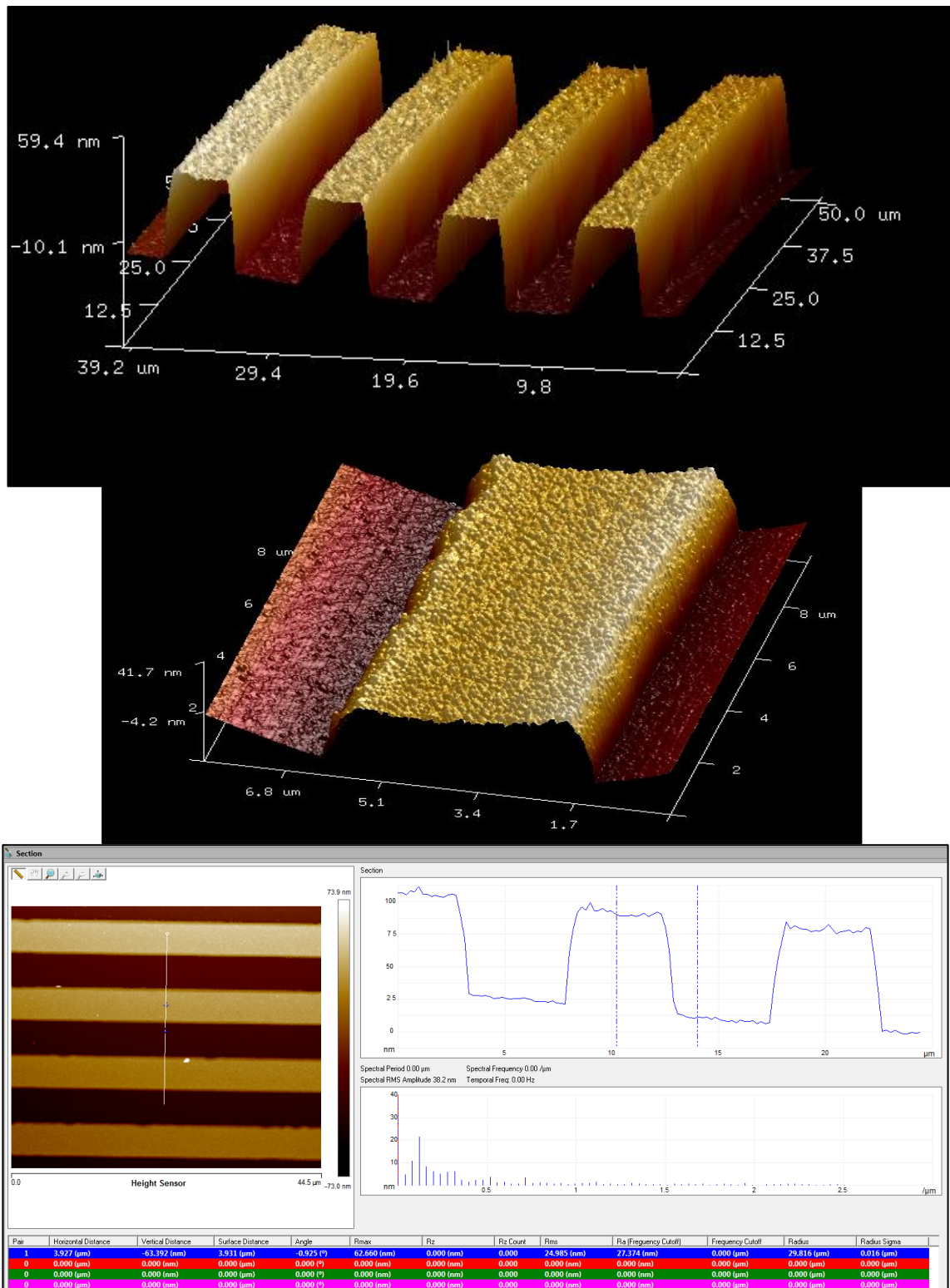


Figure 3.19. AFM images for bottom electrode covered with SiO<sub>2</sub>. The top 3D image shows 4 lines of these 10 line electrode, the middle 3D image is zoom on only one electrode to investigate the coverage of gold with silicon dioxide. The bottom 2D image shows the thickness profile for the both layer with the around 100nm, which is the confirmation of 40nm SiO<sub>2</sub> layer.

Figure 3.19 (top and middle) shows the 3D images of the bottom electrode covered with SiO<sub>2</sub> with sputtering technique. RF sputtering technique is considered as one of the best methods for preparing a thin film specially SiO<sub>2</sub> <sup>185</sup>. This is due to the fact that it can deposit films over large areas at rates comparable to evaporation method. as it is known that in the evaporation techniques the source material needs to heat to high temperature in which the material evaporates. This evaporant vapor then transfers to and impinges on the surface of the substrate where it condenses and absorbed by the surface. This process only occurs in one direction from source to substrate. Whereas in sputtering method the atoms of source material are floating in vacuum and in presence of plasma, magnetic and electric field they can travel in any direction and place on the substrate. This technique can provide a homogenous coverage for demanded surface.

The AFM images of bottom electrode before and after SiO<sub>2</sub> sputtering step (Figure 3.17 and 3.19) confirmed the coverage of bottom electrode and its side walls with insulating material. Since the side coverage of bottom electrode with SiO<sub>2</sub> is one of the important factors to avoid short-circuit between top and bottom electrodes. Nevertheless the total thickness of the both bottom electrode and SiO<sub>2</sub> (see Figure 3.19 bottom) layer is around 100 nm which indicates the 40nm coverage of SiO<sub>2</sub> layer.

## **FABRICATION OF THE TOP ELECTRODE**

In order to make the top electrode, the photolithography, metal evaporation and lift-off processes was repeated with the same parameters, except the final thickness for gold was 100 nm. For increasing the adhesion of gold layer to the SiO<sub>2</sub>, a thin layer of Chromium (10 nm) was deposited before the gold. A 100nm layer of gold was deposited for the formation of the top electrode, here for promoting a good homogenous and more rigid layer, the top electrode is thicker than bottom electrode.



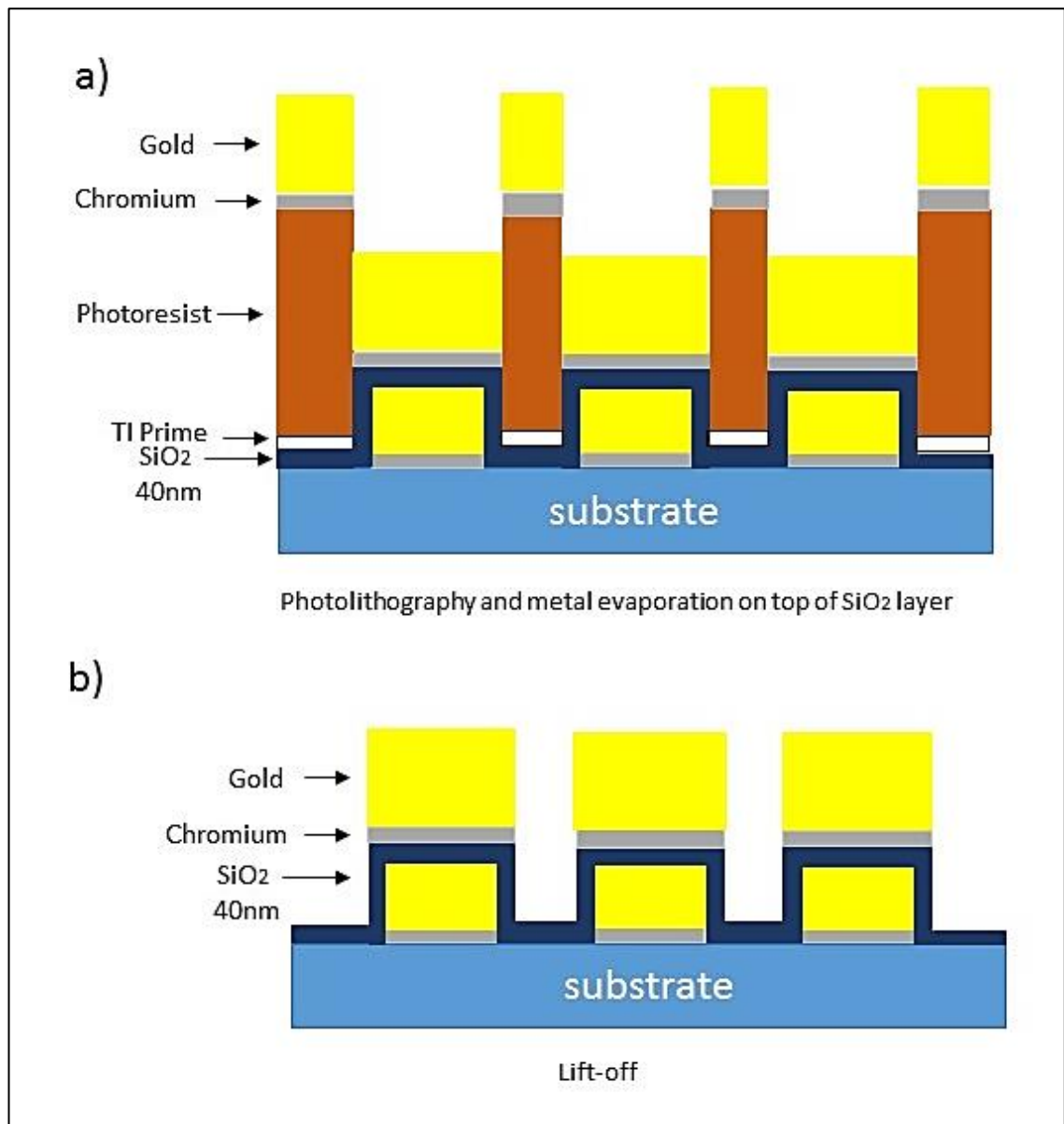


Figure 3.20. Cross sectional view of second step photolithography, metal evaporation and lift-off. a) Schematic presentation for multilayer steps, after oxide layer sputtering, second step of photolithography with a thin layer of TI prime and AZ5214E photoresist used, followed by metal evaporation (Cr/Au 10nm/100nm). b) Schematic representation of full device after second lift-off process for formation of top electrode.

Figure 3.20 illustrates the photolithography and lift-off step after SiO<sub>2</sub> sputtering. The second photolithography step in this part requires a highly skill experimental technique to align the bottom electrode on top of the structure. as can be seen from 3.20.a. the photoresist layer covers all the substrate and this includes the gap between electrode lines and the only place available for the metallization is above the bottom electrode. This photoresists layer will be removed at next step.



In the final step for the formation of the complete structure is to fabricate the top electrode with the metal evaporation technique. The thin layer of Chromium (10nm) deposition carried out prior to gold layer deposition for promoting a good adhesion of gold to SiO<sub>2</sub> layer. A lift-off process to remove all the unwanted photoresist was applied to obtain the completed device. The fact that all devices in same batch might not be in same quality and some might have a broken electrode, at this stage all fabricated devices tested for continuity and short-circuit by using the pervious setup (see Figure 3.18).

Scanning electron microscopy (SEM) and AFM (see Figure 3.21, Figure 3.22 and Figure 3.23) was used to confirm a good fabrication process result. Below are images of Nanogap capacitive biosensor before HF etching step.

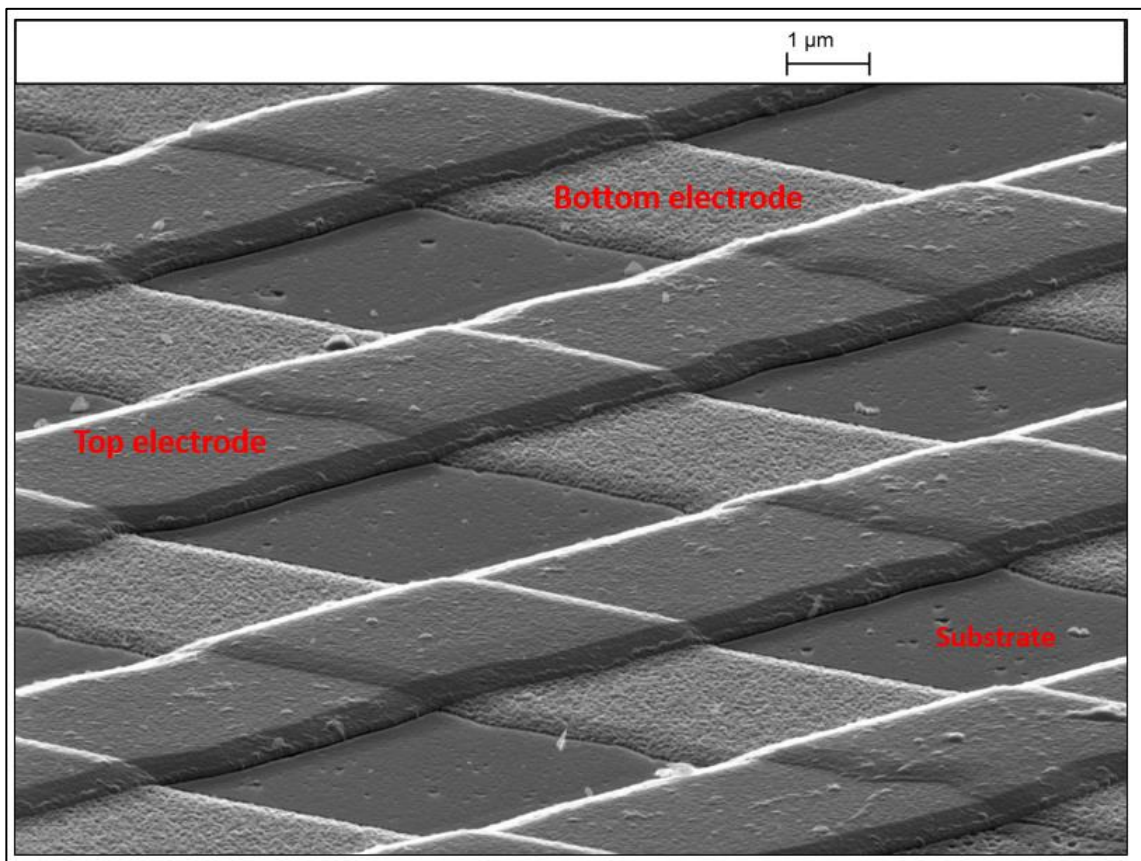


Figure 3.21. SEM image of top and bottom electrode lines. The device coated with thin layer of carbon (~5 nm) to minimize the charge effect, the electron beam voltage is 20 KV, probe current 50 pA, the substrate tilted at 45°.

Figure 3.21 shows the SEM image of the fabricated device before HF etching, the SEM images for this project are done by technical staff in hull university .for minimizing the charging effect on the surface the devices were coated with 5nm carbon. The samples

were rotated during coating at about 1 revolution per second. The coating was achieved using thermally evaporated spec-pure graphite rods in a vacuum of  $<5 \times 10^{-6}$  mBar. The probe current is 50 pA, beam voltage is 20 KV and the substrate were tilted at the 45 degree.

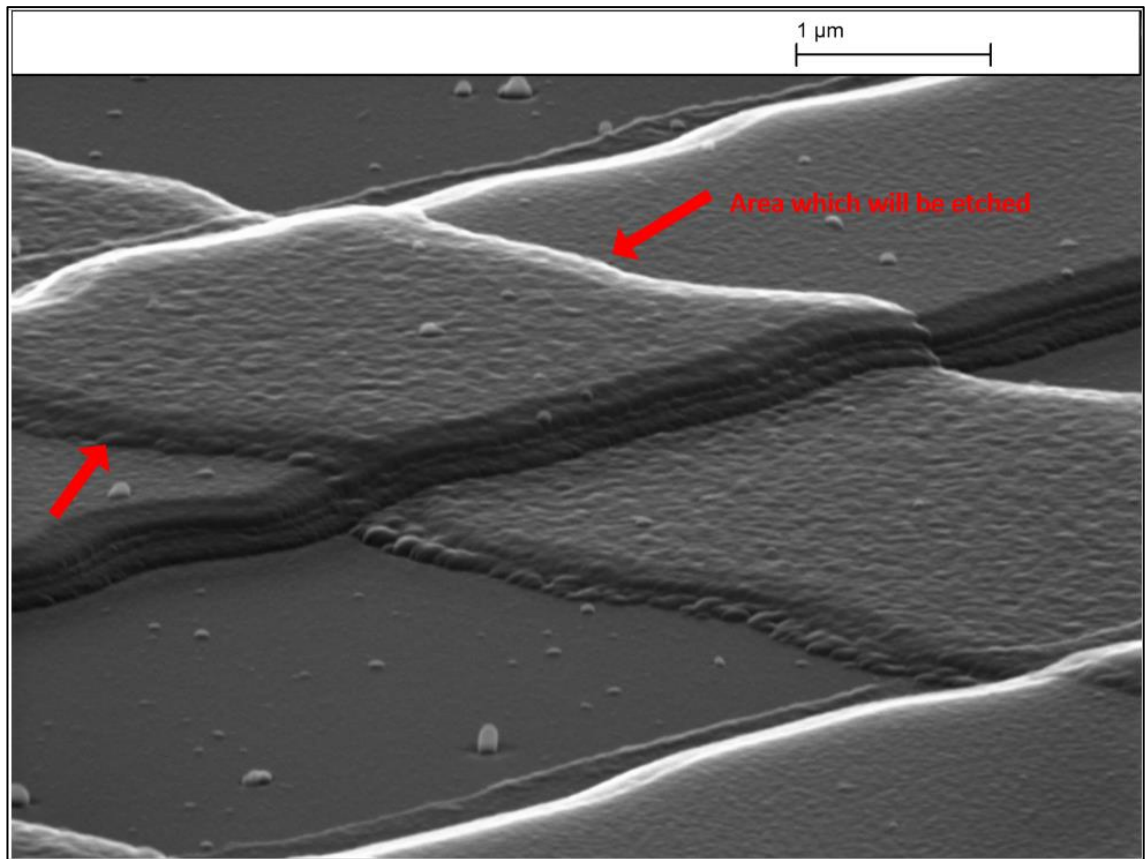


Figure 3.22. SEM image for one Nanogap capacitor before HF etching (the red arrows indicates the both side that will be etched to obtain the Nanogap). The device coated with thin layer of carbon (~5nm) to minimize the charge effect, the electron beam voltage is 20 KV, probe current 50 pA, the substrate tilted at  $45^\circ$ .

Figure 3.22 illustrates the image of a single nanocapacitor, where the arrows (in red) showing the HF sides in order to obtain the nanogap. The device were coated with 5nm carbon, the probe current is 50 pA, electron beam voltage is 20 KV and the substrate were tilted at the 45 degree.

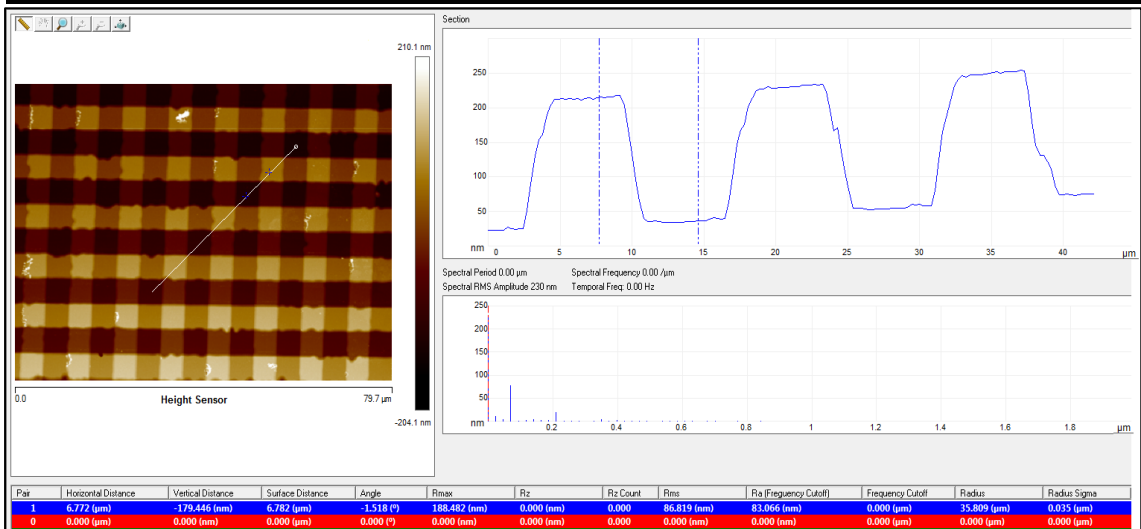
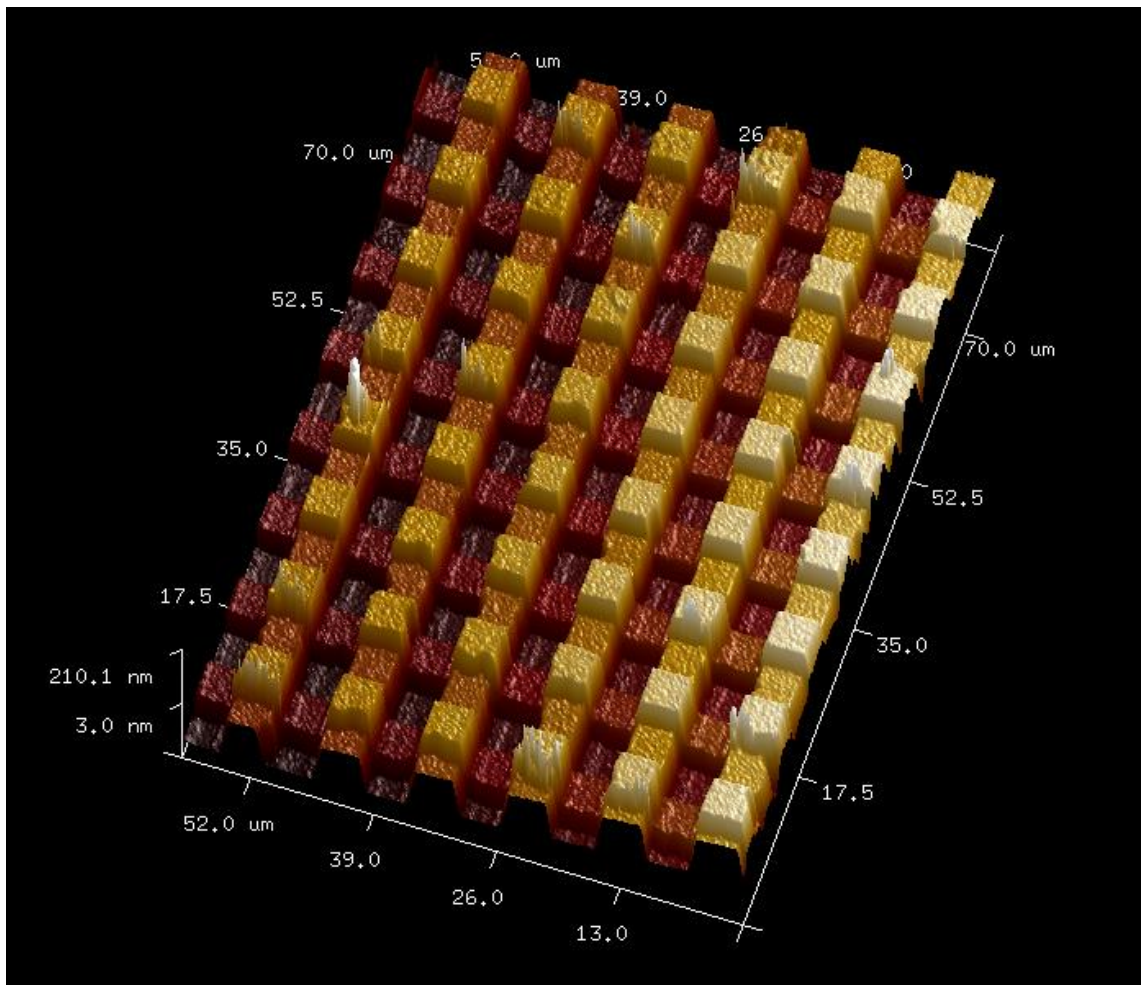


Figure 3.23. AFM images for full device before HF etching. The top image presents large area of the 10 line electrode and bottom 2D image is for the thickness profile of complete structure with bottom electrode, SiO<sub>2</sub> layer and top electrode. The total thickness is around 200nm.

Figure 3.23 shows the total thickness of the complete structure (200 nm) which is the confirmation of each individual thickness added together.

## NANO GAP FORMATION VIA HF ETCHING OF SiO<sub>2</sub> LAYER

There are two main type of etch mechanism used to remove material for modern micro/nano-electronic device manufacturing: physical and chemical. In physical etching (also known as sputtering or dry etching), the momentum of particles hitting the surface removes the material. In chemical etching, the final etch product for the removal process is soluble in an etch solution or volatile at low pressure. The most well-known practice of chemical etching is wet etching and common applications include the bulk etching of silicon or compound semiconductors. Micromachining of microelectromechanical system (MEMS) is one of the major areas which benefits from this technique <sup>186</sup>.

Wet etching is a process based on chemical reactions which includes three main steps: the reactive etching species existing in the etching solution needs to come into contact with the surface, a reaction between the etching solution and target surface takes place and, in the final step, the etch products are removed from the surface. The rate of material removal by etching is known as the etch rate and is measured in nanometre per minute (nm/min). Depending on the nature of etching process, the material removal can occur in both horizontal and vertical directions.

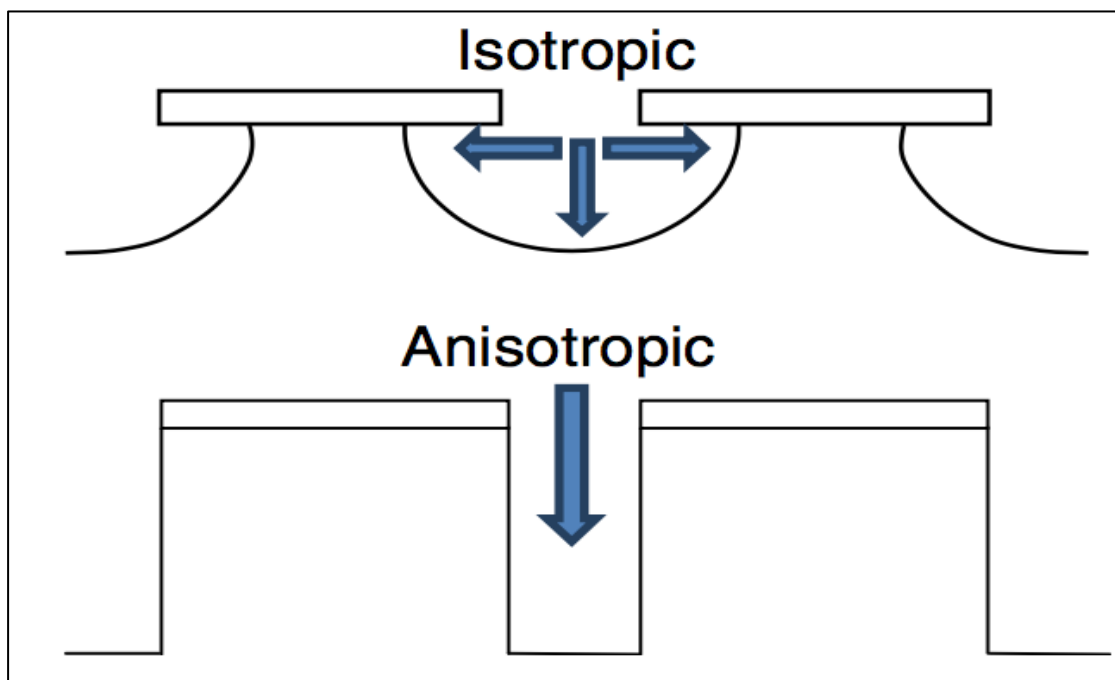


Figure.3.24. Comparison of isotropic and anisotropic etch process. Where in top the etching occurs at different direction depending on the pattern whereas in the bottom the etching direction is one <sup>187</sup>.

In the etching process, if the etching direction on both the vertical and horizontal plane proceeds equally, it is known as isotropic. On the other hand, if the etch proceeds only in the vertical direction (mainly dry etching such as plasma etching), it is known as anisotropic. The advantage of wet etching (isotropic) is that the material removal rate is faster than dry etching methods and the rate can be controlled by varying the temperature or concentration of the active species <sup>188</sup>.

Most 3D nanogap capacitive sensors are fabricated by deposition of a sacrificial layer (oxide layer) with nanometre thickness, which is used to separate two conducting (metal or semiconductor) electrodes. In the final step of fabrication, when this sacrificial layer is removed or etched away, a nanocavity is created. The thickness of sacrificial layer can be precisely controlled via controlling growth (or deposition) conditions <sup>147</sup>.

The most challenging step for the fabrication of Nanogap capacitive sensor in this project is etching the thin oxide layer using hydrofluoric acid (HF). Wet etching of SiO<sub>2</sub>, with the concentration of 10:1 (95 ml DI water mixed 5ml Hydrofluoric acid 49%) is used to form Nanogap between top and bottom electrode.

For the HF experiments each batch were taken to the etching lab at the same time and the room temperature were recorded and adjusted to keep it same at 22 °C. The prepared HF bath were set to be in the close distance with washing sink , after the required HF etching time the samples were taking out with the separate tweezers and left in DI water for minimum 10 minutes prior to drying. The samples were dried with dust-free wipes first and left in hotplate at 75 °C temperature for another 10 minutes to evaporate the water from the exciting gap between electrodes. Nitrogen gun was avoided since the high pressure of the gun could destroy the nanogap.

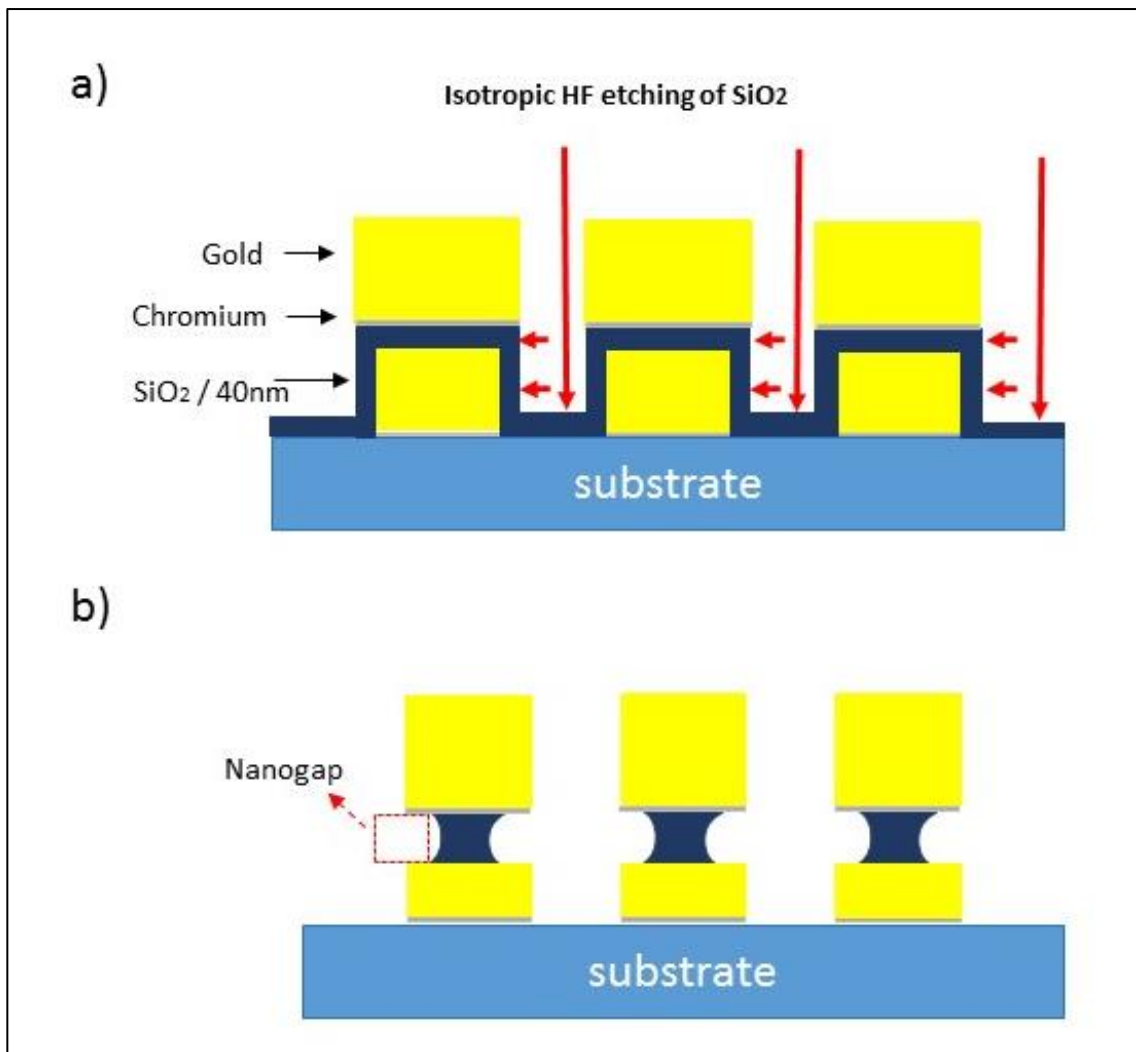


Figure 3.25. Wet etching of SiO<sub>2</sub> layer with HF, where in top sketch (a) HF attacks to oxide layer in both direction (vertical and horizontal) in order to get isotropic etch profile. b) Nanogap formation. in ideal case each of these nanocapacitors etched similarly. in order to investigate the amount of etched SiO<sub>2</sub>, capacitance measurements before and after HF performed which will be presented in the results chapter.

Figure 2.25 illustrates the HF process where the HF diffuses through the structure in isotropic approach and removes the oxide effectively. The amount of removed oxide is depends on the concentration and the time. These parameters investigated in deep detail prior to etching the complete devices (see 3.1.4).

After the HF etching step in order to eliminate working devices from the faulty and damaged devices, capacitance measurements at single frequency before and after etch performed. These measurements also indicates the amount of oxide that etched away which will be presented in results chapter. For the visual conformation of the nanogap



working devices were examined with SEM in high resolution which a single nanocapacitor can be examined.

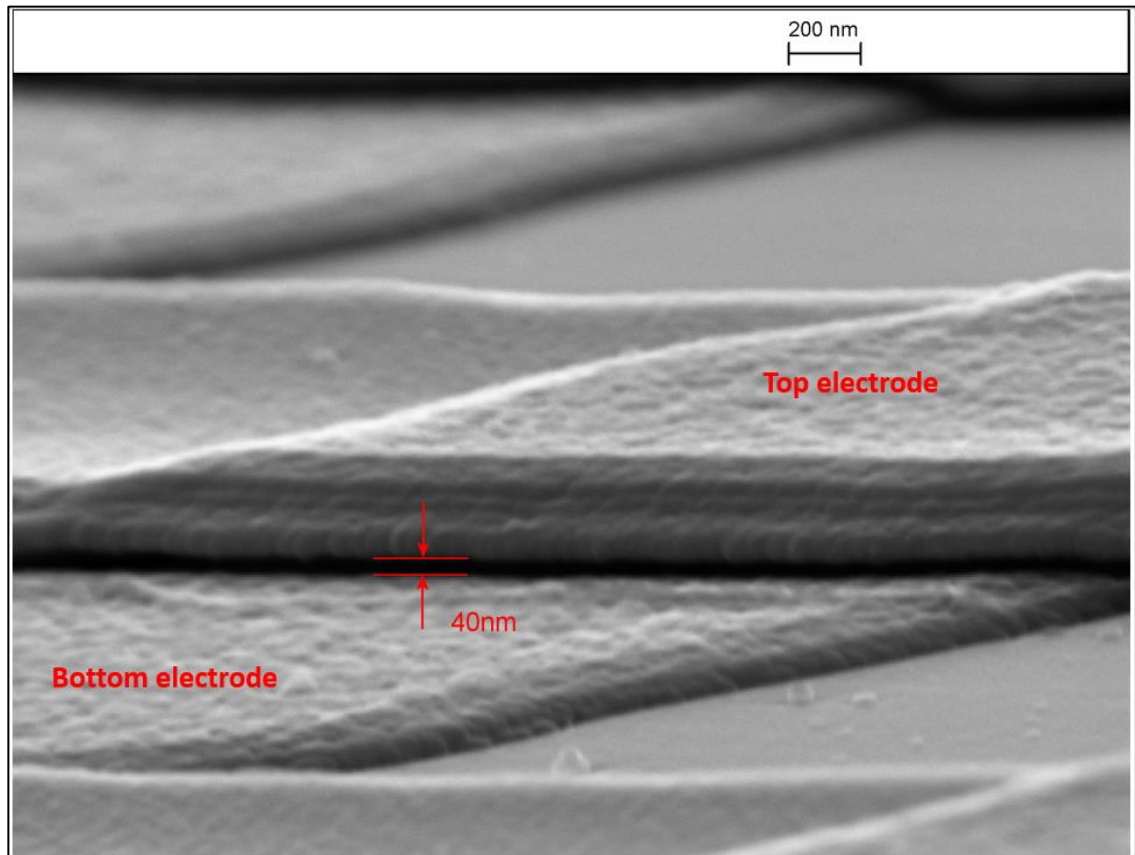


Figure 3.26. SEM image for fabricated Nanogap capacitive sensor. The device coated with thin layer of carbon (~5nm) to minimize the charge effect, the electron beam voltage is 20 KV, probe current 50 pA, the substrate tilted at 45°.

Figure 3.26 shows the final structure of a single nanocapacitor with the separation distance of 40nm between top and bottom electrode. Since each device includes 100 of these single nanocapacitors, the SEM imaging time was limited to few devices and the presented image is the best among them, however, the most important verification step carried out with capacitance measurements before and after HF etching. These data used to calculate the actual etched distance experimentally which will be presented in the results chapter.

## TOP WINDOW LITHOGRAPHY FOR INTRODUCING SOLUTION TO NANO-GAP

Localization of the sample solution to sensing area is one of the most important challenges in biosensor design and fabrication process which has led to introduce the microfluidics concept <sup>189</sup>. In other words microfluidics is the art of manipulating the sample solution inside sensors.

The exciting microfluidics components can be made of different material such as silicon, glass and polymer <sup>190</sup>. Each of these materials has its own advantages and limitations, which can be studied in more details from other sources<sup>191,192</sup>.the most important challenges for these methods including material costs, low-cost fabrication, bonding of the microfluidics part to the sensor and assembling technologies.

In this project at the very final stage of the fabrication all the devices were tested with just air inside the nanogap and DI water. In order to introduce the DI water to the sensing area, the micropipette used to put a droplet of DI water in the center of the device and the capacitance measurements performed at this point .However after introducing DI water droplet to the sensing area under the environmental condition and the nature of the droplet it is start to spreading to the neighboring area <sup>193</sup>. In our case, this effect created another parasitic capacitance between the wider part of the electrode arms and the glass substrate.

In order to solves these problems a unique approach have been designed and fabricated for allowing sample solution to enter the active sensing area of the device via photolithography technique. This methods involves a simple step of photolithography which could effectively reduce the cost of mass production and seal all parts of sensors except the sensing area.

For this step a simple plastic photomask design with AutoCAD software and order from Microlithography Service. In the designed mask a small protective window with  $160\mu\text{m}\times 160\mu\text{m}$  created in the center which will aligned on top of these 100 nanocapacitor



where the sample solution contacts with the sensor electrodes. The negative lithography method considered for this approach which will cover the rest of the sensor surface.

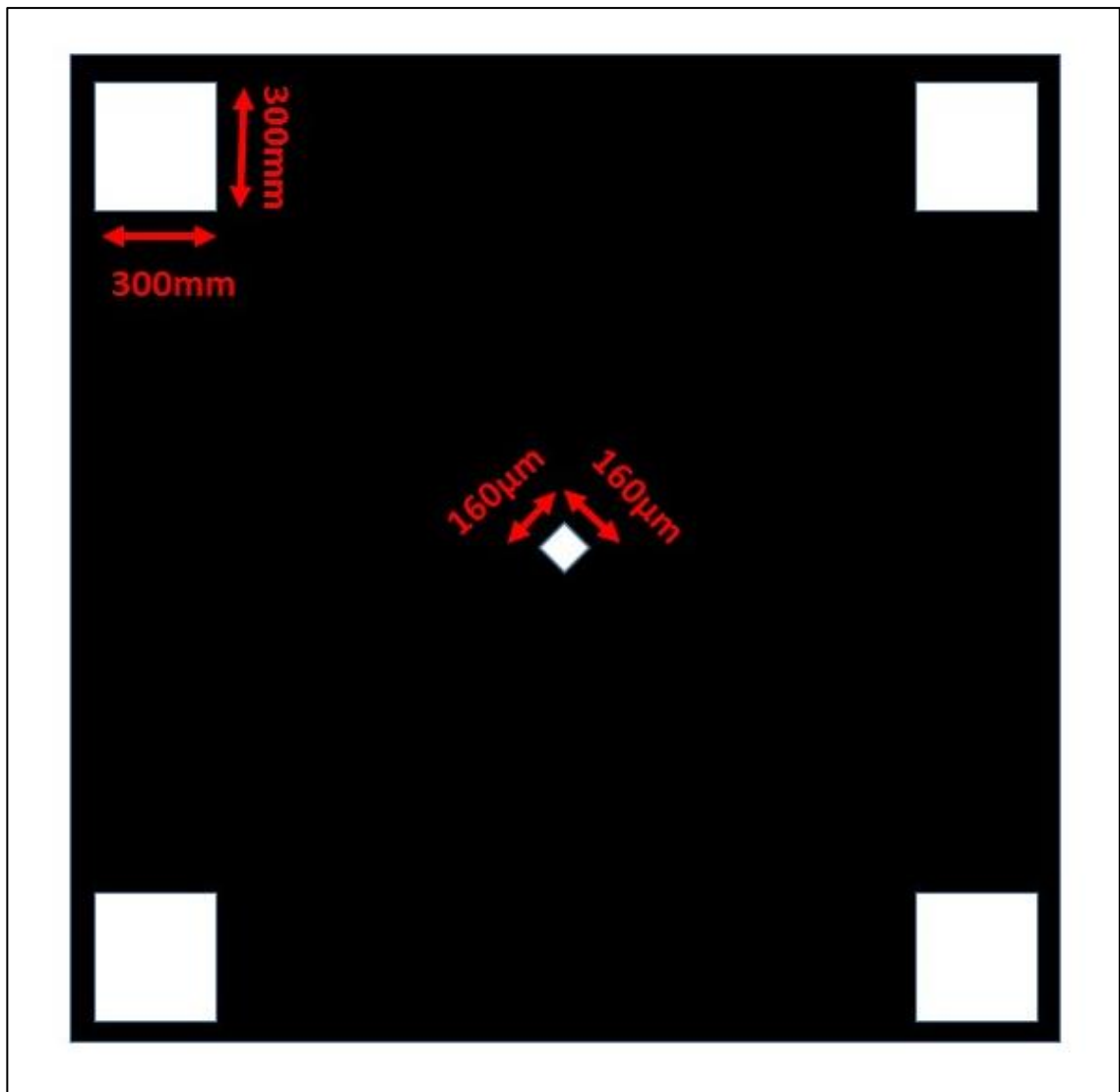


Figure 3.27. Photo mask design for the small protective window. The mask is to use for negative image reversal, where the small window in the center is  $160\mu\text{m} \times 160\mu\text{m}$  is for introducing sample solution and the 4 square pads ( $300\text{mm} \times 300\text{mm}$ ) are for the measurements probe connection.

Figure 3.27 shows the negative image reversal mask design for the small protective window (white color) which will be used to introduce the sample solution into active sensing area. The black color presents the photoresist that covers the rest of the bottom and top electrode and the 4 white boxes are the area without photoresist to make electrical connection between electrode and capacitance measurement probes.

The photolithography process for this step is similar to the previous lithography step which described in earlier section of this part. The thickness of photoresist also confirmed to be around 2  $\mu\text{m}$ . optical image of the final working device with the protective window presented in Figure 2.28.

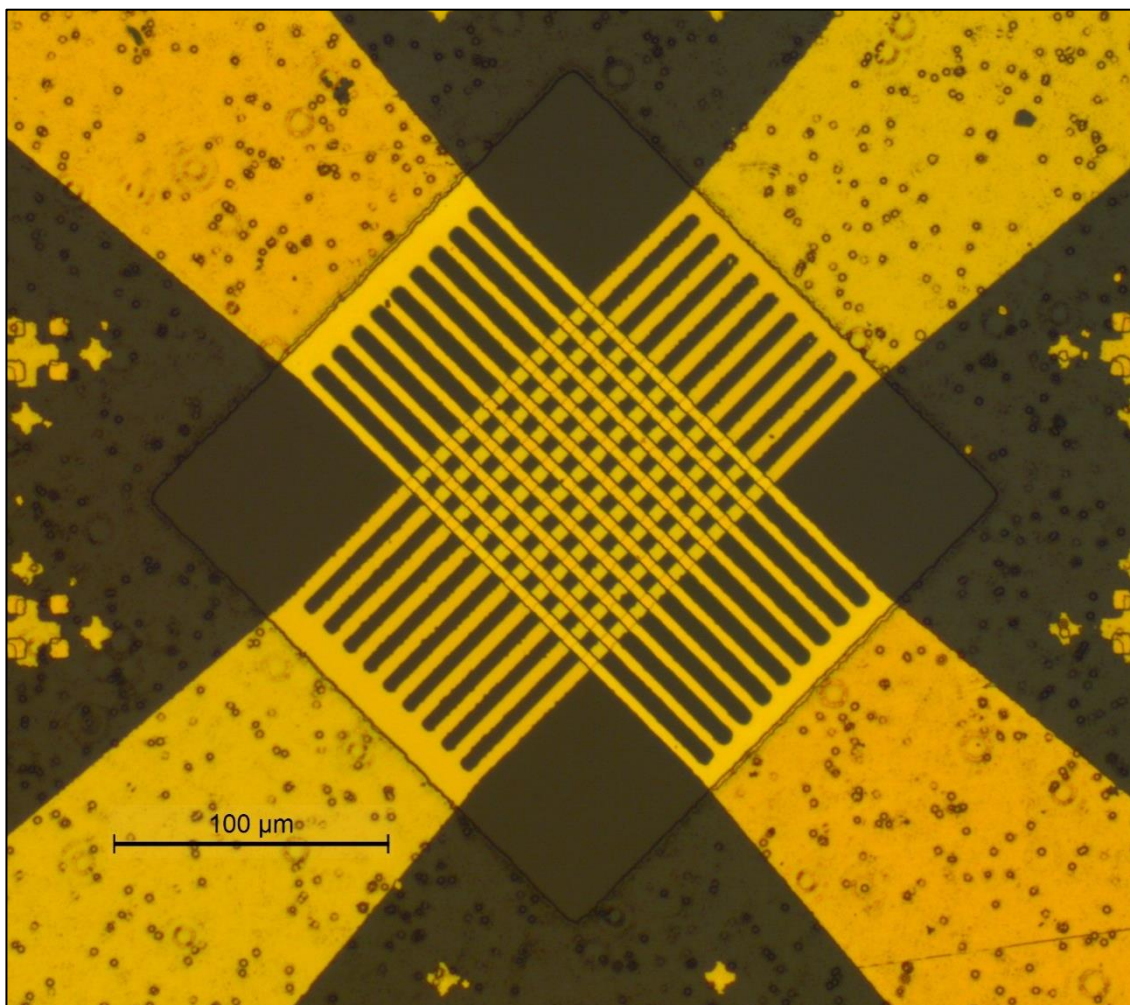


Figure 3.28. Top window lithography for final working device. The size of the window is  $160\mu\text{m} \times 160\mu\text{m}$  and the area with black dots is the area covered with photoresist to prevent the solution seeping to the electrodes.

For the capacitance measurements, a small volume of the sample ( $\sim 20 \mu\text{L}$ ) was introduced to active sensing area using a pipette. After each measurement, the devices were rinsed with an appropriate buffer solution, wiped with lint-free tissue and heated on a hotplate at  $60 \text{ }^{\circ}\text{C}$  for 1 minute.

### **3.3. SENSOR SURFACE FUNCTIONALIZATION FOR APTAMER AND HUMAN ALPHA THROMBIN PROTEIN**

Alpha-Thrombin aptamer modified with thiol linkers (GGT TGG TTT GGT TGG TTT/3ThioMC3-D) for specific binding experiments and Control-aptamer modified with thiol linker (GTG TGT GTG TGT GTG TTT/3ThioMC3-D) for control experiments, were both purchased from IDT Belgium. These Thiol-Modified Oligonucleotides (Aptamers) were shipped in their oxidized form, with the sulfur atoms protected by an S=S bond which requires a reduction step to remove the protecting group from the oligonucleotides.

The thiol-modified aptamer (12.4 OD) was reconstituted in 125  $\mu$ l of DTT (Dithiothreitol) in 100mM sodium phosphate buffer (pH 8.5) and incubated at room temperature for 1 hour. Half of the aptamer mixture was then brought to a volume of 1ml using sodium phosphate buffer (pH 6.0) and then added to a NAP-10 column (purchased from Sigma Aldrich), that has been equilibrated using sodium phosphate buffer (pH 6.0). The aptamer was eluted using 1 ml of sodium phosphate buffer (pH 6.0), collecting fractions of 100  $\mu$ l of volume. Fractions containing aptamer were identified by using a bio-spectrometer (Eppendorf).

Before the immobilization procedure, the prepared aptamer with concentration of 74.6  $\mu$ g/mL (fraction 6.0) was mixed with MCH (6-Mercapto-1-hexanol) with a 1:100 ratio and sodium phosphate buffer (pH 7.0)<sup>194</sup>. The devices were then incubated with this solution for 16 hours at 4 °C. After this step, the devices were rinsed and washed with buffer solution multiple times then backfilling with MCH (20  $\mu$ l MCH in 120  $\mu$ l sodium phosphate buffer pH 7.0) for 50 minutes prior to starting the capacitance measurements.

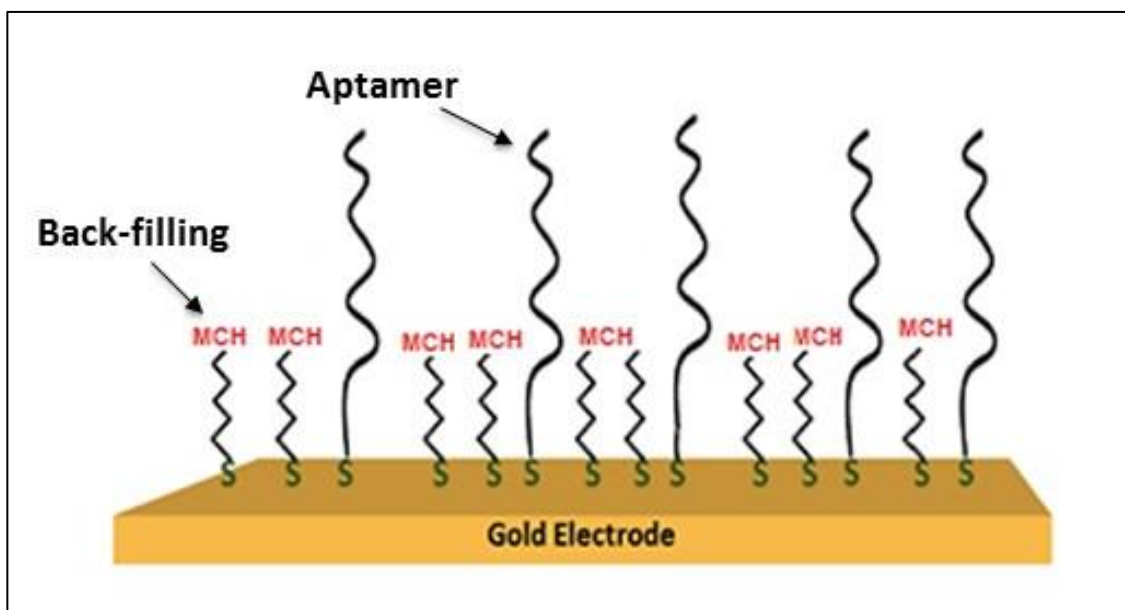


Figure 3.29. Schematic structure of one electrode after aptamer immobilization and back-filling with MCH (6-Mercapto-1-hexanol). The concentration of back-filling was 20  $\mu\text{l}$  MCH in 120  $\mu\text{l}$  sodium phosphate buffer pH 7.0 and the duration of the back-filling step was 50 minutes prior to starting the capacitance measurements. image modified from<sup>194</sup>.

Figure 3.29 illustrates the Alpha-Thrombin aptamer immobilization on the gold surface, the binding between the aptamer and gold electrode provided with modified thiol linkers (GGT TGG TTT GGT TGG TTT/3ThioMC3-D). The purpose of back-filling the surface with MCH after immobilization was to create some space between each aptamer base pair which will be used by protein to form the G-quadruplex conformation upon aptamer and protein binding<sup>194</sup>. The devices were taken for capacitance measurements of immobilized aptamer in the presence of buffer solution (0.5xSSC).

The protein solution was prepared with 1  $\mu\text{l}$  of human  $\alpha$ -Thrombin (HCT-0020 purchased from Cambridge BioScience) in 199  $\mu\text{l}$  of 0.5xSSC buffer. The same devices with SAM were incubated with this protein mixture for two hours at room temperature. Then they were rinsed and washed with 0.5xSSC buffer solution multiple times and the capacitance measurements performed in presence of the same buffer solution.

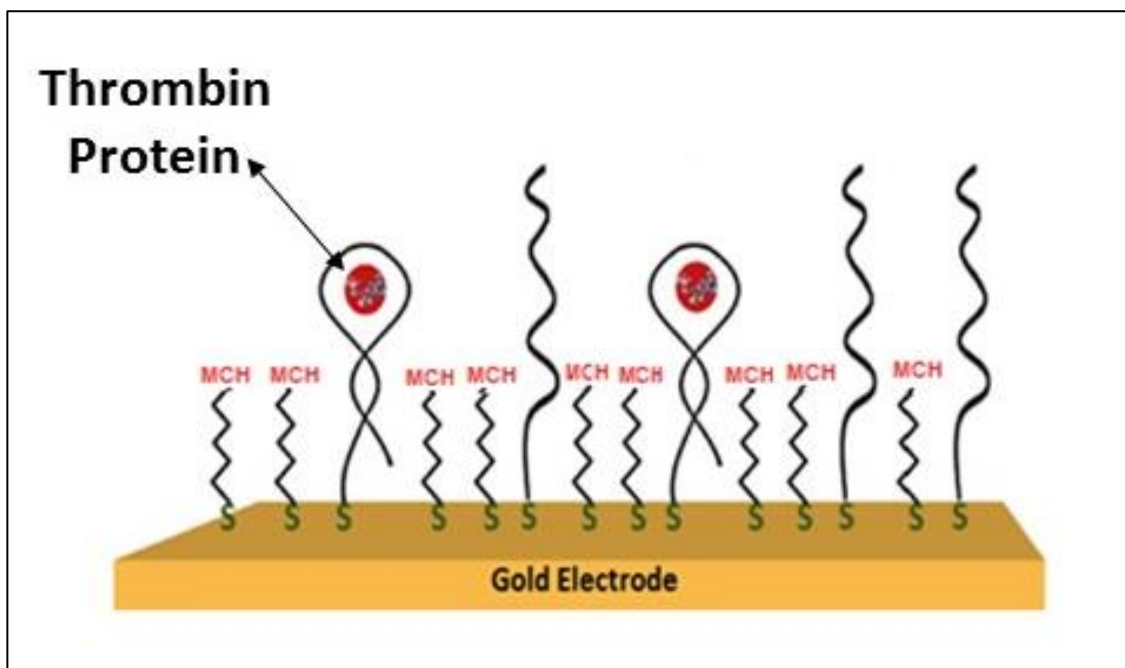


Figure 3.30. Schematic structure of one electrode after aptamer and protein binding .The concentration of alpha thrombin protein is  $1\mu\text{M}$  in  $199\ \mu\text{l}$  of  $0.5\times\text{SSC}$  buffer. the duration of incubation of electrodes with thrombin protein is 2 hours prior to starting the capacitance measurements and the measurements are performed in presence of  $0.5\times\text{SSC}$  buffer.image modified from<sup>194</sup>.

Figure 3.30 shows the structure of aptamer after binding to thrombin protein with G-quadruplex conformation. The measurements performed in presence of buffer solution ( $0.5\times\text{SSC}$ ) and after each measurements the device were washed with same buffer solution, dried with dust-free wipes and further dried in hotplate with  $60\ ^\circ\text{C}$  temperature. This step were continued by storing the devices in humidity chamber for repeat the same measurements in future , the provided data are based on 5 measurements from same devices on 5 individual devices.



### 3.4. SETUP FOR CAPACITANCE MEASUREMENT

Capacitance measurements for the fabricated Nanogap capacitive sensor were performed in two different setups, one for the single frequency measurements at 1.013 kHz and one for the frequency sweep from 1 Hz to 500 kHz.

For the single frequency measurements a lock-in amplifier (SR830 Stanford Research Systems) was connected to the probes inside a faraday cage (made in-house). With making a contact between the tips of probe to the top and bottom electrode, AC current and phase were recorded.

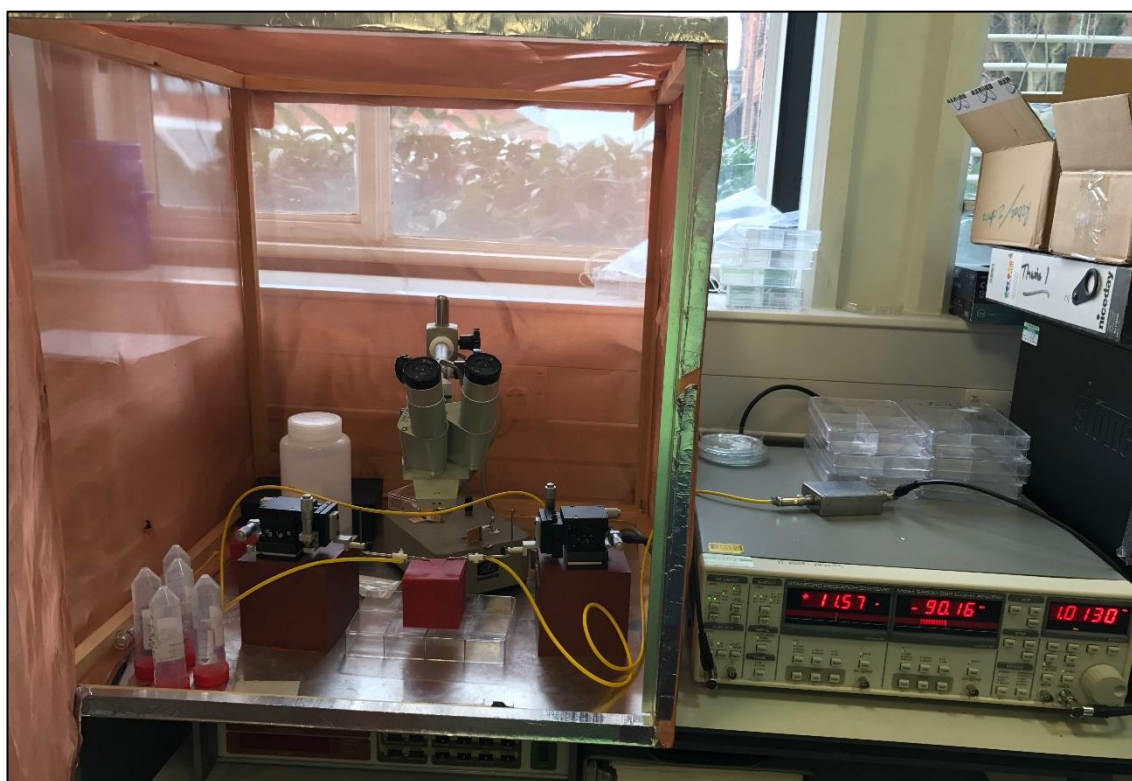


Figure 3.31. Capacitance measurement setup for single frequency measurements. The SR830 lock-in amplifier is on the right of the image and the measurement probes inside a faraday cage are to the left.

The lock-in amplifier was set to 20 mV AC signal and, after contacting the probe end with electrode, the resulting AC current and phase shift was recorded. The following equation was applied to calculate the capacitance from current and frequency reading:

$$C = \frac{I}{2\pi V f} \quad (3.5)$$

Where  $I$  is the measured AC current,  $V$  is the excitation AC voltage (20 mV) and  $f$  is the excitation frequency.

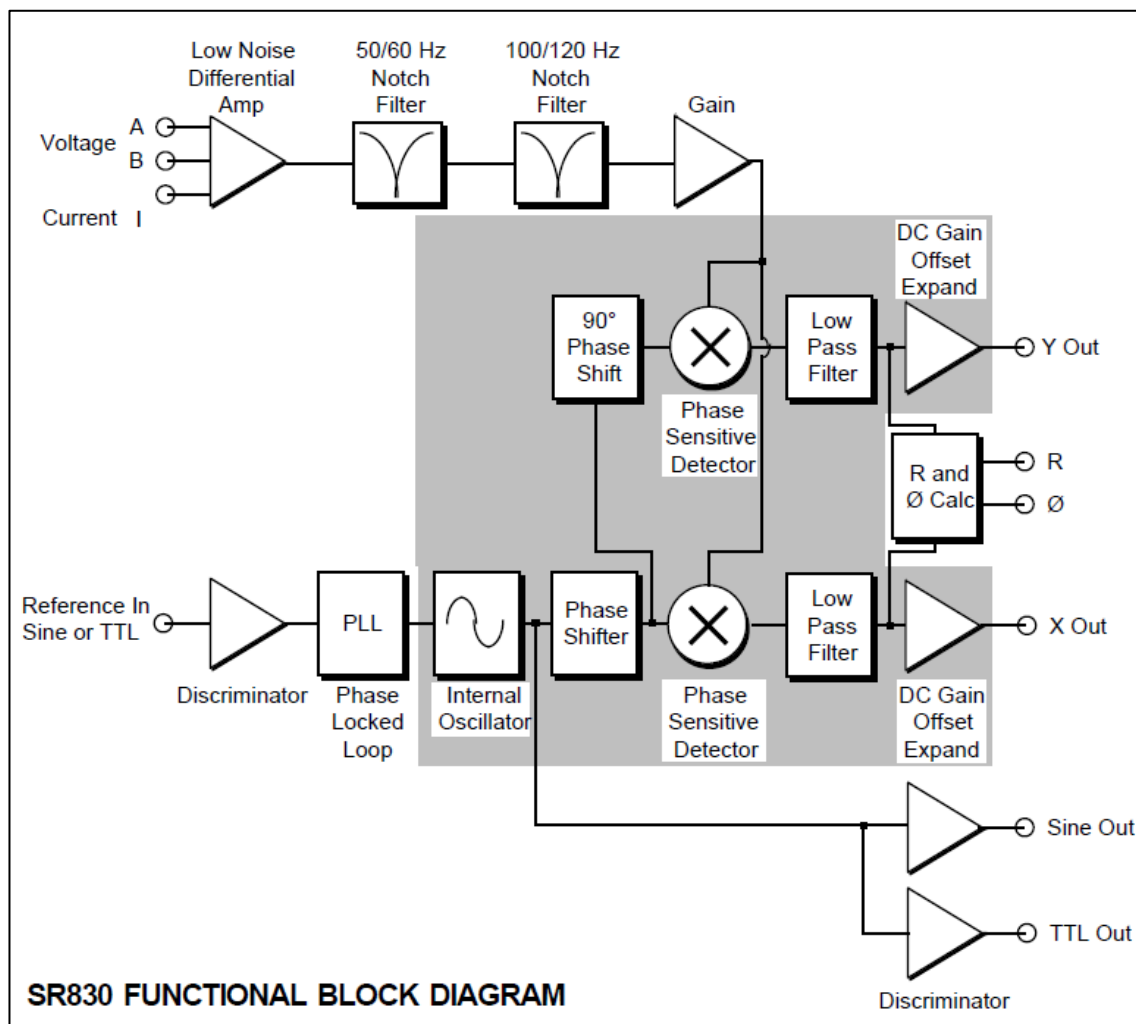


Figure 3.32. SR830 lock-in amplifier functional block diagram showing low-noise phase sensitive detection<sup>195</sup>.

The excitation AC voltage signal amplitude was 20 mV, which is very low in comparison to the I-V electrochemical spectroscopy where several volts are typically used to induce chemical re-dox reactions. In our case, higher voltages can damage the biomolecules structure and also the system might exhibit nonlinear behavior due to the high electric field and generation of harmonics from excitation frequency.

The second measurement setup performs frequency dependent capacitance measurements and, although slower to perform, the information provided is more useful since the data is collected over a range of frequencies. In this work, we performed measurements in the range 1 Hz to 500 kHz.

Typically, the low frequency range is of interest due to the fact that this range is a more sensitive regime (see chapter 2). At high frequencies, the dielectric essentially acts like short-circuit. Most studies in the literature indicate that aptamer and protein bonding can be monitored and detected at frequencies below 10 kHz<sup>96, 167</sup>.

The second measurement setup used to apply frequency dependent measurements from 1 Hz to 500 kHz is shown in Figure 3-27. This setup includes: SI1260 impedance/gain-phase analyzer (solartron analytical) combined with the low current 1296 Dielectric interface (solartron analytical), probe stage with sharp tips to make contact with top and bottom electrode and a computer program to collect the data.

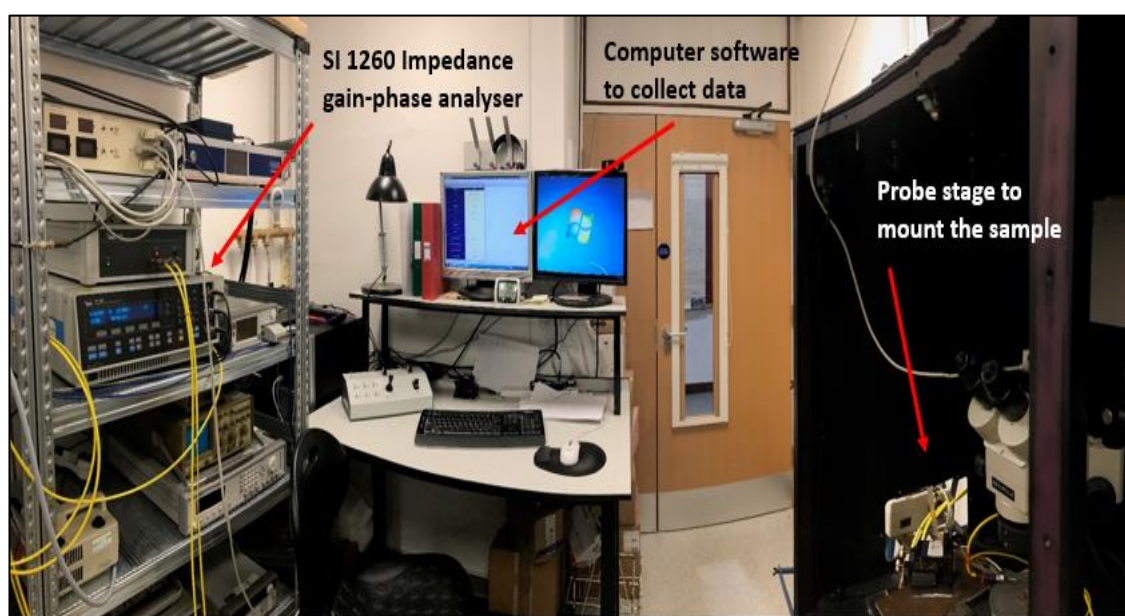


Figure 3.33. Frequency dependent measurements setup. This setup includes: SI impedance gain-phase analyzer, probe stage to mount the sample and a computer software for collecting data.



The probe stage is positioned inside a Faraday cage to block any external noise from environment. This stage has a vacuum assisted sample holder to mount the sample. Two sharp needle tips (probes) are used for making electrical contact to the device electrodes.

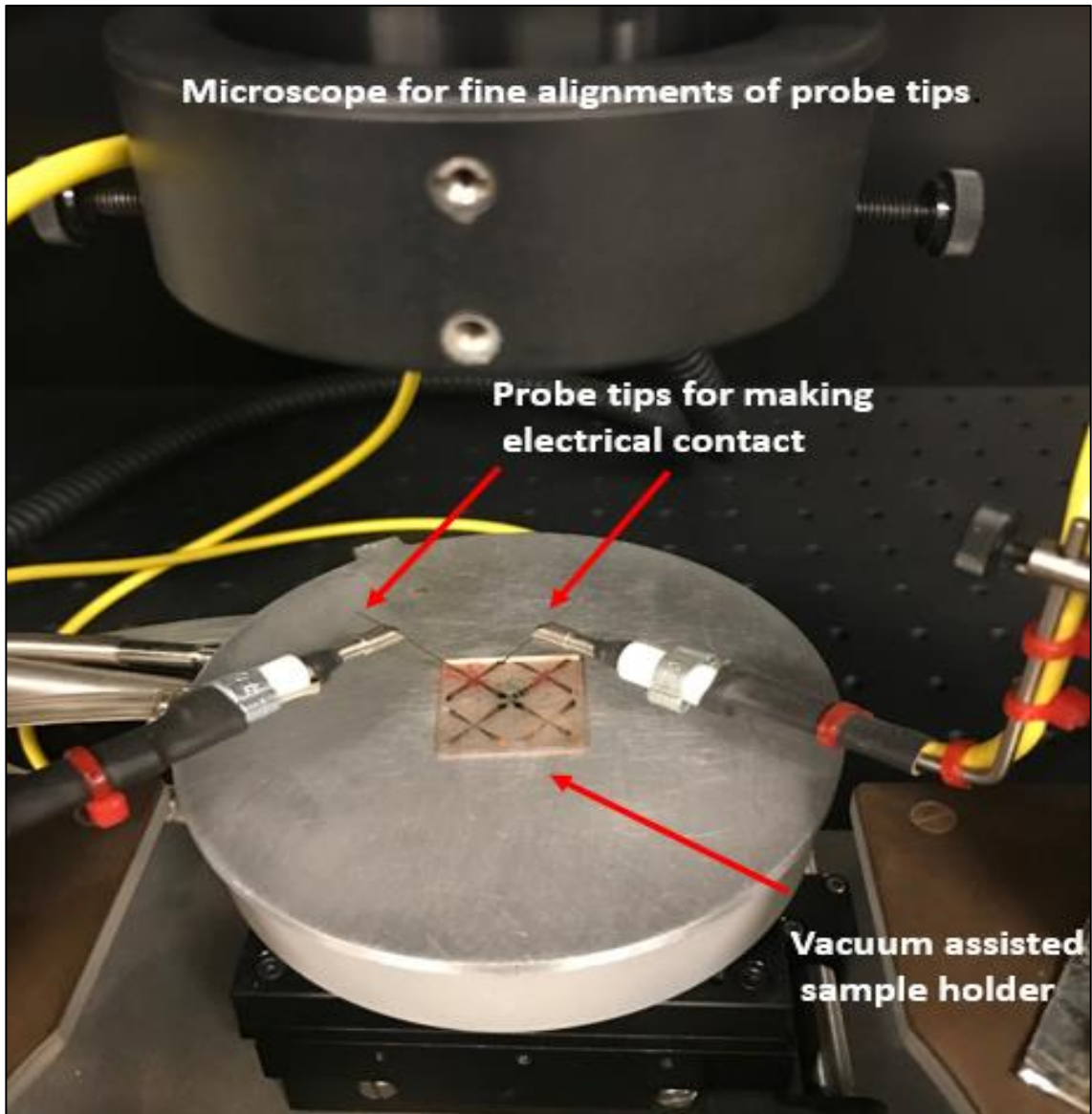


Figure 3.34. Probe station with vacuum assisted sample holder stage and sharp tips for making electrical contact with top and bottom electrode.

For the samples are positioned in the center of stage and the vacuum under the stage will keep the substrate firm during the measurements.

### **3.5. SUMMARY OF TRIAL PROTOTYPES AND FABRICATION**

#### **METHODS**

The dimensions and the distance between the electrodes of a biosensor determines the sensitivity. Increasing the area of electrodes will increase the sensitivity; however, this will lead to increase the area of the active sensing region. On the other hand, in Biosensing applications with very low concentration of target molecules, this will decrease the performance of the sensor because most of the sensing area will be blank (not enough biomolecule to cover all the area). In fact, it is the advantage of Nanogap based sensing to be able to maximize the capacitive changes while keeping the sensing region (where target molecule are bound) minimal. Therefore, very low concentrations of target protein can be detected in this method. Decreasing the electrode distance is also possible for high sensitivity purposes; however, as the distance approaches several nanometers, undercut filling of the liquid solution might be problematic as well as any congestion in the undercut entry due to molecules (aptamer, protein, ions etc.) in the target solution .

For the design of a sensor with Nano-meter gap size which can be used to analyze the capacitive behavior of organic molecules or even biomolecules, the relative requirements and constraints should be taken into account. The geometry of the interdigitated array microelectrodes (IDAME) based Nanogap capacitor for this project was investigated in the light of many essential factors which should be considered before the fabrication step.

At the very first design we considered a single electrode; 1.97cm length and 5  $\mu\text{m}$  width inside a square window with dimension 1.4 cm height x 1.4 cm width where the top electrode can be fabricated with rotating the mask 90<sup>0</sup> degree anticlockwise.

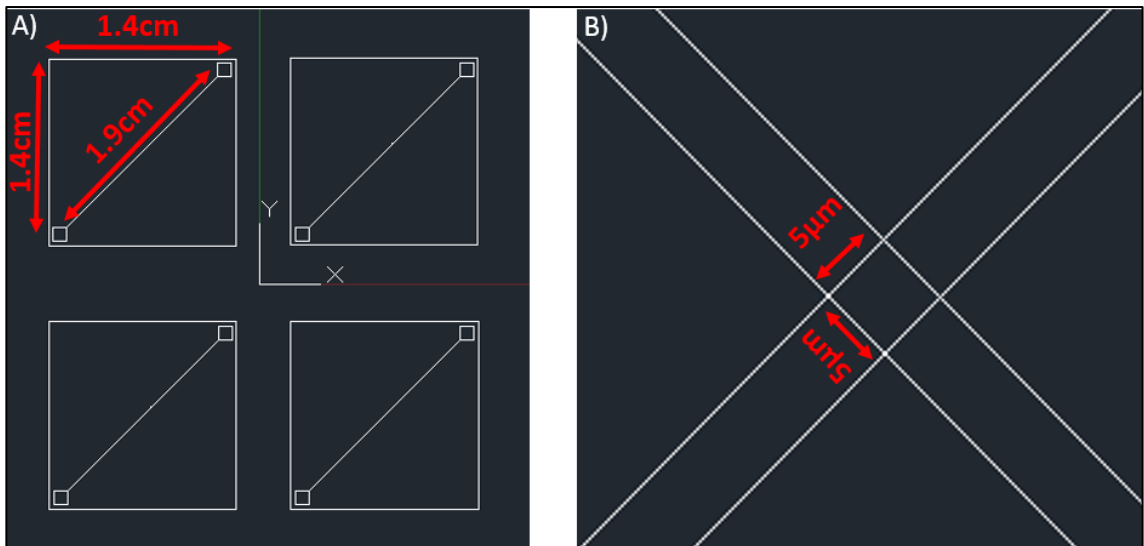


Figure 3.35. AutoCAD design for the first mask .A) Mask layout on a 4"x4" chrome quartz and four devices with 1.4cmx1.4cm dimensions, B) Zoomed image of overlapping region for top and bottom electrode with 5µmx5µm dimensions.

This design adopted here used for positive lithography and lift-off, where the dark area would be covered with photoresist and the area bordered with white line is for electrodes. After a systematic fabrication step, all the lithography and lift-off steps were characterized. The main drawback of this design arose from the lift-off step. The fabricated bottom electrode with a 5 µm width was not continuous all over the substrate (electrode length ~1.97 cm).

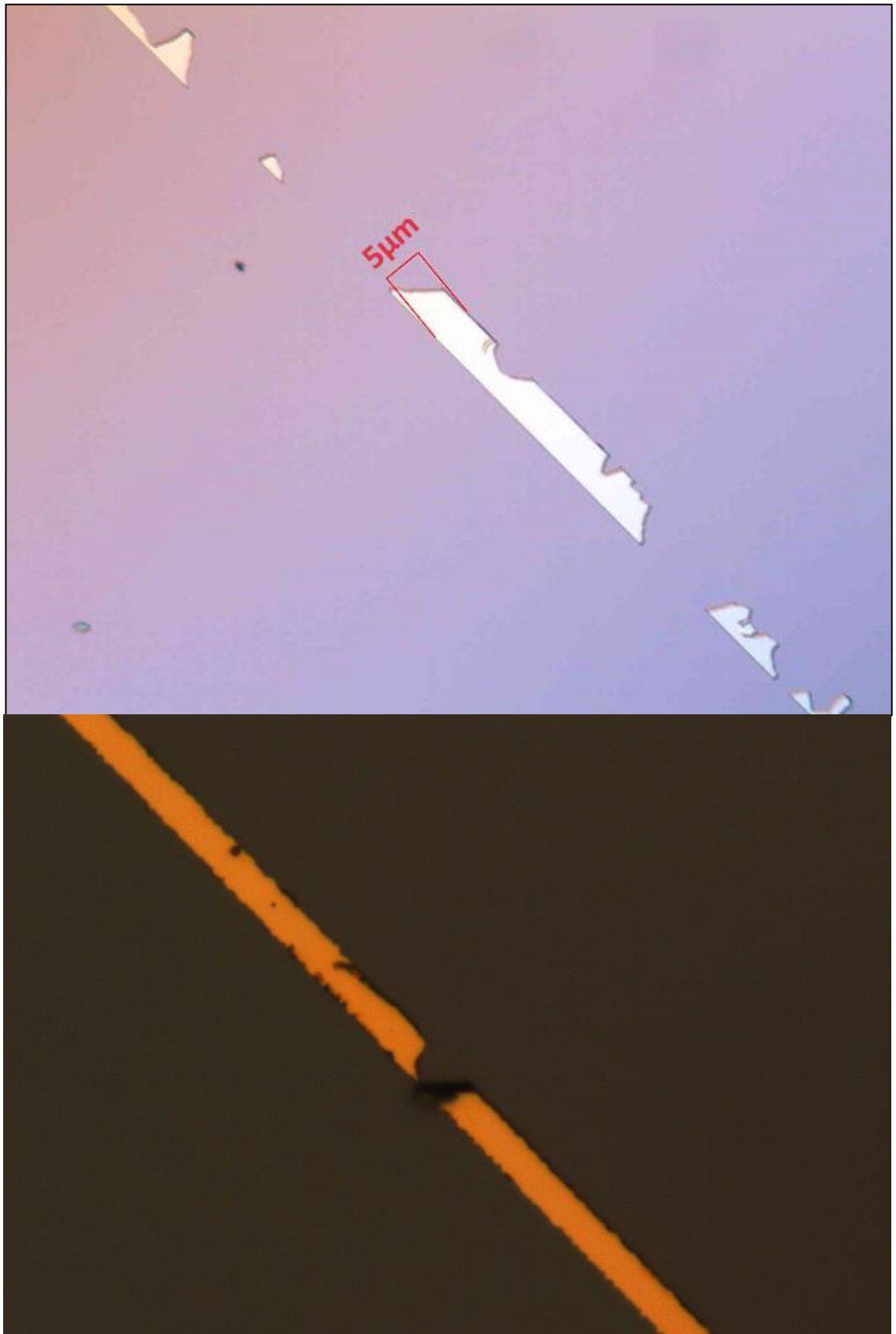


Figure 3.36. Bottom electrode formation after lift-off process. Where the continuity of the electrode is not same in all part of electrode.

The second mask design aimed to correct this problem by having a single 5  $\mu\text{m}$  width electrode in overlapping area (central distance 55  $\mu\text{m}$ ) and wider area on the outer sides (max 1.6mm). In this design, there were four devices with two positive and two negative lithography pattern.

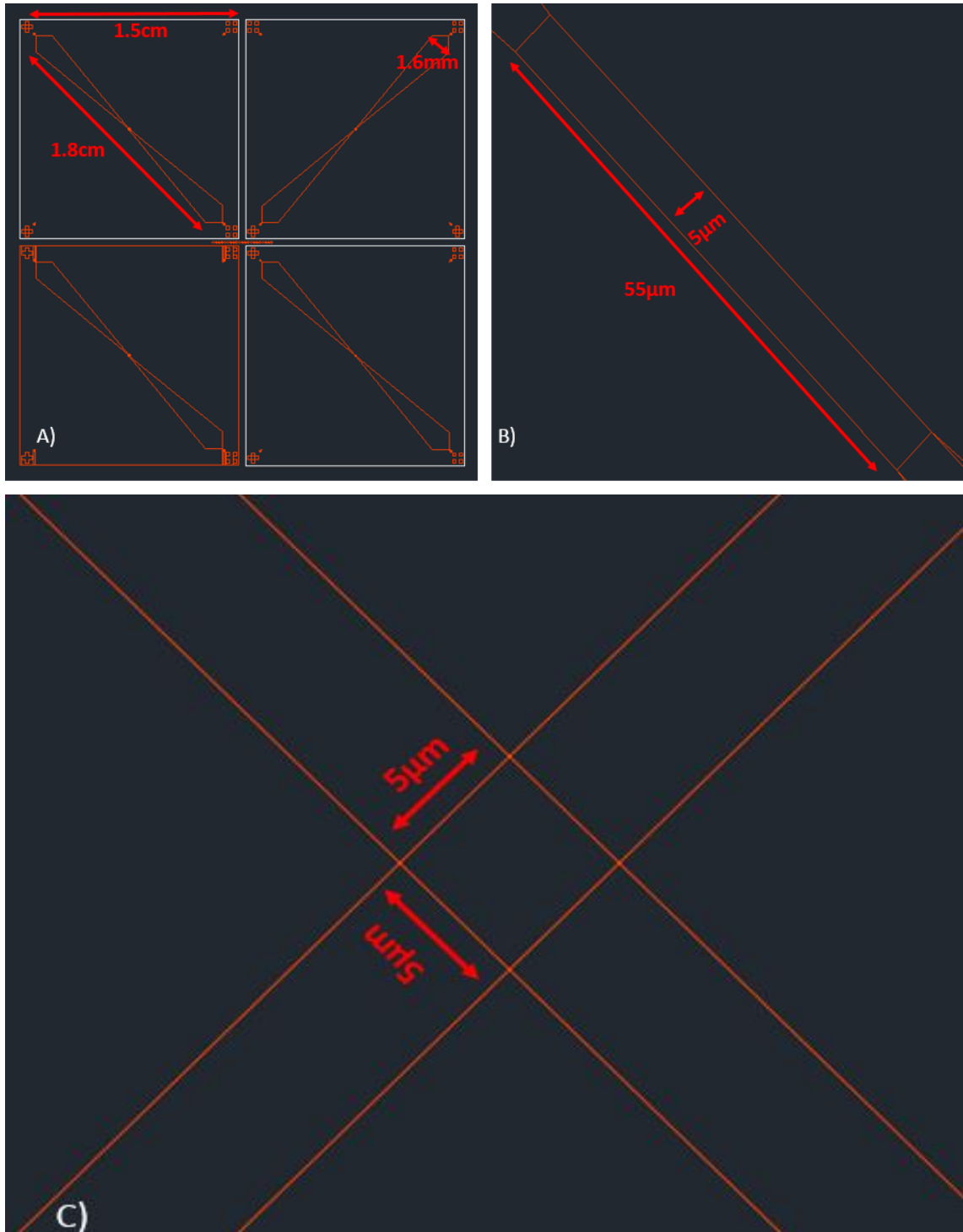


Figure 3.37. AutoCAD design for the second mask. A) Mask layout on a 4"x4" chrome quartz and four devices (two positive and two negative) with 1.5cmx1.5cm dimensions, B) Zoomed image of central part of electrode with 55 $\mu\text{m}$  x 5 $\mu\text{m}$ , C) Zoomed image of overlapping region for top and bottom electrode with 5 $\mu\text{m}$ x5 $\mu\text{m}$  dimensions.

The second design had advantages over the first design in terms of fabrication and lift-off. The electrode size in the center was  $5\ \mu\text{m}$  width x  $55\ \mu\text{m}$  length, moving out towards edge of each electrode, the shape getting wider and the maximum width on the edge of the electrode (probe contact point) was  $1.6\ \text{mm}$ . The main challenge for this design was the final full device structure was not strong enough and would break easily after top electrode formation or the HF etching step.

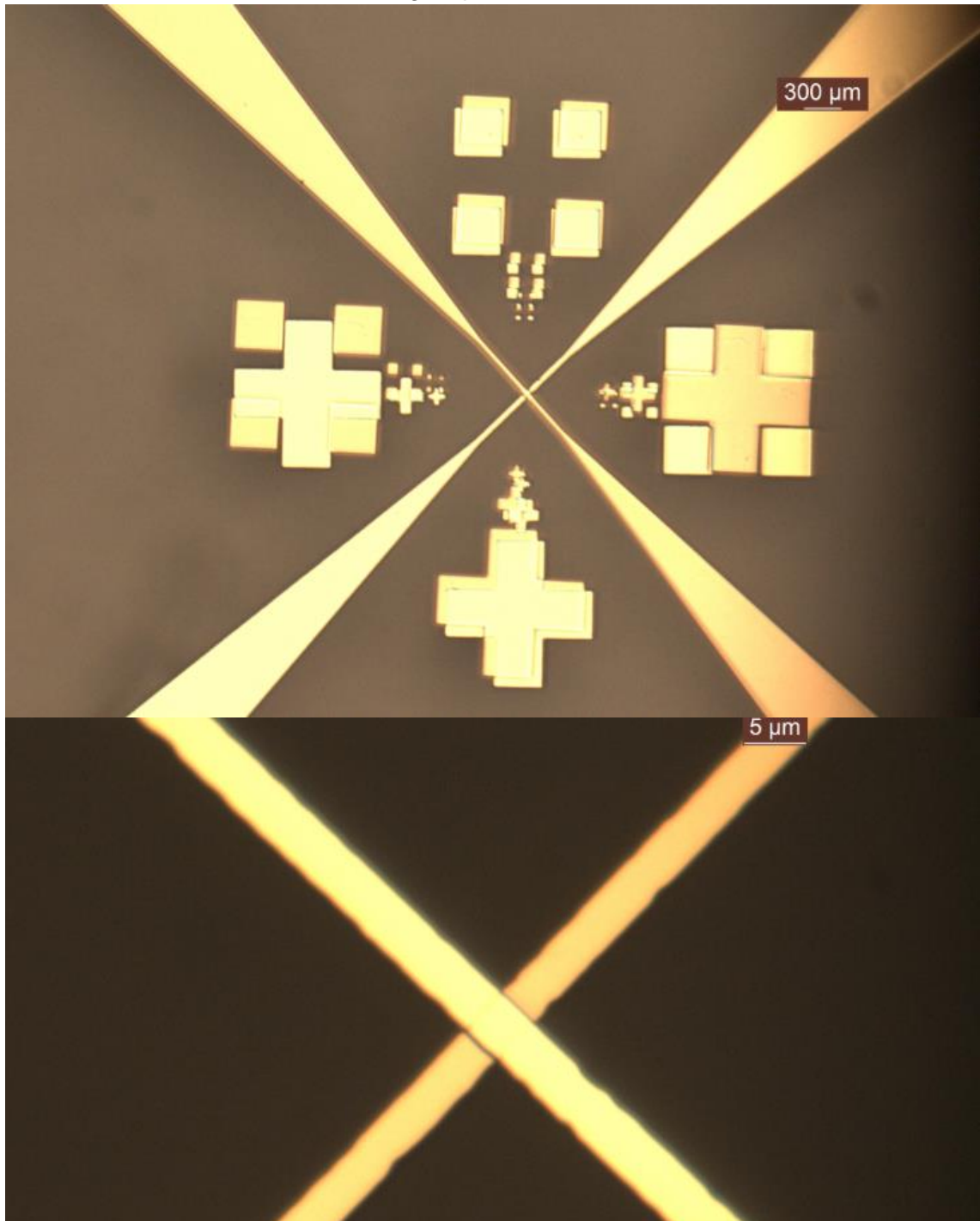


Figure 3.38. Optical images of full device before HF etching. The top image shows the larger part of electrode which will be used for probe contact and the bottom image is zoomed in higher resolution into the center.



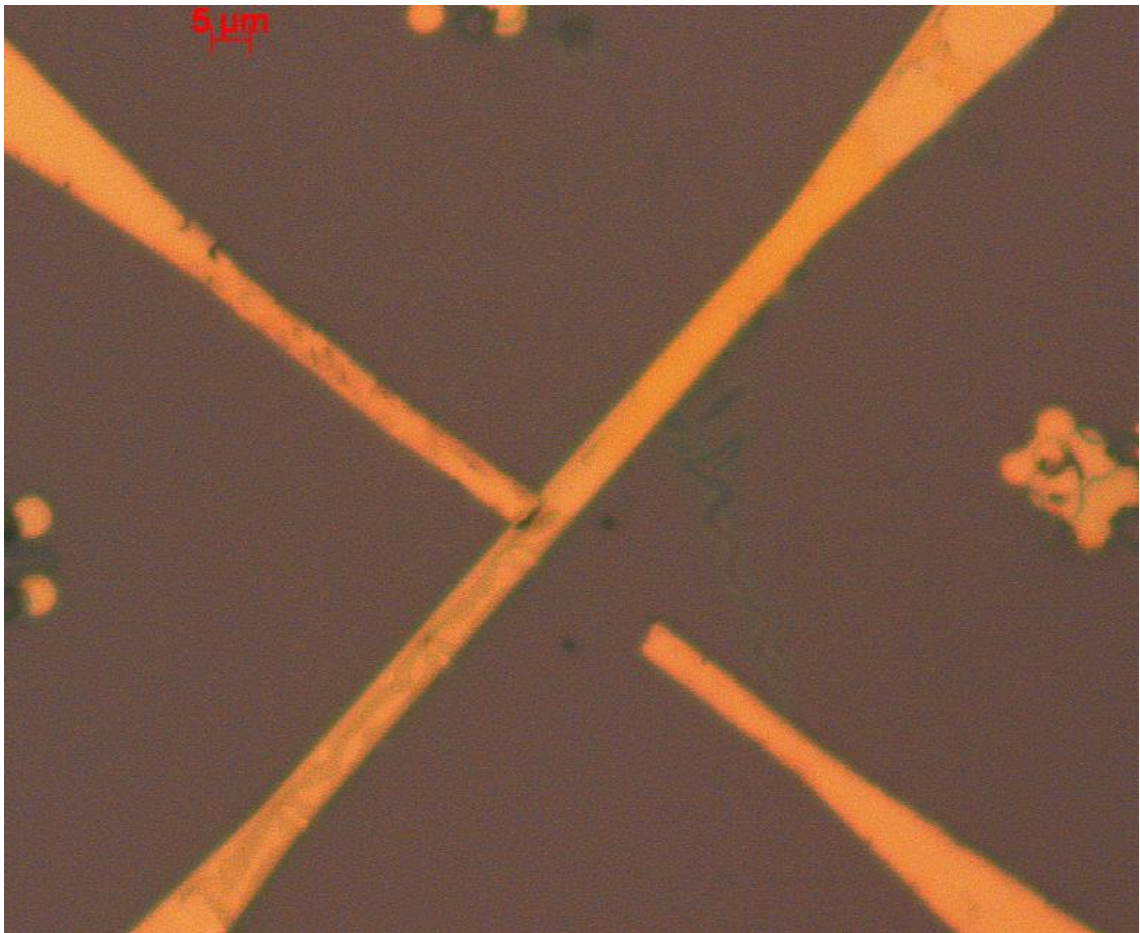


Figure 3.39. Optical image of full device after HF. where the top electrode is broken and lost the continuity in the central area which.

The final mask design was subjectively assessed, according to previous fabrication failures and had many advantages over previous designs. Since this design included 4 devices on the same substrate the number of possible working devices for the same amount of fabrication work increased.

Also, since there were 10 lines of 5 $\mu$ m electrodes in the sensing area, instead of 1 line, devices even worked if one of the lines were broken. Another advantage of having 100 capacitors instead of one is to increase the total capacitance of the device, which can improve the signal to noise ratio.

## **Chapter 4. RESULTS AND DISCUSSION**



## 4.1. INTRODUCTION

In this chapter the results for all the experimental work will be presented in two separate part. The first part of this chapter will focus on the optimization and characterization of experimental results for the SiO<sub>2</sub> sputtering, Metal-Oxide-Semiconductor (MOS) devices, substrate temperature and HF etching.

In the first part of this chapter, results for substrate temperature experiment will be introduced for both vacuum and atmospheric pressure. Further on the results for C-V (capacitance and voltage) and I-V (current-voltage) measurements of MOS devices will be presented. Finally the HF etching step analysis will be introduced in both thickness profile study and white light microscopy.

The second part of this chapter will introduce the capacitance and permittivity results for air, DI water and buffer solution with various ionic strength. Results for alpha thrombin aptamer functionalization and human alpha thrombin protein hybridization will be presented.

The final part of this chapter contains a critical discussion of the results for both MOS devices and the nanogap capacitive biosensor. This section will focus on sensitivity, reliability, detection limit and compares results from this work with other appropriate sensors in the literature.

## 4.2. OPTIMIZATION AND CHARACTERIZATION RESULTS

### 4.2.1. SUBSTRATE TEMPERATURE

The most important aspect of the fabrication of the nanogap sensor in this project was to obtain a high quality oxide layer, which isolates the bottom and top electrode and is partially etched to obtain the nanogap. The advantage of sputtering method over the evaporation have been discussed earlier also the reader is directed to the many good review studies in literature covering the RF sputtering of silicon dioxide and methods to achieve a high dielectric constant and low leakage current for the thin layer <sup>197,185,198,199</sup>. However, in this project we specifically studied the substrate temperature effect on the sputtering-deposition time.

Substrate heating during the sputtering of oxide layer has many advantages, such as: increasing the film adhesive strength, density and resistivity, decreasing the overall surface roughness and pinholes <sup>200, 201, 202</sup>. It is important to analyze the temperature effect for RF sputtered SiO<sub>2</sub> layer in order to achieve a pinhole free and low leakage current thin oxide layer in nanogap sensor fabrication.

According to the experimental setup for RF magnetron sputtering system explained in Figure 3.4 and Figure 3.5 the substrate heating element is connected to the external power supply and with increasing the DC voltage the temperature will increase. The results for the three different voltage amplitude are presented below for both vacuum pressure and atmospheric environment.

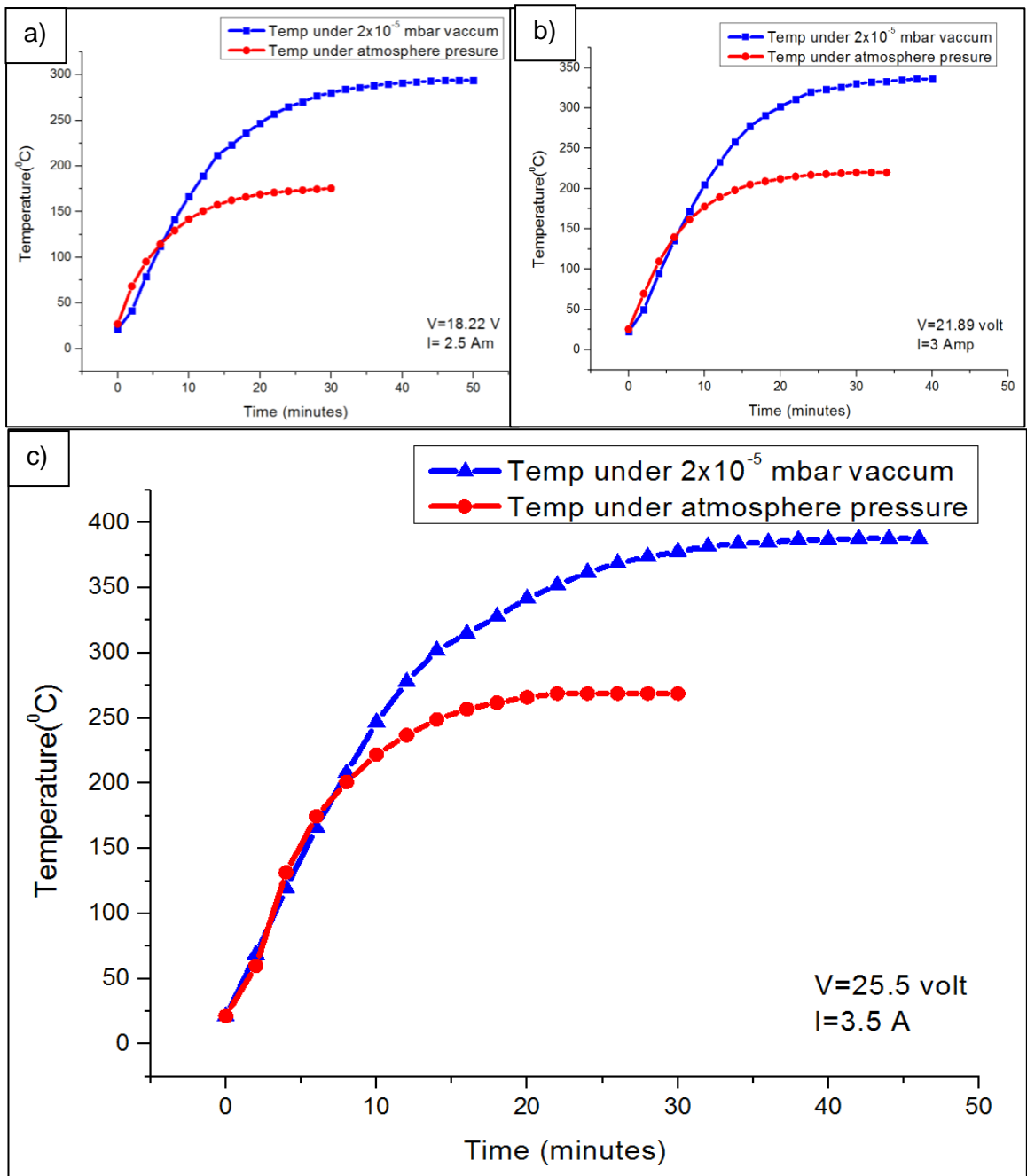


Figure 4.1. Temperature vs. Time for: a) 18.22V power applied to the substrate holder, for atmospheric pressure (red) and under vacuum (blue), b) 21.89 V power applied to the substrate holder, for atmospheric pressure (red) and under vacuum (blue), c) 25.5 V power applied to the substrate holder, for atmospheric pressure (red) and under vacuum (blue).

Figure 4.1 shows the results for applied voltage in three different amplitude, for the atmosphere pressure by increasing the voltage the temperature increases within the first 15 minutes and becomes constant for the further time. Whereas for the vacuum case it is taking a longer time (approximately 20 minutes) for the temperature to reach the

constant region .From these results temperature vs. voltage slop presented in Figure 4.2.

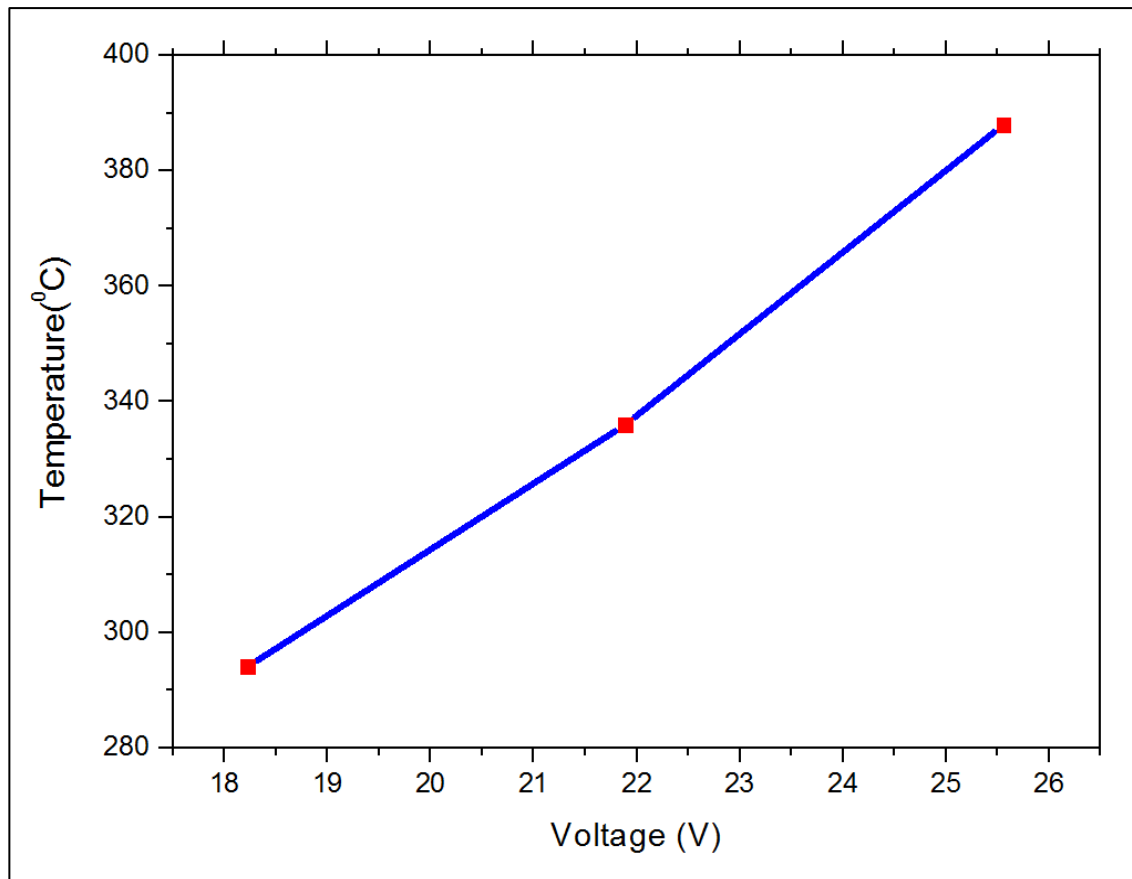


Figure 4.2.Slope for temperature vs. Voltage (data points extracted from maximum temperature reached at each voltage).

In order to heat up the substrate to 300 °C we applied the voltage of 20 V DC in the start of the SiO<sub>2</sub> sputtering process. This preparation step takes place at the point when the vacuum starts to reach 1x10<sup>-5</sup> mBar.

#### **4.2.2. METAL-OXIDE-SEMICONDUCTOR (MOS) DEVICES**

At this stage, we fabricated a MOS device in this projected, consisting of two sets of devices made at low substrate temperature (100 °C) and high substrate temperature (300 °C) during sputtering. On each set, three different oxide thicknesses were prepared (20 nm, 40 nm and 60 nm) with the top aluminum contact being a 200 μm diameter circle shape. The current-voltage (I-V) measurements were in the range of -30 V to +30 V for the 20 nm size MOS, -50 V to +50 V for the 40 nm MOS and -70 V to +70 V for the 60 nm devices. For the capacitance-voltage (C-V) measurements, the AC voltage was set to 50 mV at a frequency of 1 MHz and DV voltage on the range -10 V to +10 V.

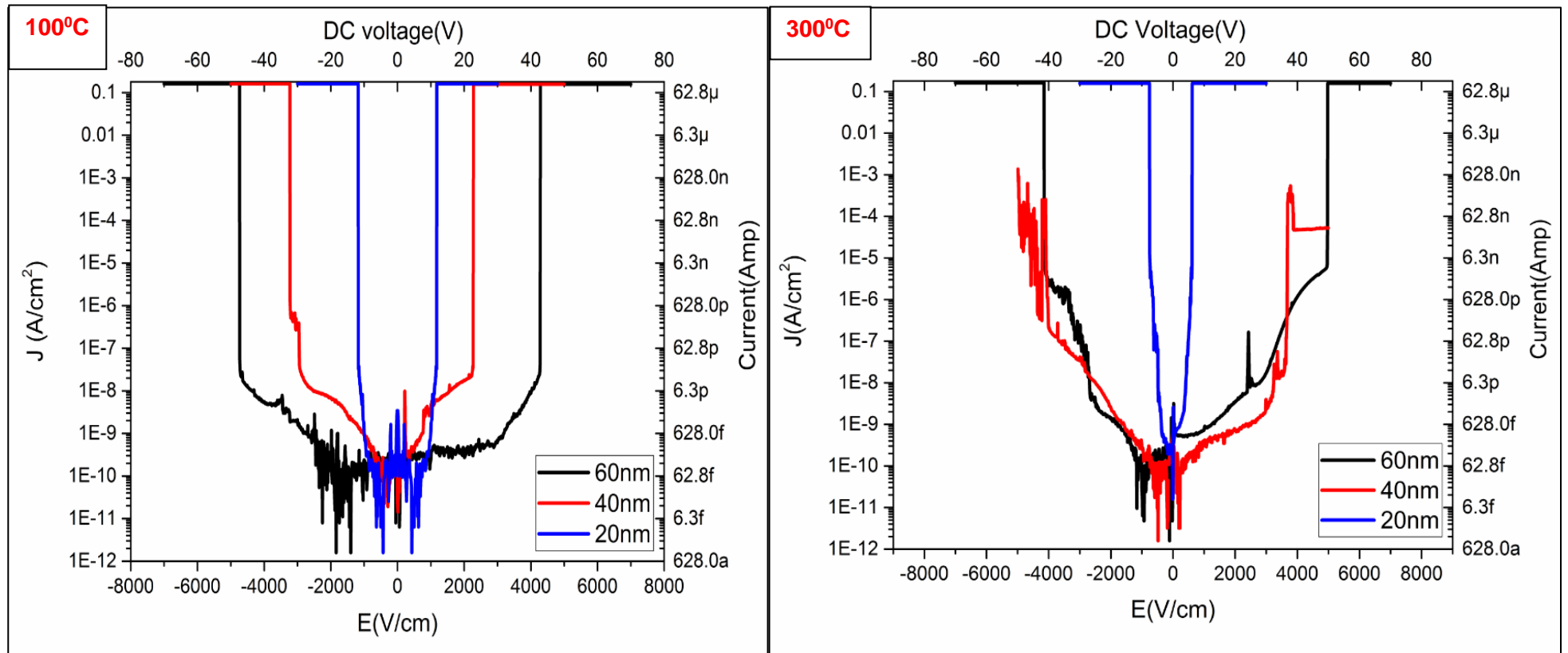


Figure 4.3. I-V measurements for MOS devices sputtered at 100 °C temperature (top) and 300 °C temperature with 20nm, 40nm and 60nm SiO<sub>2</sub> thickness.

Each device was fabricated on a substrate of dimensions 2.5 cm x 2.5 cm, thus on each substrate there are around 560 individual MOS devices with the 200  $\mu\text{m}$  diameter circle. After each I-V measurement the probes were repositioned on a different structure, because after applying a certain voltage the devices were no longer functional. Also The second set of MOS devices were sputtered at a temperature of 300  $^{\circ}\text{C}$  but the Argon/Oxygen ratio (3:1) inside chamber during deposition and the RF power (100 W) was kept constant.

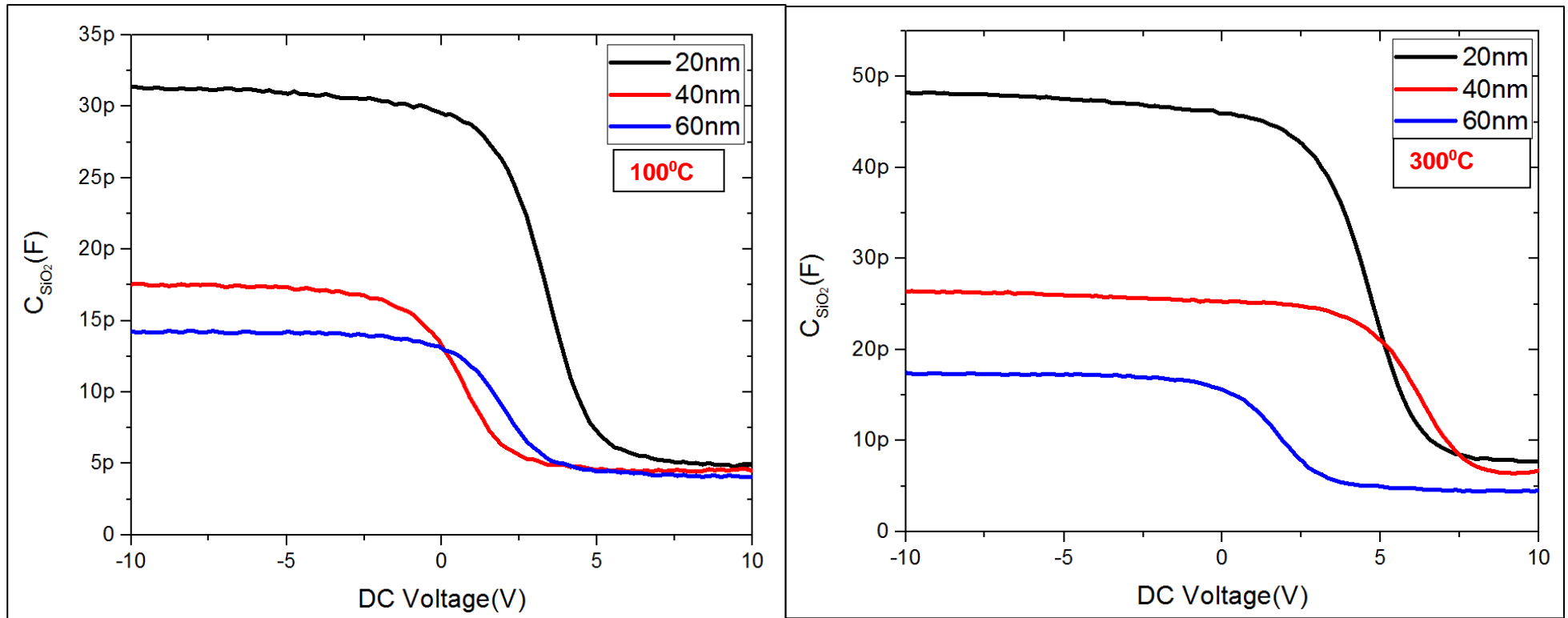


Figure 4.4.C-V measurements for the MOs devices sputtered at 100 °C (top) and 300 °C (bottom) with 20 nm, 40 nm and 60 nm SiO<sub>2</sub> layer.



As can be seen from Figure 4.4 with increasing the thickness of the silicon oxide layer, the capacitance decreases accordingly. The capacitance value in the accumulation region (negative voltage) is at a maximum value and it is mostly flat. This then starts to decrease over the depletion region and finally reaches a minimum value in the inversion region.

From the maximum capacitance ( $C_{max}$ ) for each MOS device with different thickness, the effective permittivity of silicon oxide layer can be calculated. These values can be plotted as a graph for relative permittivity vs. thickness of  $\text{SiO}_2$  for low and high temperature fabricated MOS devices. This is shown in Figure 4.5.

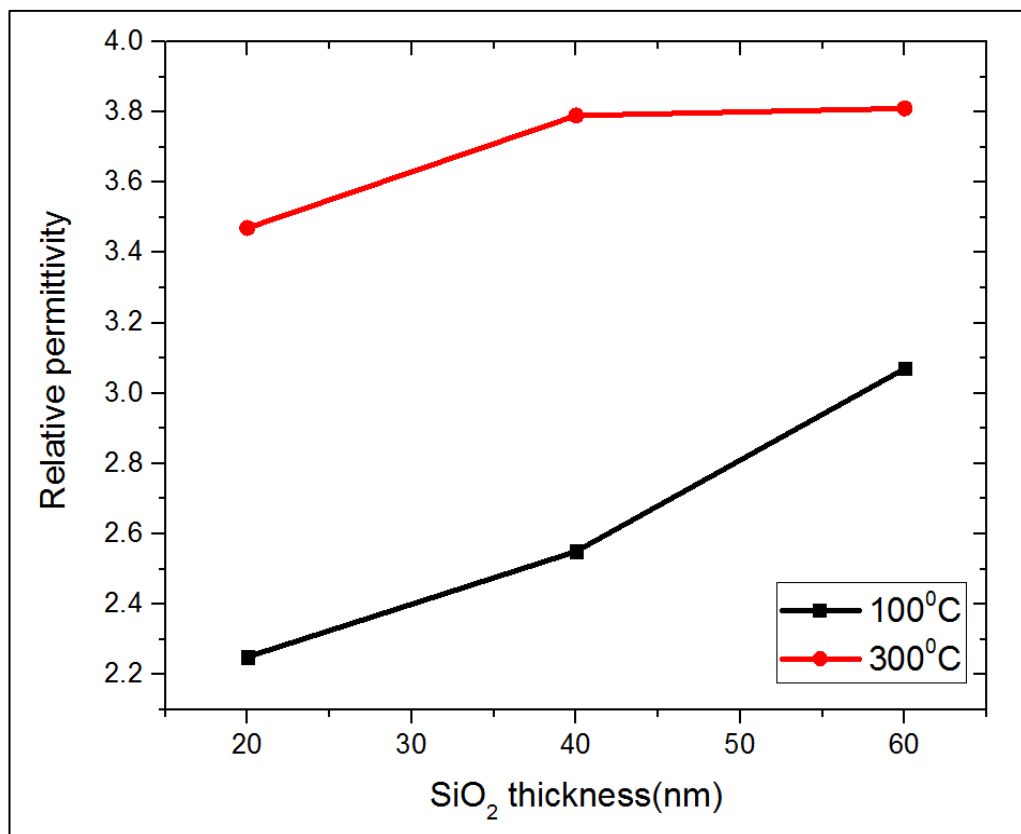


Figure 4.5. Calculated relative permittivity vs. oxide thickness for low (black line) and high (red line) temperature MOS devices.

Figure 4.5 shows the permittivity calculation based on experimental data which indicates by increasing the temperature during sputtering improves the permittivity directly.

### 4.2.3. HYDROFLUORIC ACID (HF) ETCHING

Total thickness profile for the samples presented in Figure 3.6 for the SiO<sub>2</sub> layer and added photoresist layer on top of these samples are presented below.

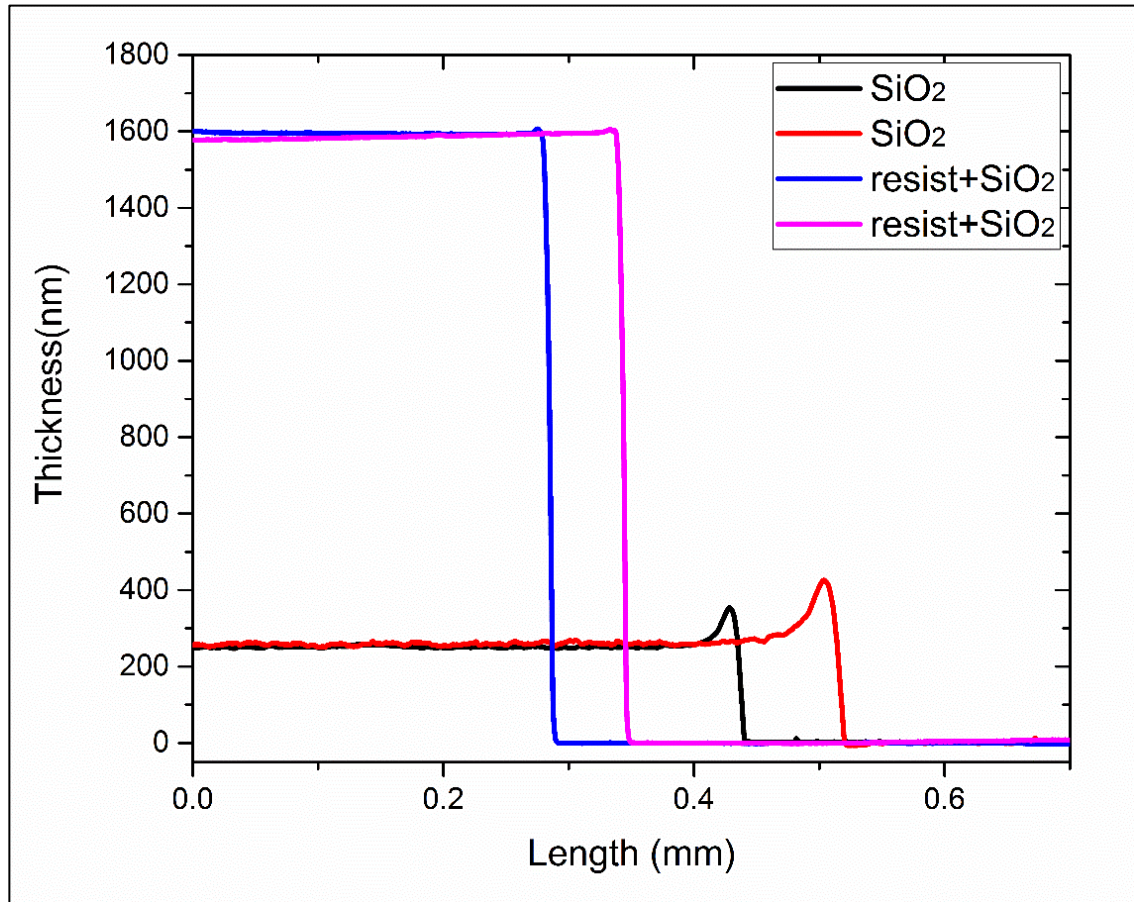


Figure 4.6. Dektak surface profiler measurement for SiO<sub>2</sub> sputtered on p-type-Si substrate (black and red, two readings) and photoresist layer on top of SiO<sub>2</sub> layer (pink and blue).

Figure 4.6 illustrates the thickness of photoresist spin coated on top of sputtered SiO<sub>2</sub>, these samples are ready for HF etching experiment. Samples are etched for different times: 30 seconds, 1 minute, 2 minutes and 3 minutes. The thickness profile measurements were carried out with Dektak surface profiler.

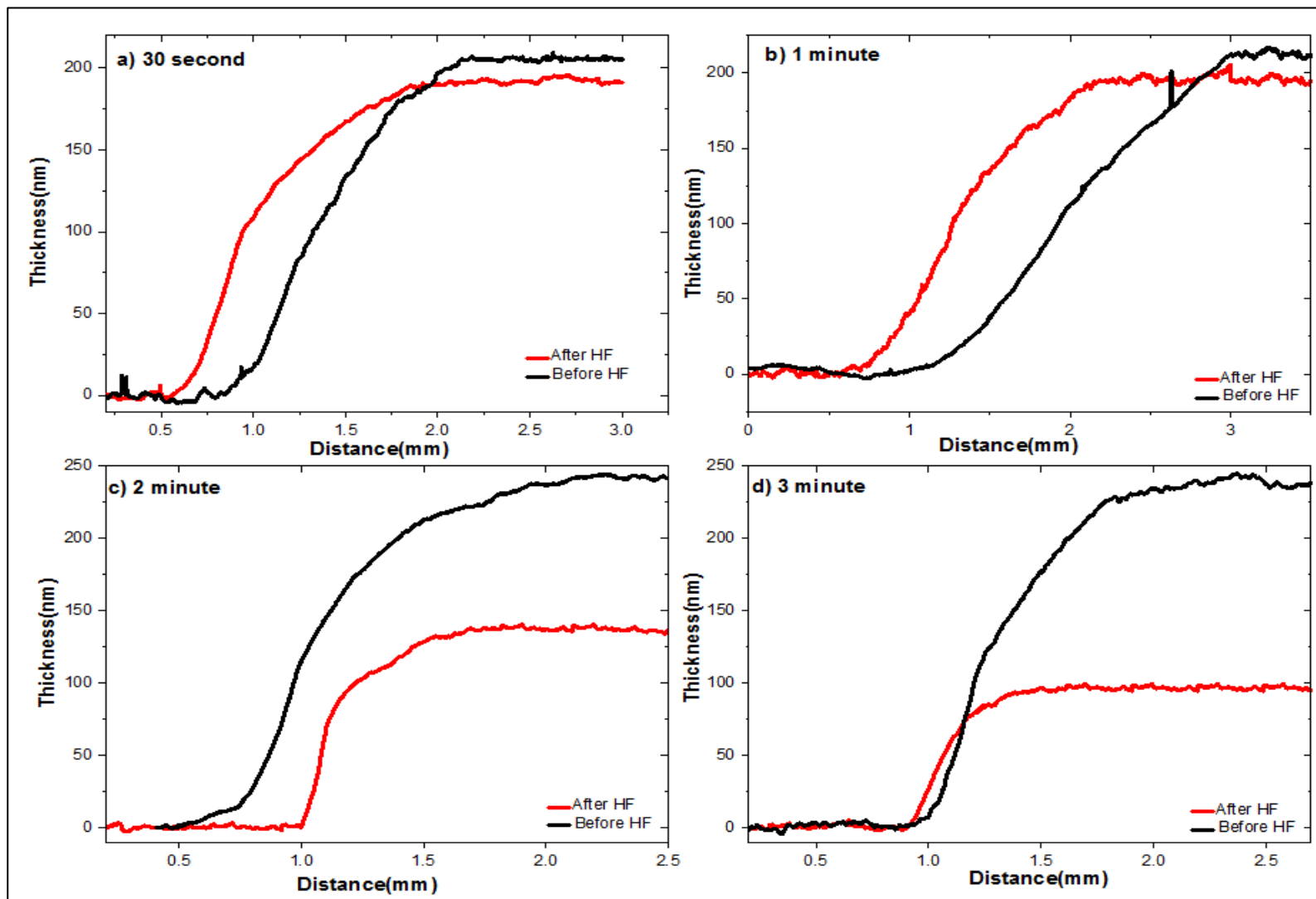


Figure 4.7. Dektak surface profile measurements before and after HF etching for a) 30 second, b) 1 minute, c) 2 minutes and d) 3 minutes. These data presents the average of 5 measurements from same sample.

Figure 4.7 shows the HF etch rate for 4 different etch time, the amount of etched SiO<sub>2</sub> in 30 second is around 20 nm, for 1 minute this amount is approximately 39 nm, 2 minutes etch time gives a total thickness difference of 84 nm and 3 minutes etch time removes around 160 nm of SiO<sub>2</sub> .these results also plotted in HF etch rate graph in below.

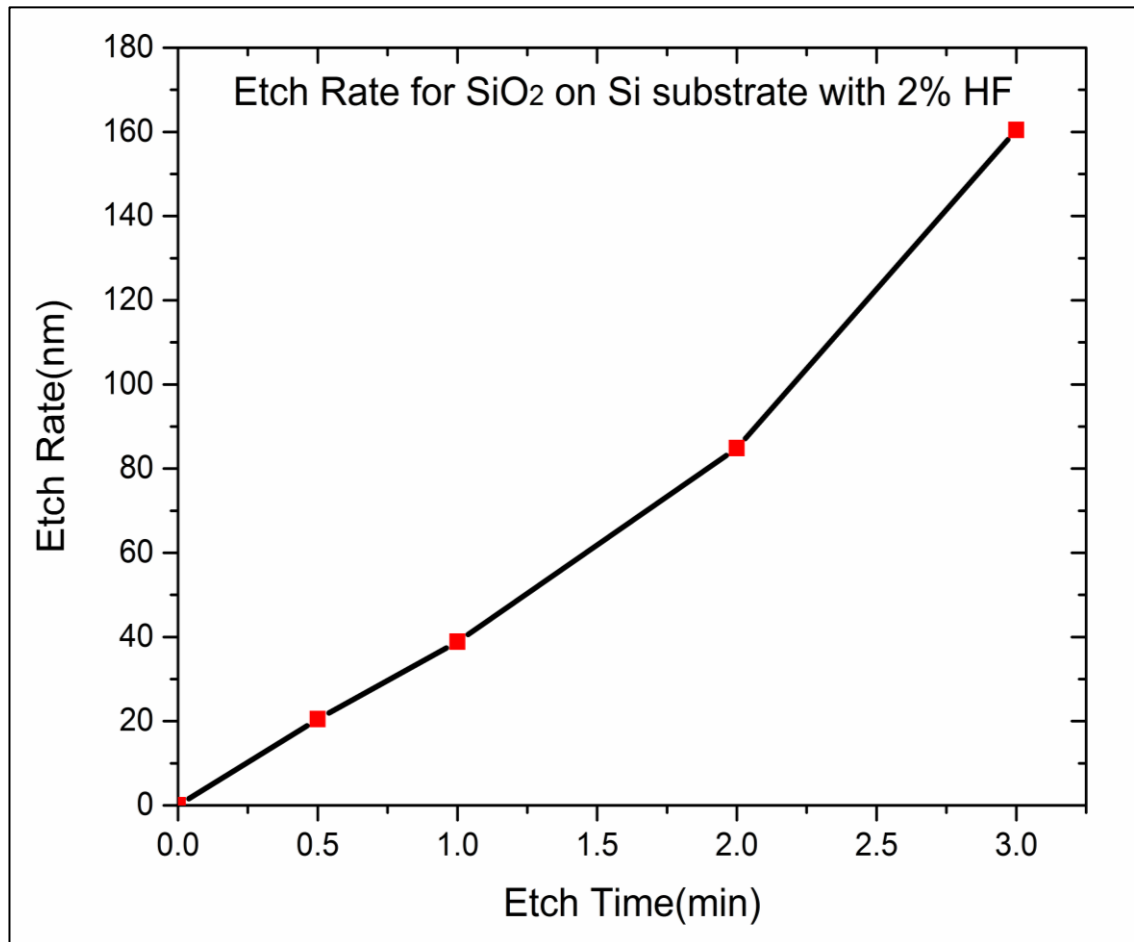


Figure 4.8. Etch rate vs. time with 2% HF for SiO<sub>2</sub> sputtered in Si substrate. Where the etch rate increases by increasing the time.

After HF optimization the 3 minutes etch time selected to investigate further since in the nanogap capacitive sensor we need to etch 1  $\mu\text{m}$  from each side of the junction. In this step the pattern (bottom electrode glass mask used for this experiment for creating the step pattern) created with photolithography first, then a thick layer of (~235 nm) SiO<sub>2</sub>

sputtered and the lift-off performed, the white light spectroscopy image of the created pattern presented below.

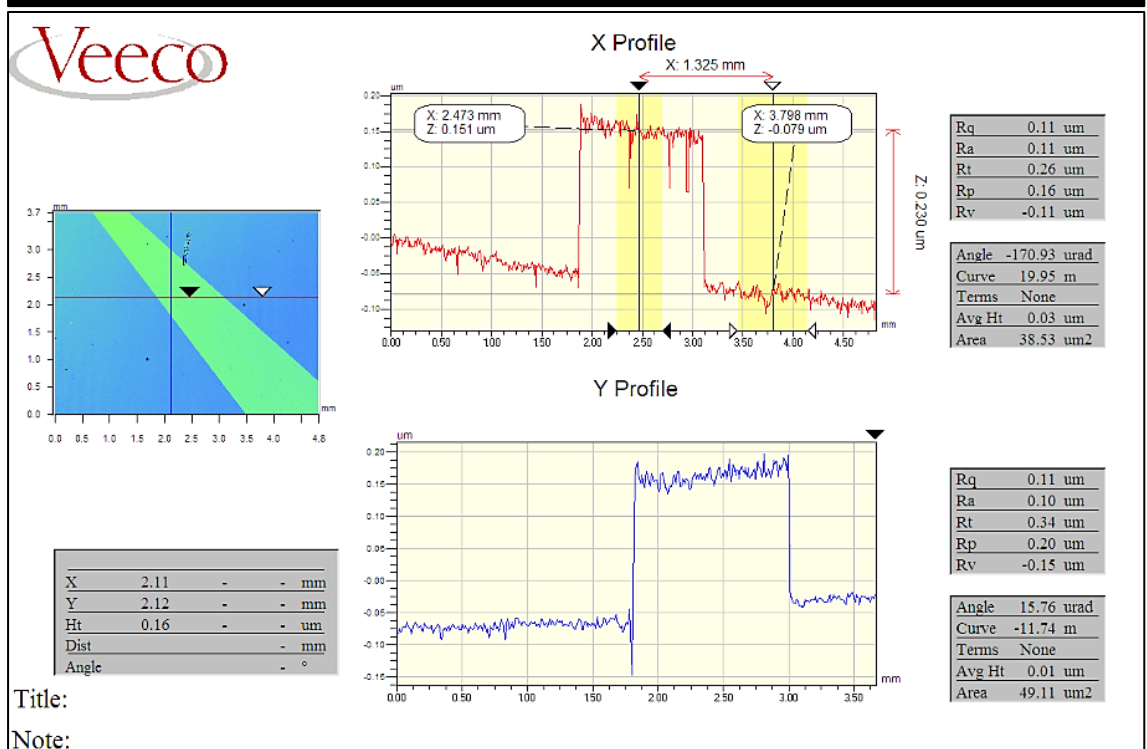
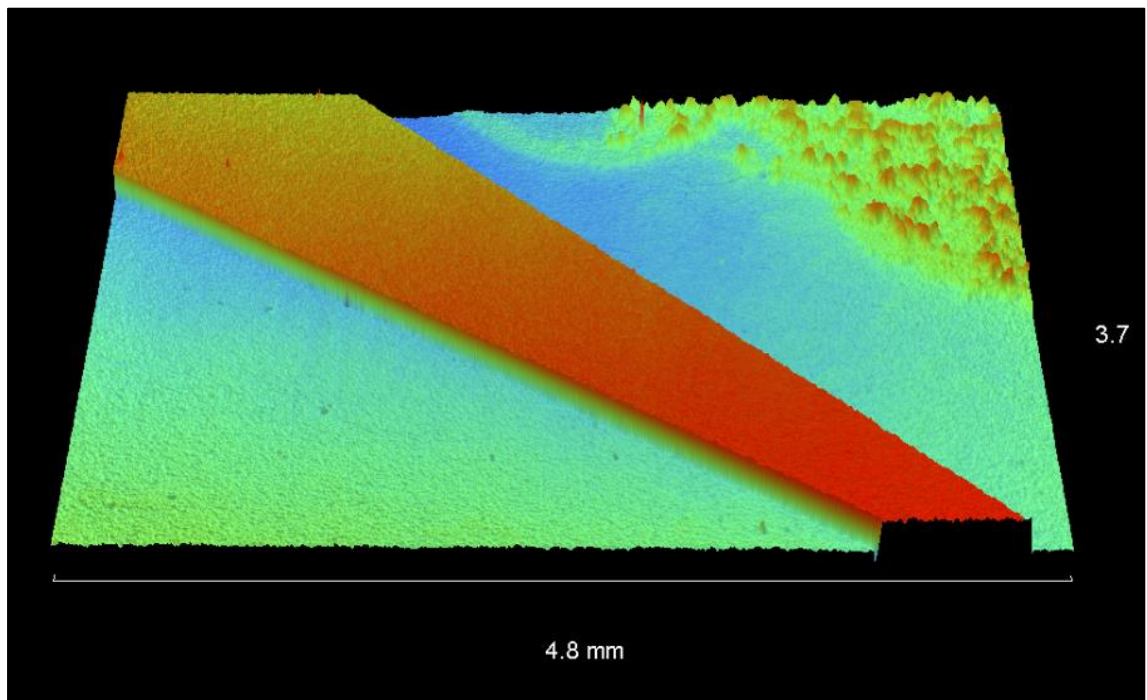


Figure 4.9. White light microscopy image of sample with SiO<sub>2</sub> pattern in Si substrate after lift-off before HF (top), thickness profile ~ 230nm (bottom). These measurements were performed in Dr. Chris Walton Laboratory with his assistance.

Figure 4.9 shows the 3D image of the glass substrate with SiO<sub>2</sub> pattern after lift-off, here the electrode pattern (orange color) is where the SiO<sub>2</sub> sputtered and the Si substrate is surrounded (green color) .

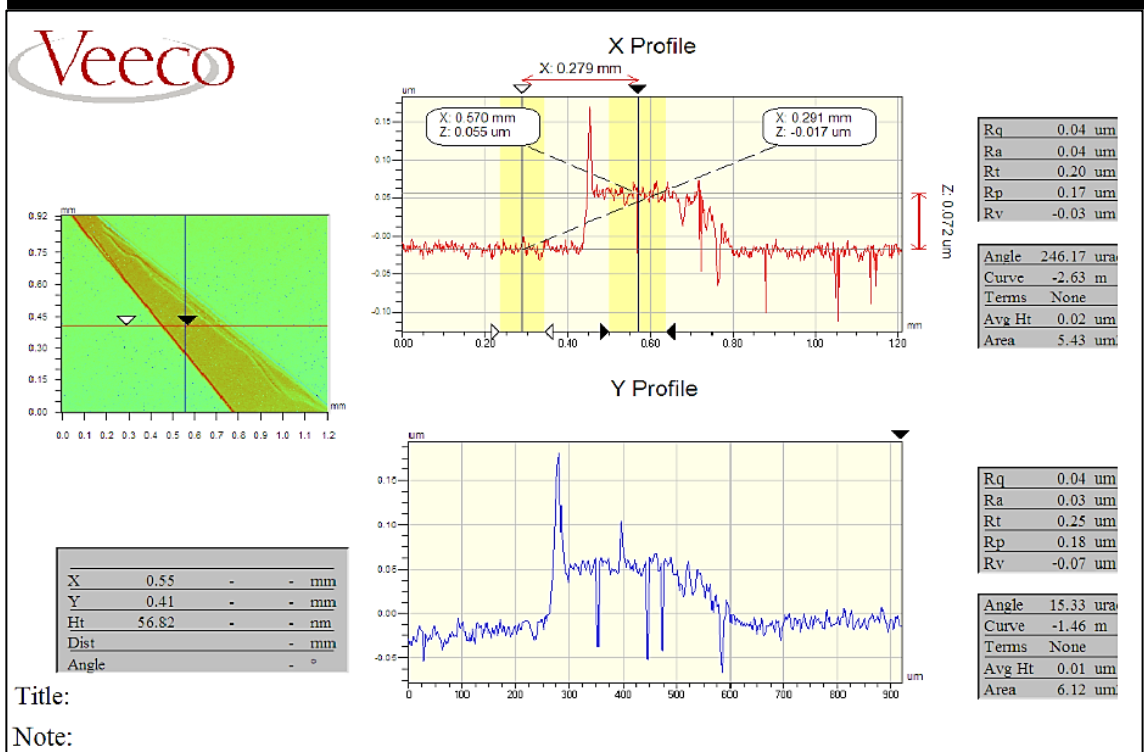
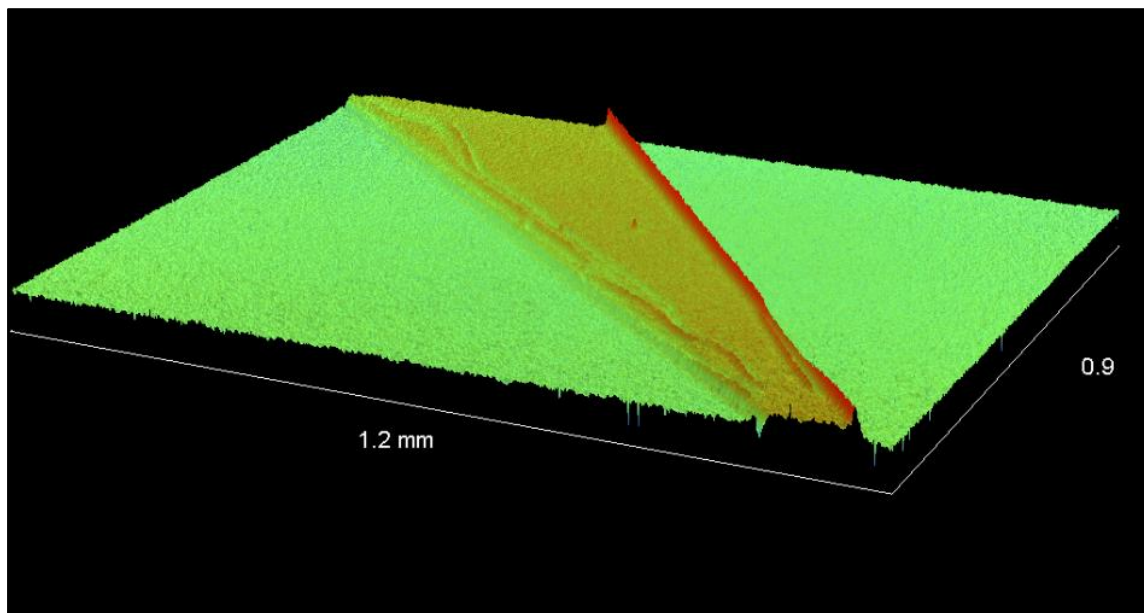


Figure 4.10. White light microscopy image of sample with SiO<sub>2</sub> pattern in Si substrate after lift-off after HF (top), thickness profile ~ 72 nm (bottom).

Figure 4.10 shows the 3D image of the same sample after HF, the effect of HF on SiO<sub>2</sub> can be seen clearly and the thickness profile is around 72 nm (before HF 235nm – after 72 nm = 160 nm). After both experiment the reliability of HF etch experiment confirmed and to achieve nearly 1 μm etch rate the required time adjusted accordingly.

#### 4.2.4. PERMITTIVITY CALCULATIONS

In the next part of this chapter the permittivity measurements for different buffer solution and aptamer protein are presented. The actual measurements on each devices is based on capacitance measurements in different frequency and then these data are converted to the permittivity. Therefore the total effective permittivity for nanogap sensor (full device) can be calculated with:

$$C_{total} = \frac{\epsilon_0 \epsilon_{effective} A_{total}}{d} \quad (4.1)$$

Where  $\epsilon_0 = 8.85 \times 10^{-12} \text{ Fm}^{-1}$  is the permittivity of free space,  $\epsilon_{effective}$  is total effective permittivity (SiO<sub>2</sub>=3.9 and air=1) which is the permittivity of the oxide layer and the medium between the two electrodes,  $A_{total}$  is the total area and  $d$  is the distance between two electrode (40 nm). In this design there are three different area of the sensors to be considered after HF etching, one containing SiO<sub>2</sub> and the other two air (where different solution will be placed) and  $d$  is the distance between two electrodes (40nm). Whereas before HF etch the total area is the sum of electrode area for 100 capacitor, which is  $100 \times (5 \mu\text{m} \times 5 \mu\text{m}) = 250 \mu\text{m}^2$ .

Before HF etching the theoretical capacitance value can be calculated from Equation 4.1 since the effective permittivity is only includes the SiO<sub>2</sub> layer. The capacitance for one capacitor is:

$$C = \frac{8.85 \times 10^{-12} \text{ Fm}^{-1} \times 3.9 \times 25 \mu\text{m}^2}{40 \times 10^{-9} \text{ m}} = 21 \text{ fF} \quad (4.2)$$



so the total capacitance for one devices is:

$$C_{total} = 100 \times 21 \text{ fF} = 2.1 \text{ pF} \quad (4.3)$$

The experimental values for total capacitance measurements before HF for 4 devices in one substrate are presented in the table below.

Table 4.1. Capacitance measurements before HF etching in 4 individual device at single frequency (1013 Hz).

Device name	Capacitance before HF
D11	2.09 pF
D12	2.11 pF
D13	2.08 pF
D14	2.1 pF

Capacitance measurement presented in Table 4.1 performed with single frequency setup at 1013 Hz (see Figure 3.31). This values can be compared with the total capacitance readings after HF to calculate the etched area. The experimental value for the total area ( $A = 5 \mu\text{m} \times 5 \mu\text{m}$ ) and the thickness of SiO<sub>2</sub> layer ( $d = 40 \text{ nm}$ ) can be different from the theoretical value. Therefore, for each individual device the total effective area after HF can be calculated.

After HF etching the total area for each device is changing and this is due to the fact that some parts of SiO<sub>2</sub> is partially etched to obtain the nanogap. The schematic of these three different areas are presented in Figure 4.11.



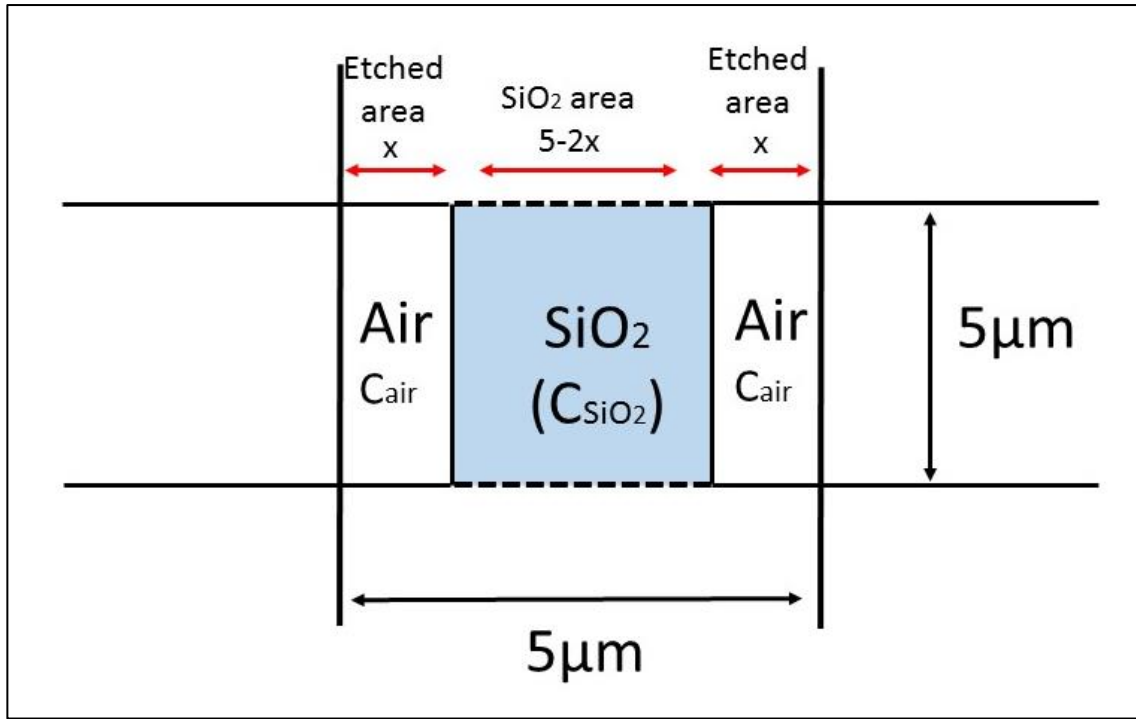


Figure 4.11. Three different area after HF etching. The two side etched gap are shown as air (with the capacitance for  $C_{air}$ ) and the middle area where the  $SiO_2$  remains to provide physical support for top electrode and act as a spacing between two electrodes.

By applying a series of mathematical equations, the total capacitance (F) for air inside Nanogap and  $SiO_2$  area can be calculated. The total capacitance can be written as:

$$C_{total} = 2 \times C_{air} + C_{SiO_2} \quad (4.4)$$

Where  $C_{air}$  is the capacitance contribution from the etched area when filled with air, and

$C_{SiO_2}$  is the capacitance contribution of  $SiO_2$ .

$$C_{total} = \frac{2 \times \epsilon_0 \times \epsilon_{air} \times (5 \times 10^{-6} m \times x)}{40 \times 10^{-9} m} + \frac{\epsilon_0 \times \epsilon_{SiO_2} \times ((5 - 2x) \times 10^{-6} m) \times 5 \times 10^{-6} m}{40 \times 10^{-9} m} \quad (4.5)$$

Where  $\epsilon_0 = 8.85 \times 10^{-12} Fm^{-1}$  is the permittivity of free space,  $\epsilon_{air}$  is the permittivity of air (~1) and  $\epsilon_{SiO_2}$  is the permittivity of  $SiO_2$  part (~3.9). The value of  $x$  can be calculated

from equation 4.5:

$$x = \frac{-\frac{C_{total}}{100} \times 40 \times 10^{-9}}{2.478 \times 10^{-16}} + 3.39 \times 10^{-6} \quad (4.6)$$

Since in our design we have 100 nano capacitors in parallel on each device therefore the total capacitance can be divided by 100 to get capacitance value for one individual nanocapacitors. For example, a nanogap sensor after HF and top window lithography had a total capacitance of  $1.6 \times 10^{-12}$  F (at 1.013 kHz, single frequency measurements), with air inside the nanogap, so the x value is calculated to be ~ 807 nm. With the calculated x value for each device, the capacitance for any solution inside the nanogap can be measured and converted to relative permittivity.

### 4.3. SENSITIVITY AND BUFFER SOLUTIONS TESTS

The fabricated Nanogap capacitive sensors were tested for sensitivity and reliability initially with air inside the Nanogap and then with DI water. Figure 4.12 shows the frequency response of the device over the range of 10 Hz to 500 kHz for air and water. The capacitance spectra for air is flat across the range of frequency while in the case of water the response is flat below 500 Hz and decreases at high frequency as expected.

For each individual device, the capacitance measurements with air inside the nanogap gives the total etched area (see equation 4.6). Therefore, by calculating the etched area and the SiO<sub>2</sub> area (remaining SiO<sub>2</sub> area), the permittivity of each buffer solution can be calculated.

The second reliability tests included measurements using a series of buffer solutions with different concentrations, prepared by Dr. C. Kemp (Hull University Biology Department) and being similar to those used by Mannoor *et al.*<sup>96</sup> so that qualitative comparisons could be made. The buffer solution was sodium citrate (SSC) with a range of concentrations varying from 0.1 x SSC to 1 x SSC, all with a pH of 6.8.

First 20x SSC (Salt Sodium Citrate) buffer were prepared with dissolving 35.06 g NaCl and 17.64 g Sodium Citrate in 200 ml of water (pH adjusted with HCl to 6.8). The final concentration of NaCl is 3 M and Sodium Citrate is 300 mM. Then 0.1x SSC, 0.2x SSC, 0.5x SSC and 1x SSC buffer solution was prepared.

The order of introducing solutions was from DI water to monotonically increasing concentrations of buffer. This was to avoid any errors due to fluid leftover from a previously higher concentration. The time from the removal of the fluid to the introduction of new fluid was around 5 min, because a small amount of fluid sample may remain in the nanogap. The fluid from the device was removed by a small strip of lint-free absorbent

paper followed by 1 minute heating on the hotplate at 60 °C to completely remove any remaining liquid.

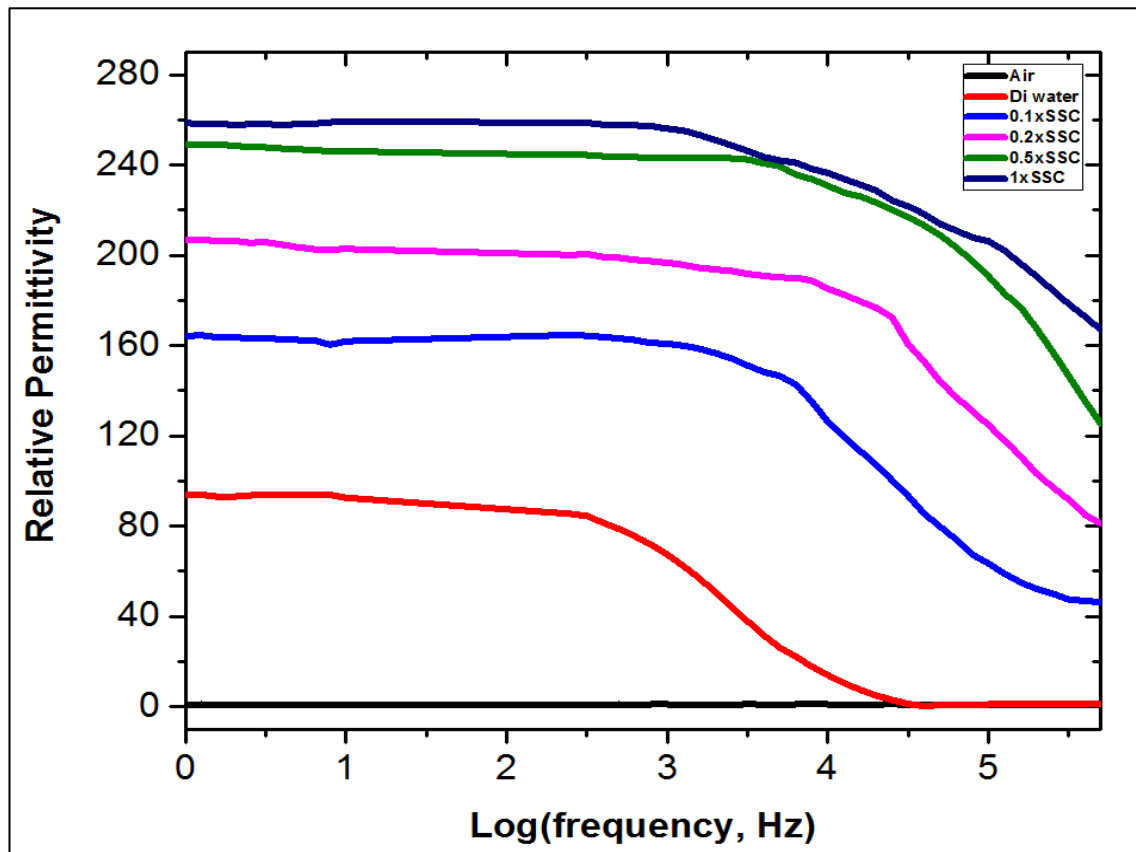


Figure 4.12. Calculated permittivity values as a function of frequency for of air(black), DI water(red) and from low to high concentration , 0.1x SSC (blue), 0.2x SSC (pink), 0.5xSSC (green) and 1xSSC (navy).

The results in Figure 4.12 show that increasing the SSC concentration produces a larger capacitance as expected, due to increase of permittivity value. In general, for frequency dependent capacitors, increasing the frequency results in the capacitance decreasing and this can be monitored using the nanogap capacitive sensor.

## 4.4. APTAMER AND PROTEIN MEASUREMENTS

All measurements were performed at room temperature in the presence of 0.5x SSC buffer solution. The capacitance changes due to hybridization were measured using the previously introduced setup (see figure 3.33) over the range of 1 Hz to 500 kHz and at 20 mV AC.

The capacitance values were then converted to the relative permittivity, the idea being to compare our results with the previous work done by Mannoor *et.al*<sup>96</sup>, for proof of concept.

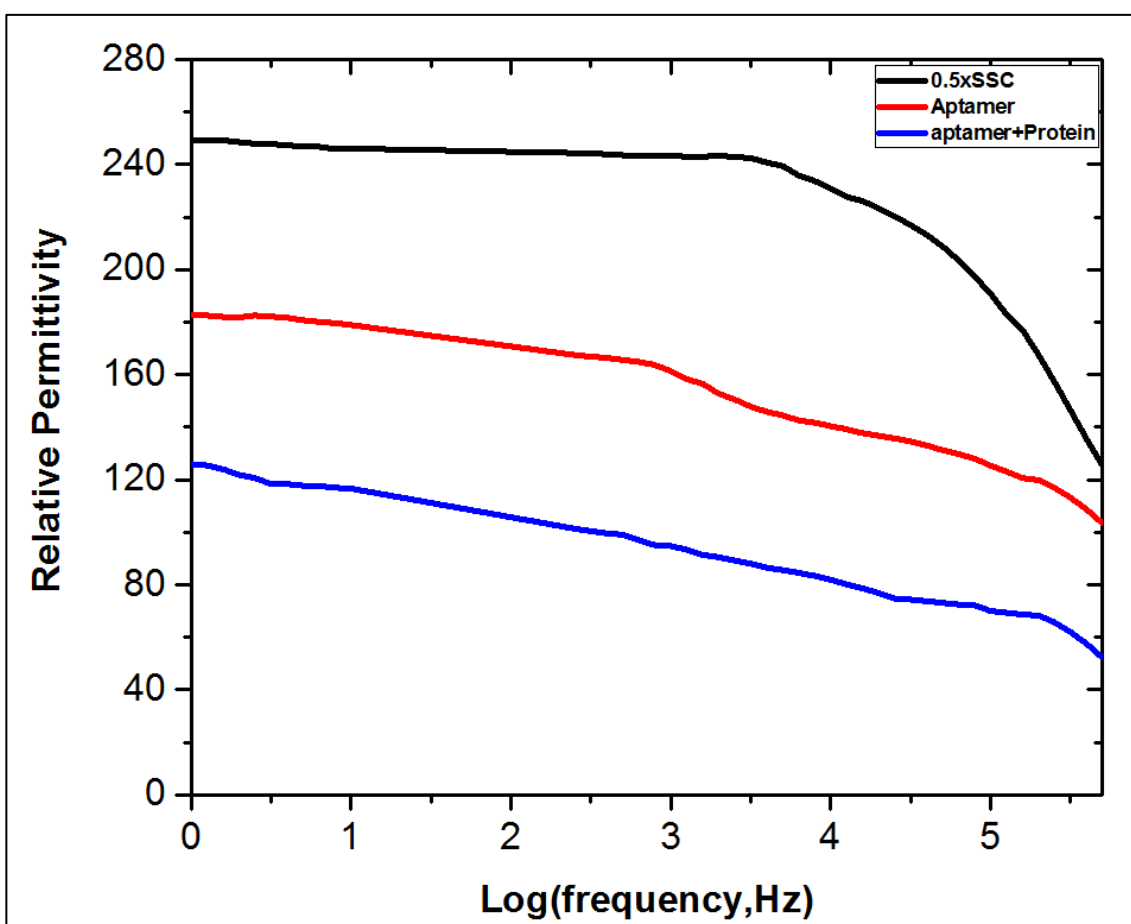


Figure 4.13. Dielectric spectrum of a bare Nanogap in the presence of 0.5x SSC buffer (black). The spectrum of the same Nanogap after coating with a SAM of 100:1 6Mercapto-1-hexanol (MCH)/thiol-modified aptamer (red). The same Nanogap after SAM formation followed by alpha-thrombin binding (Protein concentration in this experiment was 1  $\mu$ M in 0.5xSSC buffer solution).

The permittivity changes after aptamer immobilization and alpha-thrombin protein binding are shown in Figure 4.13. Clearly, the immobilization of the aptamer probes decreases the sensor capacitance and permittivity and this indicates the replacement of water molecules ( $\epsilon=80$ ) by a monolayer of lower dielectric permittivity. This effect is further enhanced with the binding of protein molecules to the immobilized aptamer.

Form the sensitivity and selectivity point of view, a further control experiment was performed in which a different control oligomer aptamer that is unable to make a bound to alpha-thrombin protein was used. The surface functionalization method and measurements process were exactly the same as the previous experiment.

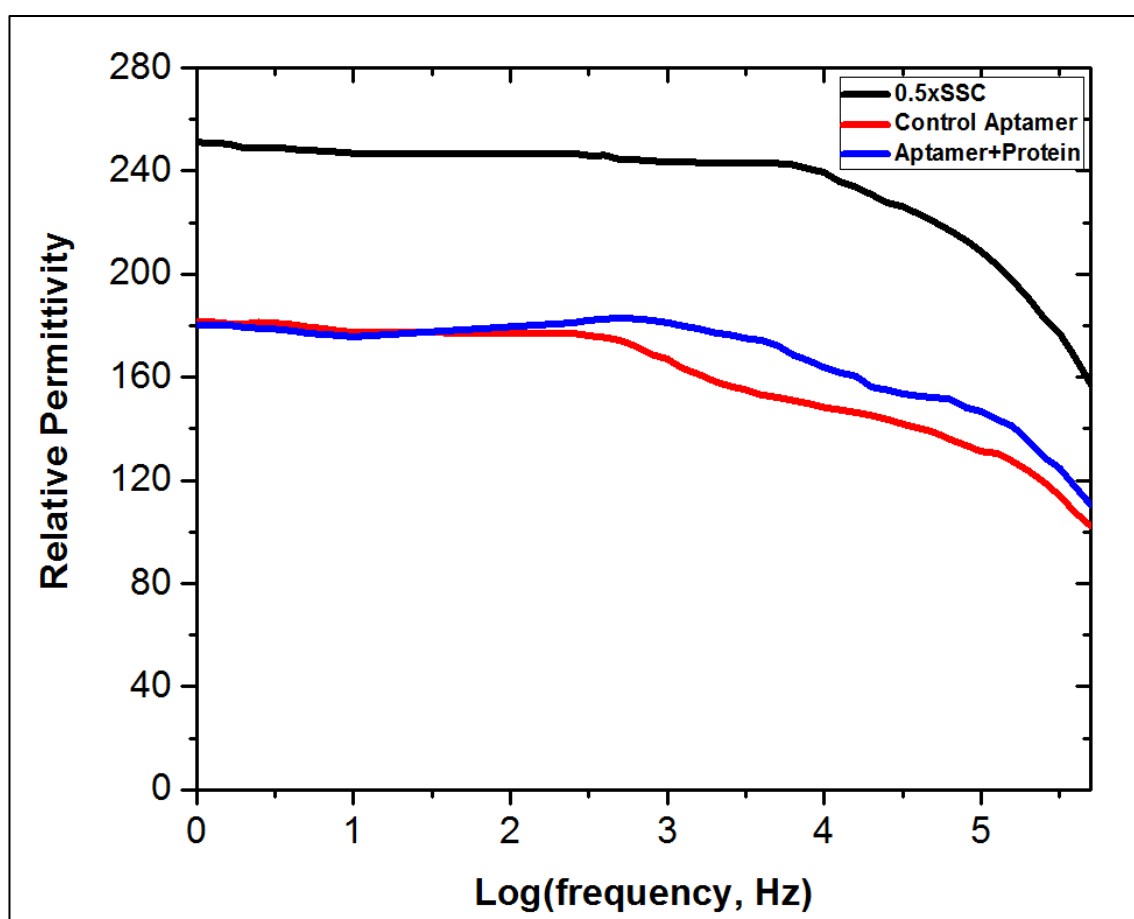


Figure 4.14. Dielectric spectrum of a bare Nanogap in the presence of 0.5x SSC buffer (black). The spectrum of the same Nanogap after coating with a SAM of 100:1 6Mercapto-1-hexanol(MCH)/ control oligomer aptamer (unable to bound with alpha-thrombin protein) (red). The same Nanogap after SAM formation followed by adding alpha-thrombin protein (protein concentration in this experiment was 1 $\mu$ M in 0.5xSSC buffer solution).

The dielectric spectra for the interaction of alpha-thrombin protein with a layer of immobilized control oligomer indicated that the proteins are not able to bond to this type of aptamer. There is a slight shift in relative permittivity for both the control aptamer and protein, which arises from the interaction between the positively charged protein molecules and the negatively charged oligonucleotide sequences.

## 4.5. DISCUSSION

Increasing the temperature of the substrate in sputtering/deposition time improves the quality of oxide layer leading to a higher permittivity constant in electrical measurements performed in this work. For a MOS device with 20 nm silicon oxide deposited at 100 °C, the accumulation region continues up to +4 V, whereas for the same device fabricated at 300 °C, this region extends up to +6 V. The corresponding results for 40 nm oxide layer at 100 °C and 300 °C are 0 V and +5 V respectively. Finally, the same values for the thicker oxide layer (60 nm) for both the low and high temperature fabricated MOS devices are around 0 V.

These results demonstrate that the 40 nm size oxide layer has the larger accumulation capacitance when compared to thinner layers (20 nm) using the RF sputtering technique. With increasing the oxide thickness, the produced layer have shown nearly the same characteristics as the 40 nm size.

The I-V characteristics of the MOS devices at 100 °C and 300 °C are shown in Figure 4.3. For the 20nm size MOS devices, the breakdown electric field increased from 180 V/cm (100 °C) to 620 V/cm (300 °C). For the 40 nm MOS devices, when increasing the temperature from 100°C to 300°C, the breakdown electric field increased from 2270 V/cm to 3650 V/cm respectively. The same results for the 60 nm devices also shown an increased 4280 V/cm to 5000 V/cm. Leakage current values obtained in our MOS devices are closely matching with other related works done for various SiO<sub>2</sub> thickness<sup>203,204</sup>.

It was demonstrated that increasing the substrate temperature during sputtering/deposition could effectively improve the quality of oxide layer. However, increasing the oxide thickness is another step towards fabricating high quality insulator for nanogap capacitive biosensor.



In this work, we have measured the response of our Nanogap capacitive sensor to DI water. The relative permittivity versus frequency curve (Figure 4.12) for air and pure water obtained using Nanogap capacitive sensor is very close to the theoretical value of 80 at low frequency (1 Hz-1.5 kHz), diminishes in the kilohertz range (from 2 kHz-250 kHz). When approaching a high frequency the value is approximately ~3, then for the higher frequency range (250 kHz-500 kHz) this reduces further to ~1 continually. There have been a few research publications with similar basic principle to our work in the literature, which we use to evaluate our results for DI water. Our results for DI water exhibit very similar trend to the work by J.T.Nevill *et al*<sup>162</sup> who measured the permittivity of water and ice. In their sensor structure, the SiO<sub>2</sub> has been partially removed which indicates that the remaining SiO<sub>2</sub> will contribute to the general relative permittivity vs. frequency curves. However, their electrode material is polysilicon whereas ours is gold. Also our results show a close similarity to those presented by Yi *et al.*<sup>167</sup> who work within the same frequency range. In their work, there is a large frequency dependence in the low frequency range (less than 1.5 kHz), whereas our data is relatively flat over this range. It is unclear yet why this occurs but it seems the elimination of electrode polarization is stronger in our devices. The results obtained in this work are similar in magnitude at both low and high frequency to those presented by Mannoor *et al.*<sup>96</sup> for their Nanogap sensor. In contrast to our results, these authors obtained the curves over the frequency range of 1 Hz to 100 kHz, whereas our work has a wider spectrum over the frequency range of 1 Hz to 500 kHz... More work needs to be done to better understand the reasons behind these effects.

As it can be seen from figure 4.12, the response of the Nanogap sensor to the various concentration of SSC buffer solution is highly dependent on the ionic concentration. With increasing concentration of buffer solution, the capacitance and therefore the relative permittivity increases. In terms of the frequency response, the results are also fairly

consistent, with the permittivity being flat in the low frequency range (1-1000Hz) and then decreasing in the kilohertz range (1 kHz-500 kHz) to reach a minimum value.

From the previous work (Mannoor *et al.*<sup>96</sup>), concentration of Sodium Citrate (SC) in water pH 6.8 were calculated to be 0.023 M (0.1x SC), 0.057 M (0.2x SC), 0.114 M (0.5x SC) and 0.227M (1x SC). The Debye length was calculated for each of these buffer solution with equation 2.4. In this equation, the relative permittivity values were added from experimental measurements. So the Debye length estimated to be around 25nm for 0.1x SSC, 17 nm for 0.2x SSC, 14 nm for 0.5x SSC and 1.1 nm for 1x SSC. These values are for one electrode, therefore for the nanogap with two electrodes, electrical double layer overlapping occurs inside nanogap. For example, in 0.1x SSC the electrical double layer overlapping in both electrode will be around 50 nm, comparing this with the physical size of nanogap 40 nm, giving a homogenous measurement condition inside the gap, which is completely occupied with electrical double layer. Nevertheless, for the higher concentration the nanogap will be partially occupied with electrical double layer, where some portion of solution will be in the region with zero electrical field.

As can be seen from Figure 4., the immobilization of aptamer probes decreases the sensor permittivity, which can be explained by the replacement of water molecules/buffer solution, which have high relative permittivity ( $\epsilon > 80$ ), by biomolecules of low relative permittivity. The binding of alpha thrombin protein to the immobilized aptamers further enhances this effect. Since these measurements were performed in presence of 0.5xSSC buffer, which has 15 nm Debye length (estimated experimental value) for each electrode, the space inside gap are partially filled with electrical double layer. These areas of electrode will be filled with aptamers and later protein. The approximate length of aptamer DNA and alpha thrombin protein are around 2 nm and 3.4 nm respectively (see part 2.4.). Although the measured capacitance and permittivity are improved,

because of achieving more constant values for low frequency, but still could be influenced from the electrode polarization effect.

Figure 4.13 illustrates the interaction of alpha thrombin protein with a layer of immobilized control oligomer. The difference between this aptamer and previous one is that this control aptamer is incapable of forming the G-quadruplex conformation to which alpha thrombin specifically binds. For the low frequency region (<1 kHz) there are no changes in the permittivity, whereas for the results above 1 kHz, a negligible change in dielectric behavior can be seen. To the best of our knowledge this occurs due to the electrostatic interaction between the positively charged protein molecules (left over inside the Nanogap) and the negatively charged aptamers.

For a solution with 150mM NaCl and 5mM KCl, in a 50mM Tris buffer, the dissociation equilibrium constant of thrombin aptamer for thrombin protein has been determined as 20 nM by surface plasmon resonance <sup>90</sup>. For our measurements, under the lower salt concentration (0.5x SSC) 75 mM NaCl and 7.5 mM KCl, even tighter binding is expected. In experiments reported in this project, the Nanogap responds passively to target protein concentration of 1 $\mu$ M. At this high concentration, the Nanogap should be fully saturated with bound thrombin. Nevertheless, in the current configuration, the effective sensing area of the Nanogap capacitive sensor has dimensions of 1  $\mu$ m x 5  $\mu$ m (for one side of each nanocapacitor) and a gap separation of 40 nm, with 100 nanocapacitors in parallel, this gives a total area of 1600  $\mu$ m<sup>2</sup>. Where all the surface is optimally coated, it is possible to obtain an active density of surface-attached DNA probe molecules in the order of 10<sup>12</sup> mol/cm<sup>2</sup>. This density corresponds to a density of 10<sup>4</sup>mol  $\mu$ m<sup>2</sup>, or 16x 10<sup>6</sup> mol/sensor element. Now, this number divided by 6.022 x 10<sup>23</sup> mol, gives 26.5 x 10<sup>-18</sup> which corresponds to a conservative estimate of sensitivity in the attomole range (theoretical value) for a saturation condition where all probe molecules are bound by target. In fact, because our current method for surface functionalization has yet to be optimized, it is

possible that we might even reach to lower detection limit. This is one area of proposed future work for this project.

## **Chapter 5. CONCLUSION AND FUTURE WORK**

## 5.1. CONCLUSION

Although many researches focused on finding solutions, environmental pollution, food safety and hygiene, early detection of many diseases and cancer are all major causes for concern for the scientific community. Biosensors are beginning to make a massive contribution in terms of offering cost effective, reliable, accurate and easy to use tools to solve these issues.

AC impedance spectroscopy based sensing is an efficient method and can be utilized for different types of biosensor applications. However, electrical double layer formation from ions at the electrode/solution interface is problematic as this can shield the applied electric field. Initial work on this concept was limited to high frequency (>100 kHz) measurements only, since at low frequency there is large electronic thermal noise ( $\langle V^2 \rangle = 4k_B T R$ ) from the electrical double layer (EDL). This was a significant drawback since this noise masks most of the important information required from biomolecular interactions. This thesis demonstrates a novel approach to remove this parasitic noise by minimizing the EDL impedance and enables low frequency (1 Hz-500 kHz) measurements to be obtained.

This thesis work demonstrates the development of a nanogap based biosensor structure, where the electrode separation size is less than the electrical double layer (EDL) thickness. This method has significant advantages since it not only removes the large parasitic capacitance from the EDL, as discussed above, but also improves sensitivity by matching better the active dielectric volume with the size of the biomolecules of interest. Nanogap capacitive biosensors are an excellent approach for detecting biomolecular interactions due to the ease of measurement, low cost equipment needed and compatibility with multiplex formats.

The extra key advantage of this methods is that the designed structure enables to perform the target molecule detection in presence of buffer solution (DI water), which the replacement of buffer solution (DI water) with biomolecules with lower relative permittivity indicates the detected volume, therefore improving sensitivity.

Moreover, the measurements technique in this project includes wash and rinse step with buffer solution, this provides more selectivity by removing the unspecifically bound biomolecules from measurements medium.

In this project, we have demonstrated the use of nanogap capacitive sensor for highly sensitive, label-free detection of alpha thrombin protein via immobilization of aptamer probe as a recognition element. Control experiments show that the method clearly distinguishes specific binding between alpha thrombin and its conjugate aptamer from nonspecific interaction between thrombin and non-binding aptamer. The 40nm gap separation between electrodes is shown to eliminate noise from electrode polarization effects and reduce the solution resistance, thereby facilitating dielectric spectroscopy at low frequencies.

Label-free detection of human alpha thrombin protein with 1 $\mu$ M concentration has been achieved. The sensitivity of the biosensor fabricated in this work for alpha thrombin is in the order of attomole and, to the best of our knowledge, this is the lowest detection limit for the Nanogap capacitive biosensing for aptamer-based human alpha thrombin detection.

## 5.2. FUTURE WORK

Since this is a relatively new area of research with only a few papers published on the topic, there are many opportunities for future work focusing on the optimization and improvement of the sensors detection capabilities. There is also significant work remaining in developing the sensor for use in medicine for the early detection of diseases.

Several immediate issues require clarification but were beyond the scope of this work. At the time of writing, we have not determined the limit of detection of the biosensor experimentally. The concentration of alpha-thrombin protein used was small (1 $\mu$ M) but is not near the expected detection limit of the device or near those of state-of-the-art biosensors in the field, which are capable of measuring 23 aM<sup>205</sup>. The device is theoretically predicted to achieve sensitivity of the order of attomole, but whether this is achievable in our device remains to be determined. Sensors that can detect at the level of 1 $\mu$ M are however important in many aspects of healthcare, for instance Alzheimer's disease and cancer<sup>140</sup>.

More extensive testing of the devices' selectivity is also needed. In this work we have tested the device with a non-binding control aptamer, however, the device has yet to be tested with solutions containing other bio-molecules or chemicals or even biologically relevant fluids (e.g. blood, urine, saliva), which may contaminate the sensors and produce false signals.

The fabricated sensor in this project has not undergone significant optimization to improve the device sensitivity. Simple improvements can be made by increasing the active volume between the metal electrodes, reducing the nanogap size to 10 nm and optimizing the concentration of the aptamer on the gold electrode.



Another possible future focus may be to study a new target biomolecule, such as a specific cancer biomarker. In this case, a recognition element related to that specific type of cancer could be used instead of the alpha thrombin aptamer used in this project. Where the special aptamer will be synthesized for surface functionalization will follow the hybridization of the specific cancer biomarker in the sensor. However, the electrical detection platform will be the same, with more advanced reduction of thermal noise coming from the experimental setup environment for high speed measurements.

Finally, the current platform has the potential to be integrated with a microfluidic system with a nano gap capacitive chip. This combination can offer novel system to the health care professional in a laboratory, where testing of patients' blood or urine are tested, for example. The low cost measurement setup can be positioned in the clinical laboratory with a computer based program for running tests with an easy to use procedure. In this approach, a pre-surface functionalized biosensor can be provided to the staff, where they only need to introduce specific samples into the fluid introduction chamber (in the microfluidic part of the system), wait for a couple of hours and perform the test.

In the pursuit of this target, this thesis investigated a Nanogap label-free capacitive biosensor as a promising candidate and demonstrated that they offer compelling attributes for the early detection of cancer and various other type of diseases.

## REFERENCES

- (1) *Expanding the Vision of Sensor Materials*; The National Academies Press: Washington, DC, 1995.
- (2) Bahadir, E. B.; Sezgintürk, M. K. Applications of Commercial Biosensors in Clinical, Food, Environmental, and Biothreat/biowarfare Analyses. *Anal. Biochem.* **2015**, *478*, 107–120.
- (3) Jayanthi, V. S. P. K. S. A.; Das, A. B.; Saxena, U. Recent Advances in Biosensor Development for the Detection of Cancer Biomarkers. *Biosens. Bioelectron.* **2017**, *91*, 15–23.
- (4) Pires, N. M. iguel M.; Dong, T.; Hanke, U.; Hoivik, N. Recent Developments in Optical Detection Technologies in Lab-on-a-Chip Devices for Biosensing Applications. *Sensors (Basel)*. **2014**, *14*, 15458–15479.
- (5) Liu, D.; Zhang, H.; Fontana, F.; Hirvonen, J.; Santos, H. A. Microfluidic-Assisted Fabrication of Carriers for Controlled Drug Delivery. *Lab Chip* **2017**, *17*, 1856–1883.
- (6) Vladislavljević, G. T.; Khalid, N.; Neves, M. A.; Kuroiwa, T.; Nakajima, M.; Uemura, K.; Ichikawa, S.; Kobayashi, I. Industrial Lab-on-a-Chip: Design, Applications and Scale-up for Drug Discovery and Delivery. *Adv. Drug Deliv. Rev.* **2013**, *65*, 1626–1663.
- (7) Nguyen, N. T.; Shaegh, S. A. M.; Kashaninejad, N.; Phan, D. T. Design, Fabrication and Characterization of Drug Delivery Systems Based on Lab-on-a-Chip Technology. *Adv. Drug Deliv. Rev.* **2013**, *65*, 1403–1419.
- (8) Mauk, M.; Song, J.; Bau, H. H.; Gross, R.; Bushman, F. D.; Collman, R. G.; Liu, C. Miniaturized Devices for Point of Care Molecular Detection of HIV. *Lab Chip*

**2017**, *17*, 382–394.

- (9) Vilela, D.; Romeo, A.; Sánchez, S. Flexible Sensors for Biomedical Technology. *Lab Chip* **2016**, *16*, 402–408.
- (10) Lonsdale, C. L.; Taba, B.; Queralto, N.; Lukaszewski, R. A.; Martino, R. A.; Rhodes, P. A.; Lim, S. H. The Use of Colorimetric Sensor Arrays to Discriminate between Pathogenic Bacteria. *PLoS One* **2013**, *8*.
- (11) Wang, Y.; Duncan, T. V. Nanoscale Sensors for Assuring the Safety of Food Products. *Curr. Opin. Biotechnol.* **2017**, *44*, 74–86.
- (12) Henao, O. L.; Jones, T. F.; Vugia, D. J.; Griffin, P. M. Foodborne Diseases Active Surveillance Network — 2 Decades of Achievements , 1996 – 2015. **2015**, *21*.
- (13) McCabe-Sellers, B. J.; Beattie, S. E. Food Safety: Emerging Trends in Foodborne Illness Surveillance and Prevention. *J. Am. Diet. Assoc.* **2004**, *104*, 1708–1717.
- (14) Mortari, A.; Lorenzelli, L. Recent Sensing Technologies for Pathogen Detection in Milk: A Review. *Biosens. Bioelectron.* **2014**, *60*, 8–21.
- (15) Li, Z.; Yu, Y.; Li, Z.; Wu, T. A Review of Biosensing Techniques for Detection of Trace Carcinogen Contamination in Food Products. *Anal. Bioanal. Chem.* **2015**, *407*, 2711–2726.
- (16) Bilitewski, U.; Turner, A. *Biosensors in Environmental Monitoring*; CRC Press, 2000, 2000.
- (17) Stanley, C. E.; Grossmann, G.; Casadevall i Solvas, X.; deMello, A. J. Soil-on-a-Chip: Microfluidic Platforms for Environmental Organismal Studies. *Lab Chip* **2016**, *16*, 228–241.
- (18) Chocarro-Ruiz, B.; Fernández-Gavela, A.; Herranz, S.; Lechuga, L. M.

Nanophotonic Label-Free Biosensors for Environmental Monitoring. *Curr. Opin. Biotechnol.* **2017**, *45*, 175–183.

- (19) Jarque, S.; Bittner, M.; Blaha, L.; Hilscherova, K. Yeast Biosensors for Detection of Environmental Pollutants: Current State and Limitations. *Trends Biotechnol.* **2016**, *34*, 408–419.
- (20) Seok Kim, Y.; Ahmad Raston, N. H.; Bock Gu, M. Aptamer-Based Nanobiosensors. *Biosens. Bioelectron.* **2016**, *76*, 2–19.
- (21) Kim, E.; Baaske, M. D.; Vollmer, F. Towards next-Generation Label-Free Biosensors: Recent Advances in Whispering Gallery Mode Sensors. *Lab Chip* **2017**, *17*, 1190–1205.
- (22) Henihan, G.; Schulze, H.; Corrigan, D. K.; Giraud, G.; Terry, J. G.; Hardie, A.; Campbell, C. J.; Walton, A. J.; Crain, J.; Pethig, R.; *et al.* Label- and Amplification-Free Electrochemical Detection of Bacterial Ribosomal RNA. *Biosens. Bioelectron.* **2016**, *81*, 487–494.
- (23) Lei, K.-M.; Mak, P.-I.; Law, M.-K.; Martins, R. P. CMOS Biosensors for in Vitro Diagnosis – Transducing Mechanisms and Applications. *Lab Chip* **2016**, *16*, 3664–3681.
- (24) Luka, G.; Ahmadi, A.; Najjaran, H.; Alocilja, E.; Derosa, M.; Wolthers, K.; Malki, A.; Aziz, H.; Althani, A.; Hoorfar, M. Microfluidics Integrated Biosensors: A Leading Technology towards Lab-on-A-Chip and Sensing Applications. *Sensors (Switzerland)* **2015**, *15*, 30011–30031.
- (25) Rusmini, F.; Zhong, Z.; Feijen, J. Protein Immobilization Strategies for Protein Biochips. *Biomacromolecules* **2007**, *8*, 1775–1789.
- (26) Mross, S.; Pierrat, S.; Zimmermann, T.; Kraft, M. Microfluidic Enzymatic

Biosensing Systems: A Review. *Biosens. Bioelectron.* **2015**, *70*, 376–391.

- (27) Kim, D.; Herr, A. E. Protein Immobilization Techniques for Microfluidic Assays. *Biomicrofluidics* **2013**, *7*.
- (28) Křenková, J.; Foret, F. Immobilized Microfluidic Enzymatic Reactors. *Electrophoresis* **2004**, *25*, 3550–3563.
- (29) Jang, E.; Kim, S.; Koh, W. G. Microfluidic Bioassay System Based on Microarrays of Hydrogel Sensing Elements Entrapping Quantum Dot-Enzyme Conjugates. *Biosens. Bioelectron.* **2012**, *31*, 529–536.
- (30) Le, Tao; Krause, K. *First Aid for the Basic Sciences, General Principles*; Second Edi.; McGraw-Hill Education / Medical.
- (31) Robinson, P. K. Enzymes: Principles and Biotechnological Applications. *Essays Biochem.* **2015**, *59*, 1–41.
- (32) Jomma, E. Y.; Ding, S. Recent Advances on Electrochemical Enzyme Biosensors. **2016**, 5–21.
- (33) Clark, L. C.; Lyons, C. Electrode Systems for Continuous Monitoring in Cardiovascular Surgery. *Ann. N. Y. Acad. Sci.* **1962**, *102*, 29–45.
- (34) Kirsch, J.; Siltanen, C.; Zhou, Q.; Revzin, A.; Simonian, A. Biosensor Technology: Recent Advances in Threat Agent Detection and Medicine. *Chem. Soc. Rev.* **2013**, *42*, 8733.
- (35) Groff, K.; Brown, J.; Clippinger, A. J. Modern Affinity Reagents: Recombinant Antibodies and Aptamers. *Biotechnol. Adv.* **2015**, *33*, 1787–1798.
- (36) Conroy, P. J.; Hearty, S.; Leonard, P.; O’Kennedy, R. J. Antibody Production, Design and Use for Biosensor-Based Applications. *Semin. Cell Dev. Biol.* **2009**,

20, 10–26.

- (37) Ricci, F.; Adornetto, G.; Palleschi, G.; Perfézou, M.; Turner, A. P. F.; Merkoçi, A.; Mattiasson, B.; Hedström, M.; Rivas, G. A.; Rubianes, M. D.; *et al.* Recombinant Antibodies and Their Use in Biosensors. *Biosens. Bioelectron.* **2016**, *34*, 3027–3038.
- (38) Pei, X.; Zhang, B.; Tang, J.; Liu, B.; Lai, W.; Tang, D. Sandwich-Type Immunosensors and Immunoassays Exploiting Nanostructure Labels: A Review. *Anal. Chim. Acta* **2013**, *758*, 1–18.
- (39) Hosu, O.; Tertiş, M.; Melinte, G.; Feier, B.; Săndulescu, R.; Cristea, C. Mucin 4 Detection with a Label-Free Electrochemical Immunosensor. *Electrochem. commun.* **2017**, *80*, 39–43.
- (40) Wu, F. F.; Zhou, Y.; Wang, J. X.; Zhuo, Y.; Yuan, R.; Chai, Y. Q. A Novel Electrochemiluminescence Immunosensor Based on Mn Doped Ag<sub>2</sub>S Quantum Dots Probe for Laminin Detection. *Sensors Actuators, B Chem.* **2017**, *243*, 1067–1074.
- (41) Wang, R.; Feng, J. J.; Liu, W. D.; Jiang, L. Y.; Wang, A. J. A Novel Label-Free Electrochemical Immunosensor Based on the Enhanced Catalytic Currents of Oxygen Reduction by AuAg Hollow Nanocrystals for Detecting Carbohydrate Antigen 199. *Biosens. Bioelectron.* **2017**, *96*, 152–158.
- (42) Afkhami, A.; Hashemi, P.; Bagheri, H.; Salimian, J.; Ahmadi, A.; Madrakian, T. Impedimetric Immunosensor for the Label-Free and Direct Detection of Botulinum Neurotoxin Serotype A Using Au Nanoparticles/graphene-Chitosan Composite. *Biosens. Bioelectron.* **2017**, *93*, 124–131.
- (43) Xu, T.; Chi, B.; Gao, J.; Chu, M.; Fan, W.; Yi, M.; Xu, H.; Mao, C. Novel

- Electrochemical Immune Sensor Based on Hep-PGA-PPy Nanoparticles for Detection of  $\alpha$ -Fetoprotein in Whole Blood. *Anal. Chim. Acta* **2017**, *977*, 36–43.
- (44) Burcu Bahadir, E.; Kemal Sezgintürk, M. Applications of Electrochemical Immunosensors for Early Clinical Diagnostics. *Talanta* **2015**, *132*, 162–174.
- (45) Gopinath, S. C. B.; Lakshmipriya, T.; Chen, Y.; Phang, W. M.; Hashim, U. Aptamer-Based “Point-of-Care Testing.” *Biotechnol. Adv.* **2016**, *34*, 198–208.
- (46) Ellington, a D.; Szostak, J. W. In Vitro Selection of RNA Molecules That Bind Specific Ligands. *Nature* **1990**, *346*, 818–822.
- (47) Tuerk, C.; Gold, L. Systematic Evolution of Ligands by Exponential Enrichment : RNA Ligands to Bacteriophage EI-T. *Science (80-. ).* **1990**, *249*, 505–510.
- (48) Robertson, D. L.; Joyce, G. F. Selection in Vitro of an RNA Enzyme That Specifically Cleaves Single-Stranded DNA. *Nature*, 1990, *344*, 467–468.
- (49) Zhou, W.; Huang, P.-J. J.; Ding, J.; Liu, J. Aptamer-Based Biosensors for Biomedical Diagnostics. *Analyst* **2014**, *139*, 2627–2640.
- (50) Chen, H.; Huang, J.; Palaniappan, A.; Wang, Y.; Liedberg, B.; Platt, M.; Tok, A. I. Y. A Review on Electronic Bio-Sensing Approaches Based on Non-Antibody Recognition Elements. *Analyst* **2016**, *141*, 2335–2346.
- (51) Lin, X.; Sun, X.; Luo, S.; Liu, B.; Yang, C. Development of DNA-Based Signal Amplification and Microfluidic Technology for Protein Assay: A Review. *TrAC - Trends Anal. Chem.* **2016**, *80*, 132–148.
- (52) Malvano, F.; Albanese, D.; Pilloton, R.; Di Matteo, M. A New Label-Free Impedimetric Aptasensor for Gluten Detection. *Food Control* **2017**, *79*, 200–206.
- (53) Erdem, A.; Congur, G. Dendrimer Enriched Single-Use Aptasensor for

Impedimetric Detection of Activated Protein C. *Colloids Surfaces B Biointerfaces* **2014**, *117*, 338–345.

- (54) Abnous, K.; Danesh, N. M.; Alibolandi, M.; Ramezani, M.; Sarreshtehdar Emrani, A.; Zolfaghari, R.; Taghdisi, S. M. A New Amplified Pi-Shape Electrochemical Aptasensor for Ultrasensitive Detection of Aflatoxin B1. *Biosens. Bioelectron.* **2017**, *94*, 374–379.
- (55) Tamayo, J.; Kosaka, P. M.; Ruz, J. J.; San Paulo, Á.; Calleja, M. Biosensors Based on Nanomechanical Systems. *Chem. Soc. Rev.* **2013**, *42*, 1287–1311.
- (56) Nanotechnological Basis for Advanced Sensors. In *Proceedings of the Nato Advanced Study Institute on Nanotechnological Basis for Advanced Sensors e-book*; Reithmaier, J. .; Paunovic, P.; Kulisch, W.; Popov, C.; Petkov, P., Eds.; Springer: Sozopol , Bulgaria, 2010.
- (57) NIH Public Access. *Arlett, J.L Mayers, E.B Roukes, M.L* **2013**, *6*.
- (58) Liu, B.; Chen, X.; Cai, H. L.; Mohanmmad, A. M.; Tian, X. G.; Tao, L. Q.; Yang, Y.; Ren, T. L. Surface Acoustic Wave Devices for Sensor Applications. *J. Semicond.* **2016**, *37*, 21001.
- (59) Rocha-Gaso, M. I.; March-Iborra, C.; Montoya-Baides, Á.; Arnau-Vives, A. Surface Generated Acoustic Wave Biosensors for the Detection of Pathogens: A Review. *Sensors* **2009**, *9*, 5740–5769.
- (60) Afzal, A.; Mujahid, A.; Schirhagl, R.; Bajwa, S. Z.; Latif, U. Gravimetric Viral Diagnostics : QCM Based Biosensors for Early Detection of Viruses. **2017**, 1–25.
- (61) Crivianu-Gaita, V.; Aamer, M.; Posaratnanathan, R. T.; Romaschin, A.; Thompson, M. Acoustic Wave Biosensor for the Detection of the Breast and Prostate Cancer Metastasis Biomarker Protein PTHrP. *Biosens. Bioelectron.*



**2015**, 78, 92–99.

- (62) Hong, S. R.; Kim, M. S.; Jeong, H. Do; Hong, S. Development of Real-Time and Quantitative QCM Immunosensor for the Rapid Diagnosis of *Aeromonas Hydrophila* Infection. *Aquac. Res.* **2017**, 48, 2055–2063.
- (63) Skládal, P. Piezoelectric Biosensors. *TrAC - Trends Anal. Chem.* **2016**, 79, 127–133.
- (64) Ferreira, G. N. M.; da-Silva, A.-C.; Tomé, B. Acoustic Wave Biosensors: Physical Models and Biological Applications of Quartz Crystal Microbalance. *Trends Biotechnol.* **2009**, 27, 689–697.
- (65) Boisen, A.; Dohn, S.; Keller, S. S.; Schmid, S.; Tenje, M. Cantilever-like Micromechanical Sensors. *Reports Prog. Phys.* **2011**, 74, 36101.
- (66) Raiteri, R.; Grattarola, M.; Butt, H. .; Skládal, P. Micromechanical Cantilever-Based Biosensors. *sensors Actuators B* **2001**, 79, 115–126.
- (67) Gauglitz, G. Direct Optical Sensors: Principles and Selected Applications. *Anal. Bioanal. Chem.* **2005**, 381, 141–155.
- (68) Nanotechnological Basis for Advanced Sensors. In *Nato Science for Peace and Security Series-B*; Reithmaier, J. .; Paunovic, P.; Kulisch, W.; Petkov, P., Eds.; Springer: Sozopol, Bulgaria, 2011.
- (69) Liu, Y.; Zhou, H.; Hu, Z.; Yu, G.; Yang, D.; Zhao, J. Label and Label-Free Based Surface-Enhanced Raman Scattering for Pathogen Bacteria Detection: A Review. *Biosens. Bioelectron.* **2017**, 94, 131–140.
- (70) Fan, X.; White, I. M.; Shopova, S. I.; Zhu, H.; Suter, J. D.; Sun, Y. Sensitive Optical Biosensors for Unlabeled Targets: A Review. *Anal. Chim. Acta* **2008**, 620, 8–26.

- (71) Cooper, M. A. Label-Free Screening of Bio-Molecular Interactions. *Anal. Bioanal. Chem.* **2003**, *377*, 834–842.
- (72) Karlsson, R.; Katsamba, P. S.; Nordin, H.; Pol, E.; Myszka, D. G. Analyzing a Kinetic Titration Series Using Affinity Biosensors. *Anal. Biochem.* **2006**, *349*, 136–147.
- (73) Im, H.; Lesuffleur, A.; Lindquist, N. C.; Oh, S. H. Plasmonic Nanoholes in a Multichannel Microarray Format for Parallel Kinetic Assays and Differential Sensing. *Anal. Chem.* **2009**, *81*, 2854–2859.
- (74) López-Muñoz, G. A.; Estevez, M. C.; Peláez-Gutierrez, E. C.; Homs-Corbera, A.; García-Hernandez, M. C.; Imbaud, J. I.; Lechuga, L. M. A Label-Free Nanostructured Plasmonic Biosensor Based on Blu-Ray Discs with Integrated Microfluidics for Sensitive Biodetection. *Biosens. Bioelectron.* **2017**, *96*, 260–267.
- (75) Singh, P. SPR Biosensors: Historical Perspectives and Current Challenges. *Sensors Actuators, B Chem.* **2016**, *229*, 110–130.
- (76) Ronkainen, N. J.; Halsall, H. B.; Heineman, W. R. Electrochemical Biosensors. *Chem. Soc. Rev.* **2010**, *39*, 1747–1763.
- (77) Bansod, B. K.; Kumar, T.; Thakur, R.; Rana, S.; Singh, I. A Review on Various Electrochemical Techniques for Heavy Metal Ions Detection with Different Sensing Platforms. *Biosens. Bioelectron.* **2017**, *94*, 443–455.
- (78) Hughes, G.; Westmacott, K.; Honeychurch, K. C.; Crew, A.; Pemberton, R. M.; Hart, J. P. Recent Advances in the Fabrication and Application of Screen-Printed Electrochemical (Bio)sensors Based on Carbon Materials for Biomedical, Agri-Food and Environmental Analyses. *Biosensors* **2016**, *6*.
- (79) Vasilescu, A.; Nunes, G.; Hayat, A.; Latif, U.; Marty, J. L. Electrochemical Affinity

Biosensors Based on Disposable Screen-Printed Electrodes for Detection of Food Allergens. *Sensors (Switzerland)* **2016**, *16*.

- (80) Chu, Z.; Peng, J.; Jin, W. Advanced Nanomaterial Inks for Screen-Printed Chemical Sensors. *Sensors Actuators, B Chem.* **2017**, *243*, 919–926.
- (81) Mohammed, M.-I.; Desmulliez, M. P. Y. Lab-on-a-Chip Based Immunosensor Principles and Technologies for the Detection of Cardiac Biomarkers: A Review. *Lab Chip* **2010**, *11*, 569–595.
- (82) Daniels, J. S.; Pourmand, N. Label-Free Impedance Biosensors: Opportunities and Challenges. *Electroanalysis* **2007**, *19*, 1239–1257.
- (83) Palchetti, I.; Mascini, M. Electroanalytical Biosensors and Their Potential for Food Pathogen and Toxin Detection. *Anal. Bioanal. Chem.* **2008**, *391*, 455–471.
- (84) Deng, B.; Lin, Y.; Wang, C.; Li, F.; Wang, Z.; Zhang, H.; Li, X. F.; Le, X. C. Aptamer Binding Assays for Proteins: The Thrombin Example-A Review. *Analytica Chimica Acta*, 2014, 837.
- (85) Maragoudakis, M. E.; Tsopanoglou, N. E. *Thrombin: Physiology and Disease*; Lecture notes in control and information sciences; Springer New York, 2010.
- (86) Arai, T.; Miklossy, J.; Klegeris, A.; Guo, J.-P.; McGeer, P. L. Thrombin and Prothrombin Are Expressed by Neurons and Glial Cells and Accumulate in Neurofibrillary Tangles in Alzheimer Disease Brain. *J. Neuropathol. Exp. Neurol.* **2006**, *65*, 19–25.
- (87) Sokolova, E.; Reiser, G. Prothrombin/thrombin and the Thrombin Receptors PAR-1 and PAR-4 in the Brain: Localization, Expression and Participation in Neurodegenerative Diseases. *Thromb. Haemost.* **2008**, *100*, 576–581.
- (88) Deep Vein Thrombosis (DVT) Can Be a Killer. Here's How to Understand and

Prevent DVT—at Any Age. *Spring* **2011**, 6, 18–22.

- (89) Soslau, G.; Goldenberg, S. J.; Class, R.; Jameson, B. Differential Activation and Inhibition of Human Platelet Thrombin Receptors by Structurally Distinct  $\alpha$ -,  $\beta$ - and  $\gamma$ -Thrombin. *Platelets* **2004**, 15, 155–166.
- (90) Hasegawa, H.; Taira, K.; Sode, K.; Ikebukuro, K. Improvement of Aptamer Affinity by Dimerization. *Sensors* **2008**, 8, 1090–1098.
- (91) Xiao, Y.; Piorek, B. D.; Plaxco, K. W.; Heeger, A. J. A Reagentless Signal-on Architecture for Electronic, Aptamer-Based Sensors via Target-Induced Strand Displacement. *J. Am. Chem. Soc.* **2005**, 127, 17990–17991.
- (92) Polsky, R.; Gill, R.; Kaganovsky, L.; Willner, I. Nucleic Acid-Functionalized Pt Nanoparticles: Catalytic Labels for the Amplified Electrochemical Detection of Biomolecules. *Anal. Chem.* **2006**, 78, 2268–2271.
- (93) Choi, J. H.; Chen, K. H.; Strano, M. S. Aptamer-Capped Nanocrystal Quantum Dots: A New Method for Label-Free Protein Detection. *J. Am. Chem. Soc.* **2006**, 128, 15584–15585.
- (94) He, P.; Shen, L.; Cao, Y.; Li, D. Ultrasensitive Electrochemical Detection of Proteins by Amplification of Aptamer-Nanoparticle Bio Bar Codes. *Anal. Chem.* **2007**, 79, 8024–8029.
- (95) Deng, C.; Chen, J.; Nie, Z.; Wang, M.; Chu, X.; Chen, X.; Xiao, X.; Lei, C.; Yao, S. Impedimetric Aptasensor with Femtomolar Sensitivity Based on the Enlargement of Surface-Charged Gold Nanoparticles. *Anal. Chem.* **2009**, 81, 739–745.
- (96) Mannoor, M. S.; James, T.; Ivanov, D. V.; Beadling, L.; Braunlin, W. Nanogap Dielectric Spectroscopy for Aptamer-Based Protein Detection. *Biophys. J.* **2010**,

98, 724–732.

- (97) Zhang, Y.; Li, B.; Jin, Y. Label-Free Fluorescent Detection of Thrombin Using G-Quadruplex-Based DNAzyme as Sensing Platform. *Analyst* **2011**, *136*, 3268.
- (98) Hu, J.; Wang, T.; Kim, J.; Shannon, C.; Easley, C. J. Quantitation of Femtomolar Protein Levels via Direct Readout with the Electrochemical Proximity Assay. *J. Am. Chem. Soc.* **2012**, *134*, 7066–7072.
- (99) Li, J.; Zhong, X.; Zhang, H.; Le, X. C.; Zhu, J. J. Binding-Induced Fluorescence Turn-on Assay Using Aptamer-Functionalized Silver Nanocluster DNA Probes. *Anal. Chem.* **2012**, *84*, 5170–5174.
- (100) Deng, N.; Liang, Z.; Liang, Y.; Sui, Z.; Zhang, L.; Wu, Q.; Yang, K.; Zhang, L.; Zhang, Y. Aptamer Modified Organic – Inorganic Hybrid Silica Monolithic Capillary Columns for Highly Selective Recognition of Thrombin. *Anal. Chem.* **2012**, *84*, 10186–10190.
- (101) Chen, Y.; Nakamoto, K.; Niwa, O.; Corn, R. M. On-Chip Synthesis of RNA Aptamer Microarrays for Multiplexed Protein Biosensing with SPR Imaging Measurements. *Langmuir* **2012**, *28*, 8281–8285.
- (102) Bai, L.; Yuan, R.; Chai, Y.; Yuan, Y.; Wang, Y.; Xie, S. Direct Electrochemistry and Electrocatalysis of a Glucose Oxidase-Functionalized Bioconjugate as a Trace Label for Ultrasensitive Detection of Thrombin. *Chem. Commun.* **2012**, *48*, 10972.
- (103) Xue, L.; Zhou, X.; Xing, D. Sensitive and Homogeneous Protein Detection Based on Target-Triggered Aptamer Hairpin Switch and Nicking Enzyme Assisted Fluorescence Signal Amplification. *Anal. Chem.* **2012**, *84*, 3507–3513.
- (104) Das, J.; Cederquist, K. B.; Zaragoza, A. A.; Lee, P. E.; Sargent, E. H.; Kelley, S.

- O. An Ultrasensitive Universal Detector Based on Neutralizer Displacement. *Nat. Chem.* **2012**, *4*, 642–648.
- (105) Zheng, D.; Zou, R.; Lou, X. Label-Free Fluorescent Detection of Ions, Proteins, and Small Molecules Using Structure-Switching Aptamers, SYBR Gold, and Exonuclease I. *Anal. Chem.* **2012**, *84*, 3554–3560.
- (106) Zhang, H.; Li, F.; Li, X. F.; Le, X. C. Yoctomole Detection of Proteins Using Solid Phase Binding-Induced DNA Assembly. *Methods* **2013**, *64*, 322–330.
- (107) Eksin, E.; Erdem, A.; Kuruc, A. P.; Kayi, H.; Öğünç, A. Impedimetric Aptasensor Based on Disposable Graphite Electrodes Developed for Thrombin Detection. *Electroanalysis* **2015**, *27*, 2864–2871.
- (108) Erdem, A.; Congur, G.; Mayer, G. Aptasensor Platform Based on Carbon Nanofibers Enriched Screen Printed Electrodes for Impedimetric Detection of Thrombin. *J. Electroanal. Chem.* **2015**, *758*, 12–19.
- (109) Hao, L.; Zhao, Q. Microplate Based Assay for Thrombin Detection Using an RNA Aptamer as Affinity Ligand and Cleavage of a Chromogenic or a Fluorogenic Peptide Substrate. *Microchim. Acta* **2016**, *183*, 1891–1898.
- (110) Zhao, Y.; Liu, X.; Li, J.; Qiang, W.; Sun, L.; Li, H.; Xu, D. Microfluidic Chip-Based Silver Nanoparticles Aptasensor for Colorimetric Detection of Thrombin. *Talanta* **2016**, *150*, 81–87.
- (111) Jiang, B.; Li, F.; Yang, C.; Xie, J.; Xiang, Y.; Yuan, R. Target-Induced Catalytic Hairpin Assembly Formation of Functional Y-Junction DNA Structures for Label-Free and Sensitive Electrochemical Detection of Human Serum Proteins. *Sensors Actuators, B Chem.* **2017**, *244*, 61–66.
- (112) Jung, Y. K.; Kim, K. N.; Baik, J. M.; Kim, B. S. Self-Powered Triboelectric

- Aptasensor for Label-Free Highly Specific Thrombin Detection. *Nano Energy* **2016**, *30*, 77–83.
- (113) Suni, I. I. Impedance Methods for Electrochemical Sensors Using Nanomaterials. *TrAC - Trends Anal. Chem.* **2008**, *27*, 604–611.
- (114) Pejčić, B.; De Marco, R. Impedance Spectroscopy: Over 35 Years of Electrochemical Sensor Optimization. *Electrochim. Acta* **2006**, *51*, 6217–6229.
- (115) Webster, G. Acoustical Impedance and the Theory of Horns and of the Phonograph. *Proc. Natl. Acad. Sci. U. S. A.* **1919**, *5*, 275–282.
- (116) Barsoukov, E.; Macdonald, J. R. *Impedance Spectroscopy*; 2005.
- (117) Randviir, E. P.; Banks, C. E. Electrochemical Impedance Spectroscopy: An Overview of Bioanalytical Applications. *Anal. Methods* **2013**, *5*, 1098–1115.
- (118) Bard, A. J.; Faulkner, L. R.; York, N.; @bullet, C.; Brisbane, W.; Toronto, S. E. *ELECTROCHEMICAL METHODS Fundamentals and Applications*; 1944.
- (119) Lisdat, F.; Schäfer, D. The Use of Electrochemical Impedance Spectroscopy for Biosensing. *Anal. Bioanal. Chem.* **2008**, *391*, 1555–1567.
- (120) Mala, G. M.; Yang, C.; Li, D. Electrical Double Layer Potential Distribution in a Rectangular Microchannel. *Colloids Surfaces A Physicochem. Eng. Asp.* **1998**, *135*, 109–116.
- (121) Gongadze, E.; Rienen, U.; Iglič, A. Generalized Stern Models of the Electric Double Layer Considering the Spatial Variation of Permittivity and Finite Size of Ions in Saturation Regime. *Cell. Mol. Biol. Lett.* **2011**, *16*, 576–594.
- (122) Du, H.; Lin, X.; Xu, Z.; Chu, D. *Electric Double-Layer Transistors: A Review of Recent Progress*; Springer US, 2015; Vol. 50.

- (123) Ishai, P. Ben; Talary, M. S.; Caduff, A.; Levy, E.; Feldman, Y. Electrode Polarization in Dielectric Measurements: A Review. *Meas. Sci. Technol.* **2013**, *24*, 102001.
- (124) Pilon, L.; Wang, H.; d'Entremont, A. Recent Advances in Continuum Modeling of Interfacial and Transport Phenomena in Electric Double Layer Capacitors. *J. Electrochem. Soc.* **2015**, *162*, A5158–A5178.
- (125) Hatsuki, R.; Yujiro, F.; Yamamoto, T. Direct Measurement of Electric Double Layer in a Nanochannel by Electrical Impedance Spectroscopy. *Microfluid. Nanofluidics* **2012**, *14*, 983–988.
- (126) Harrington, D. A.; Van Den Driessche, P. Equivalent Circuits for Some Surface Electrochemical Mechanisms. *J. Electroanal. Chem.* **2004**, *567*, 153–166.
- (127) Harrington, D. A.; Van Den Driessche, P. Mechanism and Equivalent Circuits in Electrochemical Impedance Spectroscopy. *Electrochim. Acta* **2011**, *56*, 8005–8013.
- (128) Application, A.; Eis, N. Electrochemical Impedance Spectroscopy ( EIS ) Part 3 – Data Analysis. *Metrohm Autolab* **2011**.
- (129) Xu, Q.; Davis, J. J. The Diagnostic Utility of Electrochemical Impedance. *Electroanalysis* **2014**, *26*, 1249–1258.
- (130) Bueno, P. R. Capacitance Spectroscopy : A Versatile Approach To Resolving the Redox Density of States and Kinetics in Redox-Active Self-Assembled Monolayers Capacitance Spectroscopy : A Versatile Approach To Resolving the Redox Density of States and Kinetics in Redox-. **2012**.
- (131) Pei, R.; Cheng, Z.; Wang, E.; Yang, X. Amplification of Antigen-Antibody Interactions Based on Biotin Labeled Protein-Streptavidin Network Complex



- Using Impedance Spectroscopy. *Biosens. Bioelectron.* **2001**, *16*, 355–361.
- (132) Prodromidis, M. I. Impedimetric Immunosensors-A Review. *Electrochim. Acta* **2010**, *55*, 4227–4233.
- (133) Berggren, C.; Bjarnason, B.; Johansson, G. Capacitive Biosensors. *Electroanalysis* **2001**, *13*, 173–180.
- (134) Dak, P.; Alam, M. A. *Non-Faradaic Impedance Model of a Biochemical Sensor*; 2015.
- (135) Liu, H.; Malhotra, R.; Peczu, M. W.; Rusling, J. F. Electrochemical Immunosensors for Antibodies to Peanut Allergen Ara h2 Using Gold Nanoparticle-Peptide Films. *Anal. Chem.* **2010**, *82*, 5865–5871.
- (136) *Application Note AC-1 Subject: Basics of Electrochemical Impedance Spectroscopy*; 1987; pp. 1–13.
- (137) Orazem, M. E.; Pébère, N.; Tribollet, B. Enhanced Graphical Representation of Electrochemical Impedance Data. *J. Electrochem. Soc.* **2006**, *153*, 129.
- (138) Park, S.-M.; Yoo, J.-S. Electrochemical Impedance Spectroscopy for Better Electrochemical Measurements. *Anal. Chem.* **2003**, *75*, 455 A-461 A.
- (139) Ricci, F.; Adornetto, G.; Paleschi, G. A Review of Experimental Aspects of Electrochemical Immunosensors. *Electrochim. Acta* **2012**, *84*, 74–83.
- (140) Siddiqui, S.; Arumugam, P. U.; Chen, H.; Li, J.; Meyyappan, M. Characterization of Carbon Nanofiber Electrode Arrays Using Electrochemical Impedance Spectroscopy: Effect of Scaling down Electrode Size. *ACS Nano* **2010**, *4*, 955–961.
- (141) Arya, S. K.; Chornokur, G.; Venugopal, M.; Bhansali, S. Antibody Functionalized

- Interdigitated Micro-Electrode (IDmicroE) Based Impedimetric Cortisol Biosensor. *Analyst* **2010**, *135*, 1941–1946.
- (142) Rana, S.; Page, R. H.; McNeil, C. J. Impedance Spectra Analysis to Characterize Interdigitated Electrodes as Electrochemical Sensors. *Electrochim. Acta* **2011**, *56*, 8559–8563.
- (143) Ohno, R.; Ohnuki, H.; Wang, H.; Yokoyama, T.; Endo, H.; Tsuya, D.; Izumi, M. Electrochemical Impedance Spectroscopy Biosensor with Interdigitated Electrode for Detection of Human Immunoglobulin A. *Biosens. Bioelectron.* **2013**, *40*, 422–426.
- (144) Madou, M. J.; Cubicciotti, R. Scaling Issues in Chemical and Biological Sensors. *Proc. IEEE* **2003**, *91*, 830–838.
- (145) Chen, X.; Guo, Z.; Yang, G. M.; Li, J.; Li, M. Q.; Liu, J. H.; Huang, X. J. Electrical Nanogap Devices for Biosensing. *Mater. Today* **2010**, *13*, 28–41.
- (146) Li, T.; Hu, W.; Zhu, D. Nanogap Electrodes. *Adv. Mater.* **2010**, *22*, 286–300.
- (147) Nevill, J. T.; Malleo, D. Nanogap Biosensors. In *Encyclopedia of Nanotechnology*; Bhushan, B., Ed.; Springer Netherlands, 2012; pp. 1544–1552.
- (148) Cui, A.; Dong, H.; Hu, W. Nanogap Electrodes towards Solid State Single-Molecule Transistors. *Small* **2015**, *11*, 6115–6141.
- (149) Roy, S.; Chen, X.; Li, M. H.; Peng, Y.; Anariba, F.; Gao, Z. Mass-Produced Nanogap Sensor Arrays for Ultrasensitive Detection of DNA. *J. Am. Chem. Soc.* **2009**, *131*, 12211–12217.
- (150) Zaffino, R. L.; Mir, M.; Samitier, J. Label-Free Detection of DNA Hybridization and Single Point Mutations in a Nano-Gap Biosensor. *Nanotechnology* **2014**, *25*.

- (151) Strobel, S.; Arinaga, K.; Hansen, A.; Tornow, M. A Silicon-on-Insulator Vertical Nanogap Device for Electrical Transport Measurements in Aqueous Electrolyte Solution. *Nanotechnology* **2007**, *18*.
- (152) Ionescu-Zanetti, C.; Nevill, J. T.; Di Carlo, D.; Jeong, K. H.; Lee, L. P. Nanogap Capacitors: Sensitivity to Sample Permittivity Changes. *J. Appl. Phys.* **2006**, *99*, 1–5.
- (153) Takashima, S. Dielectric Dispersion of DNA. *J. Mol. Biol.* **1963**, *7*, 455–467.
- (154) Takashima, S. Dielectric Dispersion of Deoxyribonucleic Acid. II. *J. Phys. Chem.* **1966**, *70*, 1372–1380.
- (155) Takashima, S.; Gabriel, C.; Sheppard, R. J.; Grant, E. H. Dielectric Behavior of DNA Solution at Radio and Microwave Frequencies (at 20 Degrees C). *Biophys. J.* **1984**, *46*, 29–34.
- (156) van der Touw, F.; Mandel, M. Dielectric Increment and Dielectric Dispersion of Solutions Containing Simple Charged Linear Macromolecules. II. Experimental Results with Synthetic Polyelectrolytes. *Biophys. Chem.* **1974**, *2*, 231–241.
- (157) Vreugdenhil, T.; van der Touw, F.; Mandel, M. Electric Permittivity and Dielectric Dispersion of Low-Molecular Weight DNA at Low Ionic Strength. *Biophys. Chem.* **1979**, *10*, 67–80.
- (158) Saif, B.; Mohr, R. K.; Montrose, C. J.; Litovitz, T. a. On the Mechanism of Dielectric Relaxation in Aqueous DNA Solutions. *Biopolymers* **1991**, *31*, 1171–1180.
- (159) Baker-Jarvis, J.; Jones, C. A.; Riddle, B. *Electrical Properties and Dielectric Relaxation of DNA in Solution*; NIST, 1998; Vol. 1509.
- (160) Feldman, Y.; Nigmatullin, R.; Polygalov, E.; Texter, J. Fractal-Polarization Correction in Time Domain Dielectric Spectroscopy. *Phys. Rev. E* **1998**, *58*, 7561–

7565.

- (161) Oh, S.; Lee, J. S.; Jeong, K. H.; Lee, L. P. Minimization of Electrode Polarization Effect by Nanogap Electrodes for Biosensor Applications. *Sixt. Annu. Int. Conf. Micro Electro Mech. Syst. 2003. MEMS-03 Kyoto. IEEE* **2003**, 52–55.
- (162) Nevill, J. T.; Jeong, K. H.; Lee, L. P. Ultrasensitive Nanogap Biosensor to Detect Changes in Structure of Water and Ice. *13th Int. Conf. Solid-State Sensors, Actuators Microsystems, 2005. Dig. Tech. Pap. TRANSDUCERS '05.* **2005**, 2, 1577–1580.
- (163) Seshadri, S.; Chin, K. B.; Buehler, M. G.; Anderson, R. C. Using Electrical Impedance Spectroscopy to Detect Water in Planetary Regoliths. *Astrobiology* **2008**, 8, 781–792.
- (164) Fricke, H.; Curtis, H. J. Dielectric Properties of Water-Dielectric Interphases. *J.Phys.Chem* **1937**, 41, 729.
- (165) Schwan, H. P. Electrical Properties of Tissues and Cell Suspensions: Mechanisms and Models. *Proc. 16th Annu. Int. Conf. IEEE Eng. Med. Biol. Soc.* **1994**, 70–71.
- (166) Bernengo, J. C.; Hanss, M. Four-Electrode, Very-Low-Frequency Impedance Comparator for Ionic Solutions. *Rev. Sci. Instrum.* **1976**, 47, 505–508.
- (167) Yi, M.; Jeong, K. H.; Lee, L. P. Theoretical and Experimental Study towards a Nanogap Dielectric Biosensor. *Biosens. Bioelectron.* **2005**, 20, 1320–1326.
- (168) Ionescu-Zanetti, C.; Nevill, J. T.; Di Carlo, D.; Jeong, K. H.; Lee, L. P. Nanogap Capacitors: Sensitivity to Sample Permittivity Changes. *J. Appl. Phys.* **2006**, 99.
- (169) Schwan, H. P. Alternating Current Electrode Polarization. *Biophysik* **1966**, 3, 181–201.

- (170) Nevill, J. T.; Di Carlo, D.; Liu, P.; Jeong, K. R.; Lee, L. P. Detection of Protein Conformational Changes with a Nanogap Biosensor. *13th Int. Conf. Solid-State Sensors, Actuators Microsystems, 2005. Dig. Tech. Pap. TRANSDUCERS '05.* **2005**, 2, 1668–1671.
- (171) Verwey, E. J. W. The Electrical Double Layer and the Stability of Lyophobic Colloids. *Chem. Rev.* **1935**, 16, 363–415.
- (172) Verwey, E. J. .; Overbeek, J. T. . *Theory of the Stability of Lyophobic Colloids*; Elsevier publication company.inc, 1948.
- (173) Lee, J.; Choi, Y.; Pio, M.; Seo, J.; Lee, L. Nanogap Capacitors for Label Free DNA Analysis. *Mater. Res. Soc. Symp.Proc* **2002**, 729, 185–190.
- (174) Dhahi, T. S.; Ali, M. E.; Hashim, U.; Saif, A. A.; Nazwa, T. 5 Nm Gap Via Conventional Photolithography and Pattern-Size Reduction Technique. *Int. J. Phys. Sci.* **2011**, 6, 3649–3656.
- (175) Dhahi, T. S.; Hashim, U.; Ali, M. E.; Taib, N.; Dhahi, T. S.; Hashim, U.; Ali, M. E.; Taib, N. Microelectronics International Emerald Article : Polysilicon Nanogap Fabrication Using a Thermal Oxidation Process Polysilicon Nanogap Fabrication Using a Thermal Oxidation Process. *Microelectron. Int.* **2012**, 29, 40–46.
- (176) Dhahi, T. S.; Ali, M. E.; Hashim, U. Electrical Properties of Silicon-Based Nanogap Electrodes for Label-Free Biomolecular Detection. *J. Nanoelectron. Optoelectron.* **2013**, 8, 1–4.
- (177) Dhahi, T. S. Nanogaps Formation and Characterization via Chemical and Oxidation Methods. *Microsyst. Technol.* **2016**, 22, 817–822.
- (178) Surmenev, R. A. A Review of Plasma-Assisted Methods for Calcium Phosphate-Based Coatings Fabrication. *Surf. Coatings Technol.* **2012**, 206, 2035–2056.

- (179) He, L.; Xu, J. Properties of Amorphous SiO<sub>2</sub> Films Prepared by Reactive RF Magnetron Sputtering Method. *Vacuum* **2003**, *68*, 197–202.
- (180) Lehninger, D.; Beyer, J.; Schneider, F.; Pawlik, A. S.; Heitmann, J. Size and Shape Controlled Semiconductor Nanocrystals Synthesized by RF-Sputtering Techniques for Electronic and Optoelectronic Applications. *Contrib. to Plasma Phys.* **2015**, *55*, 714–727.
- (181) Bhatt, V.; Chandra, S. Silicon Dioxide Films by RF Sputtering for Microelectronic and MEMS Applications. *J. Micromechanics Microengineering* **2007**, *17*, 1066–1077.
- (182) Jalili, N.; Laxminarayana, K. A Review of Atomic Force Microscopy Imaging Systems: Application to Molecular Metrology and Biological Sciences. *Mechatronics* **2004**, *14*, 907–945.
- (183) Müller, D. J.; Dufrêne, Y. F. Atomic Force Microscopy: A Nanoscopic Window on the Cell Surface. *Trends Cell Biol.* **2011**, *21*, 461–469.
- (184) Seker, E.; Berdichevsky, Y.; Begley, M. R.; Reed, M. L.; Staley, K. J.; Yarmush, M. L. The Fabrication of Low-Impedance Nanoporous Gold Multiple-Electrode Arrays for Neural Electrophysiology Studies. *Nanotechnology* **2010**, *21*, 125504.
- (185) Wu, W.-F.; Chiou, B.-S. Properties of Radio Frequency Magnetron Sputtered Silicon Dioxide Films. *Appl. Surf. Sci.* **1996**, *99*, 237–243.
- (186) Waser, R. *Nanoelectronics and Information Technology*; 2nd editio.; WILEY-VCH Verlag GmbH & Co.KGaA: Weinheim, 2005.
- (187) Fouad, K. A Practical Approach to Reactive Ion Etching. *J. Phys. D. Appl. Phys.* **2014**, *47*, 233501.
- (188) Nayak, A. P.; Vj, L.; Islam, M. S. Wet and Dry Etching. 1–5.

- (189) Whitesides, G. M. The Origins and the Future of Microfluidics. *Nature* **2006**, *442*, 368–373.
- (190) Roy, E.; Galas, J.-C.; Veres, T. Thermoplastic Elastomers for Microfluidics: Towards a High-Throughput Fabrication Method of Multilayered Microfluidic Devices. *Lab Chip* **2011**, *11*, 3193.
- (191) Choi, S.; Goryll, M.; Sin, L. Y. M.; Wong, P. K.; Chae, J. Microfluidic-Based Biosensors toward Point-of-Care Detection of Nucleic Acids and Proteins. *Microfluid. Nanofluidics* **2011**, *10*, 231–247.
- (192) Bange, A.; Halsall, H. B.; Heineman, W. R. Microfluidic Immunosensor Systems. *Biosens. Bioelectron.* **2005**, *20*, 2488–2503.
- (193) Samiei, E.; Luka, G. S.; Najjaran, H.; Hoorfar, M. Integration of Biosensors into Digital Microfluidics: Impact of Hydrophilic Surface of Biosensors on Droplet Manipulation. *Biosens. Bioelectron.* **2016**, *81*, 480–486.
- (194) Aliakbarinodehi, N.; Jolly, P.; Bhalla, N.; Miodek, A.; De Micheli, G.; Estrela, P.; Carrara, S. Aptamer-Based Field-Effect Biosensor for Tenofovir Detection. *Sci. Rep.* **2017**, *7*, 44409.
- (195) *MODEL SR830 DSP Lock-in Amplifier Manual*; 2011.
- (196) Byun, I.; Coleman, A. W.; Kim, B. Transfer of Thin Au Films to Polydimethylsiloxane (PDMS) with Reliable Bonding Using (3-Mercaptopropyl)trimethoxysilane (MPTMS) as a Molecular Adhesive. *J. Micromechanics Microengineering* **2013**, *23*, 85016.
- (197) Robertson, J. High Dielectric Constant Oxides. *Eur. Phys. J. Appl. Phys.* **2004**, *28*, 265–291.
- (198) Lee, S. Y.; Chang, S.; Lee, J. S. Role of High-K Gate Insulators for Oxide Thin

Film Transistors. *Thin Solid Films* **2010**, *518*, 3030–3032.

- (199) Bühler, J.; Steiner, F.-P.; Baltes, H. Silicon Dioxide Sacrificial Layer Etching in Surface Micromachining. *J. Micromechanics Microengineering* **1997**, *7*, R1–R13.
- (200) Nagata, H.; Fujino, T.; Mitsugi, N.; Tamai, M. Effect of Substrate Heating on Elimination of Pinholes in Sputtering Deposited SiO<sub>2</sub> Films on LiNbO<sub>3</sub> Single Crystal Substrates. *Thin Solid Films* **1998**, *335*, 117–121.
- (201) Kim, Y. H.; Kim, G. H.; Baek, N. S.; Jeong, J. I.; Han, Y. H.; Shin, B. C.; Chung, M.-A.; Jung, S.-D. Optimisation of Bi-Layer Resist Overhang Structure Formation and SiO<sub>2</sub> Sputter-Deposition Process for Fabrication of Gold Multi-Electrode Array. *RSC Adv.* **2015**, *5*, 6675–6681.
- (202) Choi, W. K.; Choo, C. K.; Lu, Y. F. Electrical Characterization of Rapid Thermal Annealed Radio Frequency Sputtered Silicon Oxide Films. *J. Appl. Phys.* **1996**, *80*, 5837.
- (203) Wang, Y.; Jia, R.; Zhao, Y.; Li, C.; Zhang, Y. Investigation of Leakage Current Mechanisms in La<sub>2</sub>O<sub>3</sub>/SiO<sub>2</sub>/4H-SiC MOS Capacitors with Varied SiO<sub>2</sub> Thickness. *J. Electron. Mater.* **2016**, *45*, 5600–5605.
- (204) Yu, T.; Jin, C. G.; Dong, Y. J.; Cao, D.; Zhuge, L. J.; Wu, X. M. Temperature Dependence of Electrical Properties for MOS Capacitor with HfO<sub>2</sub>/SiO<sub>2</sub> Gate Dielectric Stack. *Mater. Sci. Semicond. Process.* **2013**, *16*, 1321–1327.
- (205) Tzouvadaki, I.; Jolly, P.; Lu, X.; Ingebrandt, S.; De Micheli, G.; Estrela, P.; Carrara, S. Label-Free Ultrasensitive Memristive Aptasensor. *Nano Lett.* **2016**, *16*, 4472–4476.